

# Cosmology with Large Scale Structures using Massive Spectroscopic Surveys

Présentée le 27 octobre 2022

Faculté des sciences de base  
Laboratoire d'astrophysique  
Programme doctoral en physique

pour l'obtention du grade de Docteur ès Sciences

par

**Amélie TAMONE**

Acceptée sur proposition du jury

Prof. F. Mila, président du jury  
Prof. J.-P. R. Kneib, directeur de thèse  
Dr P. Zarrouk, rapporteuse  
Dr D. Schlegel, rapporteur  
Prof. M. Hirschmann, rapporteuse





“VLADIMIR. – Ça a fait passer le temps.

ESTRAGON. – Il serait passé sans ça.

VLADIMIR. – Oui. Mais moins vite.”

“VLADIMIR. – That passed the time.

ESTRAGON. – It would have passed in any case.

VLADIMIR. – Yes, but not so rapidly.”

— *En attendant Godot*

Samuel Beckett



# Acknowledgements

A mes parents et frères, à ma famille, mes amis pour votre confiance et votre absence de doutes (surtout toi Riccardo) ...

A mon grand-père et ta fierté sans limite, à ma grand-mère partie avant la fin ...

Peut-être pas à la pandémie du covid qui a laissé des traces, mais qui pourtant a aussi apporté beaucoup de changements (bonjour Zürich!) ...

A Jean-Paul pour la confiance que tu m'as accordée et la grande liberté que tu m'as laissée ...

Aux membres du LASTRO, doctorants, postdocs, au groupe 3D-COSMO, à Andrei, Daniel, Jiayi, Claudio pour ces discussions et soutiens hebdomadaires ...

En particulier, à Anand pour ces deux premières années où tu m'as énormément soutenue et aidée avec ces ELGs ...

A Cheng sans qui cette thèse n'aurait pas été pareille, à ta patience sans limite et ton immense aide ...

... merci, merci à tous !



# Abstract

Spectroscopic surveys aim to map large fractions of the Universe to study the Large Scale Structures (LSS). LSS evolution traces the distribution of matter as a result of the tension between the expansion of the Universe and the gravitational forces, which means that LSS can be used to test cosmological and gravity model, in particular the standard model of cosmology ( $\Lambda$ CDM) with General Relativity (GR). One usual way to study those LSS is to quantify the clustering of the galaxies with the 2-point correlation function (2PCF). The Baryon Acoustic Oscillations (BAO) signature is characterised as a peak in the 2PCF, whose position is related to the Hubble parameter. Moreover, Redshift Space Distortions (RSD) are imprinted in the 2PCF and are used to measure the growth rate of structure of the Universe.

In this thesis I measured the growth rate of structure of the emission line galaxy (ELG) sample of the extended Baryon Oscillation Spectroscopic Survey (eBOSS) from RSD in configuration space. I was able along with the Sloan Digital Sky Survey (SDSS) collaboration to participate to the final cosmological implication of the past 20 years of SDSS. By a combination of probes, the current cosmological parameters were then constrained with a high precision, outpassing the expected constraints for Stage-III dark energy experiment.

Moreover I performed a BAO analysis with voids, tracing the underdensities in the quasars (QSO) sample of eBOSS. While the method was shown to bring great improvement on other tracers, it reveals itself more difficult to deal with quasars due to their low density. I was nevertheless able to detect a BAO signal and to provide forecast for a QSO sample from a DESI-like (Dark Energy Spectroscopic Instrument) experiment.

Key words: cosmology – spectroscopic surveys – dark energy – large-scale structures – redshifts



# Résumé

L'accélération de l'expansion de l'Univers est l'un des plus grands mystères non résolus en cosmologie. Les physiciens expliquent ce phénomène par la présence d'une énergie répulsive d'origine inconnue, dominante dans l'Univers, appelée "énergie sombre". Les structures à grande échelle sont le résultat d'une tension entre l'expansion de l'Univers et la force gravitationnelle de la distribution de matière. Pour les étudier, de grandes fractions de l'Univers sont cartographiées par les relevés spectroscopiques. Comme l'évolution de ces structures résulte d'un équilibre de forces, elles peuvent être utilisées pour tester les modèles cosmologiques et gravitationnels, en particulier la relativité générale et le modèle cosmologique standard  $\Lambda$ CDM. Une méthode pour étudier ces structures est de quantifier leur répartition dans l'espace d'une manière statistique avec leur fonction de corrélation. On observe dans cette courbe un excès de galaxies séparées par une certaine distance. Cette distance correspond à une échelle particulière gravée dans le jeune Univers par des ondes acoustiques (BAO). Cette distance est liée à l'expansion de l'Univers et donc au paramètre de Hubble. De plus, des distorsions spatiales dues au décalage vers le rouge des spectres à cause du mouvement des galaxies (RSD) sont imprimées dans la fonction de corrélation. Cet effet permet de mesurer le taux de croissance des structures dans l'Univers.

Dans cette thèse, j'ai mesuré le taux de croissance des structures de l'échantillon de galaxies à raies d'émission du relevé eBOSS (extended Baryon Oscillation Spectroscopic Survey). J'ai pu avec la collaboration SDSS (Sloan Digital Sky Survey) participer à l'implication cosmologique finale des 20 dernières années de SDSS. Grâce à une combinaison de sondes cosmologiques, on a pu contraindre les paramètres du modèle standard avec une grande précision, dépassant les attentes pour une expérience de stade III.

De plus, j'ai effectué une analyse BAO avec des vides, permettant de détecter les sousdensités dans l'échantillon des quasars de eBOSS. Alors que la méthode s'est avérée fructueuse avec d'autres types d'objets astronomiques, elle se révèle plus difficile à traiter avec les quasars en raison de leur faible densité. J'ai néanmoins pu détecter un signal BAO et fournir des prévisions pour un échantillon de quasars à partir d'une expérience comme DESI (Dark Energy Spectroscopic Instrument).

Mots clefs : cosmologie – relevés spectroscopiques – énergie sombre – structures à grande échelle – décalage vers le rouge





# Contents

<b>Acknowledgements</b>	<b>i</b>
<b>Abstract (English/Français)</b>	<b>iii</b>
<b>List of figures</b>	<b>ix</b>
<b>List of tables</b>	<b>xv</b>
<b>List of symbols and abbreviations</b>	<b>xvii</b>
<b>1 Introduction</b>	<b>1</b>
1.1 A few notions of Modern Cosmology . . . . .	1
1.1.1 A brief look into General Relativity . . . . .	2
1.1.2 An expanding Universe . . . . .	4
1.1.3 Geometry and Dynamics . . . . .	7
1.1.4 Big Bang Theory and Evolution of the Universe . . . . .	12
1.1.5 Distances Measurements . . . . .	17
1.1.6 The Standard Model of Cosmology . . . . .	21
1.2 Large-Scale Structures in the Universe . . . . .	28
1.2.1 Formation . . . . .	29
1.2.2 Cosmic Density Field . . . . .	33
1.2.3 Growth of Structures . . . . .	38
1.2.4 Non-linear Approach . . . . .	44
1.2.5 Halo Model . . . . .	46
1.2.6 Galaxy-Halo Connection . . . . .	50
1.2.7 Lagrangian Dynamics . . . . .	54
1.3 Measuring the Expansion with Spectroscopic Surveys . . . . .	58
1.3.1 Cosmic Microwave Background . . . . .	58
1.3.2 Baryon Accoustic Oscillations . . . . .	61
1.3.3 Redshift Space . . . . .	67
1.3.4 Spectroscopic Surveys . . . . .	75
<b>2 RSD analysis of the ELG sample of eBOSS</b>	<b>85</b>
2.1 Cosmological Implications of SDSS . . . . .	85
2.1.1 Constraints from BAO . . . . .	86

2.1.2	Constraints from RSD . . . . .	89
2.1.3	Global Constraints . . . . .	90
2.2	EZmocks . . . . .	92
2.3	Preprint version: “The completed SDSS-IV extended baryon oscillation spectroscopic survey: growth rate of structure measurement from anisotropic clustering analysis in configuration space between redshift 0.6 and 1.1 for the emission-line galaxy sample” . . . . .	93
<b>3</b>	<b>Void BAO analysis with the QSO sample of eBOSS</b>	<b>115</b>
3.1	Cosmic Voids . . . . .	115
3.1.1	Definitions and Algorithms . . . . .	115
3.1.2	Void Properties . . . . .	116
3.1.3	Cosmology Measurements . . . . .	118
3.2	Preprint version: “Void BAO measurements on quasars from eBOSS” . . . . .	120
<b>4</b>	<b>Conclusion</b>	<b>135</b>
	<b>Bibliography</b>	<b>166</b>
	<b>Curriculum Vitae</b>	<b>167</b>

# List of Figures

1.1	Illustration to understand the redshift. On top spectral shift toward the blue from the light of an object moving in the Earth direction. In the middle the spectrum observed of an object as observed in its rest frame. On the bottom spectral shift toward the red from the light of an object moving away from Earth, it corresponds to the shift that the expansion of the Universe would cause. . . .	5
1.2	Illustration of the increased wavelength of a wave due to the Universe expansion with the balloon analogy. (Credits of the figure: James N. Imamura, University of Oregon). . . . .	6
1.3	Hubble diagram from Hubble, 1929. It shows his measurements of the recession velocities as a function of the distances of the nebulae. . . . .	6
1.4	Different Universe geometry. From left to right: closed, open, flat Universes corresponding to elliptic, hyperbolic or flat hyper-surfaces, respectively. Relation of the density $\Omega_0$ with the curvature parameter $\kappa$ is made explicit later in Equation 1.32. (Credits of the figure: (modified from) NASA / WMAP Science Team). . . .	7
1.5	Explicating scheme views of the Universe's space expansion through the different epochs it undergoes. (Credits of the figure: NASA/WMAP Science Team). . . .	12
1.6	Universe's content parameters for a flat cosmology, with $\Omega_m = 0.31$ , $\Omega_\gamma = 0.0001$ , $h = 0.7$ . The vertical dashed lines are the redshifts $z = 1100$ (drag epoch) and $z = 0$ (now). The blue area corresponds to the radiation domination period, the orange the matter area and the green the dark energy. . . . .	14
1.7	Different Universe's evolution scenarios. The curvature density parameter is fixed by the sum rule without radiation. Dashed lines show where we are currently, so now. The crossing points of the curves (on the negative time side) with $a = 0$ are the respective ages of the Universe now for the different models. . . .	16
1.8	Illustrations to understand comoving and proper distances. Space is represented at three different times, $t_2$ , $t_1$ and $t_0$ which is present time. Orange point is our location in space. . . . .	18
1.9	Scheme with angular diameter $\delta\theta$ , angular diameter distance $D_A$ and the transverse proper size $l$ . . . . .	19
1.10	Explaining scheme for standard candles on the left for which a reference luminosity is known and standard rulers on the right for which a physical scale is known. (Credits of the figure: NASA/PL-Caltech/R. Hurt (SSC)). . . . .	20

1.11	Right: Hubble diagram from Riess et al., 1998 for SNe Ia. Left: Confidence intervals in the $\Omega_m, \Omega_\Lambda$ plane from Riess et al., 1998 (on the plot $q \equiv -\ddot{a}a/\dot{a}^2$ is the deceleration parameter that can be parametrized when the radiation is neglected, i.e. $\Omega_{\gamma,0} \ll \Omega_{m,0}$ , as $q_0 = \Omega_{m,0}/2 - \Omega_{\Lambda,0}$ ). . . . .	21
1.12	Composition content of the Universe as measured today. (Credits of the figure: Spergel, 2015). . . . .	22
1.13	Rotation curve of NGC 6503 from Begeman et al., 1991. It shows the data with points, the theoretical predictions from the disk, from gas and from a dark matter halo. The solid line is the total of the three contributions. . . . .	23
1.14	Contours in the $\sigma_8$ and $\Omega_m$ planes for different lensing probes and Planck CMB measurements. It illustrates the $\sim 2\sigma$ tension seen between those probes. (Credits of the figure: Heymans et al., 2021). . . . .	27
1.15	$H_0$ measurements by different probes of the late and early Universe, exacerbating the $H_0$ tension. (Credits of the figure: Abdalla et al., 2022). . . . .	28
1.16	Large scale structures formed by galaxies as observed by the Sloan Digital Sky Survey in the early 2000's. (Credits of the figure: Park et al., 2005). . . . .	29
1.17	Simulation at different redshifts, from back to front $z = 6, 2, 0$ , within a box of $100 h^{-1}\text{Mpc}$ length. (Credits of the figure: Volker Springel, MPI). . . . .	30
1.18	Dark matter density contrast at redshift 1.48 from a simulation box used for EZmocks (introduced after in Chapters 2 and 3). Here a slice of $1000 \times 1000 \times 50 h^{-1}\text{Mpc}$ is drawn. . . . .	33
1.19	Illustration to understand the two-point correlation function. . . . .	35
1.20	Linear growth function normalized with $D_+(z=0)$ (on the left) and growth rate (on the right) as function of the redshift for different cosmological parameters. Growth function is computed from Equation 1.86, and the growth rate from Equation 1.88. Dashed lines on the right plot are the growth rate from the approximation for flat cosmologies from Equation 1.89. . . . .	41
1.21	Redshift evolution of the linear power spectrum (right) and correlation function (left) as predicted by a $\Lambda\text{CDM}$ cosmology with Planck values of the parameters (Planck Collaboration et al., 2020). . . . .	42
1.22	Linear power spectra at redshift 0 for a $\Lambda\text{CDM}$ model. From left to right: variations of $\Omega_b$ , with $\Omega_m = 0.31$ and $\Omega_k = 0$ ; variations of $\Omega_m$ , with $\Omega_b = 0.05$ and $\Omega_k = 0$ ; variations of $\Omega_k$ , with $\Omega_b = 0.05$ and $\Omega_m = 0.31$ . . . . .	42
1.23	Large scale structures simulations from Macciò et al., 2012 for different dark matter models at redshift 0. Size shown is of a length of 40 Mpc. From left to right: CDM, and two WDM models with differences in their initial thermal velocities with warmer candidate on the right. . . . .	44
1.24	On the left: Illustrated power spectrum from Frenk and White, 2012 for three natures of dark matter: cold in black, warm in red, hot in green. On the right: figure from Tegmark et al., 2004 showing the matter power spectrum normalized at redshift 0 from different probes (they are not measured at $z = 0$ ). Solid line represents a flat $\Lambda\text{CDM}$ prediction. . . . .	44

1.25 Dark matter density distribution on the left and corresponding galaxy distribution on the right populated following an abundance matching algorithm. (Credits of the figure: Wechsler and Tinker, 2018). . . . .	52
1.26 Satellite ( $N_s$ ) and central ( $N_c$ ) galaxies first moment of the HOD as function of the halo mass. Central galaxies can be described by a step function and satellite galaxies HOD is a power law with Poisson scattering. The different behaviours suggest a separated parametrization. (Credits of the figure: Kravtsov et al., 2004). . . . .	54
1.27 Illustration of the peak-background assumption. (Credits of the figure: Peacock, 2003). . . . .	55
1.28 CMB map of temperatures anisotropies measured by Planck satellite. (Credits of the figure: ESA and the Planck Collaboration). . . . .	59
1.29 Amplitude of the CMB power spectrum $D_{ll} \equiv l(l+1)C_l/(2\pi)$ from Planck Collaboration et al., 2020. . . . .	61
1.30 Linear evolution of one perturbation mass profile in the early Universe from Eisenstein, Seo, and White, 2007. Dark matter is in black, gas (so baryonic matter) in blue, photons in red, neutrinos in green. . . . .	63
1.31 Two-point correlation function from Eisenstein et al., 2005 of the LRG SDSS sample. It is the first measured BAO detection in the configuration space clustering of observed galaxies. BAO manifests itself as an excess probability of finding two galaxies separated by about $100 h^{-1}\text{Mpc}$ . . . . .	64
1.32 Alcock-Paczynski effect and separation projection schemes (radial and angular separations). . . . .	65
1.33 Explaining scheme from Padmanabhan et al., 2012 for BAO reconstruction. . . . .	66
1.34 Left: real (r-space) and redshift (z-space) space multipoles of the Indra simulations (B. Falck et al., 2021) at redshift 0. As the clustering is isotropic in real space, the quadrupole (and higher order multipoles) which contains angular information is null. Moreover we note that resulting observed overdensities are larger in redshift space due to the infall velocities. Indeed in redshift space overdensity regions are more grouped on the radial direction. This results in a higher clustering correlation below the BAO scale. Right: redshift evolution of the multipoles in redshift space. The BAO peak is dumped as it tends to redshift zero. This is due to non-linearities that increase with time (as $z$ goes to 0). . . . .	68
1.35 Redshift space distortions. . . . .	74
1.36 Two-dimensional clustering of the ELG sample of eBOSS used for the RSD analysis in configuration space. An excess ring density is seen around $s \approx 100 h^{-1}\text{Mpc}$ that corresponds to the BAO feature. Moreover we can see an overall squashing effect on large scales due to RSD. On small scales (about $s_{\perp} < 2 h^{-1}\text{Mpc}$ ) an elongated effect in the radial direction is observed that is called FoG. (Credits of the figure: Jiamin Hou, MPE, and Tamone et al., 2020.) . . . . .	75
1.37 SDSS telescope scheme. (Credits of the figures: Smee et al., 2013.) . . . . .	79

1.38 LSS map of the observable Universe as observed by SDSS, bounded by the CMB. We are at the center of the map. Each point represents an observation of a galaxy or QSO of SDSS, where each tracer is characterized by a different colour along with the BAO signal in their correlation function. (Credits of the figure: Anand Raichoor, Ashley Ross and the SDSS Collaboration.) . . . . .	80
1.39 Different eBOSS spectra for each of the tracers. (Credits of the figure: Blanton et al., 2017). . . . .	81
1.40 DESI instrument and fiber positioners. (Credits of the figures: DESI collaboration.)	83
2.1 Measurements of the expansion history and growth by SDSS collaboration as function of the redshift. Solid lines are Planck predictions for a flat $\Lambda$ CDM model (Planck Collaboration et al., 2020). The cyan points indicate the contribution of this thesis. (Credits of the figure: Alam, Aubert, et al., 2021). . . . .	87
2.2 95% and 68% contours for the different probes, relative to the expansion history. From left to right: $\Omega_k$ - $\Omega_m$ plane in an $o\Lambda$ CDM model, $\Omega_\Lambda$ - $\Omega_m$ plane in an $o\Lambda$ CDM model and $w$ - $\Omega_m$ plane in an $w\Lambda$ CDM model. The lines are the $\Lambda$ CDM parameters values. (Credits of the figures: Alam, Aubert, et al., 2021). . . . .	87
2.3 Contours in $\Lambda$ CDM in the $H_0$ - $r_s$ and $H_0$ - $\Omega_m$ planes. Distance Ladder corresponds to measurements from Riess et al., 2019, that uses Cepheids to calibrate the SN luminosity distance. (Credits of the figure: Eva Mueller and SDSS Collaboration). . . . .	88
2.4 Contours relative to the growth constraints from different probes: $\Omega_\Lambda$ - $\Omega_m$ , $w$ - $\Omega_m$ , $\sigma_8$ - $\Omega_m$ and $\mu_0$ - $\sigma_0$ planes. (Credits of the figures: Alam, Aubert, et al., 2021). . . . .	90
2.5 Cosmological parameters values for Stage-II and Stage-III experiments with and without SDSS, within a $ow\Lambda$ CDM model with free $\sum m_\nu$ . (Credits of the figure: Alam, Aubert, et al., 2021). . . . .	92
3.1 Some of the voids as found by the DIVE algorithm in a discrete distribution of tracers. Red points are the void centers, blue points the connected points associated to the voids. Solid lines are the tetrahedral edges. Large box has a length of $80h^{-1}$ Mpc and voids shown have a radius between 26 and $27h^{-1}$ Mpc. Zoomed box is of $12h^{-1}$ Mpc length and void have radius smaller than $4h^{-1}$ Mpc. (Credits of the figure: C. Zhao et al., 2016). . . . .	117
3.2 DTvoid density profile for different void sizes for mock catalogs as function of the distance to the center of the voids, rescaled by the void size. The horizontal line indicates the total mean density contrast. From top curve (black) to bottom (cyan) curve, void radii are within: (8,12), (12,16), (16,20), (20,25), $> 25h^{-1}$ Mpc. (Credits of the figure: C. Zhao et al., 2016). . . . .	118

- 3.3 On the left: volume average distance measured from BAO for different SDSS samples. The void measurements are indicated in black. We note that the measurements are rescaled to the expected values from Planck for a  $\Lambda$ CDM model (Planck Collaboration et al., 2020). On the right: Constraints on different cosmological parameters ( $\Omega_m$ ,  $\Omega_\Lambda h^2$ ,  $H_0$ ) in a flat  $\Lambda$ CDM model with BBN constraints results. Orange contours (dashed red) are eBOSS results for anisotropic (isotropic) BAO of LRGs and ELGs. Black contours comes from void constraints. (Credits of the figures: C. Zhao et al., 2022). . . . . 119





# List of Tables

1.1	List of the 6 parameters for a flat $\Lambda$ CDM model with values of Planck Collaboration et al., 2020 (last column of Table 2) with their 68% intervals. . . . .	26
1.2	Redshift ranges and total numbers of good redshifts for the different tracers of eBOSS. From Table 3 of Alam, Aubert, et al., 2021. . . . .	83
1.3	Redshift ranges and expected total number of good redshifts for the different tracers of DESI. From Table 3.1 of DESI Collaboration and et al., 2016. . . . .	84
1.4	Forecasts of DESI figure of merit $FoM_{\text{DETF}}$ . The error $\sigma_{w_p}$ on $w_p$ is evaluated at $a_p$ the pivot scale factor which gives the smallest errors. From Table 2.9 of DESI Collaboration and et al., 2016. . . . .	84
2.1	Central values and 68% confidence intervals on cosmological parameters for various extensions of the standard cosmological model, from the combination of SDSS data, DES, Planck and Pantheon SN. . . . .	91



# List of symbols and abbreviations

---

AP	Alcock-Paczynski
BAO	Baryon Acoustic Oscillations
BBN	Big Bang Nucleosynthesis
(e)BOSS	(extended) Baryon Oscillation Spectroscopic Survey
CLPT	Convolution Lagrangian Perturbation Theory
CMB	Cosmic Microwave Background
DESI	Dark Energy Spectroscopic Instrument
DT	Delaunay Triangulation
ELG	Emission Line Galaxy
FLRW	Friedmann-Lemaitre-Robertson-Walker metric
FoG	Finger-of-God
GR	General Relativity
GS	Gaussian Streaming
LRG	Luminous Red Galaxy
LSS	Large Scale Structures
Mpc	Mega parsecs
NGC	North Galactic Cap
PT	Perturbation Theory
QSO	Quasar
RIC	Radial Integral Constraint
RSD	Redshift Space Distortions
SDSS	Sloan Digital Sky Survey
SGC	South Galactic Cap
SR	Special Relativity
XCF	Cross-correlation function
ZA	Zeldovich Approximation
$\Lambda$ CDM	Lambda-Cold Dark Matter
2PCF	Two-point correlation function

---

---

$a$	Cosmic scale factor
$A_s$	Amplitude of the primordial fluctuations
$b$	Linear bias
$c$	Speed of light in vacuum
$D_+$	Growth function
$f$	Growth rate
$F$	Lagrangian bias
$h$	Rescaled Hubble constant
$H(z)$	Hubble parameter
$n_s$	Spectral index
$P(k)$	Power spectrum
$w$	Dark energy equation of state
$z$	Redshift
$\alpha_{\parallel}$	AP parameter in the line-of-sight direction
$\alpha_{\perp}$	AP parameter in the transverse direction
$\delta$	Density contrast
$\Delta^2(k)$	Dimensionless power spectrum
$\kappa$	Curvature parameter
$\Lambda$	Cosmological constant
$\mu$	Angle cosine between the line-of-sight and the vector separation
$\xi(r)$	Correlation function
$\rho$	Density
$\sigma_{\text{FoG}}$	Finger-of-God parameter
$\sigma_8$	Amplitude of the matter fluctuations
$\Phi$	Gravitational field
$\Psi$	Displacement field
$\Omega_b$	Baryon density parameter
$\Omega_c$	Dark matter density parameter
$\Omega_m$	Matter density parameter
$\Omega_{\gamma}$	Radiation density parameter
$\Omega_{\kappa}$	Curvature density parameter
$\Omega_A, \Omega_{\text{DE}}$	Dark energy density parameters

---

# 1 Introduction

About one hundred years ago, Albert Einstein introduced his famous formulation of General Relativity theory describing the law of Gravity in our Universe with a curved space-time. A few years later, his achievement provided a theoretical framework for modern cosmology with the discovery of an expanding Universe (Hubble, 1929).

At the end of the last century, two independent groups (Riess et al., 1998, Perlmutter et al., 1999) discovered that the expansion of the Universe was in fact accelerating, shaking the scientific community. This phenomenon means either a validity limitation of the laws, or the evidence of the existence of an unknown energy, called dark energy, acting against gravity.

To discriminate between those two hypothesis or to understand the nature of dark energy, very precise expansion history of the Universe is required. To this goal, Large Scale Structures (LSS) are a very powerful tool as they can help constraining the expansion measurements. Spectroscopic surveys aim to map large portions of the Universe to study the LSS. They are of crucial importance to analyse the growth of structure or clustering of LSS, that constrain the cosmological model and unveil the nature of dark energy.

In this thesis I will use data from spectroscopic surveys and simulations to try to bring a contribution in this exciting field. In this first chapter, I will present the theoretical context (Chapter 1). The second chapter will be dedicated to the analysis I performed within the eBOSS collaboration for the RSD analysis of ELGs (Chapter 2). In the third chapter I will present a BAO analysis on voids correlated with the quasars of eBOSS (Chapter 3). Last chapter will be a short conclusion, summarizing the work of this thesis (Chapter 4).

## 1.1 A few notions of Modern Cosmology

Cosmology is a branch of astrophysics that aims at studying the Universe as a whole and its evolution. This might be very ambitious, or pretentious, to claim to summarize the Universe in equations. This is why in this first chapter I will restrict myself to introduce the standard model of cosmology,  $\Lambda$ CDM, with briefly presenting the grounding equations that describe

our current understanding of the Universe related to the essence of this thesis.

Here a non exhaustive list of my guiding references: Carroll, 1997, Mortonson et al., 2013, Langlois, 2010, Ryden, 2016, Peacock, 1999, Dodelson, 2003 and the EPFL master lectures on Relativity and Cosmology of Pr. Mikhail Shaposhnikov.

### 1.1.1 A brief look into General Relativity

As already mentioned, the framework used for cosmology is the General Relativity (GR). Indeed it allowed to consider gravity not as an instantaneous attractive force but rather an interaction manifesting itself as a curvature in space-time. In this context the Universe and its content are related geometrically through a growing space-time.

#### Metric

A metric is used to describe the geometry of any space in order to measure distances within this space. In classical physics the separation of two points in space is invariant. In 1905 Einstein introduced the concept of space-time in the context of Special Relativity (SR) (Einstein, 1905). In SR or GR, the separation between two points is not anymore space- or time-invariant. Instead there is a space-time-invariance, i.e. a combination  $ds$  of the time and space separations, related by a metric tensor  $g_{\mu\nu}$  describing space-time:

$$ds^2 = g_{\mu\nu} dx^\mu dx^\nu, \quad (1.1)$$

where  $\vec{x}$  is the space time position. The space coordinates are  $x^{1,2,3}$  and the time coordinate is encoded in  $x^0 = ct$  with  $c$  the speed of light in vacuum considered independent of the choice of reference frame in SR and GR. We note that the tensor  $g^{\mu\nu}$  is defined as the inverse of the metric:  $g_{\mu\nu} g^{\nu\alpha} = \delta_\mu^\alpha$ .

The choice of the metric is very important as it encodes the geometry of space-time. In SR a Minkowski space-time, a 3D space without curvature (so in GR without mass and therefore without gravitation), is used with the metric  $g_{\mu\nu} = \eta_{\mu\nu}$  and using the  $(+ - - -)$  convention from now on:

$$\eta_{\mu\nu} = \begin{pmatrix} 1 & 0 & 0 & 0 \\ 0 & -1 & 0 & 0 \\ 0 & 0 & -1 & 0 \\ 0 & 0 & 0 & -1 \end{pmatrix}. \quad (1.2)$$

#### Geodesics

In a curved space-time the shortest path between two points, called a geodesic, is not necessarily a straight line as in a flat space. Those curves can be complex and follow the geometry

of the space-time. In GR, in absence of external forces, a free falling particle will follow a geodesic in the space-time curved by gravity. Using the Equivalence Principle (stating that the gravitational and inertial masses are the same), the geodesic equation is:

$$\frac{d^2 x^\mu}{d\lambda^2} + \Gamma_{\alpha\beta}^\mu \frac{dx^\alpha}{d\lambda} \frac{dx^\beta}{d\lambda} = 0 \quad (1.3)$$

with  $\lambda$  the proper time usually written as  $\tau$ , i.e. the time experienced by the object in its own rest frame so that the space coordinates are constant, in this frame:

$$d\tau = \sqrt{g_{00}} dx^0. \quad (1.4)$$

In the case of a mass-less particle like photons, the proper time cannot parametrize the equation. Indeed there exists no reference frame exists where photons are at rest, as  $\Delta s^2 = c\Delta t^2 - c\Delta t^2 = 0$ . Instead the parameter  $\lambda$  is chosen to be an affine parameter.

In the geodesic equation,  $\Gamma_{\alpha\beta}^\mu$  are the Christoffel symbols given by the metric derivatives  $\partial_\mu \equiv \partial/\partial x^\mu$ :

$$\Gamma_{\alpha\beta}^\mu = \frac{1}{2} g^{\mu\rho} (\partial_\alpha g_{\rho\beta} + \partial_\beta g_{\rho\alpha} - \partial_\rho g_{\alpha\beta}). \quad (1.5)$$

They are determined by the metric thus encrypt the curvature. In the absence of gravity,  $\Gamma$  is zero.

### Einstein's equation

Einstein proposed a new perspective that he developed during 10 years after SR: the gravitational interactions are embodied within the space-time geometry. The gravitational field is directly included into the metric. In 1915, Einstein related with his Field Equation the energy content of the Universe, encrypted in the energy-momentum-stress tensor  $T_{\mu\nu}$ , to the Einstein's tensor  $G_{\mu\nu}$  which describes the Universe's geometry:

$$G_{\mu\nu} \equiv R_{\mu\nu} - \frac{1}{2} g_{\mu\nu} R = \frac{8\pi G}{c^4} T_{\mu\nu} + \Lambda g_{\mu\nu}, \quad (1.6)$$

where  $G$  is the Newton's constant of gravitation,  $R \equiv g^{\mu\nu} R_{\mu\nu}$  is the Ricci scalar and  $R_{\mu\nu}$  is the Ricci tensor depending on Christoffel symbols  $\Gamma_{\alpha\beta}^\mu$  and their derivatives, so from the metric:

$$R_{\mu\nu} = \partial_\alpha \Gamma_{\mu\nu}^\alpha - \partial_\nu \Gamma_{\alpha\mu}^\alpha + \Gamma_{\mu\nu}^\alpha \Gamma_{\alpha\beta}^\beta - \Gamma_{\nu\alpha}^\beta \Gamma_{\beta\mu}^\alpha. \quad (1.7)$$

The  $\Lambda$  term, known as the cosmological constant, on the right hand side of 1.6 was introduced by Einstein in 1917 to have a static Universe (Einstein, 1917). While his reasons to add  $\Lambda$  were incorrect<sup>1</sup>, this term is kept in the current model. Indeed we will see below that Hubble's

<sup>1</sup>We understand today that a static Universe would not have been possible, as it would be gravitationally unstable.

discovery of an expanding Universe proved the incorrectness. The term will later be kept due to the accelerated expansion. This more general formulation allows to counterbalance gravity if  $\Lambda$  is positive, acting as a repulsive term.

Solutions of Einstein's equation are the metric tensor components which in turn can be used to infer the geodesics. Therefore inertial trajectories of objects follow geodesics in the curved space distorted by massive objects.

### 1.1.2 An expanding Universe

#### Cosmological principle

At the heart of our description of the Universe resides the cosmological principle assumption: the Universe is isotropic and homogeneous on large scales, 100Mpc or more.

Homogeneity of the Universe means that the properties observed are the same at any location in the Universe, so they are invariant under a translation.

The isotropy assumption states that the physics observed is the same independently of the direction, so this is rotation-invariant.

One notes that isotropy can be tested using observational data. Spatial homogeneity is more difficult to probe as observations are performed through a light-cone and not a time-constant hyper-surface. A method uses the Copernican Principle, i.e. we do not occupy a privileged location in the Universe, to infer a statistical homogeneity based on isotropy (Goodman, 1995; Maartens, 2011; Clarkson, 2012). Indeed a 2D isotropy measurement could be extended to homogeneity through translation invariance. It is therefore possible to measure a scale beyond which the Universe is homogeneous using for example spectroscopic surveys (Ntelis et al., 2017) or the cosmic microwave background (Camacho-Quevedo and Gaztañaga, 2022). This scale is usually measured between  $100\text{-}200h^{-1}\text{Mpc}$ .

#### Redshifts

The first mention of receding galaxy was proposed by Vesto Slipher. In 1912 he discovered a large shift of the spectrum of a galaxy, suggesting a high velocity, interpreted as a Doppler effect (Slipher, 1913). The same year of the completion of GR, Slipher presented the radial velocity of 25 nebulae, where many of them showed a spectral shift toward the red: those nebulae were moving away from Earth (Slipher, 1917).

These shifts in the spectrum are a key concept leading to the discovery of the Universe's expansion. The so-called redshift  $z$  is defined as the ratio between the observed and emitted



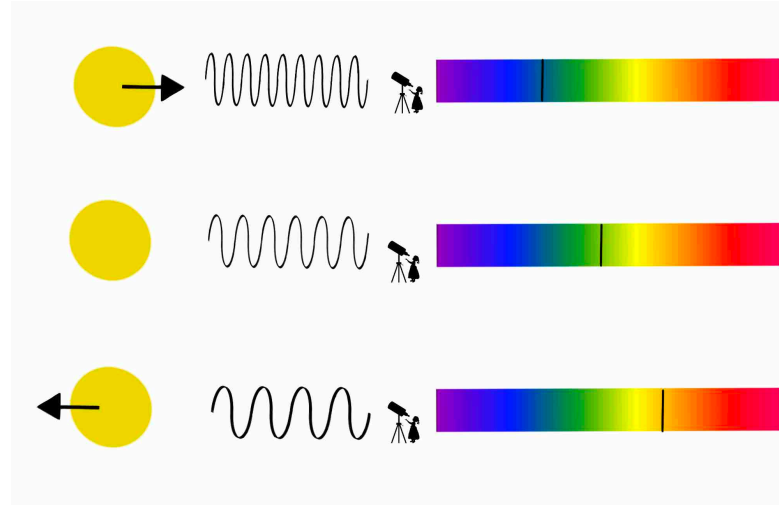


Figure 1.1: Illustration to understand the redshift. On top spectral shift toward the blue from the light of an object moving in the Earth direction. In the middle the spectrum observed of an object as observed in its rest frame. On the bottom spectral shift toward the red from the light of an object moving away from Earth, it corresponds to the shift that the expansion of the Universe would cause.

light, where the energetic photon has a wavelength  $\lambda$  and a frequency  $\nu$ :

$$1 + z = \frac{\lambda_{\text{observed}}}{\lambda_{\text{emitted}}} = \frac{\nu_{\text{emitted}}}{\nu_{\text{observed}}}. \quad (1.8)$$

Photons from a galaxy moving away (toward) from Earth will undergo an increase (decrease) in their observed frequency and the spectral lines of the galaxy will be red (blue) shifted. This effect is illustrated on Figure 1.1.

There are three main effects causing redshift. The first one, due to a relativistic Doppler effect is induced by the relative peculiar motion of the emitting object  $v$ . In flat space it results as  $1 + z_{\text{Doppler}} = \gamma(1 + v/c)$ , where  $\gamma = \left(\sqrt{1 - v^2/c^2}\right)^{-1}$  is the Lorentz factor.

The gravitational redshift comes from time dilation due to a strong gravitational well, using the GR definitions:  $1 + z = \sqrt{g_{00,\text{observed}}/g_{00,\text{emitted}}}$ , where  $g_{00}$  is the metric for the time coordinate.

Cosmological redshift is due to the expansion of the Universe. Indeed the expansion of space itself will cause a shift toward the red. This is illustrated on Figure 1.2 as a wavelength drawn over the surface of an expanding balloon. This is the dominant component of the total redshift of the observed galaxies composing the Universe.

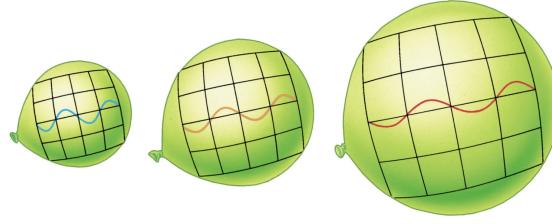


Figure 1.2: Illustration of the increased wavelength of a wave due to the Universe expansion with the balloon analogy. (Credits of the figure: James N. Imamura, University of Oregon).

### Hubble's law

In the 1920's, Alexander Friedmann used Einstein's equation to argue that the Universe was expanding (Friedmann, 1922). A few years later, Georges Lemaître confirmed independently Friedmann's conclusions (Lemaître, 1927).

This is at the end of the decade, in 1929, that the expansion is experimentally observed by Edwin Hubble (Hubble, 1929). He used the redshifts of a sample of 46 extragalactic nebulae at  $z \ll 1$  to measure their velocities (at low redshift  $z \simeq v/c$ ). He established a linear relation between the distance  $d$  and the recession velocity  $v$  of a galaxy, known as the Hubble's law:

$$v = H_0 d. \quad (1.9)$$

The constant of proportionality  $H_0$  is called the Hubble constant. This law means that the further are the galaxies, the faster they are moving away. His measurements are shown in Figure 1.3 with his regression line. Hubble obtained a value around  $H_0 = 500 \text{ km/s/Mpc}$ , which is about 5 times higher than the current measured values.

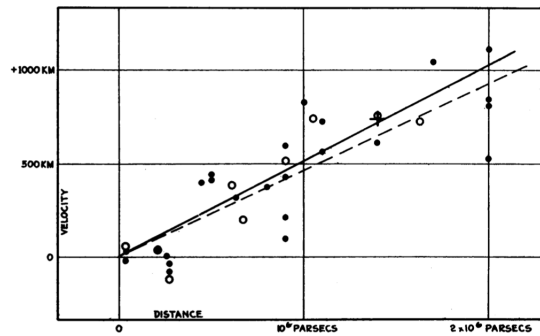


Figure 1.3: Hubble diagram from Hubble, 1929. It shows his measurements of the recession velocities as a function of the distances of the nebulae.

Nowadays the Hubble constant is interpreted as the expansion rate of the Universe as observed today. A current standard notation is the following:

$$H_0 = 100h \text{ km/s/Mpc}, \quad (1.10)$$

where  $h$  is the dimensionless Hubble constant. One can note that it is possible to obtain an estimate of the age of the Universe from  $H_0$  as  $t_0 = 1/H_0 F = 9.78 \times 10^9 \text{ Fyr}/h$  where  $F$  is a function depending on content densities in the Universe,  $F$  is close to 1.

### 1.1.3 Geometry and Dynamics

#### Friedmann-Lemaitre-Robertson-Walker metric

To describe the Universe and its expansion using GR, we need first to define a metric. Under the cosmological principle assumption, the metric depends on a curvature parameter  $\kappa$  describing the shape of the Universe which is the same everywhere to conserve isotropy property:

$$\left\{ \begin{array}{ll} \kappa > 0 & \text{closed Universe} \\ \kappa = 0 & \text{flat Universe} \\ \kappa < 0 & \text{open Universe} \end{array} \right. \quad (1.11)$$

The different options are illustrated on Figure 1.4. In particular for a null curvature, i.e.  $\kappa = 0$ , we have an Euclidean geometry and the sum of the angles formed by three points in space is  $180^\circ$ . For  $\kappa > 0$ ,  $R(t)$  is the radius of curvature of the Universe and  $R_0$  is the value today at  $t_0$ .

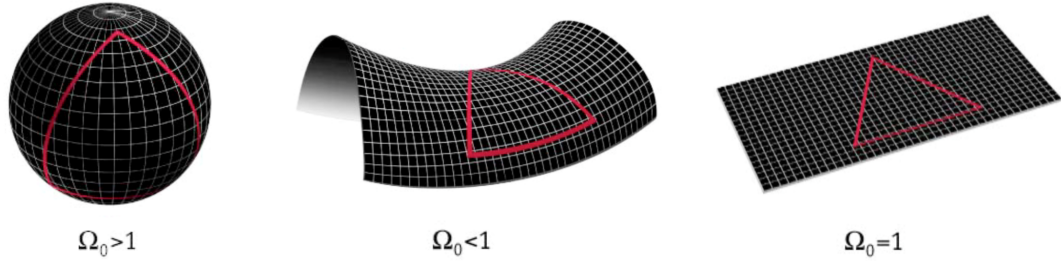


Figure 1.4: Different Universe geometry. From left to right: closed, open, flat Universes corresponding to elliptic, hyperbolic or flat hyper-surfaces, respectively. Relation of the density  $\Omega_0$  with the curvature parameter  $\kappa$  is made explicit later in Equation 1.32. (Credits of the figure: (modified from) NASA / WMAP Science Team).

Moreover to describe the expansion we introduce the dimensionless parameter  $a(t) = R(t)/R_0$ , called the scale factor describing the relative size of the Universe and function of time only to preserve homogeneity. It means that the proper distance  $d(t)$  at epoch  $t$  is related to the reference distance  $d_0$  at  $t_0$ , chosen to be today and setting  $a(t_0) = 1$ , by:

$$d(t) = a(t)d_0. \quad (1.12)$$

The scale factor is related to the redshift  $z$  by<sup>II</sup>:

$$a(t) = \frac{1}{1+z}. \quad (1.13)$$

The derivative of the scale factor with respect to time  $\dot{a}$  indicates if the Universe is in expansion, i.e.  $\dot{a} > 0$ , static,  $\dot{a} = 0$ , or in contraction, i.e.  $\dot{a} < 0$ .

To take into account the Universe's expansion for a set of spherical coordinates  $(r', \theta, \phi)$ , we thus consider the change of coordinate:  $r = r'/a(t)$ . The most generic metric with those two parameters describing the dynamic space is then the Friedmann-Lemaitre-Robertson-Walker, the FLRW metric for which the space-time separation for spherical coordinates is (Robertson, 1935, Walker, 1937) still with the convention  $(+---)$ :

$$ds^2 = c^2 dt^2 - a^2(t) \left( \frac{dr^2}{1-\kappa r^2} + r^2(d\theta^2 + \sin^2\theta d\phi^2) \right). \quad (1.14)$$

The FLRW metric can be written:

$$g_{\mu\nu} = \begin{pmatrix} 1 & 0 & 0 & 0 \\ 0 & -\frac{a^2(t)}{1-\kappa r^2} & 0 & 0 \\ 0 & 0 & -a^2(t)r^2 & 0 \\ 0 & 0 & 0 & -a^2(t)r^2 \sin^2\theta \end{pmatrix}. \quad (1.15)$$

The Ricci scalar and Ricci tensor derived from Equation 1.7 in the case of the FLRW metric are<sup>III</sup>:

$$R = -6 \left( \frac{\ddot{a}}{a} \frac{1}{c^2} + \frac{\dot{a}^2}{a^2} \frac{1}{c^2} + \frac{\kappa}{a^2} \right), \quad R_{00} = -\frac{3}{c^2} \frac{\ddot{a}}{a}, \quad R_{ij} = - \left( \frac{\ddot{a}}{a} \frac{1}{c^2} + 2 \frac{\dot{a}^2}{a^2} \frac{1}{c^2} + 2 \frac{\kappa}{a^2} \right) g_{ij}. \quad (1.16)$$

### Universe's energetic composition

As already mentioned in Section 1.1.1, in GR the Universe's energy content is encrypted in the energy-momentum-stress tensor  $T_{\mu\nu}$ . Considering the matter as a perfect fluid, the tensor  $T_{\mu\nu}$  is written as:

$$T^{\mu\nu} = \left( \frac{p}{c^2} + \rho \right) u^\mu u^\nu - p g^{\mu\nu}, \quad (1.17)$$

where  $u_\mu$  is the four-vector velocity,  $p$  the pressure and  $\rho$  the density. If the fluid reference frame is chosen at rest<sup>IV</sup>, i.e.  $u^\mu = (c, 0, 0, 0)$ , then  $T^{00} = c^2 \rho$  and  $T^{ij} = -p g^{ij}$ . We note that  $T_{\mu\nu} = T^{\alpha\beta} g_{\alpha\mu} g_{\beta\nu}$ , and thus in the rest frame  $T_{00} = T^{00}$  and  $T_{ij} = -p g_{ij}$ .

<sup>II</sup>In fact, this is the cosmological redshift which is related to the scale factor. The Doppler and gravitational redshifts are in general much smaller for any objects at cosmological distances (see also Section 1.3.3).

<sup>III</sup>We note that  $\dot{a} \equiv da/dt$  so that  $da/dx^0 = \dot{a}/c$  and  $R_{tt} = -3 \frac{\ddot{a}}{a}$ .

<sup>IV</sup>The four-velocity vector is defined as  $\vec{u} \equiv d\vec{x}/d\lambda$ , where  $\lambda$  is the proper time related to the time  $t$  with  $t = \gamma\lambda$ , with the lorentz factor  $\gamma = (1 - v^2/c^2)^{-1/2}$ ,  $v = dx^i/dt$  the spatial velocity.

Due to the conservation of  $T_{\mu\nu}$ , i.e.  $\nabla_\mu T^{\mu\nu} = 0$ , and using the FLRW metric, it gives the continuity equation:

$$\dot{\rho} + \frac{3\dot{a}}{a} \left( \frac{p}{c^2} + \rho \right) = 0 \quad \left( \Longleftrightarrow \frac{\partial}{\partial t} (\rho a^3) + \frac{p}{c^2} \frac{\partial}{\partial t} a^3 = 0 \right). \quad (1.18)$$

The second form in parenthesis is equivalent to the first law of thermodynamics,  $dE + pdV = 0$ .

### Friedmann equations

Under the assumption of the FLRW metric from Equation 1.14 with Equation 1.16, and injecting the energy-momentum-stress tensor  $T_{\mu\nu}$  at rest defined above in the time-components of Einstein's field equation, i.e.  $\mu, \nu = 0, 0$  in Equation 1.6, it gives the first Friedmann equation:

$$\frac{\dot{a}^2}{a^2} + \frac{\kappa c^2}{a^2} = \frac{8\pi G}{3} \rho + \frac{\Lambda c^2}{3}. \quad (1.19)$$

In the same way for the spatial coordinates on the diagonal of the metric, i.e.  $\mu, \nu = i, i$ , as all the other components are zero, we can write:

$$2\frac{\ddot{a}}{a} + \frac{\dot{a}^2}{a^2} + \frac{\kappa c^2}{a^2} = -\frac{8\pi G}{c^2} p + \Lambda c^2. \quad (1.20)$$

The second Friedmann equation is obtained by taking the difference between Equations 1.19 and 1.20:

$$\frac{\ddot{a}}{a} = -\frac{4\pi G}{3} \left( \rho + \frac{3p}{c^2} \right) + \frac{\Lambda c^2}{3}. \quad (1.21)$$

The set of Friedmann equations is very important in cosmology as they describe the Universe's expansion. With a combination of the Friedmann's equations we recover Equation 1.18, so the first law of thermodynamics which is equivalent to have an Universe with an adiabatic expansion. The second Friedmann equation describes the deceleration of the expansion due to the energy density and the pressure while the cosmological constant  $\Lambda$  causes an acceleration.

The Friedmann's set of equations is frequently written with respect to the expansion rate of the Universe or Hubble parameter  $H$ , defined as:

$$H(t) = \frac{\dot{a}(t)}{a(t)}. \quad (1.22)$$

### Simple expanding Universe solutions

Lets consider a flat non-static Universe, i.e.  $\kappa = 0$  and  $\dot{a} \neq 0$ , dominated by non-relativistic matter, i.e.  $p \simeq 0$ , and assuming no cosmological constant  $\Lambda = 0$ . We thus have the following

solution to the Friedmann's Equations 1.19 and 1.20:

$$\frac{\dot{a}^2}{a^2} = \frac{8\pi G}{3}\rho, \quad \frac{2\ddot{a}}{a} + \frac{\dot{a}^2}{a^2} \simeq 0. \quad (1.23)$$

The second equation is equivalent to  $\frac{d}{dt}(2\ln\dot{a} + \ln a) = 0$  and from there we can get:

$$a(t) = a_0 \frac{t^{2/3}}{t_0}. \quad (1.24)$$

It means that the scale factor  $a$  grows with time: the Universe is in expansion. This toy case corresponds to a matter dominated Universe. Injecting in the first Friedmann Equation 1.19, we get  $\rho(t) = (6\pi G t^2)^{-1}$ , where the density diverges when  $t$  goes to 0.

In a radiation dominated Universe, i.e.  $\kappa = \Lambda = 0$  and  $\rho = 3p$ , following a similar procedure, we have:

$$a(t) = a_0 \frac{t^{1/2}}{t_0}, \quad \rho(t) = \frac{3}{32\pi G t^2}. \quad (1.25)$$

Lastly for a cosmological constant domination assuming  $\rho = p = \kappa = 0$ , it gives:

$$a(t) = a_0 \exp \sqrt{\frac{\Lambda}{3}} t. \quad (1.26)$$

We will see later that the Universe underwent three phases, one dominated by radiation, one by matter and finally by the dark energy.

### Density parameters

Any Universe can be described by Friedmann's Equations 1.19 and 1.21 and therefore has an evolution driven by the dynamics of its content: the matter, the curvature, the radiation and the cosmological constant.

If those three components are considered as perfect fluids, their equation of state relating their density  $\rho$  and pressure  $p$  linearly with a constant  $w$  is:

$$p = w\rho c^2. \quad (1.27)$$

This can be injected in the continuity Equation 1.18 (which is also a combination of Friedmann's equations), where the analytical solution is the time evolution of the density:

$$\rho(t) = \rho(t_0) a(t)^{-3(w+1)}. \quad (1.28)$$

Let's now have a look at the different behaviour of the Universe's content:

- For non-relativistic matter, the pressure is negligible compared to density as it has a mass much more important than its temperature. The linear parameter is then  $w = 0$  and thus it implies  $\rho_m \propto a^{-3}$ .
- For radiation or relativistic matter, we have  $w = \frac{1}{3}$  and thus  $\rho_\gamma \propto a^{-4}$ .
- We can interpret the cosmological constant as a fluid with negative pressure and constant density. In this case  $w = -1$  and it entails  $\rho_\Lambda(t) = \rho_\Lambda(t_0)$ .

Introducing the critical density as the density for which the space is flat in an Universe without cosmological constant in the first Equation of Friedmann 1.19, using the Hubble parameter  $H$  from Equation 1.22:

$$\rho_{\text{crit}} = \frac{3H^2}{8\pi G}, \quad (1.29)$$

it allows to define the density parameters for different species:

$$\Omega_{m,\gamma,\Lambda} = \frac{\rho_{m,\gamma,\Lambda}}{\rho_{\text{crit}}}. \quad (1.30)$$

From Friedmann's equation divided by  $\rho_{\text{crit}}$  and using the previous definitions, the spatial curvature density  $\Omega_\kappa$ , also noted  $\Omega_k$ , is determined such that:

$$1 - \Omega_\kappa \equiv 1 + \frac{\kappa c^2}{a^2 H^2} = \Omega_m + \Omega_\gamma + \Omega_\Lambda \equiv \Omega_{\text{tot}}. \quad (1.31)$$

Therefore all the density parameters sum to one and the total density parameter  $\Omega_{\text{tot}}$  gives constraints on the geometry of the Universe:

$$\left\{ \begin{array}{ll} \Omega_{\text{tot}} > 1 \longleftrightarrow \kappa > 0 & \text{(closed)} \\ \Omega_{\text{tot}} = 1 \longleftrightarrow \kappa = 0 & \text{(flat)} \\ \Omega_{\text{tot}} < 1 \longleftrightarrow \kappa < 0 & \text{(open)} \end{array} \right. \quad (1.32)$$

The first Friedmann's equation 1.19 is often arranged in terms of the density parameters as measured today, i.e. at redshift  $z = 0$  or  $a(t_0) = 1$ ,  $\Omega_{i,0} \equiv \Omega_i(t_0)$ . Under the perfect fluid assumption and using the parameters defined above:

$$\frac{H^2(t)}{H_0^2} = \Omega_{\gamma,0} a(t)^{-4} + \Omega_{m,0} a(t)^{-3} + \Omega_{\kappa,0} a(t)^{-2} + \Omega_{\Lambda,0} \equiv E(a)^2. \quad (1.33)$$

The Universe's content determines fully the expansion behaviour. We thus have the following time evolution of the density parameters determined by their values at present time:

$$\Omega_\gamma(z) = \frac{\Omega_{\gamma,0}(1+z)^4}{E(z)^2}, \quad \Omega_m(z) = \frac{\Omega_{m,0}(1+z)^3}{E(z)^2}, \quad \Omega_\kappa(z) = \frac{\Omega_{\kappa,0}(1+z)^2}{E(z)^2}, \quad \Omega_\Lambda(z) = \frac{\Omega_{\Lambda,0}}{E(z)^2}. \quad (1.34)$$

### 1.1.4 Big Bang Theory and Evolution of the Universe

As seen in the precedent section, the Universe's evolution behaviour is determined by its content following Friedmann's equations. However there is a common feature observed for a matter or radiation dominated Universe as was studied in the subsection 1.1.3: the density diverges when the time goes to zero. This singularity is referred to as the Big-Bang.

Figure 1.5 illustrates the Universe expansion through the different epochs that I will describe in this section.

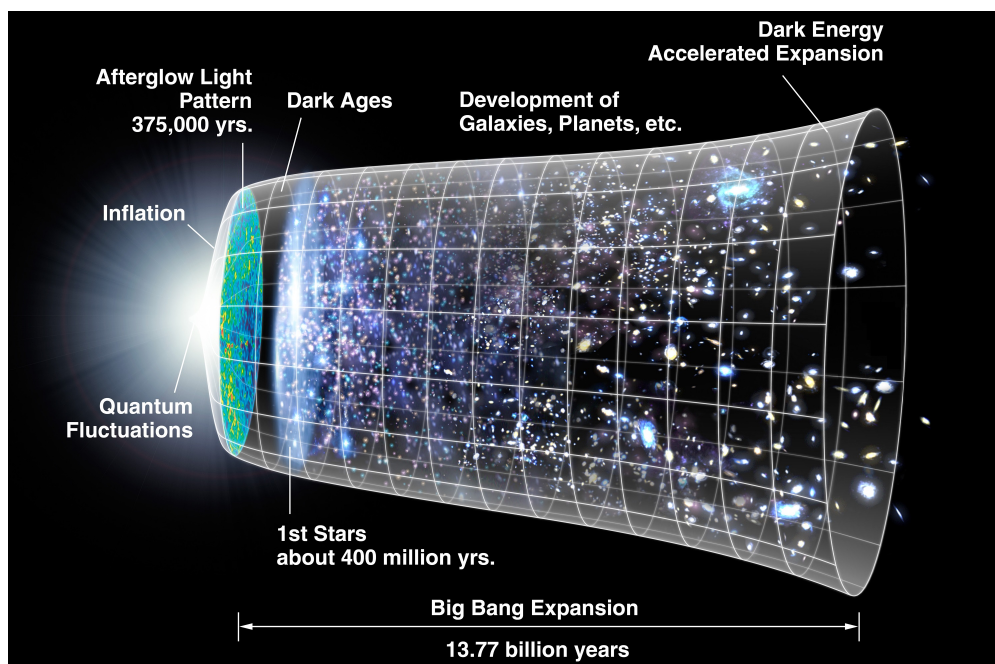


Figure 1.5: Explicating scheme views of the Universe's space expansion through the different epochs it undergoes. (Credits of the figure: NASA/WMAP Science Team).

### Big Bang

The concept was brought by George Gamov in 1948 (Alpher et al., 1948; Gamow, 1948). He was the first to use the non-static solutions of Einstein's equations established by Friedmann and Lemaître. His idea was that at the beginning of time  $t = 0$  a "primordial explosion" occurred called the Big Bang. He developed the primordial nucleosynthesis model, called Big Bang nucleosynthesis (BBN), and participated along with other scientists to predict the existence of the Cosmic Microwave Background radiation (CMB; Alpher and Herman, 1948).

The Big Bang model explains the Universe's expansion from an initial state very dense and hot. Its main success was its ability to predict different observed phenomena from the earliest observable probes to the structures observed today. Among others it described the expansion of the Universe, the CMB existence or the light elements abundances formed during BBN.



The Big Bang event is considered as the beginning of our Universe or the point from which the Universe follows our interpretation of the laws of physics. It happened 13.8 billion years ago.

### Very early Universe

As stated, the Universe was first extremely dense with an infinitely small distance between elements. The description of the Universe's first instants after the singularity requires developments in the quantum field as the particle concept is not well defined at this epoch. The current hypothesis are that all the forces, namely electromagnetic, weak, strong and gravitational, were unified as one. At the end of Planck epoch, i.e.  $10^{-43}$  s, the Universe was at a temperature of  $10^{32}$  K with a Hubble horizon<sup>V</sup> length of  $1.6 \times 10^{-35}$  m, that corresponds to Planck length. As the temperature drops, the gravitation force separates from the others.

From approximately  $10^{-36}$  s to  $10^{-32}$  s after the Big Bang the Universe enters a new phase, called the inflation during which the space grows exponentially by a factor of at least  $10^{26}$  and the Universe cools from  $10^{27}$  K down to  $10^{22}$  K. During that period the strong interaction separates from the electromagnetic and weak forces.

Cosmic inflation was proposed by Alan Guth in 1981 (Guth, 1981). The simplest realisation of this model relies on a free scalar field<sup>VI</sup>, so associating an intensity at each point in space without direction, with chaotic initial conditions filling the Universe. This leads to an exponential expansion in a very short period of time.

Even though the scalar field responsible for inflation or its associated particle, namely the inflaton (field), has not yet been discovered, another relativistic scalar field was detected in 2012, the Higgs field which explains the mass of the particles, leaving open the possibilities. While still theoretical, inflation resolves two major issues. Indeed without very fine tuning of initial conditions at the Big Bang, a Universe that expanded in radiation and matter dominated areas would rise different problems: the horizons and flatness problems. Horizon problem arises due to causally disconnected regions in space which should have the same set of initial conditions to explain homogeneity and isotropy. Regarding the flatness problem, the Universe should have been created in an extreme flatness to observe an almost flat Universe today. Those two concerns are avoided with inflation making our observed Universe more likely.

<sup>V</sup>Hubble horizon is defined through Hubble's law with a recession velocity equal to the speed of light. It is the boundary between faster and slower than light particles for an observer at a certain time. The particle horizon limits the observable and non-observable Universe as it characterizes the maximum length light particle could have traveled to the observer. Finally the event horizon is the boundary distance from which light can ever reach an observer. See Davis and Lineweaver, 2004 for a discussion on horizons.

<sup>VI</sup>The action of this field in its simplest realisation, i.e. a free massive scalar field  $\phi$  with chaotic initial conditions, is:  $S = \int \sqrt{(-g)} d^4x \left( \frac{1}{2} g^{\mu\nu} \partial_\mu \phi \partial_\nu \phi - V(\phi) \right)$ , where  $V(\phi)$  is the potential. And the dynamics of the field can thus be described with the movement equation and Einstein equations:  $\ddot{\phi} + 3H\dot{\phi} + V'(\phi) = 0$  and  $H^2 = \frac{8\pi G}{3} \left( \frac{1}{2} \dot{\phi}^2 + V(\phi) \right)$ . Such a movement is characterized by two regimes. The first when the friction is dominant so that the scalar field is overdamped, so it slowly rolls down. The second when there are quick oscillations of the scalar field around the minimum potential, the energy of  $\phi$  is therefore transferred to radiation.

### Cosmological epochs

Following cosmological inflation, the Universe continues to grow but at a slower rate. From Friedmann's Equation 1.33 with current density parameters in a flat Universe, the redshift evolution of densities presents different relative contributions at different epochs displayed in Figure 1.6.

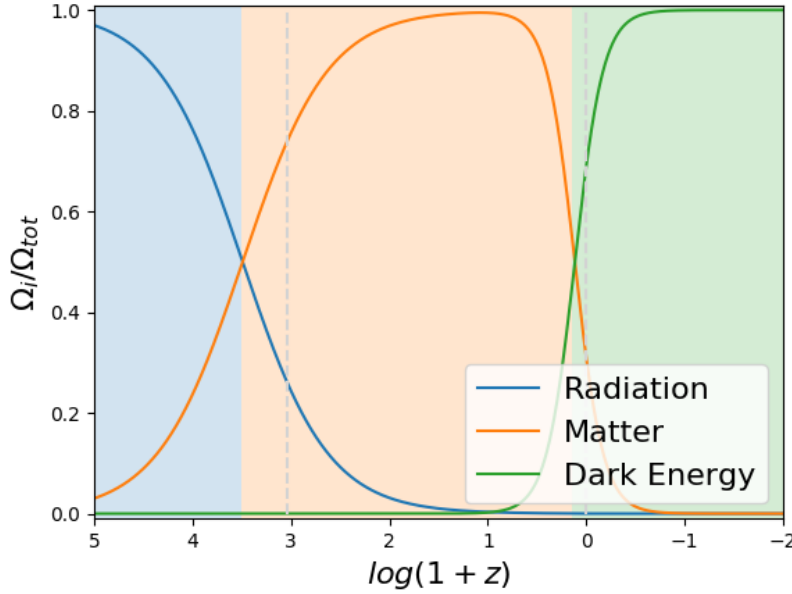


Figure 1.6: Universe's content parameters for a flat cosmology, with  $\Omega_m = 0.31$ ,  $\Omega_\gamma = 0.0001$ ,  $h = 0.7$ . The vertical dashed lines are the redshifts  $z = 1100$  (drag epoch) and  $z = 0$  (now). The blue area corresponds to the radiation domination period, the orange the matter area and the green the dark energy.

Until redshift 3600, i.e. 42 kyr after the Big Bang, there is a radiation-domination period. The space extends at a rate proportional to  $a(t) \propto t^{1/2}$ , filled with very light or massless components moving at relativistic velocities in thermal equilibrium. During this period the forces enter their low-temperature regime. They are well separated and are carried by their respective particles created by interactions. The cooling of the plasma formed by quarks, leptons and their anti-particles, allowed then the quarks to bind in order to form hadrons, including protons and neutrons. As the temperature continues to decrease, hadrons ceased to be produced and therefore the tiny excess of quarks not annihilated by their anti-matter led to a baryon's excess over anti-baryons causing the so-called baryon asymmetry. The same happened for electron and positrons. The neutrons which are not stable particles decayed into protons creating an excess of 1:6 neutron:proton ratio. Protons, neutrons and electrons are now no longer relativistic.

At about 1 s, the neutrinos stopped interacting with the baryonic matter and decoupled. From

10 s to 1000 s the temperature is roughly  $10^8$  K, it is cold enough for the BBN process to start, allowing the formation of light elements such as deuterium, helium and lithium. The Universe is at this stage a hot plasma dominated energetically by photon radiation and too high in temperature to bind electrons to nuclei. Once the temperature reaches around 4000 K, neutral atoms start to form. Photons are not anymore in thermal equilibrium with the matter and they decoupled, releasing a relic radiation, known as the CMB. This period from redshift 6000 to about 1100 (from 18 kyr to 370 kyr after the Big Bang) is called the recombination, i.e. the epoch when protons and electrons bound together.

Matter-domination epoch took place from redshift 3600 to around 0.4 (47 kyr to 9.8 Gyr after the Big Bang). During this period the Universe's dynamic is set by the matter and its expansion follows  $a(t) \propto t^{2/3}$ . The Universe continues to decrease in density and temperature until reaching 4 K. This period is marked by the creation of structures observed today in the Universe. The Dark Age lasted during the major part of matter-domination area: the only sources of photons were the CMB or photons released by the change in energy of neutral hydrogen (21 cm line). The first generation of stars were formed causing progressively the end of the Dark Age and the creation of galaxies. Formation of these first astronomical objects emits a radiation which reionizes the Universe.

The current domination established around redshift  $\sim 0.5$  up to now is the Dark Energy area. One interpretation of the  $\Lambda$  term is that the vacuum density energy causes the expansion to accelerate,  $a(t) \propto \exp \sqrt{\Lambda/3} t$ . This interpretation is not known to be true, other models suggest for example a dynamical description as introduced in Section 1.1.6.

### Future fate

Solving Friedmann's Equations 1.19 permits to describe the behaviour of the expansion with respect to time. Different scenarios for the future of the Universe are possible and depends on the content density parameters. Therefore it is really important to have precise measurements to be able to discriminate between the possible fates of our Universe.

Figure 1.7 represents scenarios of the evolution of the Universe for multiple sets of parameters. The geometry of the Universe plays a very important role for future evolution. Without the dark energy existence, i.e.  $\Omega_\Lambda = 0$ , and in the case of a closed Universe (from Equation 1.32 the matter density is larger than the critical density), the Universe will reach a maximum size, then the gravity will stop its expansion and the Universe will start to contract until collapsing to a singularity called the Big Crunch. This is the red curve in the Figure 1.7.

In opposition, for an open Universe it will continue to grow. In the presence of Dark Energy this expansion accelerates and there are two main popular scenarios: the Big Rip and the Big Freeze. This latter relies on the asymptotic drop in temperature to absolute zero going along the expansion. It will cause any structures to decompose into particles reaching a thermodynamics equilibrium, and unable to continue processes that increase entropy. The

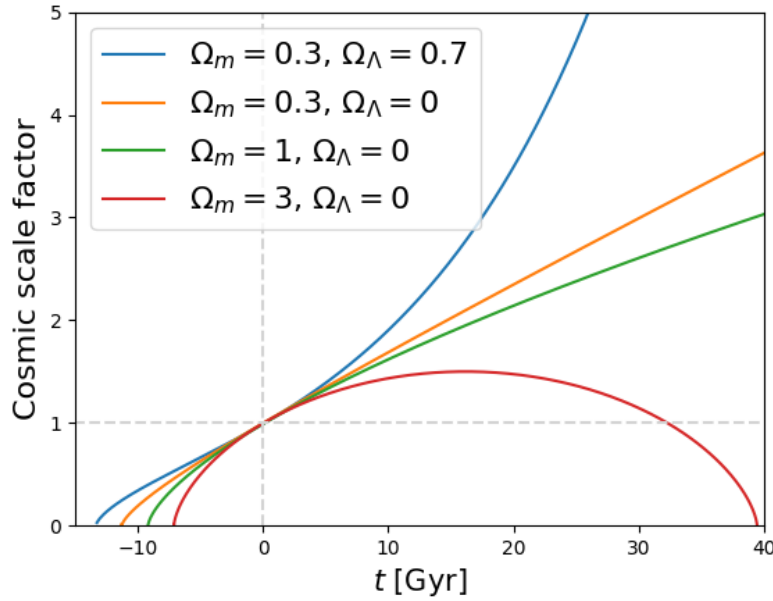


Figure 1.7: Different Universe's evolution scenarios. The curvature density parameter is fixed by the sum rule without radiation. Dashed lines show where we are currently, so now. The crossing points of the curves (on the negative time side) with  $a = 0$  are the respective ages of the Universe now for the different models.

Big Rip would happen if due to the acceleration of the expansion of space, all objects, even atomic particles will be torn apart. Energy and acceleration rate of the Universe will become infinite creating a singularity.

For an Einstein-de Sitter Universe, i.e. flat and filled with matter only  $\Omega_m = 1$  (Einstein and de Sitter, 1932), the expansion will continue forever with a rate approaching asymptotically zero. This is the green curve on the graph. With dark energy (the blue line), a flat Universe will continue to grow after an initial slow down, in an accelerate way. The future fates would be therefore similar to the ones for an open Universe. This latest case, i.e. flat Universe with dark energy, corresponds to our current most likely scenario according to our measurements.

The different scenarios depends on the nature of dark energy. While here I presented Universe's fate with a cosmological constant, this is not necessarily the intrinsic description of the Universe. As mentioned above, other models describe dark energy with a dynamic prescription (see also Section 1.1.6). Precise measurements are thus needed to understand the dynamics of the Universe's expansion.

### 1.1.5 Distances Measurements

In this section I will summarize the different distances definitions used in cosmology. I will rely on the definitions from Hogg, 1999. While in a flat geometry the distances are straightforward, in a curved space the distance between two points depends on the growing space geometry and thus on cosmological parameters of the Universe.

#### Comoving and proper distances

Comoving distance between two nearby objects moving with the Hubble flow, i.e. the expansion of the Universe, will be constant over time. Using the FLRW metric (Equation 1.14), the line-of-sight or radial comoving distance  $D_C$  (sometimes written also  $\chi$ ) is evaluated along a path followed by the photons emitted at time  $t_{\text{em}}$ , or redshift  $z_{\text{em}}$ , and observed at  $t_0$  (here we take  $t_0$  such that  $z(t_0) = 0$ ):

$$D_C = c \int_{t_{\text{em}}}^{t_0} \frac{dt'}{a(t')} = D_H \int_0^{z_{\text{em}}} \frac{dz'}{E(z')}, \quad (1.35)$$

where  $E(z)$  is defined in Equation 1.33, and  $D_H$  is the Hubble distance defined with the Hubble constant  $H_0$  and the speed of light  $c$ :

$$D_H = \frac{c}{H_0} = 3000 \text{Mpc}/h = 9.26 \times 10^{25} \text{m}/h. \quad (1.36)$$

It can be generalized to  $D_H(z) = c/H(z)$ .

The proper or physical distance is the distance as measured at the time it is observed. This distance changes due to the expansion of the Universe. The proper distance  $d(t)$  is related to the comoving distance by the scale factor:

$$d(t) = a(t) D_C. \quad (1.37)$$

When measured at the current Universe's age, these two definitions are equal. Figures in 1.8 illustrate both concepts to understand them better.

#### Transverse comoving distance and angular diameter distance

At the same redshift, the radial comoving distance of two objects measured by us would be the same value. However the observed separation between those two objects will depend on the Universe's curvature. We can define the transverse comoving distance  $D_M$  as a function of the

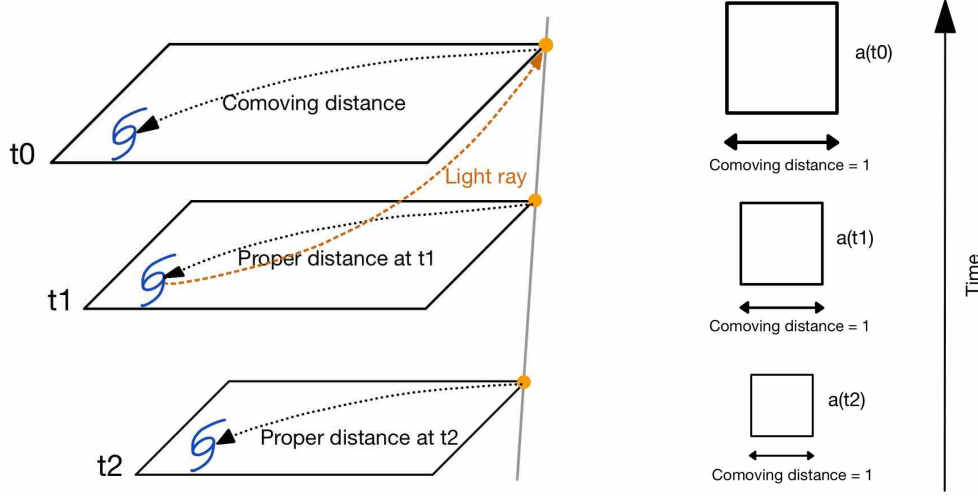


Figure 1.8: Illustrations to understand comoving and proper distances. Space is represented at three different times,  $t_2$ ,  $t_1$  and  $t_0$  which is present time. Orange point is our location in space.

radial comoving distance of these events  $D_C$ :

$$D_M = \begin{cases} D_H \frac{1}{\sqrt{-\Omega_k}} \sin(\sqrt{-\Omega_k} D_C / D_H) & \text{if } \Omega_k < 0 \\ D_C & \text{if } \Omega_k = 0 \\ D_H \frac{1}{\sqrt{\Omega_k}} \sinh(\sqrt{\Omega_k} D_C / D_H) & \text{if } \Omega_k > 0 \end{cases} \quad (1.38)$$

Therefore the comoving distance between two points at the same redshift separated by an observed angle  $\delta\theta$  is  $D_M \delta\theta$ .

Angular diameter distance  $D_A$  is the ratio between the physical (proper) size of an object  $l$  which depends on the Universe expansion so on its redshift  $z$ , and its observed angular size  $\delta\theta$ :  $D_A = l / \delta\theta$ . As for a fixed comoving size,  $\delta\theta = l_C / D_M$  we have in proper coordinates  $\delta\theta = l(1+z) / D_M$  and therefore  $D_A$  can be written:

$$D_A = \frac{D_M}{1+z}. \quad (1.39)$$

Figure 1.9 depicts the relation between angular diameter  $\delta\theta$ , angular diameter distance  $D_A$  and the proper size of the object  $l$ .

### Luminosity distance

The information we get from an astronomical object is the emitted light. For a source radiating in all directions at a given power, called luminosity, the observed flux is the source luminosity

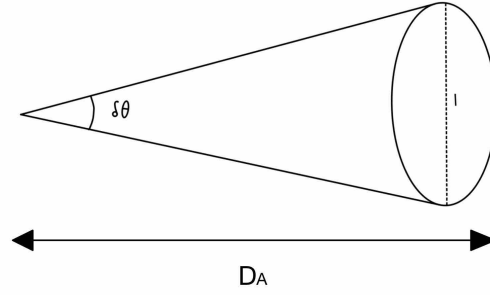


Figure 1.9: Scheme with angular diameter  $\delta\theta$ , angular diameter distance  $D_A$  and the transverse proper size  $l$ .

passing through the surface of a sphere area determined by the distance  $D_L$  to the emitted object:

$$F = \frac{L}{4\pi D_L^2}. \quad (1.40)$$

The luminosity distance  $D_L$  is therefore the distance determined from the flux of the observed object. It is related to the comoving transverse distance by:

$$D_L = (1 + z)D_M. \quad (1.41)$$

The luminosity distance can also be determined in terms of relations for the absolute and apparent magnitudes  $M$  and  $m$ , respectively:

$$M = m - 5 \log_{10} \frac{D_L}{10 \text{ pc}}. \quad (1.42)$$

The apparent magnitude in a spectral band  $x$  is defined as:  $m_x = -2.5 \log(F_x/F_{x,0})$ , where  $F_{x,0}$  is the reference flux in this band. The absolute magnitude is the apparent magnitude as observed at a distance of 10 pc.

### Cosmic distance ladder

Within a thousand of parsec to us, distances can be measured directly. However for more distant objects indirect techniques have to be exploit to determine their distances. In order to calibrate the relative distance of an astronomical object as defined in the precedent sections, we can work with ladders. In particular cosmic distance ladders can be used to measure the expansion rate of the Universe, see Figure 1.10.

For example standard rulers are reference objects for which the proper size is known. It is thus possible to compare the angular size to be able to get the angular diameter distance and thus studying the Universe expansion from a series of distance measurements. I will present later in more details the physical scale imprinted in the baryon acoustic oscillations (BAO).

Another important ladder is the category of standard candles for which the luminosity is known. This is the technique that was used to discover the acceleration of the expansion of the Universe.

Standard sirens is an event for which it is possible to predict theoretically the intensity of the emitted waves, in order to measure the distance, such as gravitational waves<sup>VII</sup>.

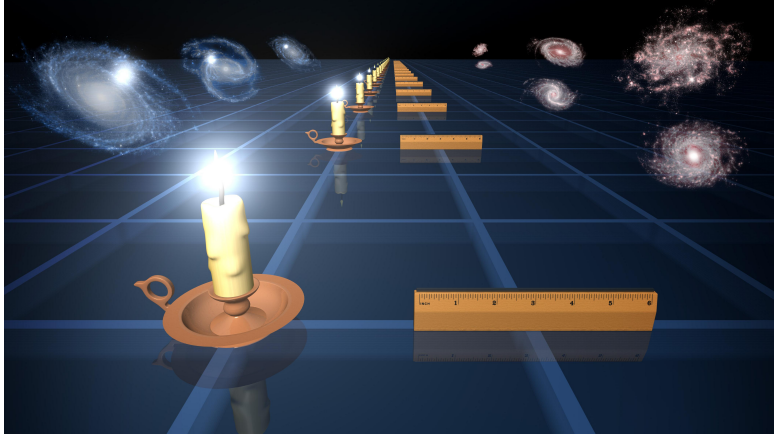


Figure 1.10: Explaining scheme for standard candles on the left for which a reference luminosity is known and standard rulers on the right for which a physical scale is known. (Credits of the figure: NASA/PL-Caltech/R. Hurt (SSC)).

### Discovery of the late-time acceleration

In 1998 two independent groups (Riess et al., 1998; Perlmutter et al., 1999) established a luminosity-redshift relationship by studying samples of type Ia Supernovae (SNe Ia), resulting from an end-of-life star implosion in a binary system containing at least a white dwarf. As the critical mass at which the white dwarf would explode is constant, the intrinsic brightness will be the same for all of supernovae, making them a good standard candle.

Figure 1.11 displays the distance modulus obtained with Equation 1.42, of the Supernovae as a function of their redshift from Riess et al., 1998. From these curves it yields that a non-zero  $\Omega_\Lambda$  is favoured as can be seen on the left plot of Figure 1.11. Moreover the deceleration parameter  $q = -\ddot{a}a/\dot{a}^2$  favors an accelerating expansion ( $q < 0$ ). This was the first observational evidence that the Universe was undergoing an acceleration of its expansion. The unknown nature of this acceleration was then given a name: the dark energy.

<sup>VII</sup>First GW detection by LIGO in 2017 (Collaboration, 2016), for a future roadmap of physics with GW which were shown to be powerful to constrain cosmological parameters see e.g. Bailes et al., 2021.



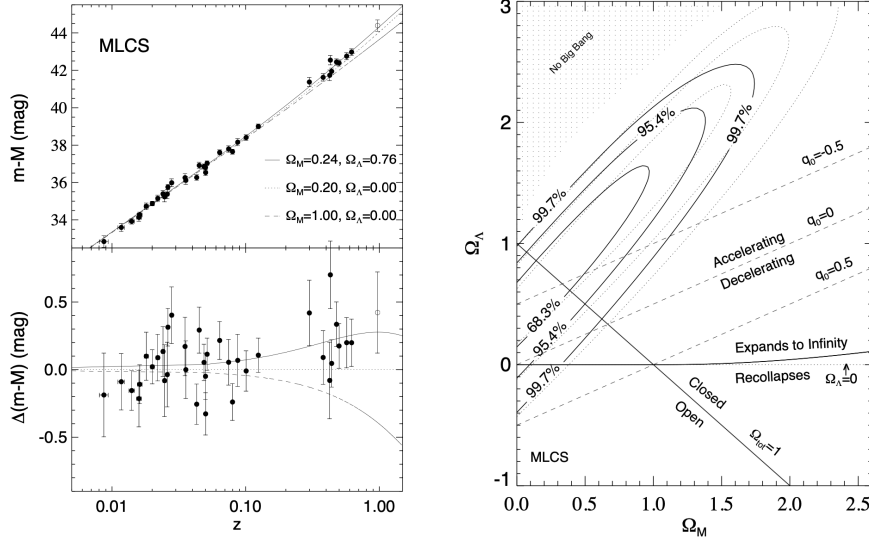


Figure 1.11: Right: Hubble diagram from Riess et al., 1998 for SNe Ia. Left: Confidence intervals in the  $\Omega_m, \Omega_\Lambda$  plane from Riess et al., 1998 (on the plot  $q \equiv -\ddot{a}a/\dot{a}^2$  is the deceleration parameter that can be parametrized when the radiation is neglected, i.e.  $\Omega_{\gamma,0} \ll \Omega_{m,0}$ , as  $q_0 = \Omega_{m,0}/2 - \Omega_{\Lambda,0}$ ).

### 1.1.6 The Standard Model of Cosmology

The standard model of cosmology, also called  $\Lambda$ CDM, is currently the simplest descriptive model we have of our Universe characterizing a Big Bang cosmology.

It relies on different assumptions that I presented earlier: space and gravity are correctly described by GR and the cosmological principle (see 1.1.2). From those it results the FLRW metric (see 1.1.3) and thus the Friedmann equations (see Equation 1.33). In its standard form the model describes the late time acceleration with a cosmological constant  $\Lambda$  associated with dark energy.

$\Lambda$ CDM model assumes the Universe to be filled with: baryonic matter, Cold Dark Matter (CDM), relativistic particles and dark energy. From current measurements, the actual division content of the Universe is shown on Figure 1.12. Dark energy and dark matter represent about 95% of the total content: most of the Universe is from an unknown nature.

#### Dark matter

Baryonic matter is the matter which surrounds us. However in  $\Lambda$ CDM it constitutes only about 5% of the total content of the Universe. Most of the matter interacting gravitationally in the Universe has not yet been discovered. This hypothetical matter is named dark matter, as it does not emit radiation so it is obscure (for some overviews on the subject here a few references: Bergström, 2000, Bertone and Hooper, 2018, Green et al., 2022, Drlica-Wagner

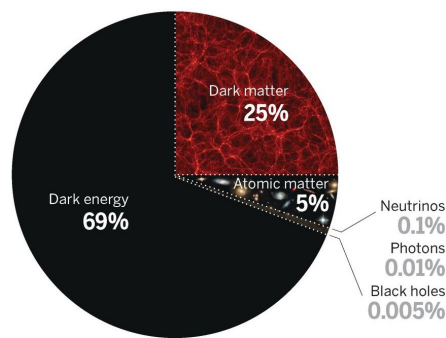


Figure 1.12: Composition content of the Universe as measured today. (Credits of the figure: Spergel, 2015).

et al., 2022).

While it has never been detected directly, there are multiple observational evidences suggesting the existence of dark matter, such as galaxy rotation curves, velocity dispersions, galaxy clusters or gravitational lensing. Dark matter would also be responsible for most of the Universe's structures bound by gravitation observed today.

In 1933, Fritz Zwicky (Zwicky, 1933) was the first to detect indirectly dark matter. He studied the Coma galaxy cluster and found an anomaly: the galaxies' rotational velocities exceeded the expected value determined using the Virial theorem with the mass computed from its luminosity. From his calculations the mass should have been around 400 times larger, suggesting the existence of a large amount of obscured matter. In 1970, Vera Rubin and Kent Ford (Rubin and Ford, 1970) confirmed this gravitational anomaly by observing the rotational curve of spiral galaxies. Figure 1.13 represents a similar rotational curve. The observed orbiting velocities of stars do not match the theoretical predictions for a disk and gas. Data present a flat curve instead of decreasing velocities with the distance to the center. The velocity curve of a massive surrounding dark halo around the galaxy should be added in order to match the observations. This halo is interpreted to be made of dark matter.

There are now other pieces of evidence for dark matter. BBN data set a bound on the maximum baryon density in the Universe, which only corresponds approximately to a fifth of the total matter content of the Universe (e.g. Copi et al., 1995).

Gravitational lensing for example can also give important insight on dark matter. Indeed light deflection has been described by Einstein's theory of GR: light rays propagating through a gravitational field are bent leading to deformation of astronomical bodies (Lynds and Petrosian, 1986; Soucail et al., 1987) or multiple images of the same object (Walsh et al., 1979). It can therefore be used to infer the underlying matter density field and thus give constraints on dark matter (Tyson et al., 1990).

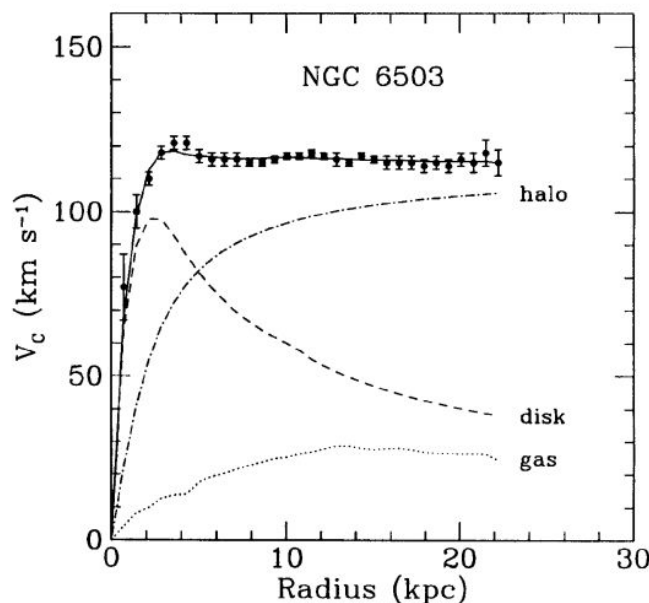


Figure 1.13: Rotation curve of NGC 6503 from Begeman et al., 1991. It shows the data with points, the theoretical predictions from the disk, from gas and from a dark matter halo. The solid line is the total of the three contributions.

### Cold dark matter and alternative models

The most popular model is the Cold Dark Matter (CDM) made of weakly interacting and cold, i.e. non-relativistic, particles (Peebles, 1982) in a  $\Lambda$ CDM model. After the Big Bang, as Universe cooled, dark matter decoupled from the expansion, collapsed and bounded gravitationally in halos, creating higher density areas. This will lead, after recombination, to a hierarchical clustering of matter and gas seeded around those areas; gravitational attraction of CDM particles will form cosmic structures (Blumenthal et al., 1984, Dodelson et al., 1996), with CDM clumping on all scales, where smaller structures merge into larger structures. Promising candidates are the Weakly Interacting Massive Particles (WIMPs, Steigman and Turner, 1985). These hypothetical particles would have weak force interactions with a mass range of approximately 100 GeV. To this day, they have never been detected. Other suitable sources of CDM are Axions which are light elementary particles (Peccei and Quinn, 1977) or Massive compact halo objects (MACHOs) such as neutron stars or blackholes.

While CDM has great success to explain the structure formation on large scales in the Universe, on smaller scales the model encounters a few issues where observations and predictions differ. The first debating issue lies in the rotation curves; they are better fitted, in the dark matter distribution, by constant density cores while models lead to a cuspy dark matter halos (Moore, 1994; Navarro et al., 1997). Secondly, halos simulations with  $\Lambda$ CDM model predict an abundance of substructures of mass greater than  $10^8 M_\odot$  within the Local Group of about 2 times larger than the number of satellite dwarf galaxies of the Milky Way that was observed

(Klypin et al., 1999, Moore et al., 1999), this is referred to as the “missing satellite” and “too big to fail” (as predictions give halos massive enough to host visible matter Boylan-Kolchin et al., 2011) problems. Indeed, it would mean that the substructures overmerged in galactic halos but not in clusters, for which the abundance is in agreement with observations (Springel et al., 2001) implying a one to one mapping of dark to luminous matter substructures. More recent observations found a certain amount of fainter dwarf elliptical galaxies in different systems such as in the neighbourhood of M81 (Chiboucas et al., 2013), M101 (Danieli et al., 2017; Merritt et al., 2014), M94 (Smercina et al., 2018), Centaurus A (Crnojević et al., 2019) or around the Milky Way (Carlsten et al., 2022).

Alternative models of dark matter exists, each of them having their strength and weakness. Warm Dark Matter (WDM) model consists of cooled hot dark matter particles, i.e. particles with significant non-relativistic velocities in the early Universe. It differs from CDM since they have a thermal motion which allows them to free out of the primordial potential well, suppressing the small-scale structure of matter. WDM particles are assumed to be around a few keV mass (Haiman et al., 2001). WDM outperforms CDM on different aspect: simulations with WDM found a halo mass function suppressed as expected (Bode et al., 2001, J. Wang and White, 2007) and which matched the observed number of satellites (Polisensky and Ricotti, 2011). Strong candidates for WDM particles are the sterile neutrino (Asaka and Shaposhnikov, 2005, Boyarsky et al., 2009) or gravitino (Baltz and Murayama, 2003). As seen on Section 1.2.3, a strong way to constrain mass of WDM is Lyman- $\alpha$  power spectrum (Viel et al., 2005, Palanque-Delabrouille et al., 2020). Mixture combinations of different DM particles are also considered (e.g. Boyarsky et al., 2009).

Hot Dark Matter (HDM) is composed of very light particles with ultra-relativistic velocities at redshift  $10^6$  with a very low interaction rate. The neutrinos are candidates for this dark matter description (Primack and Gross, 2001). The scenario of pure HDM is now excluded by observations (see also Section 1.2.3). Indeed the existence of high-redshifted quasars already contradicts this scenario.

Instead of considering those gravitational anomalies as an indication for the existence of a new matter, they are models proposing modifications of the Newtonian laws of gravity, Modified Newtonian dynamics (MOND, Milgrom, 1983).

### Dark energy

The Universe’s expansion is accelerating as seen in he Section 1.1.4. This was explained by adding dark energy, an energy from an unknown nature acting against gravitation and dominating the late Universe (see Section 1.1.4). In the  $\Lambda$ CDM paradigm dark energy is described with the cosmological constant  $\Lambda$  which manifests itself as a constant in Einstein’s Equation 1.6. Such a dark energy can be interpreted as the vacuum energy, so that the empty space has an attributed mass.

Another form of dark energy proposed is a scalar field, similarly to the inflaton which drives inflation but at a much lower scale of energy (see its description in Section 1.1.4). It leads therefore to a dynamical description of dark energy. In this context, one popular scalar field  $\phi$  is the quintessence dominated by a potential energy  $V(\phi)$  (Fujii, 1982; Ratra and Peebles, 1988; Caldwell et al., 1998). Quintessence has the following equation of state:

$$w_\phi = \frac{p_\phi}{\rho_\phi} = \frac{\frac{1}{2}\dot{\phi}^2 - V(\phi)}{\frac{1}{2}\dot{\phi}^2 + V(\phi)}. \quad (1.43)$$

It exists many different ways to describe the relation between  $V$  and  $\phi$  (see different examples in Sahni, 2002). We also note that the scalar field can vary over time and space. A parametrization for its time-evolution is the following (Chevallier and Polarski, 2001):

$$w(z) = w_0 + \frac{z}{1+z} w_a, \quad (1.44)$$

where  $w_0$  is the value now, at  $z = 0^{\text{VIII}}$ . We note that when evaluated at another redshift, defining a pivot redshift  $z_p$  or pivot scale factor  $a_p$ , the parametrization becomes:

$$w(a) = w_p + (a_p - a) w_a, \quad (1.45)$$

Injecting this  $w(z)$  in the time-evolution density of Equation 1.28, allows to describe Dark Energy within this model with three parameters. We often refer to this extended  $\Lambda$ CDM cosmological model with quintessence as  $w$ CDM.

Special cases of quintessence is  $w_\phi = -1$  and in this case as seen previously, we have a cosmological constant. Phantom energy is the particular case when  $w_\phi < -1$ , it will lead to a Big Rip.

### Current parameter values

The current simplest  $\Lambda$ CDM model possesses six parameters for a flat Universe: the baryon density  $\Omega_b$ , the cold dark matter density  $\Omega_c$ , the age of the Universe  $t_H$ , the spectral index  $n_s$ , the amplitude of the primordial fluctuations  $A_s$  and the optical depth to reionization  $\tau$ . The reionization optical depth is a measurement of the line-of-sight opacity of electrons to radiation. The other parameters are described in this first Chapter (I described the three first parameters in this Section and I will described the two left parameters in the next Section 1.2). We note that the matter density  $\Omega_m$  is related to the baryon and dark matter densities as:  $\Omega_m = \Omega_b + \Omega_c$ .

Very precise measurements of these parameters, gathered in Table 1.1, are from Planck collaboration (Planck Collaboration et al., 2020) which relies on CMB data taken with the Planck satellite, combined with other probes. They are used as reference. In this case, under the

<sup>VIII</sup>Commun fiducial values are  $w_0 = -1$  and  $w_a = 0$ .

model assumptions some parameters are fixed: the total density is equal to 1,  $w = -1$ , the effective number of neutrino species to  $N_{\text{eff}} = 3.046$  and the sum of neutrinos masses is  $\sum m_\nu = 0.06 \text{ eV}/c^2$ .

Parameters name	Symbol	Value
Baryon density	$\Omega_b h^2$	$0.02242 \pm 0.00014$
Dark matter density	$\Omega_c h^2$	$0.11933 \pm 0.00091$
Age of the Universe	$t_H$	$13.787 \pm 0.020 \text{ Gyr}$
Reionization optical depth	$\tau$	$0.0561 \pm 0.0071$
Amplitude of curvature fluctuations at $k = 0.05 \text{ Mpc}^{-1}$	$\ln(10^{10} A_s)$	$3.047 \pm 0.014$
Spectral index	$n_s$	$0.9665 \pm 0.0038$

Table 1.1: List of the 6 parameters for a flat  $\Lambda$ CDM model with values of Planck Collaboration et al., 2020 (last column of Table 2) with their 68% intervals.

Other parameters can be derived from this set such as the Hubble parameter  $H_0$ , the matter fluctuation in a sphere of  $8h^{-1} \text{ Mpc}$  radius  $\sigma_8$  or the various density parameters.

$\Lambda$ CDM parameter set can be extended from a few parameters. We have seen that the dark energy equation of state can be let free and in this case we refer to a  $w$ CDM model. When leaving the curvature as a free parameter, we often referred to a  $\text{o}\Lambda$ CDM model. It is also possible to leave the sum of the neutrino masses free or density parameter of the relativistic particles. We note that measurements of  $\Omega_\gamma$  gives  $\Omega_\gamma \sim 10^{-4}$ .

## Limitations

The  $\Lambda$ CDM standard model in its simplest form<sup>IX</sup> is very successful in describing the LSS and the cosmic content abundances. However while it has powerful predictions which were confirmed observationally,  $\Lambda$ CDM suffers from some theoretical issues or discrepancies between observational probes (for a review see e.g. Bull et al., 2016, Perivolaropoulos and Skara, 2022).

Indeed there is a lack of physical description of some key model ingredients, such as inflation, dark energy and dark matter. I already mentioned the fine tuning problem for which inflation is seen as a solution. Another fortuitous observation is the cosmic coincidence problem (Huey and Wandelt, 2006, Velten et al., 2014), that questions the fact that the matter and dark energy densities are of the same order, making the current period a special time. We have also seen above the limitations of the CDM description of dark matter such as the cusp or missing satellites issues (Del Popolo and Le Delliou, 2017).

Those last years tensions in cosmological parameters measured by different probes have been observed, namely in  $\sigma_8$  and  $H_0$ . In the  $\Omega_m$ - $\sigma_8$  plane<sup>X</sup> there is indeed an observed tension of  $2\sigma$  between Planck measurements and galaxy clusters or weak lensing measurements (Asgari

<sup>IX</sup>In literature, it is sometimes referred to as the “Vanilla” form of  $\Lambda$ CDM model.

<sup>X</sup>Equivalently it is common to define the parameter  $S_8 \equiv \sigma_8 \sqrt{\Omega_m/3}$ .

et al., 2021, T. Abbott et al., 2016, Heymans et al., 2013, Hildebrandt et al., 2017). Left panel of Figure 1.14 illustrates this tension, showing the contours in the  $\Omega_m$ - $\sigma_8$  plane, as measured by Planck or different weak gravitational lensing probes.

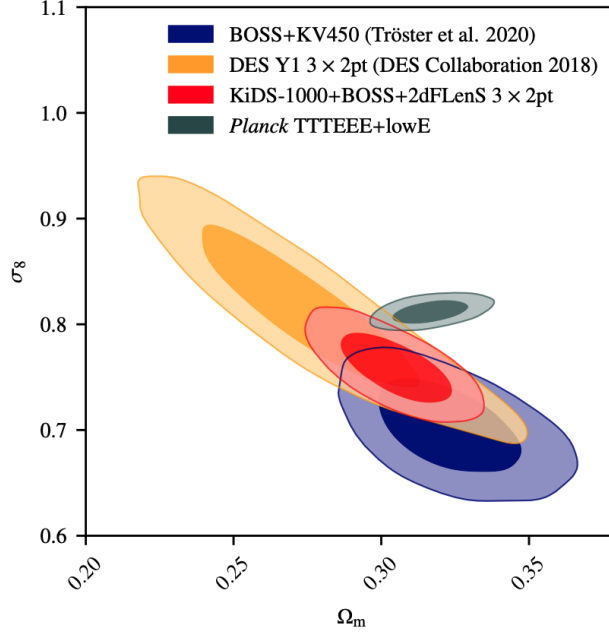


Figure 1.14: Contours in the  $\sigma_8$  and  $\Omega_m$  planes for different lensing probes and Planck CMB measurements. It illustrates the  $\sim 2\sigma$  tension seen between those probes. (Credits of the figure: Heymans et al., 2021).

Another significant tension in  $H_0$  is called the Hubble tension (Verde et al., 2019, Di Valentino et al., 2021 for an overview). A  $5\sigma$  discrepancy is observed between the late-time measurements in the local Universe, such as SN, Cepheids or time delays techniques, and the early Universe with CMB or LSS for example. Latest value of Planck is  $H_0 = 67.36 \pm 0.54 \text{ km s}^{-1} \text{ Mpc}^{-1}$  (Planck Collaboration et al., 2020), consistent values were found from LSS or WMAP (Alam et al., 2017, Alam, Aubert, et al., 2021, Hinshaw et al., 2013). Direct measurements in the local Universe gives higher values around  $73 \text{ km s}^{-1} \text{ Mpc}^{-1}$  (Riess et al., 2019, B. A. Reid and White, 2011, Bonvin et al., 2017), creating an unexplained  $5\sigma$  tension between the two sets of measurements. This tension is even more general across more experiments than mentioned here as illustrated on the right of Figure 1.15.

While solutions to these tensions could be for example from non-treated systematics, other explanations can arise by changing the model. Some tentative have been made, such as modified gravity models, dynamic dark energy models (G.-B. Zhao et al., 2017) or interacting dark energy with dark matter (von Marttens et al., 2019).

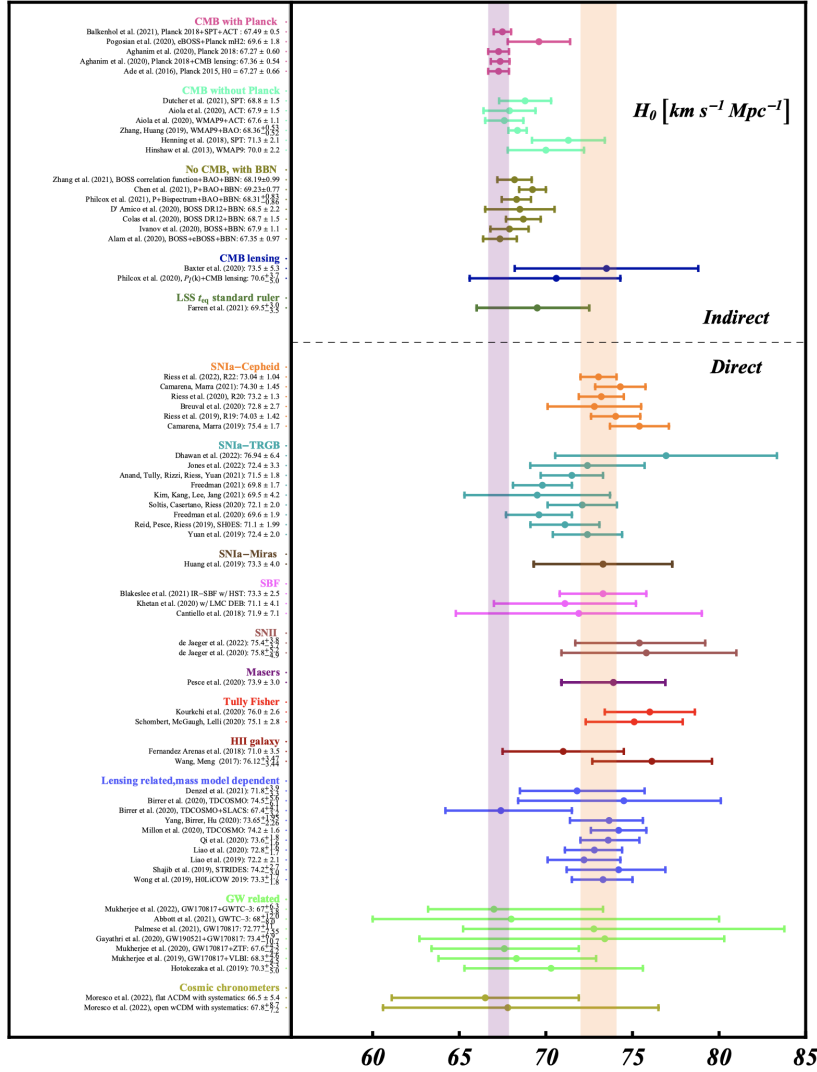


Figure 1.15:  $H_0$  measurements by different probes of the late and early Universe, exacerbating the  $H_0$  tension. (Credits of the figure: Abdalla et al., 2022).

## 1.2 Large-Scale Structures in the Universe

On large scales, galaxies in the Universe display a web-like distribution. Galaxies gather in clusters or groups at the intersection of filamentary structures, as in the Figure 1.16. Between those regions lie voids, which are large empty regions containing little or no galaxies. The study of these Large Scale Structures (LSS) can provide valuable insights about cosmic evolution history. LSS trace the matter distribution in the Universe. Their evolution results from a balance between gravitational forces and the Universe expansion, under the assumption of a  $\Lambda$ CDM cosmology. Thus LSS can help constraining cosmological parameters, such as the matter density  $\Omega_m$ , the Dark Energy density parameters,  $\Omega_\Lambda$  the equation of state of dark energy  $w$  or the Hubble constant  $H_0$ .



In this Section, I will introduce those LSS and their formation to understand their value in cosmological analysis. I will follow along others the summary works of H. Mo et al., 2010, Coles, 2001, Bernardeau et al., 2002, Peebles, 1993, Peacock, 2003, Weinberg et al., 2013 and lectures of Jaiyul Yoo (UZH) on Advanced Topics of Theoretical Cosmology. I will mainly limit myself to linear theory. Non-linear approach can be reached with simulations that resolve the equations numerically.

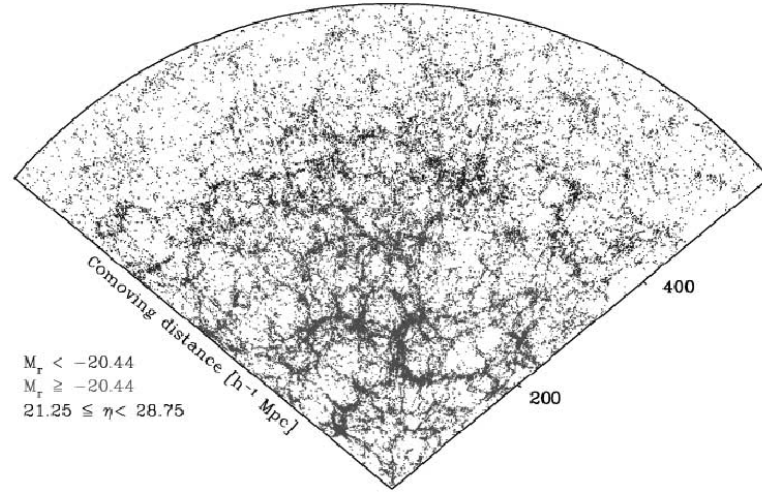


Figure 1.16: Large scale structures formed by galaxies as observed by the Sloan Digital Sky Survey in the early 2000's. (Credits of the figure: Park et al., 2005).

### 1.2.1 Formation

#### Emergence within primordial Universe

Birth of large scale structures observed today took place in the very early Universe, described briefly in Section 1.1.4. The Universe was at that moment highly homogeneous, but presenting some small density fluctuations over the space. With the rapid expansion, these primordial fluctuations became the seeds of LSS that grew during matter domination epoch.

Matter formations evolved therefore from the growth of those initial fluctuations as a result of the gravity acting against Universe's expansion and pressure. The most prevalent scenario is a bottom-up formation for LSS and galaxies, favoured in  $\Lambda$ CDM model. It relies on a hierarchical structure formation: smaller scale structures such as galaxies, first collapse gravitationally to successively merge into larger structures (Peebles, 1965). Structure formation in a  $\Lambda$ CDM Universe is shown on Figure 1.17.

Other scenario is a top-bottom formation<sup>XI</sup> in which the initial fluctuations would first grow into dense LSS that will fragment into smaller structures down to galaxies (Zel'dovich, 1970).

<sup>XI</sup>It would correspond to the scenario for a HDM.

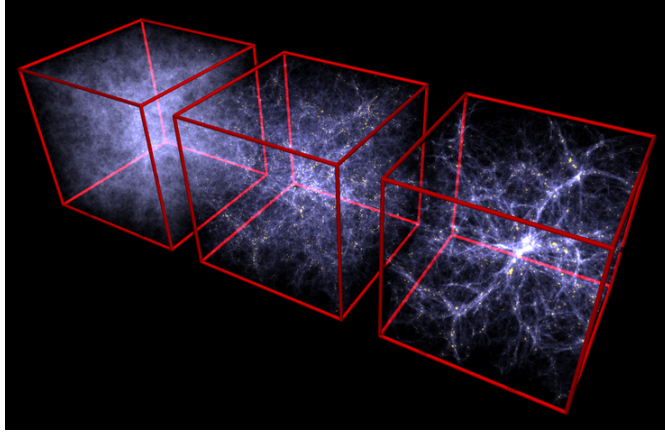


Figure 1.17: Simulation at different redshifts, from back to front  $z = 6, 2, 0$ , within a box of  $100 h^{-1}\text{Mpc}$  length. (Credits of the figure: Volker Springel, MPI).

### Universe as a fluid

Before recombination, the Universe is a plasma with its particles tightly coupled. After recombination, baryons can be described as an ideal gas as their mean free path is small compared to the scales of interest and dark matter is assumed to behave as a collision-less fluid. It results that the matter distribution can be represented as a fluid.

A fluid time evolution is governed by three main equations. The continuity equation (Equation 1.46a) describing the density transport as a function of time. Euler equations or the equations of motion (the three Equations 1.46b) give the fluid velocity with respect to gravity and pressure interactions. The Poisson equation (Equation 1.46c) relates the potential to the density field:

$$\frac{\partial \rho}{\partial t} + \nabla_r \cdot (\rho \vec{u}) = 0, \quad (1.46a)$$

$$\frac{\partial \vec{u}}{\partial t} + (\vec{u} \cdot \nabla_r) \vec{u} = -\nabla_r \phi - \frac{1}{\rho} \nabla_r P, \quad (1.46b)$$

$$\nabla_r^2 \phi = 4\pi G \rho, \quad (1.46c)$$

where  $\rho(\vec{x}, t)$  is the fluid density at space position  $\vec{x}$  and time  $t$ ,  $\vec{u}(\vec{x}, t)$  its velocity,  $P(\vec{x}, t)$  the pressure and  $\phi(\vec{x}, t)$  the gravitational potential. We note that one equation is missing in order to have the 6 unknown parameters fully described. Therefore a supplementary equation has to be added to specify the pressure: the equation of state (see below the Section 1.2.1).

Now, let's adapt those equations for an expanding Universe. Assuming a FLRW metric (see 1.1.3), the comoving positions  $\vec{x}$  are related to the proper positions  $\vec{r}$  with Equation 1.37,

therefore we have the following relations for their derivatives in comoving coordinates:

$$\vec{r} = a(t)\vec{x}, \quad (1.47a)$$

$$\vec{u}(\vec{x}, t) = \dot{a}\vec{x} + a\dot{\vec{x}} \equiv \dot{a}\vec{x} + \vec{v}, \quad (1.47b)$$

$$\nabla_r \rightarrow \frac{1}{a} \nabla_x, \quad (1.47c)$$

$$\frac{\partial}{\partial t} \Big|_r \rightarrow \frac{\partial}{\partial t} \Big|_x - \frac{\dot{a}}{a} \vec{x} \cdot \nabla_x. \quad (1.47d)$$

Using Friedmann's Equation 1.21 without pressure, we define the gravitational potential  $\Phi = \phi + X$  such that  $\nabla_x^2 X / a^2 = -4\pi G \bar{\rho}$  in order to have the gravity sourced only from the contrast  $\rho - \bar{\rho}$ , where  $\bar{\rho}$  is the mean background density:

$$\Phi \equiv \phi + \frac{1}{2} \ddot{a} a \vec{x}^2. \quad (1.48)$$

Consequently the fluid Equations 1.46 conformed for a Universe in expansion are<sup>XII</sup>:

$$\frac{\partial \rho}{\partial t} + 3 \frac{\dot{a}}{a} \rho + \frac{1}{a} \nabla_x \cdot (\rho \vec{v}) = 0, \quad (1.49a)$$

$$\frac{\partial a \vec{v}}{\partial t} + (\vec{v} \cdot \nabla_x) \vec{v} = -\nabla_x \Phi - \frac{1}{\rho} \nabla_x P, \quad (1.49b)$$

$$\nabla_x^2 \Phi = 4\pi G a^2 (\rho - \bar{\rho}). \quad (1.49c)$$

We note that the continuity expression was already expressed previously with Friedmann equations, see Equation 1.18.

### Gravitational instabilities

The primordial fluctuations in the Universe density are sources of gravitational instabilities, that can be treated as small perturbations in the cosmological fluid described above.

Let's define the density contrast  $\delta$  that describes the overdensity field from the density  $\rho$  and the mean density  $\bar{\rho}$ :

$$\delta(x, t) = \frac{\rho(x, t) - \bar{\rho}(t)}{\bar{\rho}(t)}. \quad (1.50)$$

Considering infinitesimal perturbations in the different quantities around the background

---

<sup>XII</sup>We use the divergence:  $\nabla \cdot \vec{x} = 3$ .

values such as:

$$\begin{aligned}
 \rho(x, t) &= \bar{\rho}(t) + \delta\rho(x, t), \\
 v(x, t) &= \bar{v}(t) + \delta v(x, t), \\
 P(x, t) &= \bar{P}(t) + \delta P(x, t), \\
 \Phi(x, t) &= \bar{\Phi}(t) + \delta\Phi(x, t).
 \end{aligned} \tag{1.51}$$

In the linear regime, the fluid Equations 1.49 become for a non-relativistic fluid<sup>XIII</sup> with respect to the density contrast, dropping the higher order terms such as  $v^2$ ,  $\delta^2$  or  $v\delta$ :

$$\frac{\partial\delta}{\partial t} + \frac{1}{a}\nabla_x \cdot v = 0, \tag{1.52a}$$

$$\frac{\partial v}{\partial t} + \frac{\dot{a}}{a}v = -\frac{1}{a}\nabla_x\delta\Phi - \frac{1}{a\bar{\rho}}\nabla_x\delta P, \tag{1.52b}$$

$$\nabla_x^2\delta\Phi = 4\pi G a^2 \bar{\rho}\delta. \tag{1.52c}$$

Differentiating as a function of time the continuity Equation 1.52a and injecting inside the Euler Equations 1.52b and Poisson Equation 1.52c (reinjecting as well the continuity Equation 1.52a), we have a description in the linear approximation of the evolution of density fluctuations for small perturbations, so with  $\delta \ll 1$ :

$$\ddot{\delta} + 2\frac{\dot{a}}{a}\dot{\delta} = 4\pi G\bar{\rho}\delta + \frac{1}{a^2\bar{\rho}}\nabla_x^2\delta P. \tag{1.53}$$

### Equation of state

For an ideal fluid we can assume to have an equation of state depending on the temperature  $T$  or the entropy  $S$ :

$$P = P(\rho, S) \quad \text{or} \quad P = P(\rho, T). \tag{1.54}$$

The equation of state can be used to expand the pression gradient in Equation 1.53:

$$\frac{\nabla_x T}{\bar{\rho}} = \frac{1}{\bar{\rho}} \left( \frac{\partial P}{\partial \rho} \Big|_S \nabla_x \rho + \frac{\partial P}{\partial S} \Big|_\rho \nabla_x S \right). \tag{1.55}$$

Using the sound speed definition:

$$c_s^2 = \frac{\partial P}{\partial \rho} \Big|_S, \tag{1.56}$$

<sup>XIII</sup>We use  $\rho \propto a^{-3}$  for a non-relativistic fluid of Equation 1.28 to get the continuity Equation 1.49a as a function of the density contrast:  $\frac{\partial\delta}{\partial t} + \frac{1}{a}\nabla_x \cdot ((1+\delta)\vec{v}) = 0$ .

and considering the adiabatic case, i.e.  $\frac{dS}{dt} = 0$ , the linearized fluid Equation 1.53 becomes:

$$\ddot{\delta} + 2\frac{\dot{a}}{a}\dot{\delta} = 4\pi G\bar{\rho}\delta + \frac{c_s^2}{a^2}\nabla_x^2\delta + \frac{1}{a^2}\frac{\partial P}{\partial S}\nabla_x^2 S. \quad (1.57)$$

It governs the non-relativistic time evolution of small perturbations inside the expanding Universe. On the left-hand side, the second term is the Hubble drag describing the suppression of the perturbation growth due to the Universe's expansion. On the right-hand side, the Poisson term expresses the effect of gravity which helps the perturbations to grow, and the two last terms encode the pressure effects with the spatial gradient of the density and the entropy.

## 1.2.2 Cosmic Density Field

### Statistical description

A cosmic field can be characterized by its density field  $\delta(\vec{x})$  that I defined in Equation 1.50, which specifies the density contrast at every space point  $\vec{x}$ . The density contrast is assumed to be the realisation of a random process in the very early Universe due to quantum variations in the inflaton field (see Section 1.1.4). Therefore it makes sense to have a statistical description of the random process which generates the density field. Figure 1.18 represents such a dark matter density field.

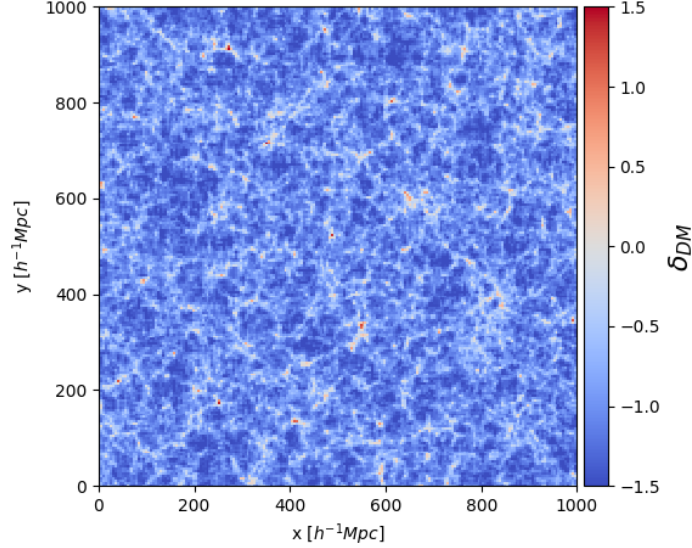


Figure 1.18: Dark matter density contrast at redshift 1.48 from a simulation box used for EZmocks (introduced after in Chapters 2 and 3). Here a slice of  $1000 \times 1000 \times 50 \ h^{-1}\text{Mpc}$  is drawn.

Writing the probability distribution function  $P$  generating random perturbation fields  $\delta_i \equiv \delta(\vec{x}_i)$  that can be seen as  $n$  infinitesimal cell divisions of the Universe centered at  $\vec{x}_i$  with

$i = 1, 2, \dots, n$ :

$$P(\delta_1, \delta_2, \dots, \delta_n) d\delta_1 d\delta_2 \dots d\delta_n, \quad (1.58)$$

the moments of  $P$  are, with integers  $p_i \geq 0$ :

$$\langle \delta_1^{p_1} \delta_2^{p_2} \dots \delta_n^{p_n} \rangle = \int \delta_1^{p_1} \delta_2^{p_2} \dots \delta_n^{p_n} P(\delta_1, \delta_2, \dots, \delta_n) d\delta_1 d\delta_2 \dots d\delta_n. \quad (1.59)$$

The cosmological principle enunciated in Section 1.1.2 requires that the cosmic density field is statistically homogeneous and isotropic, implying that the probability distribution function or its moments are invariant under spatial translations and rotations. In addition by presuming that our Universe is one stochastic realisation of the random generating density process, even without evidence of the existence of other realisations, we are also able to assume ergodicity. Ergodicity states that a large enough set of random realisations of a stochastic process is equivalent statistically than taking a single sample in its whole. It means for example that the volume average density  $\bar{\rho}$  is equivalent to averaging different realisations  $\langle \rho \rangle$ .

Therefore it implies that the mean of the density perturbation field, i.e. the first moment, and its variance are independent of the position:

$$\langle \delta(\vec{x}) \rangle = 0, \quad \langle \delta^2(\vec{x}) \rangle = \sigma^2. \quad (1.60)$$

### Two-point correlation function

A very important moment from Equation 1.59 when characterising the LSS is the two-point correlation function  $\xi(r)$ :

$$\xi(r) = \langle \delta(\vec{x}_1) \delta(\vec{x}_2) \rangle \quad (1.61)$$

where  $r = |\vec{x}_2 - \vec{x}_1|$  is the norm separation between the two vector positions  $\vec{x}_1$  and  $\vec{x}_2$ . The two-point correlation function expresses the excess probability of finding two elements separated by a distance  $r$ . This function is used to quantify the clustering of the matter. This is illustrated in Figure 1.19 for a discretization of the density field: the correlation function is the normalized count of elements separated by a radius between  $r$  and  $r + dr$ .

It can be extended to higher statistics:

$$\xi_n(\vec{x}_1, \vec{x}_2, \dots, \vec{x}_n) = \langle \delta(\vec{x}_1) \delta(\vec{x}_2) \dots \delta(\vec{x}_n) \rangle \quad (1.62)$$

However in these cases the  $n$ -point correlation functions are not anymore characterised by a single distance and depend on the separation of every pairs belonging to the  $n$  points<sup>XIV</sup>.

<sup>XIV</sup> The Fourier transform of the three-point correlation function is named the bispectrum.

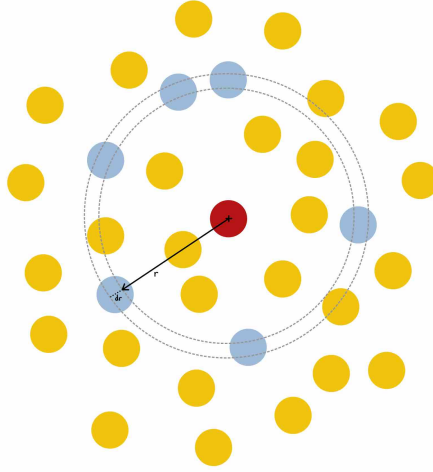


Figure 1.19: Illustration to understand the two-point correlation function.

### Power spectrum

It is often more convenient to work in Fourier space as fields can be seen as a superposition of modes, i.e. plane waves with wave number (or spatial frequency)  $k$ , and are then easier to build.

The Fourier transformation of the density perturbation field  $\delta(\vec{k})$  is defined from its configuration space version  $\delta(\vec{x})$ , and inversely with the following adopted convention:

$$\delta(\vec{k}) = \int d^3\vec{x} e^{-i\vec{k}\cdot\vec{x}} \delta(\vec{x}), \quad \delta(\vec{x}) = \frac{1}{(2\pi)^3} \int d^3\vec{k} e^{i\vec{k}\cdot\vec{x}} \delta(\vec{k}). \quad (1.63)$$

The power spectrum  $P(k)$  is thus defined as the second moment of the Fourier transform of the probability distribution  $P_k$ :

$$\langle \delta(\vec{k}_1) \delta(\vec{k}_2) \rangle = (2\pi)^3 \delta_D^3(\vec{k}_1 + \vec{k}_2) P(k), \quad (1.64)$$

where  $k$  is the norm of  $\vec{k}_1$  and  $\delta_D$  is the Dirac function, that reflects translation invariance. The power spectrum is related to the two-point correlation function as:

$$P(k) = \int d^3\vec{x} e^{-i\vec{k}\cdot\vec{x}} \xi(x), \quad \xi(r) = \frac{1}{(2\pi)^3} \int d^3\vec{k} e^{i\vec{k}\cdot\vec{r}} P(k). \quad (1.65)$$

Similarly, performing the integration over the  $\vec{k} \cdot \vec{r}$  angle we get the form<sup>XV</sup>:

$$P(k) = 4\pi \int dx x^2 \frac{\sin kx}{kx} \xi(x), \quad \xi(r) = \frac{1}{2\pi^2} \int dk k^2 \frac{\sin kr}{kr} P(k). \quad (1.66)$$

<sup>XV</sup>As  $\vec{k} \cdot \vec{r} = kr \cos(\theta)$  where  $\theta \equiv \widehat{\vec{k} \cdot \vec{x}}$ , we can choose coordinates such that  $d^3\vec{k} = k^2 \sin\theta d\theta d\phi dk$ . Moreover using the change of coordinate  $X \equiv r \cos\theta$  the integral becomes  $(2\pi)^{-3} \int_0^{2\pi} d\phi \int_{\cos(0)}^{\cos(\pi)} dX \int_0^\infty dk k^2 P(k) \int_{\cos(0)}^{\cos(\pi)} dX \exp ikrX$ , solving the angles integrals and using  $\sin x = (e^{ix} - e^{-ix})/2i$ , we get the new formulation.

As mentioned earlier, the two-point correlation expresses the probability of finding two density perturbations separated by a certain distance. Therefore the power spectrum splits the probability in different modes  $k = 2\pi/x$ , where  $x$  is the perturbation scale and the power spectrum amplitude characterises the contribution of the mode to the overall probability.

The unit of the power spectrum is a volume unit, this is sometimes easier to work with the dimensionless quantity  $\Delta$ :

$$\Delta^2(k) \equiv \frac{1}{(2\pi)^3} 4\pi k^3 P(k) = \frac{d\sigma^2}{d\ln k}, \quad (1.67)$$

where  $\sigma^2 = \langle \delta^2 \rangle$  defined in Equation 1.60.

### Gaussian random fields

As detailed previously, cosmic density fields are portrayed as the result from a stochastic process. A random process that describes well the primordial Universe density field is a  $n$ -variate Gaussian distribution:

$$P(\delta_1, \delta_2, \dots, \delta_n) = \frac{1}{(2\pi)^{n/2} |C|^{1/2}} \exp\left(-\frac{1}{2} \sum_{i,j} \delta_i C_{ij} \delta_j\right), \quad (1.68)$$

with  $C$  the covariance matrix.

The strength of Gaussian process lies in the Wick's theorem: any moments can be written as a product of the pairs moments. Its application means that even moments of  $P$  can be fully determined by its covariance, i.e. the two-point correlation function or the power spectrum. Due to its first moment, odd moments are thus zero (Equation 1.60).

We can then approximate  $\delta(\vec{k})$  as a Gaussian random field in Fourier space with the following gaussian distribution, with no correlation between the modes:

$$P(\delta(\vec{k})) = \frac{1}{\sqrt{2\pi P(k)}} \exp\left(-\frac{\delta(\vec{k})^2}{2P(k)}\right). \quad (1.69)$$

We note that however that the density perturbation field is no longer Gaussian today because of non-linearities that arise during the gravitational collapse.

### Primordial power spectrum

The initial power spectrum describing fluctuations in the early Universe, after inflation, is assumed to be a power law to avoid to have any preferred length scale in the spectrum. The power index would then adjust the large and small scales. This assumption results from inflation (see Section 1.1.4) that predicts scale-invariant perturbations.



Let's consider instead of perturbations in the density field  $\rho$ , perturbations in the gravitational potential  $\phi(\vec{x}) \equiv \bar{\phi}(\vec{x}) + \Phi(\vec{x})$ , where  $\bar{\phi}$  is the background field and  $\Phi$  is the small perturbation. The gravitational power spectrum is defined by:

$$\langle \Phi(\vec{k}_1) \Phi(\vec{k}_2) \rangle = (2\pi)^3 \delta_D^3(\vec{k}_1 + \vec{k}_2) P_\Phi(k). \quad (1.70)$$

The post-inflation power spectrum of the perturbations  $\Phi$  for the gravitational potential is a power law with scalar amplitude  $A_s$  and the spectral index  $n_s \equiv d \ln \Delta_\Phi^2 / d \ln k$ :

$$\begin{aligned} P_\Phi(k) &= A_s k^{-3+(n_s-1)}, \\ \Delta_\Phi^2(k) &= \frac{1}{2\pi^2} k^3 P_\Phi(k) \propto k^{n_s-1}. \end{aligned} \quad (1.71)$$

In particular, if  $n_s = 4$ , then we have no correlations between neighbouring points  $\langle \Phi(\vec{k}_1) \Phi(\vec{k}_2) \rangle \propto \delta_D^3(\vec{k}_1 + \vec{k}_2)$ , this is a white noise  $\Phi$ . The correlation increases as  $n_s$  decreases. For  $n_s = 1$  this is the Harrison-Zel'dovich power spectrum (Harrison, 1970, Zeldovich, 1972), the power spectrum  $\Delta_\Phi$  is constant: we have a scale invariant power spectrum.

Using the Fourier transform of the Poisson Equation 1.52c<sup>XVI</sup>:

$$-k^2 \delta \Phi(\vec{k}) = 4\pi G a^2 \bar{\rho} \delta(\vec{k}), \quad (1.72)$$

the primordial density power spectrum is related to the gravitational power spectrum as  $P_\Phi(k) \propto k^{-4} P(k)$ , and we thus have:

$$\begin{aligned} P(k) &= A_s k^{n_s}, \\ \Delta^2(k) &= \frac{1}{2\pi^2} A_s k^{3+n_s}. \end{aligned} \quad (1.73)$$

Due to the power law form of the power spectrum, the two-point correlation function would take a form:  $\xi(r) \propto 1/r^{n_s+3}$ . It gives a lower boundary on  $n_s$  with respect to the cosmological principle. Indeed, for  $n_s < -3$  the two-point correlation would go to infinity when  $r$  tends to infinity meaning that on large scale the Universe gets more inhomogeneous.

### Amplitude of the fluctuations

For LSS studies, the normalization of the power spectrum is fixed using the parameter  $\sigma_8$  which is the variance of the density in a sphere of  $8h^{-1}\text{Mpc}$ , instead of  $A_s$ . We note that this amplitude is fixed using observations as there are no predictive models.

<sup>XVI</sup> Fourier transform  $F$ ,  $f^{(n)}(k)$ , of the derivative of a function  $f(x)$  is:  $f^{(n)}(k) = F(\frac{d^n}{dx^n} f(x)) = (ik)^n \hat{f}(k)$ .

The variance of a sample distribution of spheres with radius  $R$  randomly placed is:

$$\sigma^2(R) = \frac{1}{2\pi^2} \int P(k) \hat{W}_R^2(k) k^2 dk, \quad (1.74)$$

where  $\hat{W}_R^2(k)$  is the Fourier transform of the top-hat function  $W_R(r)$ :

$$\hat{W}_R^2(k) = \frac{3}{(kR)^2} (\sin(kR) - kR \cos(kR)), \quad (1.75)$$

with the top-hat function  $W_R(r)$ :

$$W_R(r) = \begin{cases} \frac{3}{4\pi R^3} \rightarrow \text{if } r \leq R \\ 0 \rightarrow \text{if } r > R. \end{cases} \quad (1.76)$$

We chose to normalize the linear matter power spectrum  $P(k)$  at  $R = 8h^{-1}\text{Mpc}$  such that  $\sigma(R) = 1$  at this radius. We thus define for a redshift evolution of the matter power spectrum  $P(k, z)$ ,  $\sigma_8(z) \equiv \sigma_m(R = 8)$ .

### 1.2.3 Growth of Structures

In Section 1.2.1 I presented a description of the evolution of the small perturbations in the density of the Universe and in Section 1.2.2 a statistical approach to describe them. Here we are interested in the growth of the fluctuations which will produce LSS.

#### Jeans criterion

Starting from the time evolution of the density fluctuations of Equation 1.57 in Fourier space for the adiabatic Newtonian, i.e. non-relativistic, case:

$$\frac{d^2 \delta(\vec{k})}{dt^2} + 2 \frac{\dot{a}}{a} \frac{d\delta(\vec{k})}{dt} = 4\pi G \bar{\rho} \delta(\vec{k}) - \frac{c_s^2}{a^2} k^2 \delta(\vec{k}) - \frac{1}{a^2} \frac{\partial P}{\partial S} k^2 S(\vec{k}). \quad (1.77)$$

Considering only isentropic perturbations in a static Universe, i.e. no entropy perturbations so that the Fourier transform of  $S(\vec{k})$  is  $\delta_S = 0$ , there are only density fluctuations and  $\dot{a} = 0$ . We can write the following wave equation:

$$\frac{d^2 \delta(\vec{k})}{dt^2} = -w^2 \delta(\vec{k}), \quad w^2 \equiv -4\pi G \bar{\rho} + \frac{c_s^2}{a^2} k^2. \quad (1.78)$$

The Jeans mode  $k_J$  or Jeans proper length  $\lambda_J$  related to its comoving value  $\lambda_J^{\text{comoving}}$ , is the

particular case when  $w = 0$ :

$$k_J = \frac{2\sqrt{\pi G \bar{\rho}} a}{c_s}, \quad \lambda_J = a \lambda_J^{\text{comoving}} = a \frac{2\pi}{k_J} = \frac{\sqrt{\pi} c_s}{\sqrt{G \bar{\rho}}}. \quad (1.79)$$

This characteristic scale allows to have a criterion on the perturbation propagation, known as the Jeans criterion (Jeans, 1902), determining an equilibrium threshold depending on the pressure and gravity of the instability:

$$\begin{cases} \lambda < \lambda_J \rightarrow \text{sound wave} \\ \lambda > \lambda_J \rightarrow \text{static mode} \end{cases} \quad (1.80)$$

The sound wave will make the perturbation propagates in the medium creating an oscillation due to the pressure and gravity interaction. In the static mode case, the amplitude of the perturbation will exponentially increase, in growing mode, or decrease, in decaying mode, as the gravity is no longer balanced with the pressure.

In an expanding Universe (Lifshitz, 1946), the acoustic wave would be damped by the expansion in the  $\lambda < \lambda_J$  case and if  $\lambda > \lambda_J$  the growth will be slowed down and will instead follow a power law. Moreover we note that for a non-relativistic fluid, the Jeans length is smaller than the horizon which is the largest comoving distance that light could have traveled, defining a causal limit. Sub-horizon perturbations, i.e.  $\lambda_J$  smaller than the horizon, can then be distinguished from super-horizon perturbations, i.e.  $\lambda_J$  larger than the horizon. We note that on very large scales we would deal with super-horizon perturbations that should be treated with relativistic perturbation theory.

### Linear growth in matter domination

During matter domination epoch, the baryonic matter can be described as a pressure-less fluid. Therefore the speed of sound is  $c_s = 0$  and the time-evolution of a matter density  $\rho_m$  isentropic ( $\delta(S) = 0$ ) perturbation is (Peebles and Yu, 1970):

$$\frac{d^2 \delta(\vec{k})}{dt^2} + 2 \frac{\dot{a}}{a} \frac{d\delta(\vec{k})}{dt} = 4\pi G \bar{\rho}_m \delta(\vec{k}). \quad (1.81)$$

The Friedmann Equation 1.21 for the Hubble parameter defined in Equation 1.22<sup>XVII</sup>, with  $p = 0$  and  $\Lambda = 0$  yields:

$$\frac{dH}{dt} + H^2 = -\frac{4\pi G}{3} \rho_m. \quad (1.82)$$

<sup>XVII</sup>It can easily be shown that  $\frac{\ddot{a}}{a} = \dot{H} + H^2$ .

Differentiating this equation with respect to time using  $\rho_m \propto a^{-3}$  (see Section 1.1.3), we have:

$$\frac{d^2 H}{dt^2} + 2 \frac{\dot{a}}{a} \frac{dH}{dt} = \frac{4\pi G}{3} \rho_m H. \quad (1.83)$$

Both the Hubble parameter and the density follow the same equation. As those describe a time evolution, without changing the spatial evolution of the perturbation, we can write a general solution for the density fluctuations of the following form in configuration space:

$$\delta(\vec{x}, t) = D_-(t)\delta(\vec{x}) + D_+(t)\delta(\vec{x}). \quad (1.84)$$

According to Equation 1.33 the Hubble parameter is a decreasing function with time, so we can associate  $H(t)$  with the decaying mode solution  $D_-(t)$ :

$$D_-(t) \propto H(t). \quad (1.85)$$

The second solution  $D_+(t)$  which is the growing mode solution, is the growth function leading to structure formation:

$$D_+(t) \propto H(t) \int \frac{dt'}{a(t')^2 H(t')^2}. \quad (1.86)$$

### Growth rate parameter

Taking the Fourier transform of the continuity Equation 1.52a and injecting the growing solution  $D_+$  of Equation 1.81 inside, we get the velocity:

$$\vec{v}(\vec{k}) = \frac{i a \vec{k}}{|\vec{k}|^2} \frac{d\delta(\vec{k}, t)}{dt} = \frac{i \vec{k}}{|\vec{k}|^2} a H \delta(\vec{k}, t) f(z), \quad (1.87)$$

where  $f(z)$  is the linear growth rate of structures:

$$f(z) \equiv \frac{d \ln D_+(a)}{d \ln(a)} = - \frac{d \ln D_+(z)}{d \ln(1+z)}. \quad (1.88)$$

Peebles, 1980 showed that the growth rate  $f$  can be related to the matter density of the Universe through approximately the following parametrization (see also Carroll et al., 1992 for a parametrization of  $D_+$ ) for a flat Universe:

$$f(\Omega_m) \approx \Omega_m^\gamma, \quad (1.89)$$

and the growth index  $\gamma$  can be related to the dark energy equation of state  $w$  (Linder and Cahn, 2007):

$$\gamma = \frac{3(1-w)}{5-6w}. \quad (1.90)$$

For a flat  $\Lambda$ CDM cosmology under GR, the index is 0.55. The lower the matter density is, the slower the structures grow. In an observational point of view, it means that precise measurements on the growth rate can give precious insight to constrain cosmological parameters and thus dark energy, but also test deviations from GR.

Figures 1.20 show the linear growth function and growth rate. For an Einstein-de Sitter Universe the linear perturbations grow faster than in Universes with a non-zero cosmological constant or an open curvature. This is due to the larger expansion rate in these latest cosmologies which reduces the growth.

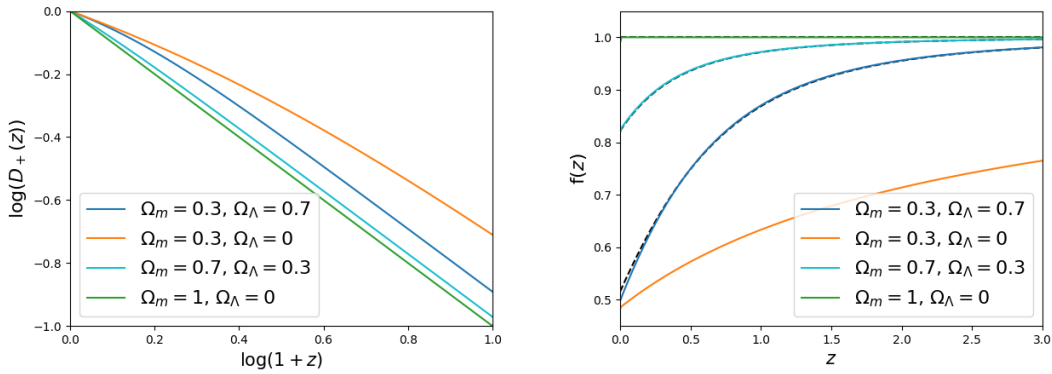


Figure 1.20: Linear growth function normalized with  $D_+(z=0)$  (on the left) and growth rate (on the right) as function of the redshift for different cosmological parameters. Growth function is computed from Equation 1.86, and the growth rate from Equation 1.88. Dashed lines on the right plot are the growth rate from the approximation for flat cosmologies from Equation 1.89.

### Transfer function

In the linear regime, the primordial power spectrum and the matter power spectrum at later time are related through the growth function and the linear transfer function. The growth function  $D_+$  was described previously for a post-recombination Universe based on the growth of initial perturbations. The transfer function establishes a relation between the initial conditions and the amplitudes of the different modes after inflation.

The linear matter power spectrum at redshift  $z$  can be written:

$$P(k, z) = P(k) T^2(k) D_+^2(z), \quad (1.91)$$

where  $P(k)$  is the primordial spectrum of Equation 1.73 and  $T(k)$  is the transfer function. Some linear power spectra and correlation functions redshift evolution are illustrated on Figure 1.21 for a  $\Lambda$ CDM cosmology.

Moreover some examples of linear power spectra at redshift 0 for different cosmological parameters are displayed on Figures 1.22.

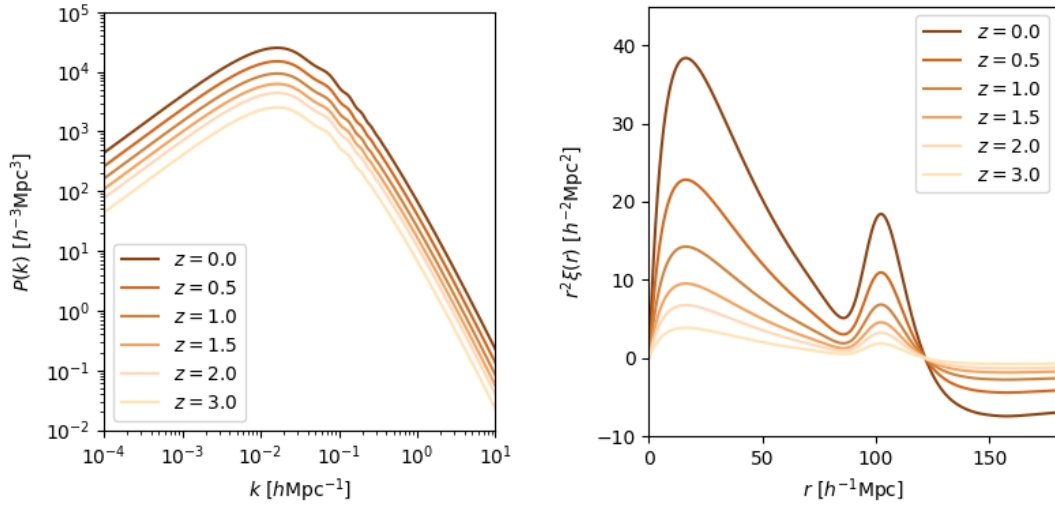


Figure 1.21: Redshift evolution of the linear power spectrum (right) and correlation function (left) as predicted by a  $\Lambda$ CDM cosmology with Planck values of the parameters (Planck Collaboration et al., 2020).

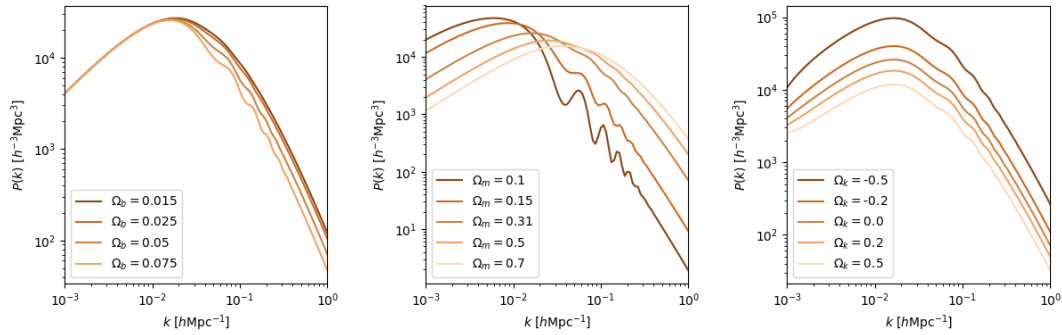


Figure 1.22: Linear power spectra at redshift 0 for a  $\Lambda$ CDM model. From left to right: variations of  $\Omega_b$ , with  $\Omega_m = 0.31$  and  $\Omega_k = 0$ ; variations of  $\Omega_m$ , with  $\Omega_b = 0.05$  and  $\Omega_k = 0$ ; variations of  $\Omega_k$ , with  $\Omega_b = 0.05$  and  $\Omega_m = 0.31$ .

When the linear evolution of the perturbations were presented previously, we treated the growth in a matter dominated Universe with negligible pressure and very small perturbations. However the form of the matter and different physical laws can suppress the growth on certain length scales.

In radiation domination epoch the Jeans length given by Equation 1.79 is approximately equal to the horizon, i.e.  $\lambda_J \approx c/H$ . According to the criterion (Equation 1.80) it means that perturbations that entered the horizon will not grow. Let's consider the time when the perturbations with corresponding comoving mode  $\vec{k}$  enters the horizon. At matter-radiation equality  $t_{\text{eq}}$ , occurring around redshift  $z_{\text{eq}} = 3400$  (scale factor  $a_{\text{eq}}$ ), the perturbations that have just entered the horizon have the mode  $k_{\text{eq}}$ . For long wavelength  $k < k_{\text{eq}}$ , they enter

the horizon in the matter domination epoch and their growth slows down at this moment from  $\delta \propto a^2$  to  $\delta \propto a$ . Therefore a perturbation with  $k < k_{\text{eq}}$  that starts to grow at time  $t_i$  will evolve until now at time  $t_0$  as  $\delta(\vec{k}, t_0) = \left(\frac{a_{\text{eq}}}{a_i}\right)^2 \frac{a_0}{a_{\text{eq}}} \delta(\vec{k}, t_i)$ . They are therefore mode-independent. The wavelength  $k > k_{\text{eq}}$  enters the horizon during the radiation era, their growth amplitude will be suppressed by photon-matter interactions following a logarithmic law until  $t_{\text{eq}}$  when its growth will resume as  $\delta \propto a$ . By assuming the suppressing of the growth to be constant (instead of logarithmic), a perturbation with  $k > k_{\text{eq}}$  entering the horizon at  $a_{\text{enter}}$  will then have the following grow:  $\delta(\vec{k}, t_0) = \left(\frac{a_{\text{enter}}}{a_i}\right)^2 \frac{a_0}{a_{\text{eq}}} \delta(\vec{k}, t_i) = \left(\frac{a_{\text{enter}}}{a_{\text{eq}}}\right) \left(\frac{a_{\text{eq}}}{a_i}\right)^2 \frac{a_0}{a_{\text{eq}}} \delta(\vec{k}, t_i)$ .

So with the simplified precedent considerations and as in radiation area  $a \sim k^{-1}$ , we have the following post recombination transfer function for non-relativistic matter:

$$T(k) \propto \begin{cases} 1, & \text{if } k < k_{\text{eq}} \\ \frac{k_{\text{eq}}^2}{k^2}, & \text{if } k > k_{\text{eq}} \end{cases} \quad (1.92)$$

Every form of matter will have its own transfer function.

### Role of dark matter

Dark matter nature plays an important role in structures formation. As dark matter interacts with ordinary matter only by gravitational interactions, it would then frame the general structure of LSS that would therefore attract baryonic matter which falls into the gravitational well.

CDM model, described in Section 1.1.6, was shown to follow a hierarchical formation following the bottom-up scenario. Smaller structures would first collapse and then gather by gravitation to form larger structures.

For WDM or HDM models the collapsing phenomenon would occur later in time. Indeed even if they are collision-less, their relativistic particles would cause to suppress the perturbation growth as they would move rapidly causing a free streaming that damp the perturbations. As a result, this would lead to less clumpy substructures on the Universe smaller scales. This difference is illustrated on Figure 1.23 with simulations. While the models present similar overall structures, CDM has more small substructures.

Therefore the dark matter nature would also impact their transfer function and thus their resulting matter power spectrum. Left figure 1.24 illustrates the difference between the three nature of dark matter in their late time power spectrum. The smallest structures that can form in WDM are much larger than in the CDM paradigm. This results in a different cutoff of the power spectrum that can be observed on small scales (so large  $k$ ) of the Figure. The measured power spectrum at small scales can therefore be used to constrain the dark matter nature. In particular, Lyman- $\alpha$  measurements have a strong constraining power. A lower limit in the dark matter particle mass can thus be fixed, excluding pure HDM scenario and setting constraints

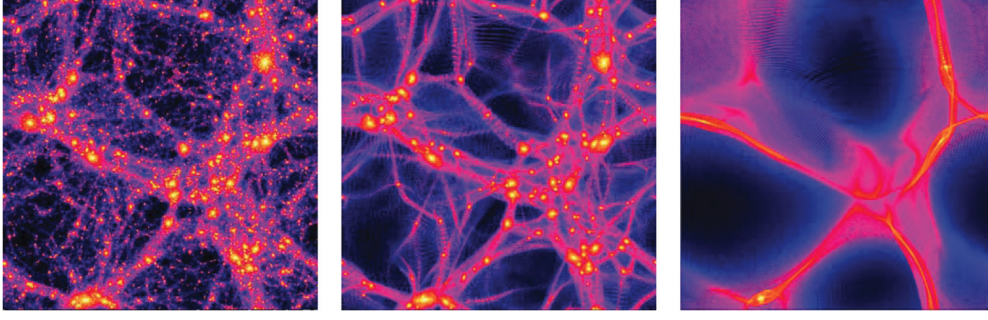


Figure 1.23: Large scale structures simulations from Macciò et al., 2012 for different dark matter models at redshift 0. Size shown is of a length of 40 Mpc. From left to right: CDM, and two WDM models with differences in their initial thermal velocities with warmer candidate on the right.

for an eventual WDM or mixtures of models (Viel et al., 2013, Garzilli et al., 2021). Right panel of Figure 1.24 displays the power spectrum now as measured by different probes.

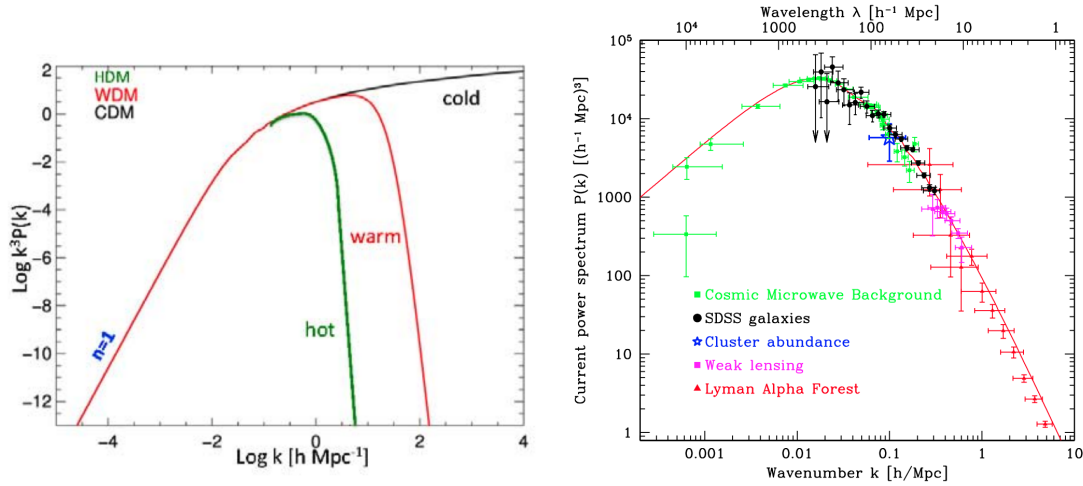


Figure 1.24: On the left: Illustrated power spectrum from Frenk and White, 2012 for three natures of dark matter: cold in black, warm in red, hot in green. On the right: figure from Tegmark et al., 2004 showing the matter power spectrum normalized at redshift 0 from different probes (they are not measured at  $z = 0$ ). Solid line represents a flat  $\Lambda$ CDM prediction.

#### 1.2.4 Non-linear Approach

To get the presented evolution of density perturbations of Equation 1.57 we considered only linear scale. However below approximately  $50 h^{-1} \text{Mpc}$  some non-linear effects arise.

Let's go back to the full set of Equations 1.49 for our fluid description in an expanding Universe as function of the density contrast  $\delta$ . As before we differentiate with respect to time the continuity Equation 1.46a and we inject inside the gradient  $\nabla_x((1 + \delta)\dot{v} + \delta\dot{v})$ , the sum of  $(1 + \delta)$



times the continuity Equation 1.49a and  $v$  times Euler's Equations 1.49b. We get an equivalent form of the Equation 1.57 but without linearization:

$$\ddot{\delta} + 2\frac{\dot{a}}{a}\dot{\delta} = \frac{1}{\bar{\rho}a^2}\nabla_x^2 P + \frac{1}{a^2}\nabla_x \cdot ((1+\delta)\nabla_x \Phi) + \frac{1}{a^2}\nabla_x^2 ((1+\delta)v^2). \quad (1.93)$$

In Fourier space, in absence of pressure for simplicity, using Poisson equation, this latest equation and Euler equations become respectively<sup>XVIII</sup>:

$$\ddot{\delta}_k + 2\frac{\dot{a}}{a}\dot{\delta}_k = 4\pi G\bar{\rho}\delta_k + 2\pi G\bar{\rho} \sum_{k' \neq 0, k} \left( \frac{\vec{k} \cdot \vec{k}'}{k'^2} + \frac{\vec{k} \cdot (\vec{k} - \vec{k}')}{|\vec{k} - \vec{k}'|^2} \right) \delta_{k'} \delta_{k-k'} - \int d^3 \vec{x} (1+\delta) \cdot \left( \frac{\vec{k} \cdot \vec{v}}{a} \right)^2 e^{i\vec{k} \cdot \vec{x}}, \quad (1.94a)$$

$$\dot{\vec{v}}_k + \frac{\dot{a}}{a}\vec{v}_k = 4\pi G a \bar{\rho} \delta_k \frac{i\vec{k}}{k^2} - \frac{i}{a} \sum_{k'} (\vec{k}' \cdot \vec{v}_{k-k'}) \vec{v}_{k'}. \quad (1.94b)$$

From those we can see that Fourier modes are coupled, leading to non-linear evolution of the perturbations. This is not the case in the linear regime where all the modes are independent.

Those equations are difficult to solve. While below  $10h^{-1}$  Mpc the general behaviour is highly non-linear, between 20 to 50-60  $h^{-1}$  Mpc it is a quasi-linear regime where it is possible to use perturbation theory (PT) up to higher order. Indeed at these scales the fluctuations are small enough to be treated by a PT approach. The density contrast and the velocity field are expanded in a series as follows:

$$\begin{aligned} \delta(\vec{x}, t) &= \sum_n \delta_{(n)}(\vec{x}, t), \\ \nabla \cdot \vec{v} &\equiv \theta(\vec{x}, t) = \sum_n \theta_{(n)}(\vec{x}, t), \end{aligned} \quad (1.95)$$

where  $\delta_{(n)}$ ,  $\theta_{(n)}$  are the  $n$ -order contribution. The first order corresponds to the linear approximation. Those high-order corrections can be treated as loops and added to the linear solution. These two expansion are thus solution of the general continuity Equation (see footnote XIII) and the gradient of Euler equations<sup>XIX</sup> in Fourier space (without pressure)<sup>XX</sup>:

$$\begin{aligned} \dot{\delta}_k(\vec{k}) + \theta_k(\vec{k}) &= - \int d^3 \vec{k}_1 d^3 \vec{k}_2 \delta_D(\vec{k} - (\vec{k}_1 + \vec{k}_2)) \alpha(\vec{k}_1, \vec{k}_2) \theta_k(\vec{k}_1) \delta_k(\vec{k}_2), \\ \dot{\theta}_k(\vec{k}) + H\theta_k(\vec{k}) + \frac{3}{2}\Omega_m H^2 \delta_k(\vec{k}) &= - \int d^3 \vec{k}_1 d^3 \vec{k}_2 \delta_D(\vec{k} - (\vec{k}_1 + \vec{k}_2)) \beta(\vec{k}_1, \vec{k}_2) \theta_k(\vec{k}_1) \theta_k(\vec{k}_2). \end{aligned} \quad (1.96)$$

where  $\vec{k}_2 = \vec{k} - \vec{k}_1$  and  $\alpha(\vec{k}_1, \vec{k}_2) \equiv \frac{(\vec{k}_1 + \vec{k}_2) \cdot \vec{k}_1}{k_1^2}$ ,  $\beta(\vec{k}_1, \vec{k}_2) \equiv \frac{(\vec{k}_1 + \vec{k}_2)^2 (\vec{k}_1 \cdot \vec{k}_2)}{2k_1^2 k_2^2}$ .

Different methods treating those non-linearities have been proposed such as using a halo

<sup>XVIII</sup>We use the fact that the Fourier transform of a product is the convolution of the two functions (as  $F(f * g) = F(f)F(g)$  and  $(f * g)(x) = \int f(x-y)g(y)dy$ ) and the Fourier definition as defined in Equation 1.64. Moreover we use that  $(f * g)(x) = \int f(x-y)g(y)dy = \int f(x)g(x-y)dy$  and therefore  $(f * g)(x) = \frac{1}{2} \int (f(x-y)g(y) + f(y)g(x-y))dy$ .  
<sup>XIX</sup> $\dot{\theta} + H\theta + \nabla(u \cdot \theta) = -\nabla^2 \theta = 4\pi G a^2 \bar{\rho} \delta = 3/2 \Omega_m H^2 \delta$ , where for the last equality we used  $\Lambda = \kappa = 0$  in Friedmann's equation.

<sup>XX</sup>see footnote XVIII)

model (Cooray and Sheth, 2002, HALOFIT (Smith et al., 2003; Takahashi et al., 2012)), standard PT (SPT, Bernardeau et al., 2002; Jeong and Komatsu, 2006; Scoccimarro and Frieman, 1996), renormalized PT (RPT, Crocce and Scoccimarro, 2006), regularized PT (RegTP, Taruya et al., 2012), closure theory (Taruya and Hiramatsu, 2008) or time renormalization (Pietroni, 2008).

Broadly, standard PT treats the power spectrum as an infinite expansion of terms (corresponding to the loop corrections) truncated at a certain order:

$$P(k) = P^{(0)}(k) + P^{(1)}(k) + P^{(2)}(k) + \dots \quad (1.97)$$

The 0th order is the linear power spectrum  $P^{(0)} = P_{\text{lin}}$ , the first loop is  $P^{(1)} = 2P_{13} + P_{22}$ , where the term  $P_{ij}$  corresponds to  $\langle \delta_{(i)}(\vec{k}) \delta_{(j)}(\vec{k}') \rangle = (2\pi)^3 \delta^D((\vec{k}) + (\vec{k}')) P_{ij}(k)$ .

RPT perform a reorganisation of the PT terms, resumming some of the terms in a factor, called propagator  $\mathcal{N}$ , outside of the series:

$$P(k) = (P_{\text{lin}}(k) + P_{22}(k) + P_{33}(k) + \dots) \mathcal{N}_i^2. \quad (1.98)$$

Carlson et al., 2009 and Gil-Marin et al., 2012 proposed a comparison between models using N-body simulations as references. Overall linear PT remains valid on large scales below  $k \sim 0.1$  h/Mpc. Passing to a two-loop corrections improves the power spectrum accuracy without a high computational gain. Moreover 2-loop STP or RPT models reach a 1% precision up to  $k \sim 0.1$  h/Mpc at redshift 0 and  $k \sim 0.2$  h/Mpc at redshift 1.

We note that effective field theory (EFT; Carrasco et al., 2012, Vlah et al., 2016, Porto et al., 2014) is a method to incorporate non-perturbative effects into PT through various free parameters included by additional terms, to describe the non-linear effects better. It can extract information considering the Universe as a fluid at a relevant scale length, improving the small-scale description.

### 1.2.5 Halo Model

Complementary to PT, a halo model is an analytical description of the dark matter density field as an assembly of halos, under the assumption that dark matter is split into distinct halos (Seljak, 2000, Peacock and Smith, 2000, Cooray and Sheth, 2002). It helps to provide a statistical description beyond linearity<sup>XXI</sup>, in particular the non-linear clustering, by combining halo mass function and density profile.

---

<sup>XXI</sup>That can also be obtain by N-body simulations, that resolve the equations numerically with a partitioned CDM density field for which each particles are of a certain mass (typically  $\sim 10^{10} M_{\odot}$ ).

### Spherical collapse

Let's first describe the units of the halo models, i.e. the halos. We assume that objects are formed from an initial top-hat density perturbation that undergoes spherical collapse (first proposed by Gunn and Gott, 1972).

Let's consider an initial perturbation in an Einstein-de Sitter Universe, i.e. filled only with matter  $\Omega_m = 1$ . The region of this perturbation is described within a radius  $R$  with an overdensity  $\delta$ . The mass  $M$  within  $R$  is  $M = \frac{4}{3}\pi R^3 \bar{\rho}(1 + \delta)$ , where  $\bar{\rho}$  is the comoving background density. We can apply Birkhoff's theorem<sup>XXII</sup> to get the time evolution of its size:

$$\ddot{R} = \frac{GM}{R^2} \quad \rightarrow \quad \frac{\dot{R}}{2} - \frac{GM}{R} = E, \quad (1.99)$$

where the second equality comes from the integration of the equation of motion<sup>XXIII</sup> with  $E$  the total energy of the perturbation.

A solution to this equation in the case of a negative energy, i.e.  $E < 0$  (that corresponds to a bounded system which in turn implies that the initial perturbation will eventually collapse) yields:

$$\begin{aligned} R &= R_m (1 - \cos \theta) \\ t &= t_m (\theta - \sin \theta), \end{aligned} \quad (1.100)$$

where  $R_m$  and  $t_m$  are specified from initial conditions, so at  $\theta \ll 1$ , as the parameter  $\theta$  is a rescaling of the conformal time.. It yields  $R_m = -GM/(2E)$  and  $t_m = \sqrt{GMR_m^3}$ .

First, when  $t < \pi t_m$ , the perturbation grows linearly as described in 1.1.3 for the case with matter only. The density will grow as  $\delta \propto D(a) \propto a \propto t^{\frac{2}{3}}$ .

At turnaround, i.e.  $\theta = \pi$ , the radius reaches its maximum  $R = 2R_m$  (before collapsing) corresponding to time  $t = \pi t_m$  which corresponds to the point when the maximum expansion is obtained. The linear density using a expansion perturbation at first order is  $\delta(t_m) = 1.06$  (H. Mo et al., 2010).

Then the perturbation will shrink to  $R = 0$  when  $\theta = 2\pi$ . The collapse happens at  $t = 2\pi t_m$  and the density is predicted to be infinite. Using the linear expansion at first order, the so-called critical density is  $\delta_c(t_m) = 1.686$  (H. Mo et al., 2010). The exact value of  $\delta_c$  depends on Universe's cosmology. The critical value is the required density for the collapse.

<sup>XXII</sup>It states that a solution to Einstein's equation in a spherically symmetric problem is static and asymptotically flat. So the solution would be the Schwarzschild's solution. Intuitively it means that the solution represents an isolated object, so that there is no force from outside exerted on the sphere and the sphere exerts no force on the outside. It means that the expanding background is not disturbed by the perturbation. In our case, it means that the perturbation can be treated as a closed Universe.

<sup>XXIII</sup>We multiply each sides with  $\dot{R}$  and the integration becomes obvious as  $\dot{R}\ddot{R} = \frac{1}{2}d(\dot{R}^2)/dt$  and  $-GM\dot{R}/R^2 = GMd(R^{-1})/dt$ .

The density does not really attain infinite but rather reach an equilibrium value due to dissipative effects and shell-crossing. This equilibrium is given by the Virial theorem when the absolute potential energy  $U$  is twice the kinetic one  $E_{\text{kin}}$ ,  $2E_{\text{kin}} + U = 0$ . It means that the total energy is  $E = E_{\text{kin}} + U = U(R_{\text{vir}})/2$ , implying that the radius of the virialized object is half the maximum radius, i.e.  $R_{\text{vir}} = R_m$  as  $E = U(R_{\text{turnaround}})$ . The corresponding overdensity of the perturbation reaches  $\delta_{\text{vir}} \sim 177$ . The remaining virialized object is identified as a halo. This dark matter halo, bounded gravitationally, forms therefore when the corresponding density perturbation becomes denser than the density background of about 150-200 times<sup>XXIV</sup>.

### Density profile

After virialization we end up with a halo whose mass distribution can be described using different profiles. A common universal form of the density profile  $\rho(r)$  is the following:

$$\rho(r) = \frac{\rho_s}{(r/R_s)^\gamma (1 + (r/R_s)^\alpha)^{(\beta-\gamma)/\alpha}}. \quad (1.101)$$

$R_s$  is the radius of the core that has a density  $\rho_s$ . Navarro-Frenk-White profile is given by  $(\gamma, \alpha, \beta) = (1, 1, 3)$  (NFW; Navarro et al., 1997) and Hernquist profile by  $(\gamma, \alpha, \beta) = (1, 1, 4)$  (Hernquist, 1990). Defining the concentration  $c \equiv R_{\text{vir}}/R_s$  (higher  $c$  means halo center denser), the profile can be fully characterize by its concentration  $c$  and the halo mass  $M$  (got from the integration of  $\rho(r)$ ).

### Halo mass function

The halo mass function  $n(M)$  can be written as:

$$n(M)dM \equiv \frac{dn}{dM}dM = \frac{\bar{\rho}}{M} f(v) dv. \quad (1.102)$$

It expresses the halos number density with respect to the mass. The function  $f(v)$  relies on the parameter  $v$  which characterises the peak height,  $v \equiv (\delta_c/\sigma(R(M)))^2$ , with  $\sigma(R(M))$  the linear density fluctuations variance in a sphere defined in Equation 1.74. So the abundance is described as a function of the heights of the density peaks of the density contrast.

The first ones to express analytically  $f(v)$  were Press and Schechter, 1974. For this they assumed that the probability of having a density contained in a sphere of radius  $R(M)$  larger than the critical density  $\delta_c$  is the half of the mass fraction in a halo with a mass larger than  $M$ , i.e.  $2P(\delta_M > \delta_c) = F(> M)$ . A generic function yields<sup>XXV</sup>:

$$v f(v) \propto \left(1 + \frac{1}{(av)^p}\right) (av)^{\frac{1}{2}} e^{-av/2}, \quad \text{with } \int dv f(v) = 1, \quad (1.103)$$

<sup>XXIV</sup>This is why we often refer to the radius  $R_{200}$ .

<sup>XXV</sup>Integral is one as the matter is assumed to be fully contained in the halos.

where  $(a, p) = (1, 0)$  for PS (Press and Schechter, 1974) mass function, that was shown to have some limitations for low mass halos (Bond et al., 1991).

ST mass function uses  $(a, p) = (0.707, 0.3)$  based on N-body simulations (Sheth and Tormen, 1999). They also provided a formulation of the halo bias compared to the underlying dark matter density (the bias is discussed more in next Section 1.2.6):

$$b(v) = 1 + \frac{av - 1}{\delta_c} + \frac{2p}{\delta_c(1 + (av)^p)}. \quad (1.104)$$

### Dark matter clustering

As seen above, we describe the dark matter distribution as residing in halos. Therefore we have that on small scales the matter distribution is within halos, whose density profile can be described as done previously. On large scales the distribution is driven by the spatial positions of halos of different masses.

So writing the density profile of a halo as  $M\gamma(x|M)$  where  $\gamma$  is normalized<sup>xxvi</sup>, the occupation number  $N_i \in \{0, 1\}$  of the  $i$ th small volume partitioning the space  $\Delta V_i$  and  $M_i$  the mass of a halo located in  $\Delta V_i$ , the dark matter density field is:

$$\rho(x) = \sum_i N_i M_i \gamma(x - x_i | M_i). \quad (1.105)$$

The density field correlation function can be written as:

$$\langle \rho(x_1) \rho(x_2) \rangle = \sum_{i,j} \langle N_i M_i N_j M_j \gamma(x_1 - x_i | M_i) \gamma(x_2 - x_j | M_j) \rangle, \quad (1.106)$$

and we note that  $\langle N_i M_i \gamma(x - x_i | M_i) \rangle = \int dM n(M) M \Delta V_i \gamma(x - x_i | M)$ . Separating the contribution  $i = j$ , that corresponds to correlations within a halo, from the  $i \neq j$  which is the contribution between halos, we get that the two-point correlation function is divided into two terms, the 1-halo ( $i = j$ ) and 2-halo ( $i \neq j$ ) terms:

$$\xi(r) = \langle \delta(x_1) \delta(x_2) \rangle = \xi_{1h}(r) + \xi_{2h}(r), \quad \text{with } r = |x_1 - x_2|, \quad (1.107)$$

where (H. Mo et al., 2010):

$$\begin{aligned} \xi_{1h}(r) &= \frac{1}{\bar{\rho}^2} \int dM M^2 n(M) \int d^3x \gamma(x - x_1 | M) \gamma(x - x_2 | M) \\ \xi_{2h}(r) &= \frac{1}{\bar{\rho}^2} \int dM_1 M_1 n(M_1) \\ &\quad \cdot \int dM_2 M_2 n(M_2) \int d^3x \gamma(x_1 - x | M) \int d^3x' \gamma(x_2 - x' | M) \xi_{hh}(x - x' | M_1, M_2). \end{aligned} \quad (1.108)$$

---

<sup>xxvi</sup>So  $\int d^3x \gamma(x|M) = 1$ .

with  $\xi_{hh}(x - x'|M_1, M_2)$  the correlation between halos with mass  $M_1$  and mass  $M_2$ . The 2-halo term is a convolution, which is more convenient to treat in Fourier space.

In Fourier space we thus have, as in configuration space, the non-linear power spectrum of dark matter  $P(k)$  split into two terms:

$$P(k) = P_{1h}(k) + P_{2h}(k), \quad (1.109)$$

where

$$\begin{aligned} P_{1h}(k) &= \frac{1}{\bar{\rho}^2} \int dM M^2 n(M) y(k, M)^2, \\ P_{2h}(k) &= \frac{1}{\bar{\rho}^2} \int dM_1 M_1 n(M_1) y(k, M_1) \int dM_2 M_2 n(M_2) y(k, M_2) P_{hh}(k, M_1, M_2). \end{aligned} \quad (1.110)$$

The 1-halo term  $P_{1h}$  accounts for the correlation inside a halo and the 2-halo term  $P_{2h}$  accounts for the correlation between two halos. The function  $y(k, M)$  is the Fourier transform of the halo density profile:  $y(k, M) = \frac{4\pi}{M} \int dr r^2 \rho(r, M) \frac{\sin(kr)}{kr}$ .

On scales large enough, larger than the individual halos sizes, the 2-halo term is dominant and  $y(k, M)$  ( $y(x|M)$ ) can be replaced by one (by a delta function). Therefore we have that  $P_{hh}(k|M_1, M_2) = b_h(M_1) b_h(M_2) P_{\text{lin}}(k)$  ( $\xi_{hh}(r|M_1, M_2) = b(M_1) b(M_2) \xi_{\text{lin}}(r)$ ), where  $P_{\text{lin}}$  is the linear matter power spectrum. This remains valid only on large scales as  $P_{\text{lin}}$  is not accurate on very small scales and furthermore there are halo exclusion effects. Using Equation 1.102 they can thus be expressed as (Seljak, 2000):

$$\begin{aligned} P_{1h}(k) &= \int d\nu f(\nu) \frac{M(\nu)}{\bar{\rho}} y(k, M(\nu))^2, \\ P_{2h}(k) &= P_{\text{lin}}(k) \left( \int d\nu f(\nu) b(\nu) y(k, M(\nu)) \right)^2. \end{aligned} \quad (1.111)$$

### 1.2.6 Galaxy-Halo Connection

#### Galaxy bias

All the above description for the matter density field growth is considered to model the dark matter perturbations as it seeds the overall gravitational wells of the Universe creating an underlying layer of matter. Galaxies, or other discrete astronomical objects, are made of ordinary matter and create a point-like sampling distribution of the density field that biases its estimate. This dark matter density field to galaxies connection through a discretisation is illustrated in Figure 1.25.

Therefore for an underlying dark matter field  $\rho_m$  with contrast  $\delta_m$ , the galaxy density field  $n$  is

treated as a point-like distribution:

$$n(\vec{x}) = \sum_{\vec{x}'} \delta_D(\vec{x} - \vec{x}'), \quad (1.112)$$

where  $\delta_D$  is the Dirac function.

On linear regime, i.e. on large scales, we assume a proportionality relation between  $n$  and  $\delta_m$  with a linear bias parameter  $b$  that is scale independent (Peebles, 1973, Kaiser, 1984):

$$\frac{\delta n(\vec{x})}{\bar{n}} = b \frac{\delta \rho_m(\vec{x})}{\bar{\rho}_m} = b \delta_m(\vec{x}). \quad (1.113)$$

For this bias prescription, we have a relation between the power spectrum of a biased tracer, subscript  $t$ , and the power spectrum of the matter with a time dependent bias:

$$P_{tt}(k, z) = b^2(z) P_m(k), \quad \xi_{tt}(r, z) = b(z)^2 \xi_m(r). \quad (1.114)$$

The value of  $b$  is usually measured directly on the data.

By smoothing the tracer density  $\hat{\delta}_g$  and the underlying field  $\hat{\delta}_m$  over a scale  $R$  around the same position, we get the local Eulerian bias model:

$$\hat{\delta}_t(\vec{x}) = F[\hat{\delta}_m(\vec{x})], \quad \hat{f} \equiv \int_{|\vec{x}'| < R} d^3 \vec{x}' f(\vec{x} - \vec{x}') W(\vec{x}'), \quad (1.115)$$

where  $W$  is window function that filters the function (so the density). For small  $\hat{\delta}_g$ , i.e. large  $R$ , the bias function  $F$  can be expanded into a Taylor series:

$$\hat{\delta}_t(\vec{x}) = \sum_{n=0}^{\infty} \frac{b_n}{n!} \hat{\delta}_m^n(\vec{x}). \quad (1.116)$$

The first order term  $b_1$  corresponds to the linear approximation.

There is a large variety of bias modelling that exists. The simplest is the one described here with a mapping between galaxies and dark matter. Other models consider the formation of dark matter halos first, and then distribute the galaxies inside the halos.

In practice, the bias is typically made to agree with N-body simulations (quantified generally on scales larger than 10 Mpc/h) and considered to evolve with redshift while scale independent (typically in redshift surveys it assumed that  $b(z)D(z) = C$ , with  $C$  a constant that depends on the tracer selected under different criteria).

## Relation with halo model

I present here the relation of the halo model formalism presented above in Section 1.2.5 to the galaxy clustering. Let  $N$  be the number of galaxies inside a halo of mass  $M$ ,  $\langle N \rangle$  the mean

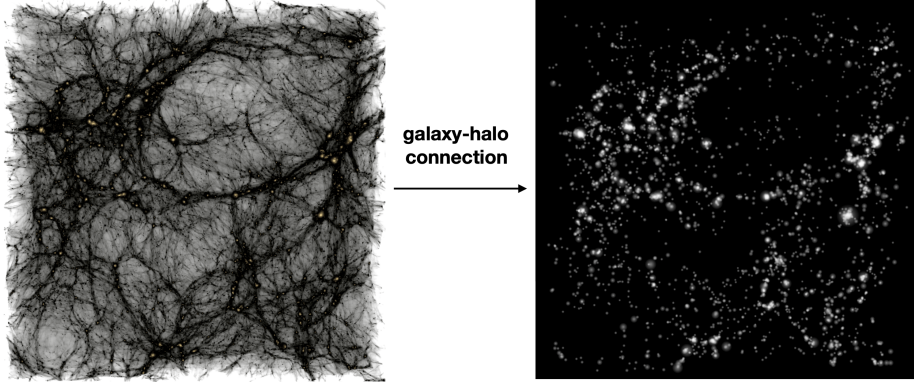


Figure 1.25: Dark matter density distribution on the left and corresponding galaxy distribution on the right populated following an abundance matching algorithm. (Credits of the figure: Wechsler and Tinker, 2018).

occupation number and  $\bar{n}$  the mean total galaxy density, we have for galaxies:

$$\int \frac{\langle N \rangle}{M} d\nu f(\nu) = \frac{\bar{n}}{\bar{\rho}}. \quad (1.117)$$

The 1- and 2- halo terms of Equation 1.111 become, assuming that galaxies follow the profile of dark matter (Seljak, 2000):

$$\begin{aligned} P_{t,1h}(k) &= \frac{\bar{\rho}^2}{\bar{n}^2} \int d\nu f(\nu) \frac{M(\nu)}{\bar{\rho}} \frac{\langle N(N-1) \rangle}{M(\nu)^2} y(k, M(\nu))^2, \\ P_{t,2h}(k) &= P_{\text{lin}}(k) \left( \frac{\bar{\rho}}{\bar{n}} \int d\nu f(\nu) b(\nu) \frac{\langle N \rangle}{M} y(k, M(\nu)) \right)^p. \end{aligned} \quad (1.118)$$

The 2-halo term  $P_{t,2h}(k)$ , i.e. between two halos, on large scales follows:

$$P_{t,2h}(k) = \langle b \rangle P_{\text{lin}}(k), \quad \text{where} \quad \langle b \rangle = \int d\nu f(\nu) b(\nu) \frac{\langle N \rangle}{M}. \quad (1.119)$$

On small scales  $P_{t,2h}(k)$  is much smaller than  $P_{t,1h}(k)$ . The 1-halo term depends on the exponent  $p$  which is 2 when  $\langle N(N-1) \rangle > 1$  (satellite galaxies dominated) and 1 otherwise (only pairs composed of a central and satellite galaxy). We note that satellite and central galaxies have usually different behaviour so shouldn't be treated in the same way. Satellite galaxies reside in the center of sub-halos (i.e. distinct density peaks within the radius range of a dark matter halo) orbiting around larger host halos. Central galaxies reside at the center of dark matter host halos.

PT approach including the bias prescription can be obtained for the power spectrum, e.g. described in McDonald and Roy, 2009.



## Empirical models

To predict the power spectrum, we thus need an estimate of the probability of finding galaxies within a halo. This requires semi-analytical models (e.g. GALFORM; Cole et al., 2000, LGALAXIES; Springel et al., 2001), or prescriptions such as halo occupation model (HOD) or abundance matching that populate halos with galaxies. These different prescriptions help understanding the galaxy-halo connection. We note that galaxy-halo connection can also be studied using hydrodynamical simulations that relies on the resolution of physical descriptions (and not empirical).

Semi-analytical models are complex models with simplifications that relies on different parameters that have to be tuned on data, such as the data clustering. S. Contreras et al., 2013 provide a comparison between different semi-analytical models.

Abundance matching assume a monotonic relationship between a host halo property, such as the mass or circular velocity, and a galaxy property, such as the stellar mass or luminosity, to populate halos with galaxies. The algorithm will then assign one galaxy (pulled for example from the luminosity function) per halo (e.g. in a high resolution simulation) in a ranked manner according to the chosen properties, until the chosen number density is reached (Colin et al., 1999; Trujillo-Gomez et al., 2011, for an overview e.g. Wechsler and Tinker, 2018). This prescription was extended to sub-halos, Sub-Halo Abundance Matching (SHAM) (Behroozi et al., 2010; Conroy et al., 2006; Q. Guo et al., 2010; Kravtsov et al., 2004; Vale and Ostriker, 2004), that was shown to be successful at reproducing observational sample properties (e.g. Moster et al., 2010).

HOD is another category to describe the galaxy-halo relationship. HOD specifies the probability distribution function  $P(N|M)$ , which describes the probability that  $N$  galaxies corresponding to a certain set of criteria are contained in a dark matter halo of mass  $M$  (Berlind and Weinberg, 2002; Peacock and Smith, 2000; Seljak, 2000). The PDF  $P(N|M)$  is usually split into two contributions, one for central galaxies and one for satellite galaxies (for an overview e.g. Wechsler and Tinker, 2018), see Figure 1.26. Under the assumption that central galaxies follow for example a Bernoulli law and satellite galaxies a Poisson law (e.g. Kravtsov et al., 2004; Zheng et al., 2005),  $P(N|M)$  can be fully characterized by the mean  $\langle N|M \rangle$ .

HOD are usually constrained either by fits onto semi-analytical models or onto galaxy clustering. Small scale galaxy clustering below  $\sim 1$  Mpc/h, which corresponds to the transition scale from 2-halo to 1-halo terms, is sensitive to the fraction of satellite galaxies (Zehavi et al., 2004; Zehavi et al., 2005). Indeed the number of pairs in a halo is proportional to the square of the number of satellite galaxies. On large scales galaxy clustering can be quantified using a bias by comparing to the dark matter clustering, so is sensitive to the halo mass and scatter, and the properties used for galaxy selection. Standard HOD models assume a large scale environmental independence of halos of a certain mass on their galaxy content. However it was shown that secondary properties (other than mass), such as e.g. formation time or concentration, can have an influence on the halo clustering. This effect is called halo assembly

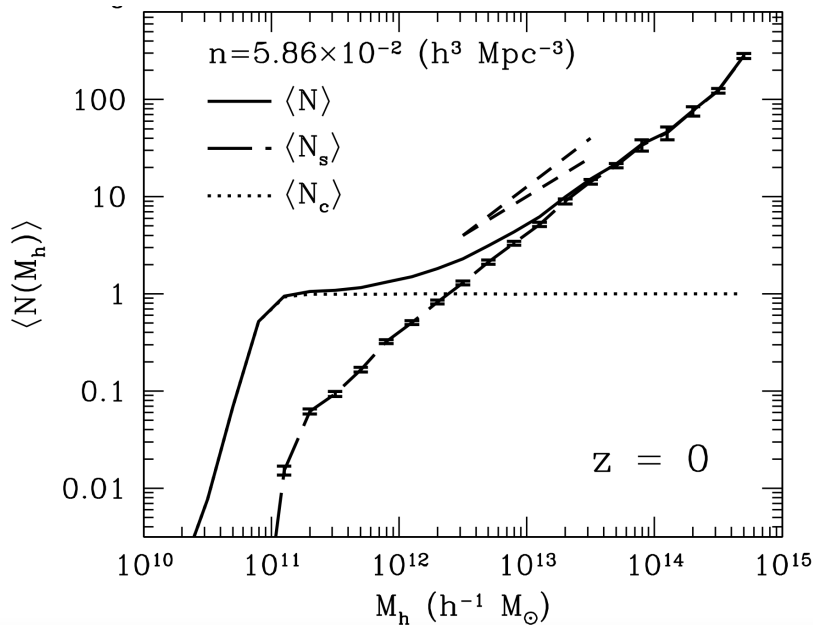


Figure 1.26: Satellite ( $N_s$ ) and central ( $N_c$ ) galaxies first moment of the HOD as function of the halo mass. Central galaxies can be described by a step function and satellite galaxies HOD is a power law with Poisson scattering. The different behaviours suggest a separated parametrization. (Credits of the figure: Kravtsov et al., 2004).

bias. There is also a galaxy assembly bias that affect galaxy properties due to halos secondary properties (Gao et al., 2005; Y.-Y. Mao et al., 2018; Wechsler et al., 2002).

### Peak-background split

The high-peak bias concept relies on the following assumption: peaks in the initial density field are the location where galaxies or astronomical objects would form (Kaiser, 1984, Bardeen et al., 1986). It can be generalized to various objects that form in high density regions that have already collapsed (Cole and Kaiser, 1989, H. J. Mo and White, 1996).

The peak-background split model decomposes the density  $\delta$  into two components, a long and a short wavelengths. Then collapsing of object would happen for density peak of  $\delta$  above a threshold  $\delta_c$ , the critical density. In an Einstein-de Sitter Universe, this value is  $\delta_c = 1.686$  for spherical collapse. This is illustrated on Figure 1.27.

### 1.2.7 Lagrangian Dynamics

Until now we worked in an Eulerian framework, i.e. the different quantities were expressed with respect to their comoving coordinates  $\vec{x}$ . The observer position was therefore staying at the same position over time, and the fluid flows around the perturbations at fixed positions. In Lagrangian framework the observer moves with the fluid particle. In analogy with a river,

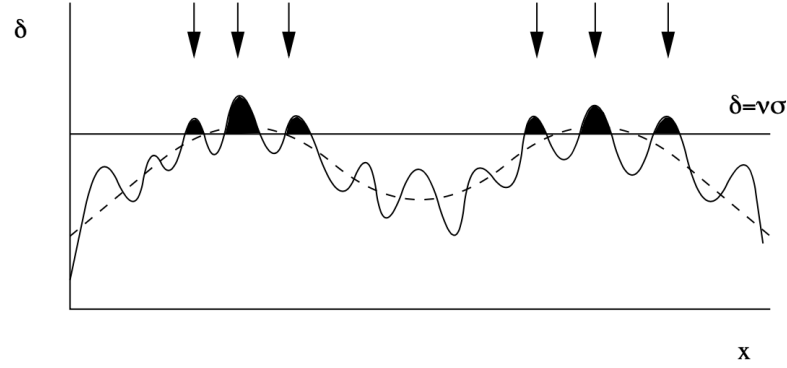


Figure 1.27: Illustration of the peak-background assumption. (Credits of the figure: Peacock, 2003).

an Eulerian reference frame would be on the river bank while Lagrangian on a boat.

### Equation of motion

The Lagrangian point of view deals with the initial positions  $\vec{q}$ . The final comoving coordinate can be written as:

$$\vec{x}(\vec{q}, t) = \vec{q} + \Psi(\vec{q}, t), \quad (1.120)$$

where  $\Psi$  is the displacement field. As the mass is conserved under the change of coordinates, it requires:

$$\rho d^3 \vec{x} = \bar{\rho} (1 + \delta(\vec{x})) d^3 \vec{x} = \bar{\rho} d^3 \vec{q}, \quad (1.121)$$

and the Jacobian of the transformation is:

$$J(\vec{q}, t) = \left| \frac{d\vec{x}}{d\vec{q}} \right| = \text{Det} \left( \delta_{ij}^K + \frac{\partial \Psi_i}{\partial q_j} \right) \rightarrow 1 + \delta(\vec{x}) = \frac{1}{J(\vec{q}, t)}, \quad (1.122)$$

with  $\delta^K$  the Kronecker delta function.

In this context we can write the Lagrangian equations of motion. Let's use the velocity previously for comoving coordinates,  $\vec{v} = a\dot{x}$  from Equation 1.47b. As  $q$  is fixed with time we have the peculiar velocity  $\vec{v} = a\dot{\Psi}$ . In Lagrangian framework we travel along with the fluid particle:

$$\frac{d}{dt}|_{\text{Lagrangian}} \rightarrow \frac{\partial}{\partial t}|_{\text{Eulerian}} + \frac{1}{a} \vec{v} \cdot \nabla, \quad (1.123)$$

which relates to the left-hand-side of Euler Equations 1.49b for pressure-less fluid in La-

grangian description as:

$$\frac{d\vec{v}}{dt} + \frac{\dot{a}}{a}\vec{v} = -\frac{1}{a}\nabla_x\Phi \quad \rightarrow \quad \frac{da\vec{v}}{dt} = -\nabla_x\Phi, \quad (1.124)$$

where  $\Phi$  comes from Equation 1.48. Replacing now in the Euler equations the form of the velocity, i.e.  $\vec{v} = a\vec{\Psi}$ , we get the equation of motion:

$$\ddot{\Psi} + 2\frac{\dot{a}}{a}\dot{\Psi} = -\nabla_x\Phi. \quad (1.125)$$

The Poisson Equation 1.49c becomes by replacing the density contrast by the inverse Jacobian (see Equation 1.122):

$$\nabla_x^2\Phi = -4\pi G a^2 \bar{\rho} (J^{-1} - 1). \quad (1.126)$$

### Zel'dovich approximation

Taking the divergence of the Equation of motion 1.125 and inserting the Lagrangian Poisson equation, we get:

$$\nabla_q \cdot \left( \ddot{\Psi} + 2\frac{\dot{a}}{a}\dot{\Psi} \right) = 4\pi G a^2 \bar{\rho} (1 - J^{-1}). \quad (1.127)$$

In the linear approximation from a perturbation approach it was shown that the Equation of motion 1.127 in a Lagrangian framework has two solutions of similar form than the growth of perturbations of Equation 1.81. The growing mode solution in the linear regime corresponds to the Zel'dovich approximation (ZA, Zel'dovich, 1970):

$$\nabla_q \cdot \Psi = -D_+(t)\delta(\vec{q}), \quad (1.128)$$

where  $D_+$  is the growth function as defined in Equation 1.86 and  $\delta(\vec{q})$  is the density contrast from the initial conditions  $\vec{q}$ . The ZA is a local description of the evolution of the fluid particles. They are independent from the rest of the fluid.

The ZA once inserted into the Jacobian allows to write the density in the following form:

$$1 + \delta(\vec{x}, t) = \frac{1}{(1 - \lambda_1 D_+(t))(1 - \lambda_2 D_+(t))(1 - \lambda_3 D_+(t))}, \quad (1.129)$$

where  $\lambda_i$  are the eigenvalues of the tensor  $\frac{\partial \Psi_i}{\partial q_j}$  that describes the deformation. The ZA helps thus to discriminate between the different structure collapsing mechanisms. Indeed there is gravitational collapse when  $\lambda_i D_+ \rightarrow 1$  for at least one of the eigenvalue. We can outline three main cases that depend on the relative values of  $\lambda_i$  (Hahn, Porciani, et al., 2007, Forero-Romero et al., 2009):

- $\lambda_1 > 0$  and  $\lambda_{2,3} < 0$ : planar collapse (walls, also referred to as pancakes)
- $\lambda_{1,2} > 0$  and  $\lambda_3 < 0$ : filament collapse (filaments)
- $\lambda_{1,2,3} > 0$ : spherical collapse (knots)
- $\lambda_{1,2,3} < 0$ : under-dense regions (voids)

In general Lagrangian PT (LPT) presents good results on large scales for high redshifts. However on lower scales, shell crossing is dominant and LPT is no longer a good description. We note that the second order Lagrangian PT (2LPT) of  $\Psi$  is now more common, as it significantly improves, compared to ZA, the density and velocity fields properties. 3LPT was shown to bring little improvement compared to 2LPT (Buchert et al., 1994, Melott et al., 1995).

### Lagrangian bias

Assuming the bias to be in a local Lagrangian space, which is not equivalent to a local Eulerian bias, we can write the Lagrangian bias function  $F_L$ :

$$1 + \delta_t(\vec{q}) = F_L[\hat{\delta}_m(\vec{q})], \quad (1.130)$$

where  $\hat{\delta}_m(\vec{q})$  is the smooth density field (defined in Equation 1.115) at the initial conditions  $\vec{q}$ .

The Lagrangian biases can be described using the formalism of Matsubara, 2008 as the  $n$ th derivatives of  $F(\delta)$ :

$$\langle F^{(n)} \rangle = \frac{1}{2\pi\sigma_R} \int d\delta e^{-\delta^2/2\sigma_R^2} \frac{d^n F_L}{d\delta^n}, \quad (1.131)$$

where  $\sigma_R^2$  is the variance  $\langle \delta_m^2 \rangle$ .

Explicit formulations of the two first biases can be found using a Sheth-Tormen mass function (Matsubara, 2008):

$$\begin{aligned} F' &= \frac{1}{\delta_c} \left[ av^2 - 1 + \frac{2p}{1 + (av^2)^p} \right], \\ F'' &= \frac{1}{\delta_c^2} \left[ a^2 v^4 - 3av^2 + \frac{2p(2av^2 + 2p - 1)}{1 + (av^2)^p} \right], \end{aligned} \quad (1.132)$$

where  $a = 0.707$ ,  $p = 0.3$  correspond to the Sheth-Tormen mass function (Sheth and Tormen, 1999) and  $\delta_c = 1.686$  is the critical density from collapse. Under the peak-background splitting assumption, the two bias parameters are related via the  $v$  parameter (note that  $v$  as defined here is the square root of the one defined in the halo model Section 1.2.5).

Moreover, following the Eulerian description of Equation 1.116, the biased density contrast in

Lagrangian quantities is:

$$\hat{\delta}_{L,t}(\vec{q}) = \sum_{n=0}^{\infty} \frac{F^{(n)}}{n!} \hat{\delta}_{L,m}^n(\vec{q}). \quad (1.133)$$

Using the mass conservation Equation 1.121 that can be extended to the tracers as their the total number is conserved  $\rho_t d^3 \vec{x} = \rho_{L,t} d^3 \vec{q}$ , and using the Jacobian of Equation 1.122, we have:

$$(\hat{\delta}_t) = (\hat{\delta}_m)(\hat{\delta}_{L,t}). \quad (1.134)$$

We can thus have relations between the Eulerian and Lagrangian biases. The first two biases are related through (e.g. Sheth et al., 2013, Desjacques et al., 2018):

$$b_1 = F' + 1, \quad b_2 = F'' + \frac{8}{21} F', \quad b_3 = F^{(3)} - \frac{13}{7} F'' - \frac{796}{1323} F'. \quad (1.135)$$

### 1.3 Measuring the Expansion with Spectroscopic Surveys

As mentioned in the previous Section 1.2, LSS in the Universe are a very powerful probe to study cosmology and unravel the nature of dark energy. Their observations are made possible due to spectroscopic surveys which aim to map effectively large fractions of the Universe to study them.

One of the key objectives of the massive spectroscopic surveys is to measure the expansion history of the Universe using the Baryon Acoustic Oscillations (BAO) imprinted in the clustering of the galaxies. To this goal they gather spectra based on a target selection at different overall redshifts. Each redshift range has their specificity and complexities, so for consistency spectroscopic surveys use different biased tracers for their selection of specific targets over a defined redshift range. Besides BAO measurements, LSS from a galaxy survey contain extra information, such as the bias which is the link between the galaxies and the dark matter field, and Redshift Space Distortions (RSD).

In this Section, I will start by presenting these different features in the matter clustering of the LSS, and then present some of the spectroscopic surveys used for cosmology up to now.

#### 1.3.1 Cosmic Microwave Background

The Cosmic Microwave Background (CMB) introduced in Section 1.1.4, is a very powerful probe to study the Universe at a redshift of around 1100 when it was only 380'000 years old. It was discovered by Penzias and Wilson, 1965.

The CMB photons are considered as the relic radiation following the recombination of protons and electrons. Indeed the Universe became transparent at recombination to photons and

photons decoupled. They were then able to travel freely in the Universe at the light velocity, keeping the density variations from their emission time. As in the early Universe, photons were emitted and absorbed in the dense and ionized plasma with a large spectrum of energies in all directions, CMB photons kept those black-body properties. Due to the finite light velocity, the last scattering surface defines the boundary of our observable Universe (in practice) as a spherical surface.

Cosmic Background Explorer (COBE) a satellite launched by NASA in 1989, was the first experiment to successfully measure the anisotropies (beyond the dipole) in the CMB radiation (Smoot et al., 1992). They showed that the CMB spectrum is following precisely the black-body emission of a plasma at 2.725 K. CMB also displays temperature fluctuations that was shown later to be of the order  $\Delta T/T \sim 10^{-5}$ . Those anisotropies led to the growth of the LSS observed today. Different other experiments were launched, among others the Wilkinson Microwave Anisotropy Probe (WMAP) satellite (Bennett et al., 2003) which provided very detailed temperature and polarization maps.

The most precise measurement to date have been measured by Planck satellite with high precision, leading to tight constraints on the cosmological parameters (Planck Collaboration et al., 2020). The temperature fluctuations taken by Planck are shown on Figure 1.28. We note that Planck also measured CMB polarization, that separates into E and B modes. E modes are mainly generated by scalar perturbations in the density of the early Universe. B modes are tensor generated by gravitational waves, they would allow to prove inflation. Planck then produces different power spectra TT (temperature-temperature), TE (temperature-E modes) and EE (E modes-E modes).

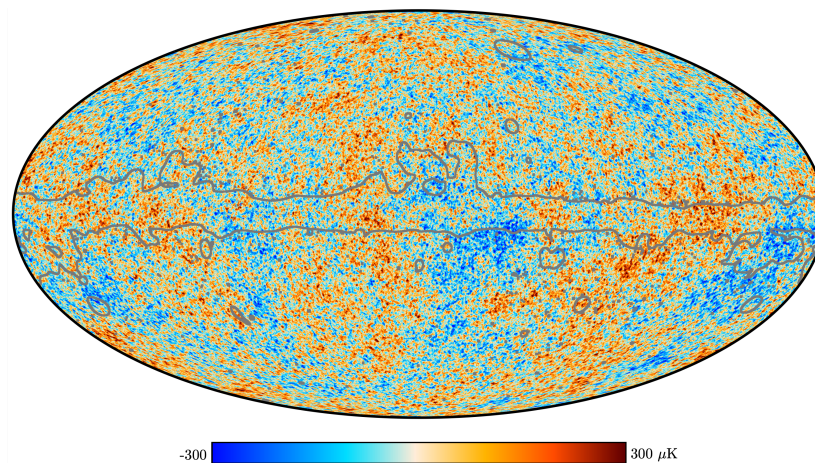


Figure 1.28: CMB map of temperatures anisotropies measured by Planck satellite. (Credits of the figure: ESA and the Planck Collaboration).

The temperature fluctuations can be quantified by a decomposition onto the spherical harmonic basis  $Y_{lm}$ , convenient due to their spherical surface, for angular coordinates  $\theta, \phi$ :

$$\frac{\Delta T}{T}(\theta, \phi) = \sum_{l,m} a_{l,m} Y_{l,m}(\theta, \phi), \quad (1.136)$$

where  $a_{l,m}$  are measured harmonic coefficients. The multipole moments are defined as:

$$\langle |a_{l,m}|^2 \rangle Y_{l,m}(\theta, \phi) C_l = \frac{1}{2l+1} \sum_m \langle |a_{l,m}|^2 \rangle. \quad (1.137)$$

Figure 1.29 shows the CMB power spectrum. Different physical effects responsible for temperature anisotropies can be observed at different modes of the power spectrum on the plot. The Sachs-Wolf (SW) effect causes a plateau in the power spectrum observed at large scale fluctuations due to gravitational potentials on CMB (Sachs and Wolfe, 1967). The effect caused a redshift of the photons when they were escaping the potential wells formed by baryonic matter. The ordinary SW effect occurs at the last scattering surface while the integrated SW (iSW) effect happens between the surface and the observation. Assuming the last scattering surface was already during matter domination epoch the correlation function of the amplitude modes can be related to the gravitational power spectrum  $P_{\Phi}(k)$  through:

$$C_l = \langle |a_{l,m}|^2 \rangle \propto \int df k^2 P_{\Phi}(k) j_l^2(kr), \quad (1.138)$$

where  $j_l$  are the spherical Bessel functions. For a Harrison-Zel'dovich spectrum  $C_l \approx (l(l+1))^{-1}$ . The angular separation length above which two perturbations are in super-horizon zone is roughly above  $1^\circ$ . It means that above this limit the perturbations are dominated by SW effect<sup>XXVII</sup>.

On smaller scales (so large  $l$ ), we can see that the oscillations are damped. This is due to the Silk damping (Silk, 1968) that describes the damping of oscillations on small scales at the end of recombination due to photon diffusion of baryons.

These large oscillations on the Figure 1.29 are due to acoustic waves that will be discussed below in the next Section 1.3.2.

While primary anisotropies and polarization give insight on the primordial Universe, secondary anisotropies of CMB encode other effects such as the Sunyaev-Zeldovich effects (thermal (tSZ) and kinetic (kSZ) Sunyaev and Zeldovich, 1980) or gravitational lensing (Lewis and Challinor, 2006). In particular, CMB weak lensing arises because of the gravitational deflection of the paths from CMB photons by the matter. As this effect is imprinted on the observed CMB, it means that CMB lensing can trace the matter density field and therefore the LSS. Measures with a high signal-to-noise of this effect were obtained, e.g. by the Planck

<sup>XXVII</sup>Photons of the last scattering surface have nearly same temperatures with anisotropies of the order of  $10^{-5}$  even for super-horizons scales, i.e. on scales which are supposed to be not in causal contact. This problem is referred to as the horizon problem.



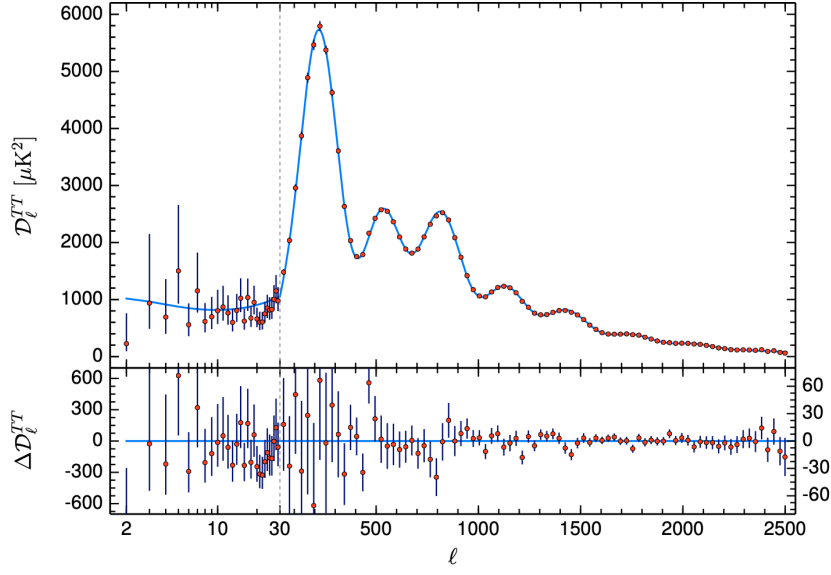


Figure 1.29: Amplitude of the CMB power spectrum  $D_{ll} \equiv l(l+1)C_l/(2\pi)$  from Planck Collaboration et al., 2020.

collaboration and the Atacama Cosmology Telescope (ACT, Sherwin et al., 2017), and in the future CMB-S4 (Abazajian et al., 2019).

### 1.3.2 Baryon Acoustic Oscillations

#### Acoustic waves

In the early Universe between redshift 1100 and 3400, the space was filled by the baryon-photon plasma in thermal equilibrium, with the matter already dominant at this epoch. Due to the tight coupling of baryons, electrons and CMB photons, their mean free paths were shorter than the horizon. Therefore the perturbations oscillate as acoustic waves propagating into the plasma as the radiation pressure engendered exceeds the perturbation gravitational attraction. Those oscillations are called the baryonic acoustic oscillations (BAO, Peebles and Yu, 1970, Sunyaev and Zeldovich, 1970).

The wave propagation has a relativistic sound speed determined mainly by the photons of  $c_s \approx c/\sqrt{3}$ . As a consequence the Jeans length for baryons is larger than for dark matter, both kind of matter behave therefore in different manner. Dark matter which is treated collision-less has already decoupled from photons and its perturbations are growing during this period.

At redshift  $z_d \approx 1100$  baryons decouple, this is the drag epoch<sup>XXVIII</sup>. Mean free path of photons have increased, leaving baryon perturbations exposed to gravitation as generated by dark mat-

<sup>XXVIII</sup>The drag epoch is defined at the redshift when optical depth of baryons is one. This happens at a later time than for photons as photons stop noticing baryons before.

ter. The acoustic waves are frozen after having travelled a characteristic distance predictable theoretically:

$$r_s(z_d) = \int_{z_d}^{\infty} \frac{c_s(z)}{H(z)} dz \approx 150 \text{ Mpc.} \quad (1.139)$$

This distance  $r_s$  is called the sound horizon (Eisenstein and Hu, 1998). We note moreover that at this redshift dark matter already started its growth of the perturbations initiating structure formation. It then seeds the Universe with gravitational wells in which baryonic matter will fall after decoupling.

Figure 1.30 illustrates the process for one perturbation evolution in the linear manner discussed above. All the different species start first around the density peak. The neutrinos are decoupled, so they leave. Photons and baryonic matter are tightly coupled creating a high pressure that produces oscillations of the perturbations and propagates as an acoustic wave, while the collision-less dark matter perturbation grow seeding the gravitational environment in the primordial Universe. When photons decouple, baryonic matter is then subject mainly to gravitational interactions. Dark matter and baryons slowly balance by gravitation and initiate structure formation.

### BAO as a feature of the matter density

As those acoustic waves stopped propagating after recombination, they have left an excess fluctuation still observable at later epoch. Indeed as we have seen above, the dark matter and baryons balance gravitationally, falling into the potential wells created by the baryons overdensities produced by the waves around the initial perturbations seeded by dark matter. Thus BAO manifests itself in the clustering of LSS as a peak around  $100 h^{-1} \text{ Mpc}$  in the matter correlation function or as wiggles in the power spectrum.

Eisenstein et al., 2005 and Cole et al., 2005 were the first studies to report BAO detection with galaxies in configuration space with SDSS (York et al., 2000) data and Fourier space with 2dFGRS (Colless et al., 2001), data, respectively. Figure 1.31 displays the correlation function as measured by Eisenstein et al., 2005 for the sample of LRG of SDSS.

The radius that BAO travelled, which scales to the sound horizon  $r_s$ , became a characteristic comoving length that can be used as a standard ruler for cosmology (Seo and Eisenstein, 2005). Measuring its size at different cosmic time enlightens on the evolution history of the Universe and thus dark energy. In particular it was shown (Tegmark, 1997, Eisenstein and Hu, 1998, Goldberg and Strauss, 1998) that combining CMB and BAO measurements from LSS can break the degeneracy between the cosmological parameters such as  $\Omega_m$  and  $H_0$ , that arises in CMB alone fitting measurements (Efstathiou and Bond, 1999).

Many other BAO measurements have now be evaluated with data coming from different surveys and tracers. In particular some measures have now been made also on voids (Kitaura

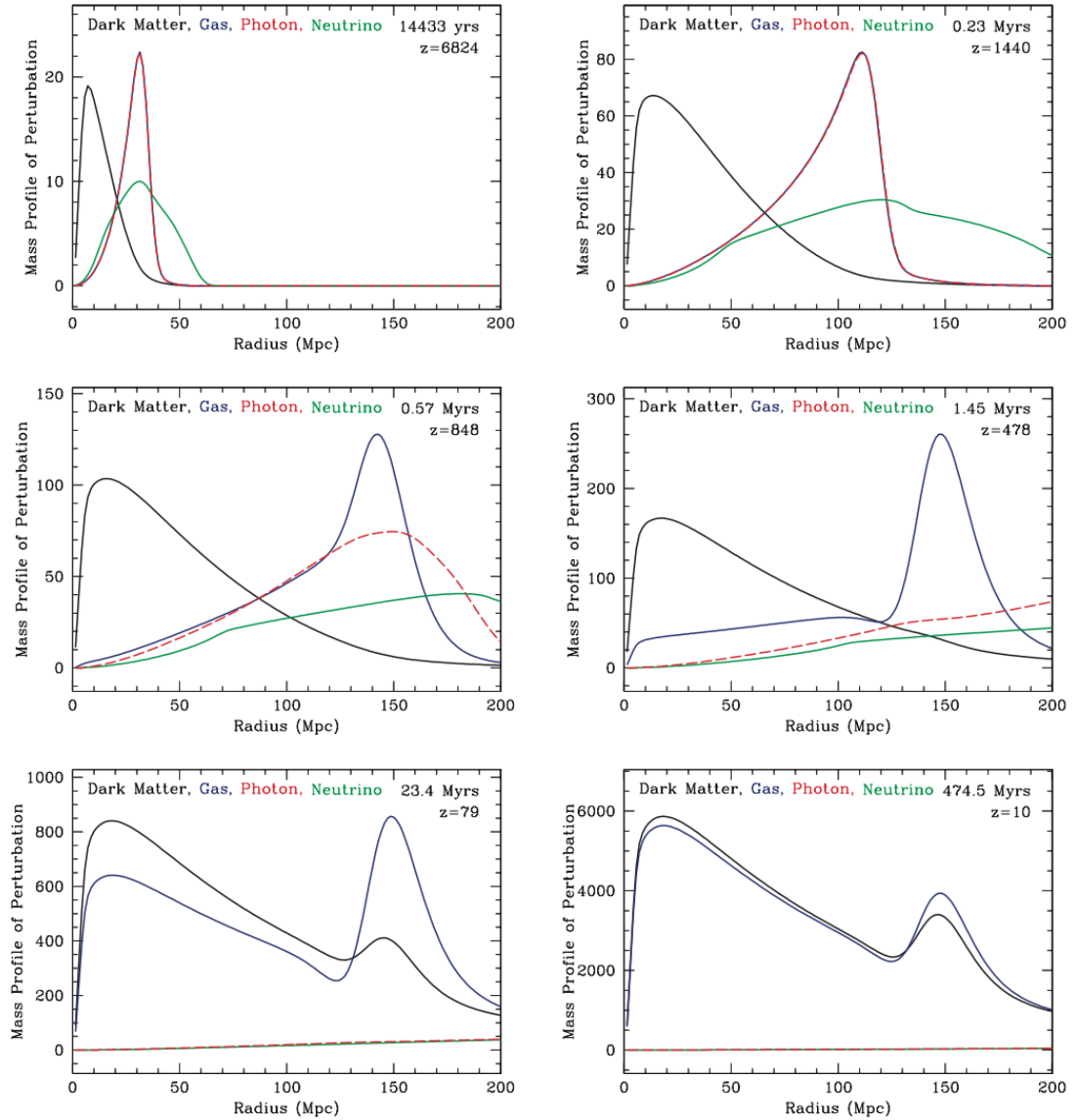


Figure 1.30: Linear evolution of one perturbation mass profile in the early Universe from Eisenstein, Seo, and White, 2007. Dark matter is in black, gas (so baryonic matter) in blue, photons in red, neutrinos in green.

et al., 2016), QSO (Ata et al., 2018) or Lyman- $\alpha$  forest (Busca et al., 2013), reaching the 1% level precision with LRG of BOSS (Alam et al., 2017).

### Alcock-Paczynski effect

The coordinates of the observational data as measured by spectroscopic surveys are the redshifts and the angular positions. However to compute the clustering of the targets, the

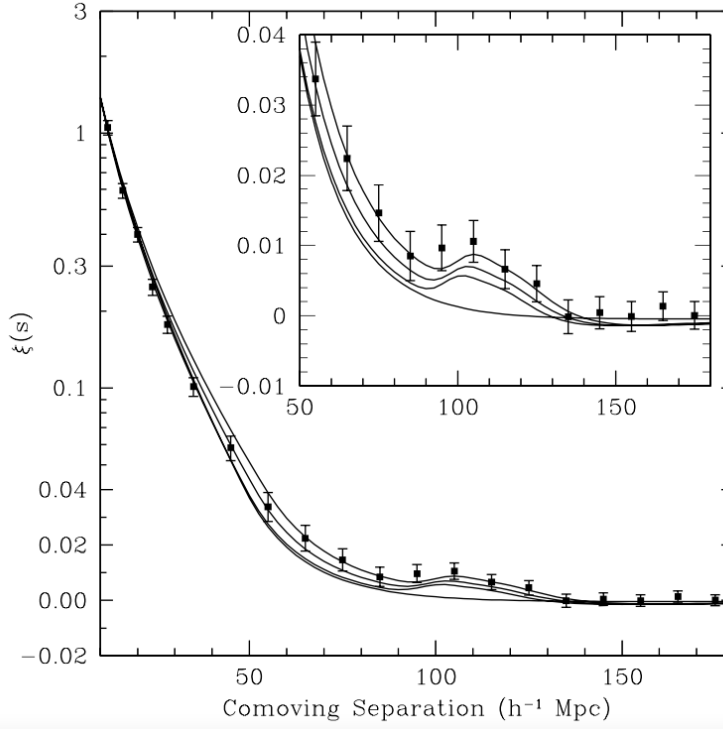


Figure 1.31: Two-point correlation function from Eisenstein et al., 2005 of the LRG SDSS sample. It is the first measured BAO detection in the configuration space clustering of observed galaxies. BAO manifests itself as an excess probability of finding two galaxies separated by about  $100 h^{-1} \text{Mpc}$ .

positions used are comoving distances. By consequence, we convert the observed positions into comoving distances to measure the separations, assuming a fiducial cosmology. So if this fiducial cosmology used is not the true one, intrinsic to the Universe, it will bring anisotropies in the clustering, i.e. the correlation between the targets will be distorted accordingly to the direction. This is the Alcock-Paczynski effect (AP, Alcock and Paczynski, 1979).

The angular and radial separations,  $d\theta$  and  $dz$ , can be related to their comoving counterparts  $dr_{\perp}$  and  $dr_{\parallel}$  for two objects separated by a distance  $r$ :

$$dr_{\perp} = D_A(z) d\theta, \quad dr_{\parallel} = \frac{c}{H(z)} dz. \quad (1.140)$$

This is illustrated on Figure 1.32.

In practice, BAO analysis measure the deviation from an assumed fiducial cosmology, with subscript 'fid', by fitting the AP parameters to the data using the sound horizon  $r_s$  (Equation 1.139) in the line-of-sight and transverse directions:

$$\alpha_{\parallel} = \frac{H^{\text{fid}}(z) r_s^{\text{fid}}}{H(z) r_s}, \quad \alpha_{\perp} = \frac{D_A(z) r_s^{\text{fid}}}{D_A^{\text{fid}}(z) r_s} dz. \quad (1.141)$$

For an isotropic fit, we measure the component of the AP parameter corresponding to an isotropic shift of the BAO peak position:

$$\alpha_{\text{iso}} = \alpha_{\parallel}^{1/3} \alpha_{\perp}^{2/3} = \frac{D_V(z) r_s^{\text{fid}}}{D_V^{\text{fid}}(z) r_s} dz, \quad (1.142)$$

where the volume average distance  $D_V$  is a combination of  $D_A$  and  $H$ :

$$D_V(z) = \left( cz \frac{D_A(z)^2 (1+z)^2}{H(z)} \right)^{1/3}. \quad (1.143)$$

When measured in the two directions, BAO allow then to break the degeneracy between  $H(z)$  and  $D_A(z)$ <sup>XXIX</sup>, and therefore help constraining  $\Omega_m$  and  $\Omega_{\Lambda}$ .

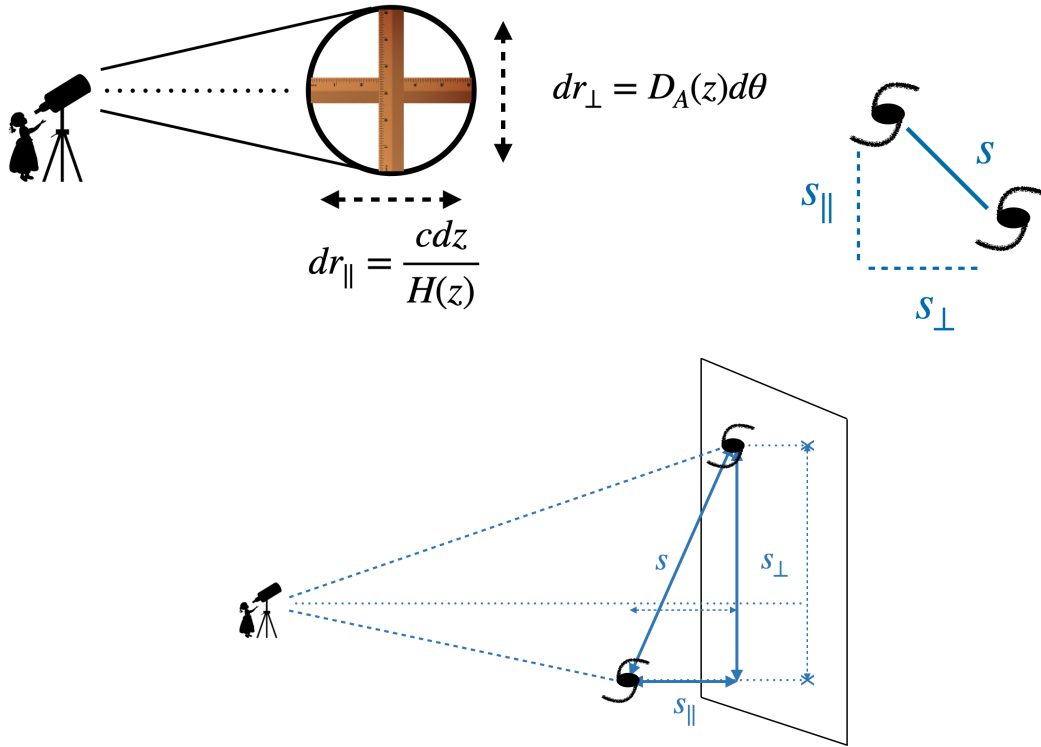


Figure 1.32: Alcock-Paczynski effect and separation projection schemes (radial and angular separations).

The method to obtain  $H_0$  from BAO is called inverse distance ladder: the distance used for calibration is measured at high redshift and is in turn used to infer the value at redshift 0 by extrapolation. However as seen above, the constraint values depend on  $r_s$ . Usually CMB is

<sup>XXIX</sup>Indeed while the BAO peak position constrain the combination  $(D_A^2 H^{-1})^{1/3} / r_s$ , the relative dilation, i.e. due to AP effect, constrain  $\alpha_{\parallel} / \alpha_{\perp} \approx H D_A$ .

used to calibrate  $r_s$  and thus BAO. Indeed  $r_s$  depends only<sup>xxx</sup> on  $\Omega_b h^2$  and  $\Omega_c h^2$  that can be constrain by CMB.

### BAO reconstruction

While on BAO scales the behaviour is dominantly linear, non-linearities still affect the BAO peak. It would impact the separation of two dark matter halos at redshift 0 by a total of about  $\sim 10 h^{-1} \text{Mpc}$  (Eisenstein, Seo, and White, 2007). At BAO scale, these small deviations from 150 Mpc broaden the peak, or damp the oscillations in Fourier space. While the BAO is not significantly biased by the broadening, it reduces the measurement precision.

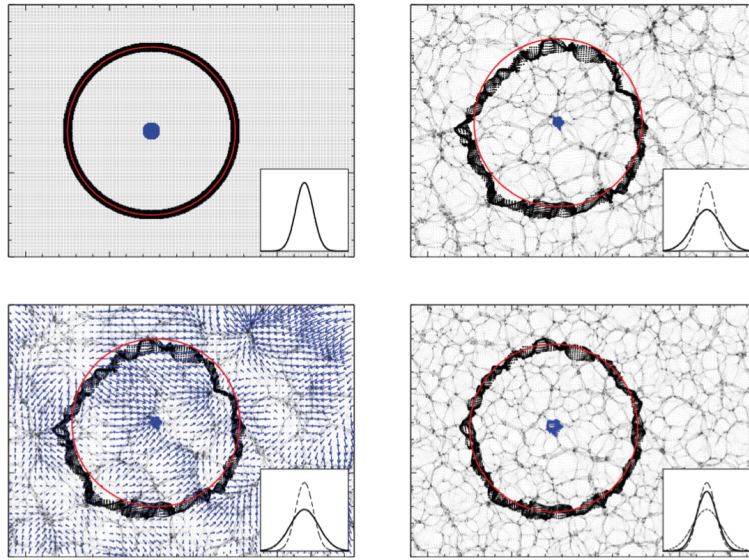


Figure 1.33: Explaining scheme from Padmanabhan et al., 2012 for BAO reconstruction.

A common method to correct for this effect is the reconstruction (Eisenstein, Seo, Sirko, et al., 2007). From the density field measured from the data, the idea is to move the particles backward to their originate position using their displacement field, this method is called reconstruction. The most simple reconstruction models use the Zel'dovich approximation, see Section 1.2.7. We note that on tracers with low number density such as quasars, the reconstruction procedure is usually not applied. Indeed reconstruction requires an estimation of the density field from the tracer distribution. If the number density is not high enough the shot noise contamination in the density field is too significant that the reconstructed results can be biased in addition it will increase the noise.

The explanatory illustration taken from Padmanabhan et al., 2012 for the BAO reconstruction is shown on Figure 1.33. It shows the density field around an initial overdensity (central blue point) with the acoustic ring feature of 150 Mpc (black circle). The inset plots represent the

<sup>xxx</sup>Under assumption of a smooth expansion, a CMB mean temperature well measured and standard prerecombination physics.

radial distribution of the black positions to the blue. The top left panel displays the smooth density field in the early Universe, which is then degraded due to non-linear evolution, in the top right panel. Large-scale velocities caused a broadening of the acoustic peak as the black positions are spread out. The smoothed Lagrangian displacement field is shown on the bottom left panel. Bottom right plot displays the density field where positions are moved back using the displacement field.

### 1.3.3 Redshift Space

The line-of-sight observable distance is the redshift. However individual galaxies have peculiar velocities induced by their gravitational environment. These velocities affect the redshift measurement by moving slightly the observed position of the galaxy. This distorted space which is the observed one is called redshift space in opposition to the real space. It can be used to measure to growth rate of structure  $f$  and therefore  $\Omega_m$ .

Right panel of Figure 1.34 compares the correlation function in real and redshift spaces in simulations. The clustering is compressed into a multipole expansion using a projection on the Legendre basis (see Chapter 2). While in the real space all the information is contained in the radial correlation, in redshift space peculiar velocities and non-linearities informations bring an anisotropic signal. The higher order even Legendre multipoles (2,4) are thus non-zero<sup>XXXI</sup>. A redshift evolution of the clustering in redshift space is shown on the left of Figure 1.34.

### Peculiar velocities

The total proper velocity of an astronomical object is the time derivative of its proper distance  $d$  so from Equation 1.37:

$$v(t) = \frac{d}{dt} d(t) = \dot{a}\chi + a\dot{\chi} \equiv v_{\text{cos}} + v_{\text{pec}}, \quad (1.144)$$

where  $v_{\text{cos}} = H(t)d(t)$  is the velocity induced by the Hubble flow, i.e. the expansion of the Universe, and  $v_{\text{pec}}$  is the peculiar velocity caused by the gravitational field surrounding the object.

The observed redshift depends then on these two velocity components<sup>XXXII</sup>:

$$z_{\text{obs}} = (1 + z_{\text{cos}})(1 + z_{\text{pec}}). \quad (1.145)$$

<sup>XXXI</sup> Due to the symmetry on the line-of-sight, the odd multipoles cancel out (see for an extension on wide angles in Fourier space e.g. Raccañelli et al., 2014, Castorina and White, 2018, Beutler et al., 2019). Moreover in linear theory, the expanded sum goes only up to the hexadecapole (Hamilton, 1998). We note that the quadrupole can help breaking degeneracies (Yamamoto et al., 2006).

<sup>XXXII</sup> This results from the redshift definition:  $z_{\text{obs}} = \frac{\lambda_{\text{obs}}}{\lambda_{\text{em}}} = \frac{\lambda_i}{\lambda_{\text{em}}} \frac{\lambda_{\text{obs}}}{\lambda_i}$ , where  $\lambda_i$  is the wavelength as measured by an observer located at the same proper distance than the object from the final observer.

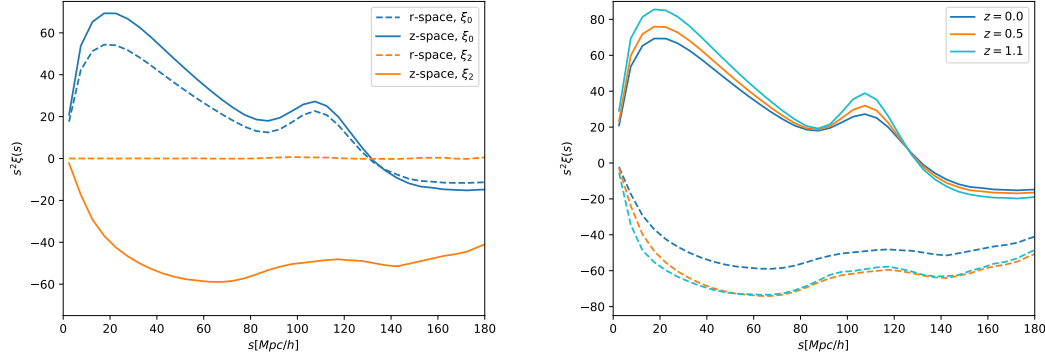


Figure 1.34: Left: real (r-space) and redshift (z-space) space multipoles of the Indra simulations (B. Falck et al., 2021) at redshift 0. As the clustering is isotropic in real space, the quadrupole (and higher order multipoles) which contains angular information is null. Moreover we note that resulting observed overdensities are larger in redshift space due to the infall velocities. Indeed in redshift space overdensity regions are more grouped on the radial direction. This results in a higher clustering correlation below the BAO scale. Right: redshift evolution of the multipoles in redshift space. The BAO peak is dumped as it tends to redshift zero. This is due to non-linearities that increase with time (as  $z$  goes to 0).

This shift in redshift affects the line-of-sight, or radial, component of observed position. The mapping between redshift space position  $\vec{s}$  and the real position  $\vec{r}$  is<sup>XXXIII</sup>:

$$\vec{s} = \vec{r} + \frac{v_{\text{pec}}(\vec{r})}{aH} \hat{e}_z \equiv \vec{r} + u_z(\vec{r}), \quad (1.146)$$

where  $u_z$  is the comoving peculiar velocity in the line-of-sight direction. We note that in simulations the radial direction  $\hat{e}_z$  is usually considered fixed for all observations under the plane-parallel assumption.

On linear regime, we described previously the peculiar velocity induced by gravitational growth of perturbation in Equation 1.87. In particular on scales above approximately  $60\text{--}80 h^{-1}\text{Mpc}$ , we can thus established a relation between the peculiar velocity field divergence and the density contrast as<sup>XXXIV</sup>:

$$\theta \equiv \nabla_r \cdot v_{\text{pec}}(\vec{r}, z) = -a(z)H(z)f\delta(\vec{r}, z). \quad (1.147)$$

<sup>XXXIII</sup>It comes from:  $\vec{s} = \vec{r} + \Delta t v_{\text{pec}} \hat{e}_z$ , with  $\Delta t = \chi / v_{\text{cos}} = \chi / (Ha\chi)$ .

<sup>XXXIV</sup>Fourier transform of Equation 1.87 is:  $v = -aHf\nabla^{-1}\delta$ .



### Real-to-redshift space mapping

Every element in the real space should correspond to an element in redshift, we thus have conservation of the number of particles in volume elements:

$$n_s(\vec{s})d^3\vec{s} = n(\vec{x})d^3\vec{r} \quad \rightarrow \quad (1 + \delta_s(\vec{s}, t))d^3\vec{s} = (1 + \delta(\vec{r}, t))d^3\vec{r}. \quad (1.148)$$

With  $s$  and  $r$  the radial components of the vector positions in redshift and real spaces respectively, and using the inverse of the Jacobian  $\frac{d^3s}{d^3r}$ <sup>XXXV</sup>, we have:

$$1 + \delta_s(\vec{s}, t) = (1 + \delta(\vec{r}, t)) \left(1 + \frac{u_z}{r}\right)^{-2} \left(1 + \frac{du_z}{dr}\right)^{-1}. \quad (1.149)$$

We use a perturbation approach in the linear approximation, i.e.  $\delta \ll 1$  and  $\nabla u(\vec{r}) \ll 1$ , and we assume that  $u_z \ll r$ :

$$\delta_s(\vec{s}, t) = \delta(\vec{r}, t) - \frac{2u_z}{r} - \frac{du_z}{dr} + O(2), \quad (1.150)$$

where  $O(2)$  indicates second order and higher terms. We further assume the distant-observer approximation, i.e very large  $r$ , so that the second term can be neglected on the right hand side.

From Equation 1.147, we can write the comoving peculiar velocity  $\vec{u}$  as<sup>XXXVI</sup>:

$$\vec{u} \equiv u(\vec{r}) = -f\nabla_r^{-1}\delta(\vec{r}) \quad \rightarrow \quad u_z = \frac{\partial}{\partial r}\nabla_r^{-1}\vec{u} = -f\frac{\partial}{\partial r}\nabla_r^{-2}\delta, \quad (1.151)$$

The line-of-sight derivative of  $u_z$  is then:

$$\frac{du_z}{dr} = -f\frac{\partial^2}{\partial r^2}\nabla_r^{-2}\delta = \frac{\partial^2}{\partial r^2}\frac{\nabla}{\nabla^2}\vec{u} = \frac{1}{aH}\frac{\partial^2}{\partial r^2}\nabla^{-2}\theta \equiv \frac{\partial^2}{\partial r^2}\nabla^{-2}\hat{\theta}, \quad \text{with } \hat{\theta} = f\delta. \quad (1.152)$$

In Fourier space the density contrast in redshift space becomes, using Equation 1.152:

$$\delta_s(\vec{k}, t) = \delta(\vec{k}, t) + \mu_k^2\hat{\theta}_k, \quad \text{where } \mu_k \equiv \frac{\hat{e}_z \cdot \vec{k}}{k}. \quad (1.153)$$

Parameter  $\mu_k$  is the cosine of the angle between the line-of-sight and the mode. The power spectrum in redshift space of the biased matter, subscript  $t$  is for tracer, is (Scoccimarro, 2004):

$$P_t^s(k, t) \equiv \langle |\delta_s|^2 \rangle = \langle |\delta|^2 \rangle + 2\mu_k^2\langle \delta\hat{\theta} \rangle + \mu_k^4\langle \hat{\theta}^2 \rangle \equiv P_{\delta\delta,t} + 2\mu_k^2P_{\delta\theta,t} + \mu_k^4P_{\theta\theta,t}. \quad (1.154)$$

The power spectra  $P_{\delta\delta,t}$ ,  $P_{\delta\theta,t}$  and  $P_{\theta\theta,t}$  are respectively the density, density-velocity and

<sup>XXXV</sup>The Jacobian is:  $\frac{d^3\vec{s}}{d^3\vec{r}} = \frac{3s^2}{3r^2}\frac{ds}{dr} = \frac{(r+u_z)^2}{r^2}(1 + \frac{du_z}{dr}) = (1 + \frac{u_z}{r})^2(1 + \frac{du_z}{dr})$ .

<sup>XXXVI</sup>We note that  $\nabla_r = d/dr$

velocity power spectra.

Under linear approximation, we have seen above that the matter density and velocity fields are linearly related from Equation 1.147. We assumed a linear bias  $b(k) = b$  such that  $\delta_t = b\delta_m$ . If we further assume that central galaxies are at rest in the dark matter halo and that satellite galaxies distribution follows the mass distribution we have no velocity bias, i.e.  $\theta_t = \theta_m$ . Moreover we recall that we have a linear coupling of  $\hat{\theta}$  and  $\delta$  through the growth rate parameter  $f$  (see Equation 1.152). We thus find the Kaiser relation (Kaiser, 1987) with the matter power spectrum in real space  $P_m$ :

$$P_t^s(k, t) = b^2 (1 + 2\beta\mu_k^2 + \beta^2\mu_k^4) P_m(k, t) = b^2 (1 + \beta\mu_k^2)^2 P_m(k, t), \quad (1.155)$$

where  $\beta \equiv f/b$ . We note from this expression that the bias and the growth rate are degenerate with  $\sigma_8$  (which normalized  $P_m$ ). Therefore in practice we measure  $b\sigma_8(z)$  and  $f\sigma_8(z)$ .

Expanding the power spectrum  $P^s(k)$  into harmonics of  $\mu_k$ , using the Legendre polynomials of order  $\ell$ ,  $\mathcal{L}_\ell$ :

$$P^s(\vec{k}) = \sum_{\ell} \mathcal{L}_{\ell}(\mu_k) P_{\ell}^s(k), \quad \text{with} \quad P_{\ell}^s(k) = \frac{2\ell+1}{2} \int_{-1}^1 P^s(\vec{k}) \mathcal{L}_{\ell}(\mu_k) d\mu_k. \quad (1.156)$$

In the linear approximation with the Kaiser formula we get as non-zero multipoles, with  $P(k)$  the linear real space matter power spectrum:

$$P_0^s(k) = \left(1 + \frac{2}{3}\beta + \frac{1}{5}\beta^2\right) P(k), \quad P_2^s(k) = \left(\frac{4}{3}\beta + \frac{4}{7}\beta^2\right) P(k), \quad P_4^s(k) = \frac{8}{35}\beta^2 P(k). \quad (1.157)$$

From those we understand that the redshift space power spectrum is enhanced by a factor depending only on  $\beta$ . Indeed the infall peculiar velocities are proportional to  $\beta$  (in the linear approximation) which produces this enhancement of the density contrast in redshift space. We notice furthermore that ratios between harmonics allow us to obtain the parameter  $\beta$ .

### Non-linear redshift-space approach

Equivalently the Fourier density can be written as a Fourier transform of the configuration space density (using the definitions of Equation 1.65):

$$\delta_s(\vec{k}) = \int d^3\vec{r} \left( \delta(\vec{r}) - \frac{du_z(\vec{r})}{dr} \right) e^{-i(\vec{k} \cdot \vec{r} + k\mu_k u_z)}. \quad (1.158)$$

Defining  $\vec{x} \equiv \vec{r} - \vec{r}'$  and  $\Delta u_z \equiv u_z(\vec{r}) - u_z(\vec{r}')$ , the density power spectrum in redshift space can thus be expressed as:

$$P^s(\vec{k}) = \int d^3\vec{x} e^{-i(\vec{k} \cdot \vec{x})} \langle e^{-i(k\mu_k \Delta u_z)} \left( \delta(\vec{r}) - \frac{du_z(\vec{r})}{dr} \right) \left( \delta(\vec{r}') - \frac{du_z(\vec{r}')}{dr} \right) \rangle. \quad (1.159)$$

Another notation is sometimes used, where the comoving velocity  $\vec{u}$  is scaled with the growth rate such as  $\hat{u} \equiv -\vec{v}/(f(a)H(a)a)$  and thus the line-of-sight derivative becomes  $du_z/dt = -f d\hat{u}_z/dt$ . In this case the growth rate dependency is clearer and we understand better the enhancement of the density contrast produced by RSD (see next Section 1.3.3) on the line-of-sight. On smaller scales (more clustered), there is a damping causing a power suppression controlled by the exponential factor.

Using perturbation theory, the linear approximation expressed above can thus be extended to non-linear regime. A very used model is the one of Taruya et al., 2010 (TNS) relying on one-loop standard PT. Two extra terms are added to Equation 1.154 and writing the growth rate dependency explicitly:

$$P_t^s(k, t) = b(k)^2 P_{\delta\delta, t} + 2b(k)\mu_k^2 f P_{\delta\theta, t} + f' 2\mu_k^4 P_{\theta\theta, t} + A(k, \mu_k, b) + B(k, \mu_k, b). \quad (1.160)$$

The two terms  $A$  and  $B$  come from linear and non-linear coupling arising from the interactions between the damping and enhancement terms in Equation 1.159. TNS model can be extended with two-loop corrections.

TNS model reaches an accuracy of 1% at  $k \leq 0.15$  h/Mpc at redshifts below approximately 1 (Gil-Marín et al., 2012).

While PT approach in the clustering modelling in redshift space is quite fast to compute, it breaks down on small scales and fails to reproduce the non-perturbative features (as the FoG effect described below). To model the clustering on quasi- and non-linear scales, i.e. small scales, in redshift space, another approach exist that was introduced in Section 1.2.6 based on empirical prescriptions. Indeed HOD semi-analytical models could be used to capture the redshift space clustering on small scales. Those models require parameter calibration on N-body simulations (Tinker et al., 2006, Tinker, 2007, Zu and Weinberg, 2013). Measurements on small scale clustering have been done using HOD based models tuned on simulations to provide measurements on data. (B. A. Reid et al., 2014, Chapman et al., 2022, H. Guo et al., 2015, Hikage, 2014). Approach relying on a mixture of PT and N-body simulations with a halo model has also been explored reaching a modeling up to  $k < 0.4$  (Hand et al., 2017). The challenges of such HOD approaches are computational as individual simulations are expensive and the parameter space is often more limited.

### Redshift-space correlation function

The correlation function in redshift space  $\xi^s$  becomes:

$$\xi^s(\vec{s}) = \langle \delta^s(\vec{r}) \delta^s(\vec{s} + \vec{r}) \rangle, \quad \text{where} \quad \delta^s(\vec{s}) = \delta(\vec{x}) - \frac{du_z(\vec{x})}{dr}. \quad (1.161)$$

In linear theory  $\xi^s(\vec{s}) \equiv \xi^s(s_{\parallel}, s_{\perp}) = \xi(s, \mu)$ , with  $s_{\perp}$  is the angular separation in redshift space and  $s_{\parallel} \equiv \mu s$  the radial ( $s^2 = s_{\perp}^2 + s_{\parallel}^2$ ), is fully specified:

$$\xi^s(s, \mu) = \xi_0^s(s) \mathcal{L}_0(\mu) + \xi_2^s(s) \mathcal{L}_2(\mu) + \xi_4^s(s) \mathcal{L}_4(\mu), \quad (1.162)$$

where the multipoles  $\xi_{\ell}^s(s) \equiv \frac{2\ell+1}{2} \int_{-1}^1 \xi^s(s, \mu) \mathcal{L}_{\ell}(\mu) d\mu$  are:

$$\begin{aligned} \xi_0^s(s) &= \left(1 + \frac{2}{3}\beta + \frac{1}{5}\beta^2\right) \xi(s), & \xi_2^s(s) &= \left(\frac{4}{3}\beta + \frac{4}{7}\beta^2\right) \left(\xi(s) - \frac{3J_3(s)}{s^3}\right), \\ \xi_4^s(s) &= \frac{8}{35}\beta^2 \left(\xi(s) + \frac{15J_3(s)}{2s^3} - \frac{35J_5(s)}{2s^5}\right). \end{aligned} \quad (1.163)$$

The function  $J_{\ell}$  is  $J_{\ell} = \int_0^x \xi(y) y^{\ell-1} dy$ . Again we see that ratios between monopole and quadrupole help us infer  $\beta$ .

### Streaming model

In configuration space, models of the clustering in redshift space can be derived from the Fourier transform of the power spectrum models. A second class of models also directly works in configuration space. The redshift space correlation is expressed as a convolution of the correlation in real space  $\xi(r)$  with the line-of-sight velocity probability distribution  $F(v)$ .

We can write the excess probability of finding a pair at positions  $(\vec{s}_1, \vec{s}_2)$  separated by  $(s_{\parallel}, s_{\perp})$  as  $dP = \bar{n}^2 d^3\vec{s}_1 d^3\vec{s}_2 (1 + \xi^s(s_{\parallel}, s_{\perp}))$  with  $\bar{n}$  the galaxy mean density. Then the so-called streaming model will assume that  $dP = \bar{n}^2 d^3\vec{s}_1 d^3\vec{s}_2 (1 + \xi(r)) F(v) \delta^D(r_{\perp} - y - \frac{y}{r} v_{12}(r) - v) dv dy$ , where  $r^2 = r_{\parallel}^2 + y^2$  is the separation in real space and  $v_{12}(r)$  is the mean relative peculiar velocity of the two galaxies, i.e. the infall pairwise velocity. Integrating over  $y$  and  $v$  (which are unobserved quantities) gives the streaming model (Peebles, 1980, Peebles, 1993):  $\xi^s(s_{\parallel}, s_{\perp}) = \int d^y \xi(r) F(r_{\perp} - y - \frac{y}{r} v_{12}(r))$ . We now generalize to allow density-velocity couplings, note that we change the notation by replacing  $y$  by  $r_{\parallel}$  (Fisher, 1995; Scoccimarro, 2004):

$$1 + \xi^s(s_{\parallel}, s_{\perp}) = \int d_{\parallel}^r (1 + \xi(r)) \mathcal{P}(r_{\parallel} - s_{\parallel}, v_{12}, \sigma_{12}). \quad (1.164)$$

This probability distribution function  $\mathcal{P}$  can be approximated by a scale-dependent Gaussian centered on  $\mu v_{12}$  (B. A. Reid and White, 2011):

$$\mathcal{P}(r_{\parallel} - s_{\parallel}, v_{12}, \sigma_{12}) = \frac{1}{\sqrt{2\pi\sigma_{12}^2(r, \mu)}} e^{-\frac{(s_{\parallel} - r_{\parallel} - \mu v_{12}(r))^2}{2\sigma_{12}^2(r, \mu)}}, \quad (1.165)$$

where  $\mu = r_{\parallel}/r$ ,  $\sigma_{12}(r)$  is the pairwise dispersion velocity and  $\mu v_{12}(r)$  is the projection of

$v_{12}(r)\hat{r}$  on the line-of-sight, with  $\hat{r}$  the direction vector of the real space separation  $\vec{r}$ :

$$\begin{aligned} v_{12}(r)\hat{r} &= \langle \vec{v}_{12}(\vec{r}) \rangle = \langle (\nu(\vec{x} + \vec{r}) - \nu(\vec{x}))(1 + \delta(\vec{x}))(1 + \delta(\vec{x} + \vec{r})) \rangle, \\ \sigma_{12}(r, \mu) &= \langle (\nu(\vec{x} + \vec{r}) - \nu(\vec{x}))^2 (1 + \delta(\vec{x}))(1 + \delta(\vec{x} + \vec{r})) \rangle. \end{aligned} \quad (1.166)$$

Linear predictions for those quantities are provided in Fisher, 1995 or B. A. Reid and White, 2011. On quasi- or non-linear scales, more complex expressions have to be obtained for  $\xi(r)$ ,  $v_{12}(r)$  and  $\sigma_{12}(r, \mu)$ . Originally those scale dependent function were computed from SPT, mentioned in Section 1.2.4 for the real space clustering. L. Wang et al., 2014 extended the Gaussian streaming (GS) formalism using predictions from Convolution Lagrangian Perturbation Theory (CLPT) that was developed by Carlson et al., 2013 to improve the work from Matsubara, 2008 in Fourier space. This model, i.e. GS+CLPT, is introduced in Chapter 2. The GS+CLPT model works well for scales above  $20 h^{-1}\text{Mpc}/h$ .

White et al., 2015 compared different redshift space models in configuration space, and concluded that most models fitted well the monopole and quadrupole in  $40 < s < 80 \text{ Mpc}$ . GS model provides unbiased measurements above  $25 \text{ Mpc}$ .

However we note that Gaussian approximation for the velocity PDF has some limits. Indeed the real velocity distribution cannot be described by one single PDF but rather multiple ones each corresponding to different scales and angles (Scoccimarro, 2004, de la Torre and Guzzo, 2012, Kuruvilla and Porciani, 2018). Moreover it was shown that the PDF is non-Gaussian, being rather complex with scale dependent skewness and kurtosis (see also Bianchi et al., 2016 that added skewness and kurtosis to the Gaussian). Tinker, 2007 showed that the PDF is determined by the halo local densities of the pair. For a fixed density the PDF is closer to a Gaussian. To overcome these issues a solution would be to pull information from N-body simulations and inject them in the model (see e.g. Pellejero Ibañez et al., 2022 for a N-body simulation based model).

### Redshift space distortions

This space modification brings anisotropies in particular in the two-dimensional clustering,  $\xi(s_{\parallel}, s_{\perp})$ , where isotropy and homogeneity are not anymore observed. The velocity field will deviate the observed density field, accordingly to its direction and strength.

Figure 1.35 illustrates the consequence in the observation that produces the peculiar velocities around spherical overdensities. In the linear regime, over  $60 h^{-1}\text{Mpc}$  scales, we observe a squashing effect in the redshift space due to the radial component of the peculiar velocities, as on these scales the peculiar velocity is much smaller than the Hubble flow. We refer to this this effect as the Redshift Space Distortions (RSD). At the turnaround radius around the overdensity, i.e. largest radius for which we have no expansion from the center, line-of-sight peculiar velocity and Hubble flow cancel out.

At smaller scales, below  $10\text{-}20 h^{-1}\text{Mpc}$ , velocity dispersion inside a dark matter halo produces

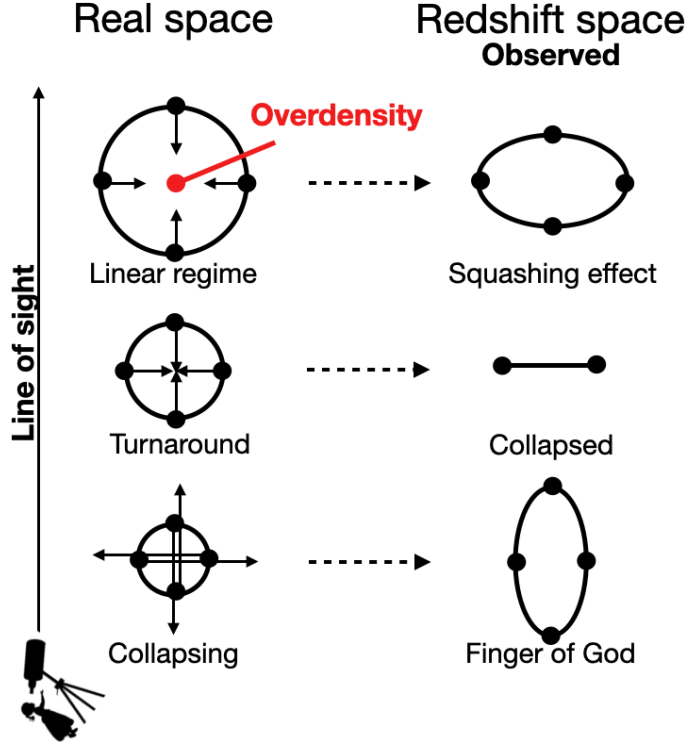


Figure 1.35: Redshift space distortions.

the Finger-of-God, FoG, effect, that causes an elongated distortion on the radial direction (Jackson, 1972)<sup>XXXVII</sup>. This effect can be treated phenomenologically by adding a damping factor on small scales  $D_{\text{FoG}}$  on the power spectrum of Equation 1.155:

$$P^s(k, z) = D_{\text{FoG}}(k, \mu, \sigma_{\text{FoG}}) P_l^s(k, z), \quad (1.167)$$

where  $\sigma_{\text{FoG}}$  is the velocity dispersion on line-of-sight and  $D_{\text{FoG}}$  can be modeled as a noise with different prescriptions (e.g. Peacock and West, 1992):

$$D_{\text{FoG}}(k, \mu, \sigma_{\text{FoG}}) = \begin{cases} e^{-k^2 \mu^2 \sigma_{\text{FoG}}^2}, & \text{for a Gaussian prescription} \\ (1 + \frac{1}{2} k^2 \mu^2 \sigma_{\text{FoG}}^2)^{-1}, & \text{for a Lorentzian prescription.} \end{cases} \quad (1.168)$$

Figure 1.36 shows the two-dimension correlation function of the ELG sample of eBOSS. RSD are well visible. A clear squashing effect can be observed. FoG are not completely distinguishable but we can guess them at the very center of the plot for small separations, where a small elongated pattern on the  $r_{\parallel}$  direction can be seen. Moreover BAO is also detectable. It manifests itself as the excess density ring around  $100 h^{-1} \text{Mpc}$  from the center.

<sup>XXXVII</sup>We note that FoG effect causes a suppression of  $\xi^s(s, \mu)$  on small scales, while RSD enhance the clustering on large scales.

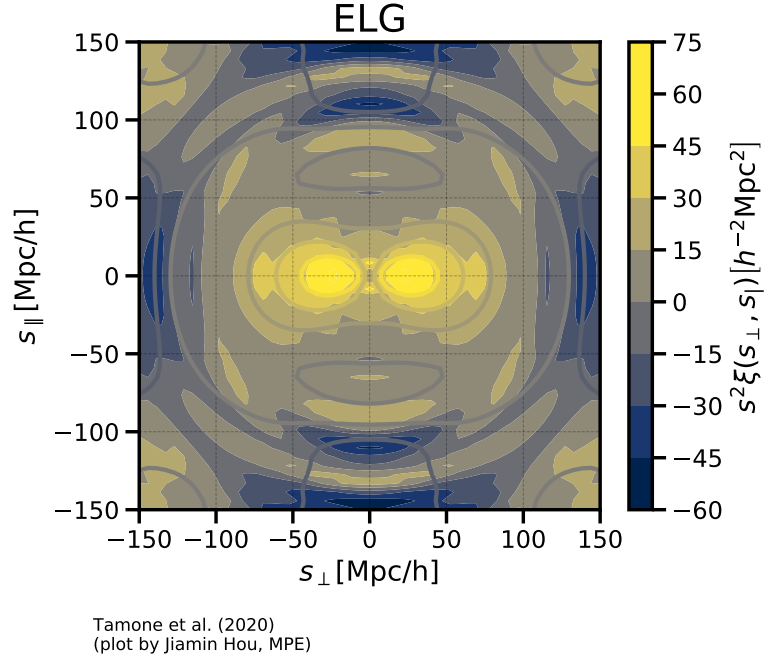


Figure 1.36: Two-dimensional clustering of the ELG sample of eBOSS used for the RSD analysis in configuration space. An excess ring density is seen around  $s \approx 100 h^{-1} \text{Mpc}$  that corresponds to the BAO feature. Moreover we can see an overall squashing effect on large scales due to RSD. On small scales (about  $s_{\perp} < 2 h^{-1} \text{Mpc}$ ) an elongated effect in the radial direction is observed that is called FoG. (Credits of the figure: Jiamin Hou, MPE, and Tamone et al., 2020.)

### 1.3.4 Spectroscopic Surveys

BAO or RSD measurements on clustering of galaxies allow to constrain cosmological measurements with high precision. However one limiting factor in the measurement precision is statistical. To reduce the statistical errors, i.e. suppress cosmic variance, large volume fractions of the Universe are required. To reduce shot noise contamination a sufficiently large number density is also required. We note moreover that systematics errors can also limit the final accuracy of the measurements.

By observing the redshifts of galaxies, spectroscopic surveys aim at creating three-dimensional maps of the Universe, allowing precise clustering measurements to obtain RSD and BAO parameters in order to constrain the cosmological models.

#### Brief overview vocabulary

Here a small guideline/timeline of how a spectroscopic surveys is conducted to introduce some of the vocabulary (Percival, 2013).

In order to use LSS for cosmology a very large amount of data over a very wide range is needed.

This is the goal of spectroscopic surveys which aim to collect a large amount of spectra from a selection of targets covering a large area over a certain redshift range. First step is thus to perform a target selection using a photometric surveys that provides imaging in different bands. Each different type of target (e.g. different types of galaxies, quasars) is selected according to different criteria, such as color magnitude cuts, to obtain a complete and abundant sample within a redshift range estimated from photometry, i.e. photometric redshifts. Then those targets are observed through spectroscopy to get their spectra. Comparing them with known and expected position of their spectral lines, we obtain their corresponding redshifts. Finally assuming a fiducial cosmology their redshifts and angular positions are converted to get their 3D positions and gathered in a catalog of positions. Observations from the survey delimit a certain window of the Universe (not only where are the observed galaxies). This window is defined by an angular survey mask from the observed area, i.e. from the survey footprint, and a radial distribution.

We want afterward to estimate the observed density from those 3D maps. To correct for non-cosmological fluctuations different weights are applied to each galaxy (such as fiber collisions (physical size of fibers), redshift failures, angular photometric systematics (e.g. galaxy extinction, stellar density, depth)). A weight is also usually assumed to optimize the clustering amplitude, by balancing the shot noise and cosmic variance<sup>xxxviii</sup> (i.e. minimize the cosmic error, (Bernardeau et al., 2002)). There are different effects causing cosmic error (which arises as the real density is not exactly equal to the averaged observed one): cosmic variance produced as a consequence of the fact that we have access to a finite volume<sup>xxxix</sup>, edge effects partially corrected by assigning a smaller weights to galaxies closer to the edges, effects due to the fact that the observed tracer is discrete<sup>xl</sup>. We note that the effective volume defined for example in B. Reid et al., 2016 is smaller than the actual survey volume.

To evaluate the clustering from the catalogs, a random catalog, with number density  $n_r(\vec{x})$ , is needed. Galaxies from this random catalog are sampled following a Poisson distribution capturing the survey radial function and with the same angular mask as the survey, i.e. it accounts for the selection function of the survey  $W(\vec{r})$ , containing  $\alpha$  times the number of object compared to the data catalog that has number density  $n_g(\vec{x})$ . The true selection function is however difficult to evaluate and therefore the mean density  $\bar{n}$  is computed from the observed data, i.e. a finite volume. This means that the integral of the density over the survey area is artificially set to 0 to ensure  $\delta(0) = 0$ . This leads to a (global) integral constraint (Peacock and Nicholson, 1991, Wilson et al., 2017, Beutler et al., 2017, de Mattia and Ruhlmann-

<sup>xxxviii</sup>For a tracer from survey with number density  $n$  and power spectrum at a fixed scale  $P_0$ , i.e. bias dependent, if the quantity  $nP_0 \ll 1$ , it indicates that the sample is shot noise (i.e. Poisson noise that can be modelled by a Poisson law, see footnote XL) dominated. If the quantity  $nP_0 \gg 1$ , it indicates that the sample is dominated by cosmic variance.

<sup>xxxix</sup>For a survey of size  $L$ , finite volume effects roughly scale with the correlation average  $\bar{\xi}(L)$ . Larger volume usually means better constraints but not only as seen in footnote xxxviii.

<sup>xl</sup>Under the assumption that the discrete distribution follows a Poisson law, discreteness effects are proportional to  $1/N_g$ , where  $N_g$  is the number of galaxies in the catalog (see Bernardeau et al., 2002 for more details). Moreover we note that the expectation number of galaxies in a volume  $v$  with an average density  $\bar{n}_g$  is  $\bar{N}_g = \bar{n}_g v$ .



Kleider, 2019).

The power spectrum can be obtained by defining the overdensity field  $F(\vec{x}) = n_g(\vec{x}) - n_r(\vec{x})/\alpha$ , we have (Feldman et al., 1994):

$$\langle |F(\vec{k})|^2 \rangle = \int \frac{d^3 k'}{(2\pi)^3} (P(\vec{k}') - P(0)\delta^D(\vec{k}')) |W(\vec{k} - \vec{k}')|^2 + (1 + \frac{1}{\alpha}) \int d^3 x \bar{n}(\vec{x}), \quad (1.169)$$

where the last term on the left corresponds to the shot noise  $P_{\text{SN}}$  (see footnote XL) and  $W(\vec{k})$  is the Fourier transform of the window function:  $W(\vec{k}) = \int d^3 x \bar{n}(\vec{x}) e^{i\vec{k}\vec{x}}$ . The term  $P(\vec{k}') - P(0)\delta^D(\vec{k}')$  is to ensure that the observed power spectrum is zero at  $k = 0$ , i.e.  $P_{\text{obs}}(0) = 0$  (Peacock and Nicholson, 1991, Wilson et al., 2017). Therefore the multipoles of the observed power spectrum can be estimated from  $F(\vec{k})$  (Yamamoto et al., 2006).

To obtain the correlation function, we use estimators relying on the pair counts in the different catalogs, such as  $DD(r)$ ,  $RR(r)$ ,  $DR(r)$  which are respectively the normalized (over the total number of pairs) data-data, random-random, data-random pair counts within a bin centered in  $r$ . An estimate of  $\xi(r)$  is:

$$\xi(r) = \frac{DD(r)}{RR(r)} - 1. \quad (1.170)$$

Other estimators exist such as the very used Landy-Szalay estimate (Landy and Szalay, 1993). We note that they are still affected by the integral constraint. Legendre multipoles are obtained by integrating over  $\mu$  and weighting with Legendre polynomials. Wedges are obtained by weighting with  $\mu$  top-hat windows (Kazin et al., 2012).

### Timeline of dark energy experiments

In 2006, the Dark Energy Task Force, DETF (Albrecht et al., 2006) defined a categorization of the different experiments dedicated to the discovery of the dark energy nature. They described the surveys and the research associated into four stages focusing on Supernovae projects, BAO, weak lensing and galaxy clusters.

Stage I regroups all projects related to dark energy completed by the time of DETF, so prior 2005. Stage-II were the on-going projects in 2005 so lasted until about 2008. Together it includes the data used for first BAO detection from Sloan Digital Sky Survey, SDSS-I and SDSS-II data (Eisenstein et al., 2005, Percival et al., 2010) or the 2 degree Field Galaxy Redshift Survey (2dFGRS, Cole et al., 2005). Weak lensing or supernovae analysis were led for example within Canada-France-Hawaii Telescope Legacy Survey (CFHTLS) programs (Conley et al., 2011, Haiman et al., 2001), or Hubble Space Telescope (HST, Riess et al., 2007). Overall results over this period from different probes combined, including with WMAP (Bennett et al., 2003, Hinshaw et al., 2013) CMB data, are consistent with a flat Universe,  $\Omega_{\Lambda} \sim 0.75$  and  $w \sim \pm 0.1$  with a precision of 1-2 sigma.

Stage III is currently coming to an end, with most the projects completed or close to an end. For BAO and RSD, up to now the completed spectroscopic survey with the largest amount of observations is the Baryon Oscillation Spectroscopic Survey (BOSS, Dawson et al., 2013) part of SDSS-III, extended a few years later in SDSS-IV (Blanton et al., 2017) by the extended Baryon Oscillation Spectroscopic Survey (eBOSS, Dawson et al., 2016) which observed targets at higher redshifts. The Dark Energy Survey (DES) is a photometric survey that ran from 2013 to 2019 (Omori et al., 2019, DES Collaboration et al., 2022). Along others there are also WiggleZ (Blake, Davis, et al., 2011), Subaru (Okumura et al., 2016), 6dFGRS (Beutler et al., 2012), KIDs (Kuijken et al., 2019), or GAMA (Driver et al., 2009). This period had for CMB the measures of Planck satellite which presents the tightest constraints to date (Planck Collaboration et al., 2020). In particular, I will present in more detail in Chapter 2 the final cosmological results of SDSS for clustering analysis and combined with different other probes.

We are now in the Stage IV for which the results are not yet ready or published. It includes all new generation surveys which has just started. The Dark Energy Spectroscopic Instrument (DESI, DESI Collaboration and et al., 2016, DESI Collaboration et al., 2016) at the 4m-Mayall telescope, has started taking data a bit more than one year ago. It plans to observe more than 35 million objects up to redshift 3.5, allowing sub-percent level measurements. The James Webb Space Telescope (Gardner et al., 2006) was launched a few months ago. The Large Synoptic Survey Telescope (LSST) will observe its first light very soon (Ivezić et al., 2019). The ESO 4-metre Multi-Object Spectroscopic Telescope (4MOST, de Jong et al., 2012) will start to take data in the very near future. Euclid space mission (Laureijs et al., 2011) is planned to be launched in 2023, designed in particular for weak lensing.

It can now be extended to stage V and VI (Karkare et al., 2022) with future experiments in the medium-future or longer term projects (see also for overviews of dark energy status and future optics e.g. Annis et al., 2022, Flaugher et al., 2022, Ferraro et al., 2022), such as CMB-S4 (Abazajian et al., 2019), the LIGO Voyager or Explorer (Collaboration, 2016), a possible extension of DESI-II (D. J. Schlegel et al., 2022), MegaMapper (D. Schlegel et al., 2019, D. J. Schlegel et al., 2022) or the Square Kilometre Array (SKA, Huynh and Lazio, 2013).

## SDSS Instrument

A telescope located at the Apache Point Observatory (AOP) in New Mexico USA at an altitude of 2800m was build by the SDSS collaboration, ready to collect data in 1998 (York et al., 2000). The telescope has an aperture of 2.5m with a wide field of view of  $3^\circ$  with a focal ratio of  $f/5^{\text{XLI}}$  (Gunn et al., 2006). It was also designed to be able to take imaging and spectroscopic observations by a replacement of the mounted imaging camera by a fiber plate, as the spectrographs were already in place. It is a Ritchey-Chrétien telescope with a primary mirror of 2.5m diameter, a focal ratio of  $f/2.25$  and a central opening of 1.17m diameter in the primary mirror. The secondary mirror located at 3.6m from the primary one has a diameter of 1.08m.

<sup>XLI</sup>The focal ratio is the focal length divided by the aperture diameter.

Figure 1.37 displays a schematic view of the SDSS telescope.

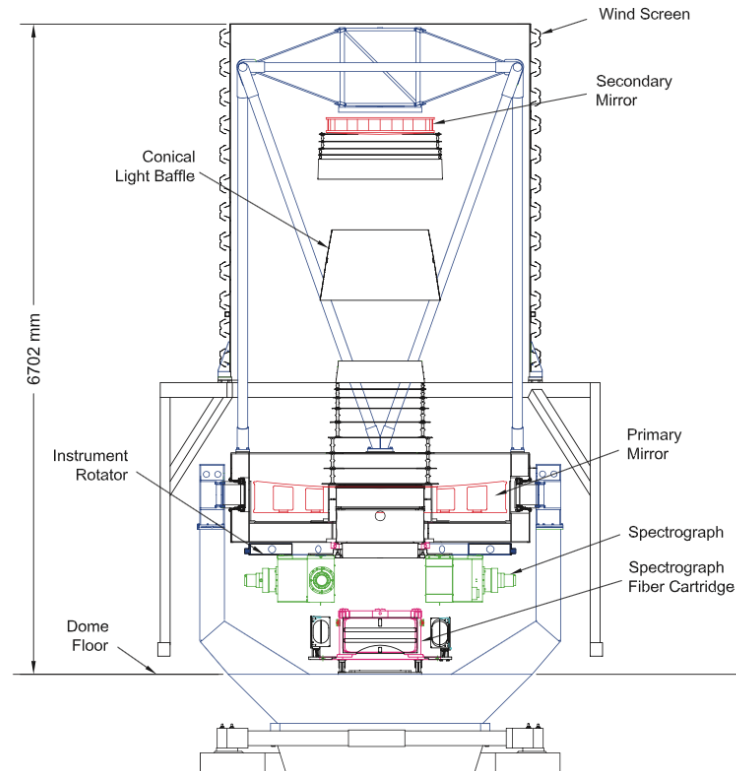


Figure 1.37: SDSS telescope scheme. (Credits of the figures: Smee et al., 2013.)

The imaging camera used for photometric survey of SDSS is composed of an array of CCDs<sup>XLII</sup> of 5 rows and 6 columns, with each rows assigned to one filter ordered as  $r$ ,  $i$ ,  $u$ ,  $z$ ,  $g$  with effective wavelengths of 3590Å, 4810Å, 6230Å, 7640Å and 9060Å, respectively (Gunn et al., 1998).

After SDSS-I and II, spectrographs were redesigned to meet BOSS requirements (Smee et al., 2013). The BOSS instrument is formed of two-arms spectrographs that orient the light toward two cameras, a red and a blue one. In total the spectrographs are composed of 1000 optical fibers with a size of  $120\mu\text{m}$ , i.e.  $\sim 2''$  on the sky, collecting the light in the focal plane. The fibers are maintained by mobile cartridges: the fibers extremity are hand-plugged inside an aluminium plate drilled with the target positions to observe, which in turn is attached to the spectrographs.

### eBOSS and tracers

The extended Baryon Oscillation Spectroscopic Survey, eBOSS, is one of the three experiments of SDSS-IV (Blanton et al., 2017), namely APOGEE-2 (Majewski et al., 2017), eBOSS (Dawson

<sup>XLII</sup> Charged Coupled Device: microchip made of a grid of pixels that collect light and release electrons that are afterward counted.

et al., 2016) and MANGA (Bundy et al., 2015). It was thought as an extension of BOSS, observing data in an unexplored redshift range at the time, with a total redshift range from 0.6 to 3.5, to obtain a more complete expansion history with BAO measurements. Started in 2015, eBOSS collaboration completed its observations in 2019 on the SDSS telescope and released the final cosmological implications gathering the data results from the past 20 years of SDSS in July 2020.

eBOSS three-dimensional map along with the previous BOSS and SDSS-I and II data are shown on Figure 1.38<sup>XLIII</sup>. eBOSS targeted four different tracers: emission line galaxies (ELG), luminous red galaxies (LRG), quasars (QSO), and quasars for Lyman- $\alpha$  forest. On the plot the different tracers have different colors, making clearer the different target redshift ranges. Figure 1.39 shows one example optical spectrum for each tracer of eBOSS.

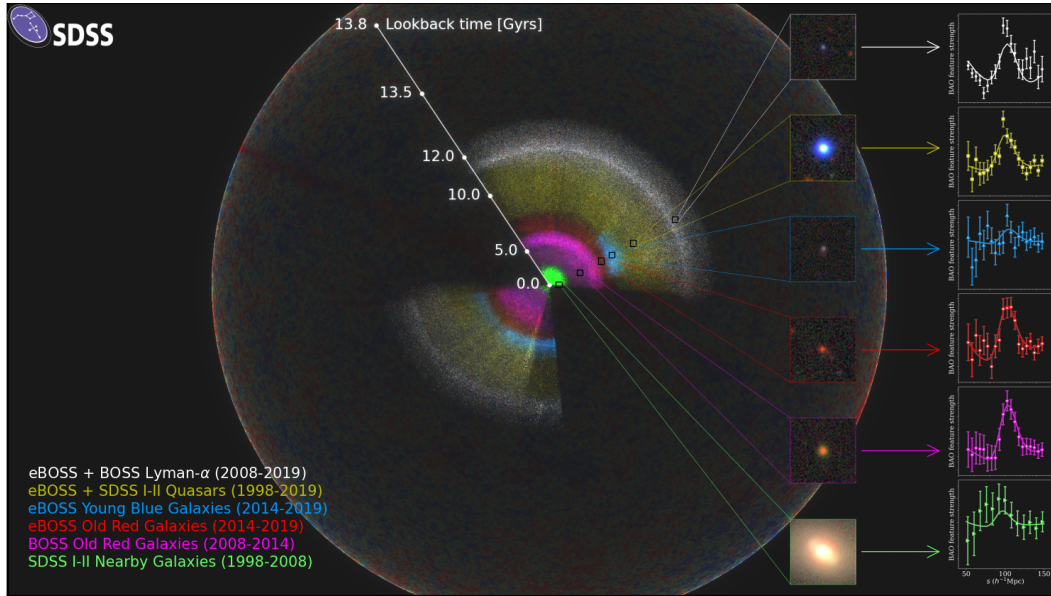


Figure 1.38: LSS map of the observable Universe as observed by SDSS, bounded by the CMB. We are at the center of the map. Each point represents an observation of a galaxy or QSO of SDSS, where each tracer is characterized by a different colour along with the BAO signal in their correlation function. (Credits of the figure: Anand Raichoor, Ashley Ross and the SDSS Collaboration.)

Below I briefly describe the different tracer types, in particular in the context of eBOSS whose statistics are summarized in Table 1.2 (along with BOSS galaxies):

- Luminous Red Galaxy: An environmental dependence was shown to exist for the galaxy properties such as mass, morphology or stellar formation (Postman and Geller, 1984, Kauffmann et al., 2004). Indeed red massive elliptical galaxies reside mainly in massive dark matter halos and they tend to cluster more. Moreover the brightest galaxies in galaxy clusters occupy a

<sup>XLIII</sup> See also the videos from the 2020 eBOSS press release: <https://www.youtube.com/watch?v=KJJXbcf8kxA&t=190s>, <https://www.youtube.com/watch?v=UTiYUxucEZA>.

narrow range of color and intrinsic luminosity (Postman and Lauer, 1995). In addition to have a strong clustering, LRGs also have a relatively high bias that increase the power spectrum amplitude and enhance the BAO signal. These properties make this selected kind of galaxies, namely the LRG, a very good tracer for galaxy clustering.

Target selection of LRG from eBOSS was effectuated by Prakash et al., 2016, using the photometric data of SDSS. eBOSS LRG were selected by color with their magnitude in the  $z$  and  $i$  bands, within a redshift range of  $0.6 < z < 1.0$ . We note that at these redshifts the identifiable spectral absorption feature of LRG at  $4000\text{\AA}$  overlaps with the one from stars<sup>XLIV</sup>. The final data release of eBOSS, DR16, presented a catalog of 377'458 LRGs (Ross et al., 2020) over an area of  $9493 \text{ deg}^2$ . The clustering measurements and BAO and RSD analysis were done in Fourier and configuration space by Gil-Marín et al., 2020 and Bautista et al., 2021, combining also with the high redshifts LRG BOSS sample (Alam et al., 2017).

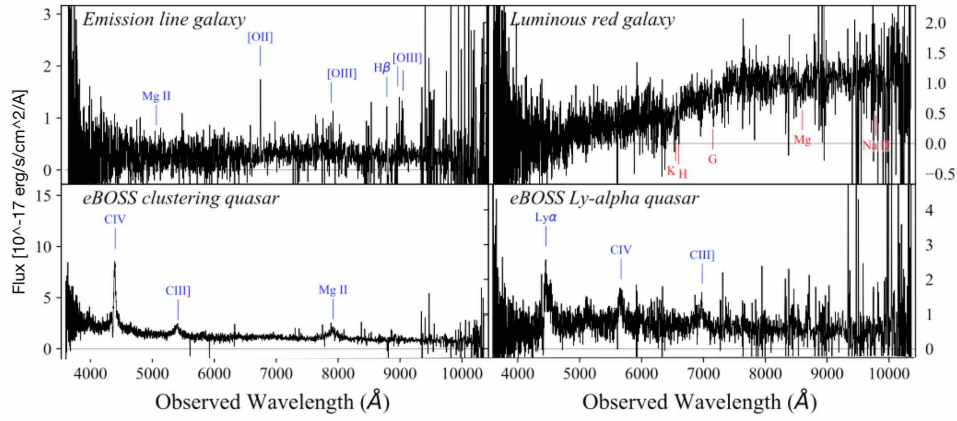


Figure 1.39: Different eBOSS spectra for each of the tracers. (Credits of the figure: Blanton et al., 2017).

- Emission Line Galaxy: ELG are star-forming galaxies, bluer and fainter than LRG, characterized by strong emission lines, in particular the  $O_{II}$  doublet associated with star formation with wavelengths  $3723\text{\AA}$  and  $3729\text{\AA}$  or  $H\alpha$  at  $6563\text{\AA}$ , observable in visible or infrared ranges due to the expansion. These emission lines are very convenient to measure the galaxy spectroscopic redshift requiring a limited amount of exposure time, as in this case the continuum is not necessary. Because of their high star formation density, ELG are abundant in the redshift range of  $0.5 < z < 2.0$  (Madau et al., 1998, Lilly et al., 1996, Madau and Dickinson, 2014) and they present a different favoured environment than LRG. Indeed different physical processes (e.g Gunn and Gott, 1972) could quench the star-formation in massive halos (Kauffmann et al., 2004, Dekel and Birnboim, 2006), moreover it was shown that their distributions in cosmic web is different as LRG are more present in nodes than ELG<sup>XLV</sup> (Q. Guo et al., 2013, Kraljic et al.,

<sup>XLIV</sup>The redshifts of eBOSS LRG and ELG samples were measured with the algorithm REDROCK.

<sup>XLV</sup>We also note that while high mass LRG are almost all central galaxies, this is absolutely not the case for ELG that shows a much larger satellite fraction (Gonzalez-Perez et al., 2018).

2018, Malavasi et al., 2017, Gonzalez-Perez et al., 2018). As a disadvantage it results in a lower amplitude in the ELG clustering than LRG, and thus lower bias, requiring therefore a larger number density to minimize the shot noise, while their low-density environment protect them more from non-linearities (Drinkwater et al., 2010). Nevertheless their observational spectral features and their abundance make them a very good tracer choice. WiggleZ (Blake, Davis, et al., 2011, Blake, Brough, et al., 2011, C. Contreras et al., 2013) was the first survey to make massive ELG observations, followed by eBOSS. Next survey generation will focus on this tracer, as DESI (DESI Collaboration et al., 2016), 4MOST (de Jong et al., 2019) or Euclid (Laureijs et al., 2011).

ELG sample from eBOSS is composed of 173'736 galaxies between redshift  $0.6 < z < 1.1$  within a covering area of  $1170 \text{ deg}^2$ , selected on the  $grz$ -bands (Raichoor et al., 2017) of the DECaLS survey, i.e. the imaging survey of DESI (Dey et al., 2019), allowing a target selection at higher redshift. The clustering results and measurements are presented in Raichoor et al., 2021, Tamone et al., 2020 and de Mattia et al., 2021 in Fourier space.

- Quasars: Quasi-stellar objects, also known as quasars are events discovered in the 1950s as very energetic and luminous radio sources but with a small optical size that can be compared to a star. The first quasar spectrum was observed by Schmidt, 1963 that measured the high redshifts of these objects, surprising with their far distance and thus high luminosity. Theoretical explanation emerged later, by associating the quasars as an extremely luminous subclass of Active Galactic Nuclei (AGN, Lynden-Bell, 1969, Salpeter, 1964). An AGN is a region very compact at the center of a galaxy with a very high non stellar luminosity produced by matter accretion of a supermassive black hole (SMBH). Indeed the black hole is surrounded by a matter accretion disk in which the particles are accelerated. Some relativistic particles are then redirected by the magnetic field forming jets located at the black hole poles. Due to their very high brightness, observation of quasars allow us to reach high redshift ranges.

QSO catalog for the quasar clustering analysis gathered 343'708 objects on a covering area of  $4808 \text{ deg}^2$  and redshift of  $0.8 < z < 2.2$  (Ross et al., 2020), with BAO and RSD measurements made by Neveux et al., 2020 and Hou et al., 2021.

- Lyman- $\alpha$  forest: During its journey to the observer, the light emitted by a quasar<sup>XLVI</sup> will be absorbed by matter on the line-of-sight. As most of the encountered gas cloud from the intergalactic medium are composed mainly of hydrogen, below the wavelength  $(1 + z_{\text{QSO}})\lambda_{\text{Ly}\alpha}$  corresponding to the observed  $\text{Ly}\alpha$  from the quasar, we will observe many spectral absorption lines corresponding to  $\text{Ly}\alpha$  absorption of photons by hydrogen<sup>XLVII</sup> (Gunn and Peterson, 1965). This series of absorption lines is the Lyman- $\alpha$  forest and can be used to infer the neutral hydrogen density along the line of sight, that can in turn be used for clustering (McDonald, 2003, McDonald and Eisenstein, 2007). We note that Lyman- $\alpha$  absorbers used as a tracer has a negative bias.

<sup>XLVI</sup>This is true with any object, however it is more convenient with quasars due to their high observable redshifts, so high distance. The spectral lines are then in the observable spectrum.

<sup>XLVII</sup>As hydrogen  $\text{Ly}\alpha$  transition has the highest cross-section. We note that a  $\text{Ly}\alpha$  absorption make the hydrogen particles pass from ground base  $n = 1$  to its first excited state  $n = 2$ .

du Mas des Bourboux et al., 2020 analysed the BAO signal of the  $\text{Ly}\alpha$  forest of eBOSS with 210'005 quasars used for the  $\text{Ly}\alpha$  absorptions with redshifts higher than 2.1. They also performed a cross-correlation analysis with 341'468 QSO at redshift  $z > 1.77$ .

	LRG	ELG	QSO	QSO ( $\text{Ly}\alpha$ )	BOSS (LOWZ)	BOSS (CMASS)
Redshift range	0.6-1.0	0.6-1.1	0.8-2.2	$>2.1$	0.2-0.5	0.4-0.6
$N_z$	377'458	173'736	343'708	210'005	604'001	686'370

Table 1.2: Redshift ranges and total numbers of good redshifts for the different tracers of eBOSS. From Table 3 of Alam, Aubert, et al., 2021.

## DESI

Located at Kitt Peak in Arizona USA, DESI has started taking data for its five years main survey in May 2021, on the Mayall 4m telescope (see the picture on the left of Figure 1.40). The instrument has a field of view of  $7.5 \text{ deg}^2$ . Instead of the aluminium plate supporting the fibers from SDSS telescope, DESI telescope is provided with 5000 robotic fiber positioners, developed belong others in EPFL that was involved in their construction<sup>XLVIII</sup>, related to the spectrographs were some are shown on the right of Figure 1.40 (DESI Collaboration et al., 2016). The spectrographs have a resolution  $\lambda / \Delta\lambda$  between 2000 and 5500 depending on  $\lambda$ , and are thus able to resolve the  $\text{O}_{II}$  doublet, facilitating ELG redshift measurements.

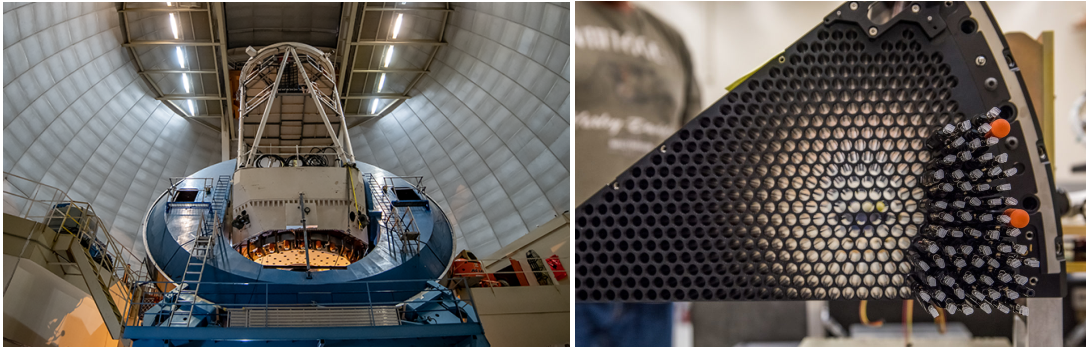


Figure 1.40: DESI instrument and fiber positioners. (Credits of the figures: DESI collaboration.)

DESI survey targets bright galaxies (Bright Galaxy Survey, BGS), LRG, ELG, QSO and QSO for  $\text{Ly}\alpha$  forest, covering an area of  $14'000 \text{ deg}^2$ . Table 1.3 summarizes the goal statistics of the DESI tracers. Comparing with the eBOSS statistics of Table 1.2, DESI will then observed 100 times more ELG than the ELG eBOSS sample and about 3 times LRG more than the total SDSS sample.

The prime goal of DESI is to perform BAO and RSD analysis to constrain the nature of dark energy. Defining the DETF figure of merit Albrecht et al., 2006 that quantifies the measurement

<sup>XLVIII</sup><https://actu.epfl.ch/news/5000-eyes-will-track-the-expansion-of-the-univer-2/>



	BGS	LRG	ELG	QSO	QSO (Ly $\alpha$ )
Redshift range	0.05-0.4	0.4-1.0	0.6-1.6	<2.1	>2.1
$N_z$ [ $\cdot 10^6$ ]	9.8	4.0	17.1	1.7	0.7

Table 1.3: Redshift ranges and expected total number of good redshifts for the different tracers of DESI. From Table 3.1 of DESI Collaboration and et al., 2016.

precision on the parameters of the equation of state of dark energy (see Equation 1.45):

$$FoM_{\text{DETF}} \propto \frac{1}{\sigma(w_p)\sigma(w_a)}. \quad (1.171)$$

DESI forecast constraints on dark energy of state are gathered in Table 1.4 for DESI galaxies and Lyman- $\alpha$  forest and adding (or not) the broadband power spectrum. Adding the broadband, i.e. performing a full-shape fit, up to  $k$  allows AP and RSD measurements instead of just the isotropic shape.

	$FoM_{\text{DETF}}$	$a_p$	$\sigma_{w_p}$
BAO from galaxy	133	0.67	0.023
BAO from galaxy + Ly $\alpha$	169	0.71	0.022
BAO + broadband up to $k < 0.1 \text{ hMpc}^{-1}$	332	0.74	0.015
BAO + broadband up to $k < 0.2 \text{ hMpc}^{-1}$	704	0.73	0.011

Table 1.4: Forecasts of DESI figure of merit  $FoM_{\text{DETF}}$ . The error  $\sigma_{w_p}$  on  $w_p$  is evaluated at  $a_p$  the pivot scale factor which gives the smallest errors. From Table 2.9 of DESI Collaboration and et al., 2016.

DETF figure of merit expected Stage-IV (Stage-III) experiment to improve Stage-II by a factor of 10 (3). Sullivan et al., 2011 combined different Stage-II probes and found a  $FoM_{\text{DETF}}$  of 11. This means that already from galaxy BAO alone the requirements are met, and in the best scenario  $FoM_{\text{DETF}}$  is outpassed by a factor of 7.

While observational systematics treatment in full-shape analysis will be a limiting factor as they will be required to be well understood, the encouraging forecasts promise a very optimistic future.



## 2 RSD analysis of the ELG sample of eBOSS

A lot of this thesis work was part of the data release 16 (DR16) of eBOSS. I was in charge of the RSD analysis of the ELG sample in configuration space. In this context we performed a test of the fitting RSD models we used in Fourier and configuration spaces that we adopted for ELG analysis by participating to a mock challenge. We were then able to provide a systematic error budget coming from the model, assessed with N-body simulations with different Halo Occupation Distribution (HOD) models suited for ELGs. We presented the mock challenge results in Alam, de Mattia, et al., 2021 and Avila et al., 2020.

The ELG sample from eBOSS suffered from strong observational systematics that we were not able to correct, described in Raichoor et al., 2021. In Fourier space those systematics were mitigated using a pixelisation scheme to null the angular modes within each pixel. In configuration space we used a modified correlation function to aim at the same effect. We further used this modified clustering estimator for a multi-tracer analysis of eBOSS LRG and ELG samples, whose results are presented in Y. Wang et al., 2020.

The Fourier space RSD and BAO analysis was presented in de Mattia et al., 2021 and the ELG catalog along with the isotropic BAO measurements in configuration space in Raichoor et al., 2021. We also provided a consensus measurements from the two spaces growth rate and AP parameters. These consensus values were then used along with other tracers constraints for a global cosmological analysis summarizing the last 20 years of SDSS (Alam, Aubert, et al., 2021).

In this chapter I will summarize the cosmological results from eBOSS (Alam, Aubert, et al., 2021) that includes the ELG study. Subsection 2.3 is the ELG RSD analysis paper that I led (Tamone et al., 2020) and that was published in the Monthly Notices of the Royal Astronomical Society (MNRAS) journal in December 2020.

### 2.1 Cosmological Implications of SDSS

I will summarize here some results as presented by the eBOSS collaboration (Alam, Aubert, et al., 2021). The global cosmological analysis considered 8 SDSS samples: the ones presented in

Table 1.2 and Section 1.3.4<sup>I</sup>, plus the Main Galaxy Sample (MGS) from SDSS-I and II (Ross et al., 2015). They are combined with external datasets such as: CMB temperature, polarisation or lensing measurements from Planck (Planck Collaboration et al., 2020), Pantheon SNIa (Scolnic et al., 2018) and DES Year 1 results from clustering and weak lensing (T. M. C. Abbott et al., 2018)<sup>II</sup>.

The eBOSS BAO measurements (with the AP parameters of Equations 1.142 and 1.141) of radial and transverse distance  $D_H(z)$ ,  $D_A(z)$  (equivalent to  $D_M(z)$ ) defined in Equations 1.35 and 1.39 (1.38), and the growth rate  $f\sigma_8(z)$ <sup>III</sup> measured from RSD by eBOSS (see Equation 1.88), are shown on Figure 2.1. They present a good agreement with Planck bestfit predictions.

In the following different extended cosmological models will be tested and mentioned, namely: a flat Universe with cosmological constant  $\Lambda$ CDM (baseline), a free curvature model  $o\Lambda$ CDM (open Universe), a model with free equation of state for a flat Universe  $w\Lambda$ CDM or open  $ow\Lambda$ CDM, a model with its dark energy equation of state parametrized with Equation 1.44 in a flat Universe  $w_0w_a\Lambda$ CDM or open  $ow_0w_a\Lambda$ CDM. We note that all the values presented below are at redshift 0.

### 2.1.1 Constraints from BAO

Using only the information coming from the BAO expansion history of SDSS data<sup>IV</sup> combined with SN and CMB without lensing, we can have strong constraints on the curvature and the dark energy equation of state. We note that BAO data can constrain the matter density  $\Omega_m$ , the curvature parameter  $\Omega_k$  and a combination of the sound horizon and the Hubble parameter  $r_d H_0/c$ . Over a wide redshift range BAO data alone are thus able to constrain these three parameters independently by breaking degeneracies.

Let's first analyse the constraints in an  $o\Lambda$ CDM model. CMB measurements alone favor a negative value of the curvature parameter  $\Omega_k$ , so a closed Universe, while SN and BAO strongly refute this result. Combining the CMB with BAO yields  $\Omega_k = -0.0001 \pm 0.0018$ , which is consistent with a flat geometry. This can be observed in the left panel of Figure 2.2. Middle panel of Figure 2.2 shows the constraints on the dark energy and matter density parameters still in an  $o\Lambda$ CDM model. The CMB  $\Omega_\Lambda$  is strongly degenerate with  $\Omega_m$ , and it can be seen that SN and BAO can help remove this degeneracy once combined.

Relieving the constraint for a cosmological constraint with a  $w\Lambda$ CDM model, CMB measurements are degenerate in the  $w$ - $\Omega_m$  plane with a significant shift in the central values

<sup>I</sup>Note that the Ly $\alpha$  has two samples, the one for their auto-correlation and the one for the cross-correlation with quasars.

<sup>II</sup>We note that lensing measurements give access to growth of structure information, so for BAO constraints only they are not used.

<sup>III</sup>As both parameters are degenerate they are usually measured together.

<sup>IV</sup>We note that in SDSS BAO measurements QSO and Ly $\alpha$  values are included. They are tracers at those redshifts of the matter domination period.

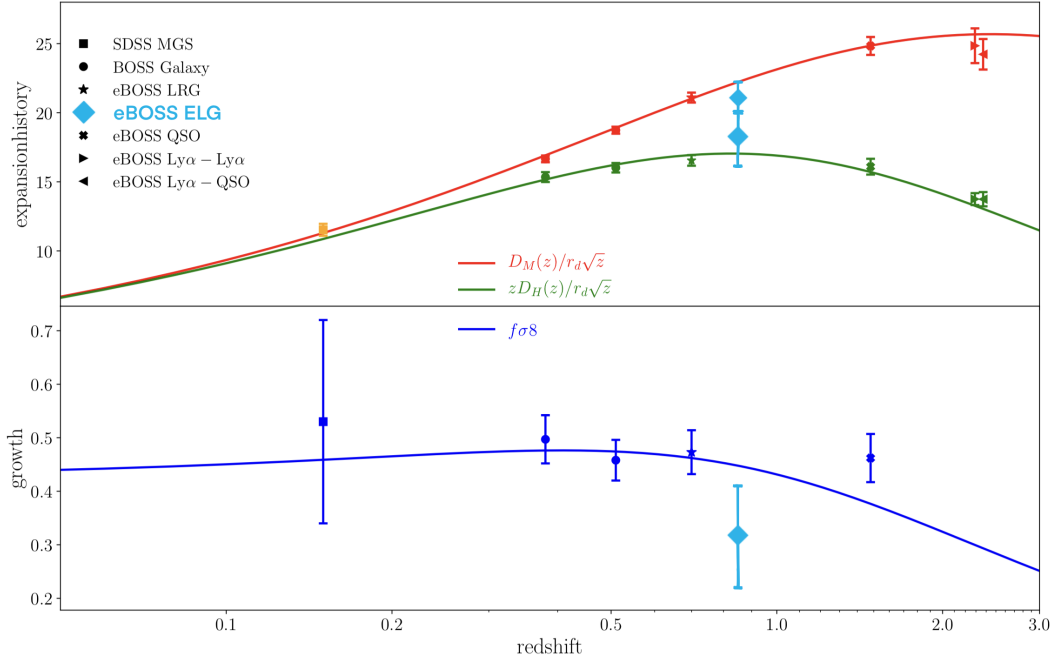


Figure 2.1: Measurements of the expansion history and growth by SDSS collaboration as function of the redshift. Solid lines are Planck predictions for a flat  $\Lambda$ CDM model (Planck Collaboration et al., 2020). The cyan points indicate the contribution of this thesis. (Credits of the figure: Alam, Aubert, et al., 2021).

compared to the  $\phi\Lambda$ CDM model, as can be seen in the right plot of Figure 2.2. CMB value of  $w$  favours a phantom energy. While BAO do not show strong degeneracies, SN degeneracies are orthogonal to CMB contour. Combining the three probes together yields a tight constraint  $w = -1.026 \pm 0.033$  consistent with a cosmological constant.

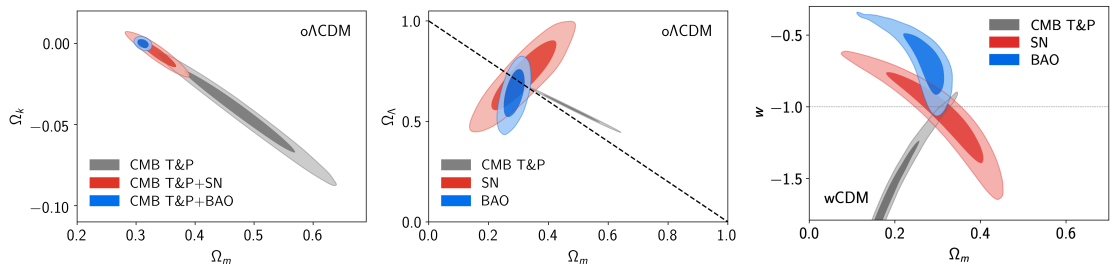


Figure 2.2: 95% and 68% contours for the different probes, relative to the expansion history. From left to right:  $\Omega_k$ - $\Omega_m$  plane in an  $\phi\Lambda$ CDM model,  $\Omega_\Lambda$ - $\Omega_m$  plane in an  $\phi\Lambda$ CDM model and  $w$ - $\Omega_m$  plane in an  $w\Lambda$ CDM model. The lines are the  $\Lambda$ CDM parameters values. (Credits of the figures: Alam, Aubert, et al., 2021).

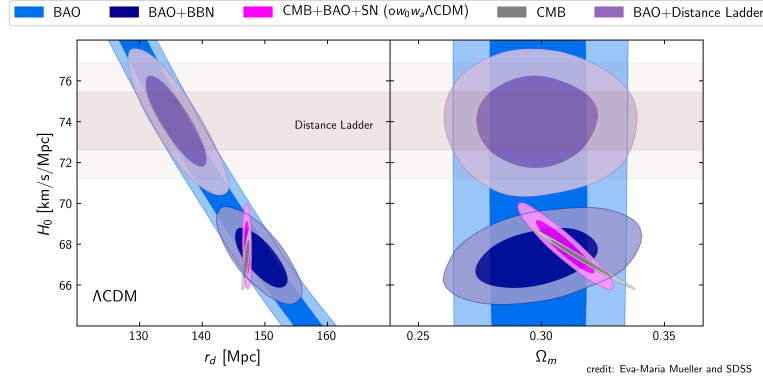


Figure 2.3: Contours in  $\Lambda$ CDM in the  $H_0$ - $r_s$  and  $H_0$ - $\Omega_m$  planes. Distance Ladder corresponds to measurements from Riess et al., 2019, that uses Cepheids to calibrate the SN luminosity distance. (Credits of the figure: Eva Mueller and SDSS Collaboration).

As we have seen in Section 1.3.2, to measure the Hubble parameter  $H_0$  using BAO as an inverse distance ladder extra information from another probe has to be assumed to calibrate the sound horizon  $r_s$ . There are two main options to do it: either using CMB, or to use BBN information (Big Bang nucleosynthesis, see Section 1.1.4) which allows to set constraints on  $\omega_b \equiv \Omega_b h^2$ <sup>V</sup>. Figure 2.3 displays the contours in the  $H_0$ - $r_s$ , noted  $r_d$  in the plot, and  $H_0$ - $\Omega_m$  planes. As expected BAO alone has  $H_0$  completely degenerate with  $r_s$ , however breaking the degeneracy with BBN or CMB gives similar central values for a  $\Lambda$ CDM Universe. The resulting  $H_0$  from BAO is then insensitive to CMB systematics. Moreover we note that BAO can help breaking the CMB strong degeneracy between  $H_0$  and  $\Omega_m$ . In particular when BAO, SN and CMB are combined together within the very free model  $ow_0w_a\Lambda$ CDM, we have a very precise measurement on  $H_0 = 67.61 \pm 0.44$  km/s/Mpc, while CMB alone in this model gives poor constraints. As for CMB alone, this value is still in tension with late-time probes, presenting a  $5\sigma$  tension that therefore cannot be explained by Planck systematic errors nor the strict  $\Lambda$ CDM assumption.

We note that CMB combined with BAO or SN measurements can also help constraining the neutrino masses when leaving free the sum of the neutrinos  $\sum m_\nu$ <sup>VI</sup>, a  $\nu\Lambda$ CDM model. Indeed lighter neutrinos are relativistic at recombination and can thus affect the observations of CMB as it can modify the late-time expansion and  $D_M(r_{\text{rec}})$ , i.e. the angular diameter distance at recombination. The sum  $\sum m_\nu$  is then degenerate for example with  $\Omega_m$  or  $H_0$  and this degeneracy can be broken by bringing later-time measurements as BAO.

<sup>V</sup>In Alam, Aubert, et al., 2021 they used information from Cooke et al., 2018 and Adelberger et al., 2011 to set  $\omega_b = 0.02235 \pm 0.00037$ ,  $\Omega_c$  and  $H_0$  are then let free.

<sup>VI</sup>To include neutrinos, the mass density becomes  $\Omega_m = \Omega_c + \Omega_b + \Omega_\nu$ , where  $\Omega_\nu$  is the neutrino density and  $\Omega_\nu = \frac{\sum m_\nu}{93h^2\text{eV}}$  (Lesgourgues and Pastor, 2006 (eq. 12), Font-Ribera et al., 2014, see also Dolgov, 2002 (eq. 66)). Sometimes the ratio  $f_\nu = \frac{\Omega_\nu}{\Omega_m}$  can be used.

### 2.1.2 Constraints from RSD

Here different measurements from growth are considered, from RSD, from weak lensing (WL) and from CMB lensing.

As previously with the expansion history, we look at growth constraints on curvature within a  $\Lambda$ CDM model. Combined result from growth with CMB measurements of temperature and polarization favors a value consistent with no curvature as can be seen on the top left panel of Figure 2.4 where the combined contour meets the line indicating a flat Universe. The results are mainly driven by WL.

In a  $w$   $\Lambda$ CDM model, adding CMB lensing to CMB constraints does not change the preference of Planck toward a phantom energy<sup>VII</sup>. While WL does not change CMB contours significantly, RSD has a very strong constraining power as the redshift range from 0.2 to 1.1 of SDSS lays constraints on the  $f\sigma_8$  curve shape. The combined contours, with adding RSD, are consistent with a cosmological constant, see top right panel of Figure 2.4.

Similarly to the  $\Lambda$ CDM consistency test of  $H_0$  for expansion history, growth of structure measurements alone can be used to constrain  $\sigma_8$  as a test for this baseline model, by comparing to CMB measurements without lensing. Bottom left plot of Figure 2.4 shows the  $\sigma_8$ - $\Omega_m$  plane. All the different probes present a general consistency.

Within  $\Lambda$ CDM, growth of structure measurements are a powerful tool to test GR. Let's consider the metric FLRW, defined in Equation 1.14, with a scalar perturbation and choosing a Newtonian gauge with a diagonal scalar part of the metric. The perturbed metric is (Bardeen, 1980):

$$ds^2 = a^2(\tau) \left( (1 + 2\Psi) d\tau^2 - (1 - 2\Phi) \gamma_{ij} dx^i dx^j \right), \quad (2.1)$$

where  $\tau$  is the conformal time and  $ad\tau = dt$ , and  $\gamma_{ij}$  is the spatial part of FLRW as can be defined from Equation 1.14. The time perturbation  $\Psi$  and space perturbation  $\Phi$  are the Bardeen potentials. The Poisson Equation 1.52c in Fourier space for the perturbed metric can be written, introducing the parameters  $\mu(a)$  and  $\Sigma(a)$ :

$$\begin{aligned} k^2 \Psi &= -4\pi G a^2 (1 + \mu(a)) \bar{\rho} \delta, \\ k^2 (\Psi + \Phi) &= -8\pi G a^2 (1 + \Sigma(a)) \bar{\rho} \delta. \end{aligned} \quad (2.2)$$

We use the following parametrization for the time dependence of  $\mu(a)$  and  $\Sigma(a)$ , establishing a relation with their values at redshift 0 (T. M. C. Abbott et al., 2019):

$$\mu(a) = \mu_0 \frac{\Omega_\Lambda(a)}{\Omega_{\Lambda,0}}, \quad \Sigma(a) = \Sigma_0 \frac{\Omega_\Lambda(a)}{\Omega_{\Lambda,0}}. \quad (2.3)$$

In the framework of GR those two potentials are identical, i.e.  $\Psi = \Phi$ , and thus  $\mu_0 = \Sigma_0 = 0$ . In

<sup>VII</sup> More negative values of  $w$  means an increasing slower growth on lower redshifts.

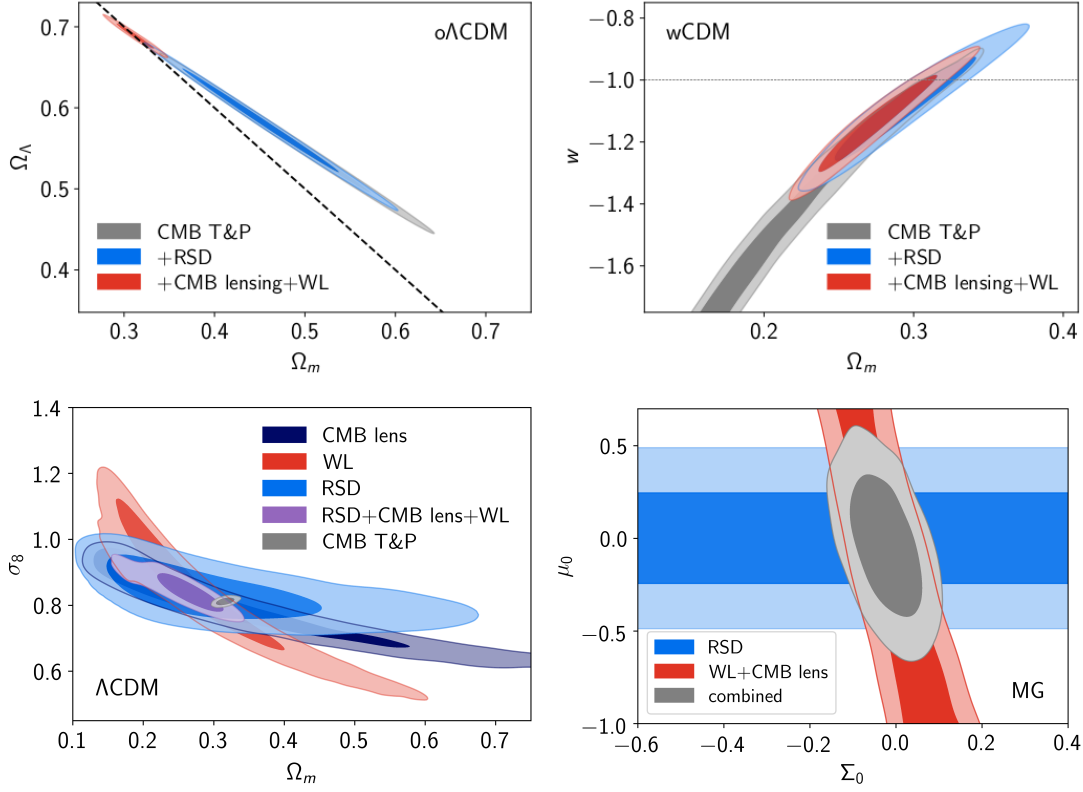


Figure 2.4: Contours relative to the growth constraints from different probes:  $\Omega_\Lambda$ - $\Omega_m$ ,  $w$ - $\Omega_m$ ,  $\sigma_8$ - $\Omega_m$  and  $\mu_0$ - $\sigma_0$  planes. (Credits of the figures: Alam, Aubert, et al., 2021).

the case of a modified gravity (MG) model this is not necessarily true.

Bottom right plot of Figure 2.4 shows the contours on these two parameters. RSD is sensitive to  $\mu_0$  only, as the matter growth depends on the space deviation  $\Psi$ . Lensing constrains mainly  $\Sigma_0$ , as lensing probes the light deviations that depend on  $\Psi+\Phi$ . A combination of both probes is then necessary for degeneracy breaking. The combined results yield  $\mu_0 = -0.04 \pm 0.25$  and  $\Sigma_0 = -0.024 \pm 0.054$ . This is consistent with GR.

### 2.1.3 Global Constraints

From above, we have seen that BAO main constraining power resides in the one parameter extension model  $o\Lambda$ CDM by constraining the curvature, and  $w\Lambda$ CDM model for SN. The growth strength is its ability to observe deviation from GR in a  $\Lambda$ CDM cosmology. We now look at the combination using full-shape fits from SDSS, CMB with lensing, SN and DES WL, shear and clustering. Table 2.1 summarizes the derived cosmological values for the global combination for different cosmological model extensions<sup>VIII</sup>.

<sup>VIII</sup>For  $n_s$  and  $\omega_b$ , priors of Planck are used:  $n_s = 0.96 \pm 0.02$  and  $\omega_b = 0.0222 \pm 0.0005$ , that mainly help constraining  $r_s$ .

	$\Omega_\Lambda$	$H_0$	$\sigma_8$	$\Omega_k$	$w_0$	$w_a$
$\Lambda$ CDM	$0.6959 \pm 0.0047$	$68.19 \pm 0.36$	$0.8073 \pm 0.0056$	-	-	-
$o\Lambda$ CDM	$0.6958 \pm 0.0048$	$68.21 \pm 0.55$	$0.8076 \pm 0.0065$	$0.0001 \pm 0.0017$	-	-
$w$ CDM	$0.6992 \pm 0.0066$	$68.64 \pm 0.73$	$0.8128 \pm 0.0092$	-	$-1.020 \pm 0.027$	-
$ow$ CDM	$0.6997 \pm 0.0069$	$68.59 \pm 0.73$	$0.8127 \pm 0.0091$	$-0.0004 \pm 0.0019$	$-1.020 \pm 0.027$	-
$w_0 w_a$ CDM	$0.6971 \pm 0.0069$	$68.47 \pm 0.74$	$0.8139 \pm 0.0093$	-	$-0.939 \pm 0.073$	$-0.31^{+0.28}_{-0.24}$
$ow_0 w_a$ CDM	$0.6988 \pm 0.0072$	$68.20 \pm 0.81$	$0.8140 \pm 0.0093$	$-0.0023 \pm 0.0022$	$-0.912 \pm 0.081$	$-0.48^{+0.36}_{-0.30}$

Table 2.1: Central values and 68% confidence intervals on cosmological parameters for various extensions of the standard cosmological model, from the combination of SDSS data, DES, Planck and Pantheon SN.

While adding growth constraints to the SDSS expansion history only decreases the errors by 6% within  $o\Lambda$ CDM, in  $w$ CDM the improvement is of 22% as RSD has more constraining power on  $w$ .

Overall the central values of the different cosmological parameters within different models assumptions are all consistent with  $\Lambda$ CDM values. The largest deviation from the standard model is of 0.8% for  $\sigma_8$  within the extended model with three more free parameters,  $ow_0 w_a$ CDM. The increase in uncertainties within  $ow_0 w_a$ CDM compared to  $\Lambda$ CDM represents a factor 1.5 for  $\Omega_\Lambda$  and 2.3 for  $H_0$ .

We note that no improvement is observed passing from a one ( $w$ CDM) to two parameters ( $w_0 w_a$ CDM) equation of state with consistent constraints together and with  $\Lambda$ CDM. It suggests that no critical information is encoded in the additional parameter. In addition letting the curvature free in a  $ow_0 w_a$ CDM model, does not increase the uncertainties in  $w_0$ ,  $w_a$  compared to a flat Universe. Moreover the error on  $\Omega_k$  increases by only 30% compared to a  $o\Lambda$ CDM model. Within  $ow_0 w_a$ CDM the combination of all data is consistent with a  $\Lambda$ CDM model at  $1.1\sigma$  for  $w_0$ ,  $1.3\sigma$  for  $w_a$  and within  $1\sigma$  for  $\Omega_k$ .

To quantify the global contribution of SDSS in the dark energy research, let's have a look at the DETF figure of merit as defined in Equation 1.171. We choose a scale factor in order to have  $w_p$  and  $w_a$  uncorrelated ( $w_p$  is defined in Equation 1.45). It yields the pivot redshift  $z_p = 0.34$  and for the combined data  $w_p = -1.018 \pm 0.028$  and  $w_a = -0.31^{+0.28}_{-0.24}$ , constraining the dark energy of state at an earlier epoch. The time variation parametrization generates minimal changes compared to redshift 0. We can therefore have the figure of merit which is of  $FoM_{\text{DETF}} = 38.4$  within  $w_0 w_a$ CDM model for SDSS and Planck combined. Adding SN and DES increases this number by 3.5, yielding  $FoM_{\text{DETF}} = 134$  within  $w_0 w_a$ CDM model, and  $FoM_{\text{DETF}} = 93$  within  $ow_0 w_a$ CDM model for SDSS+Planck+SN+DES. This result is above the threshold for Stage-III experiments.

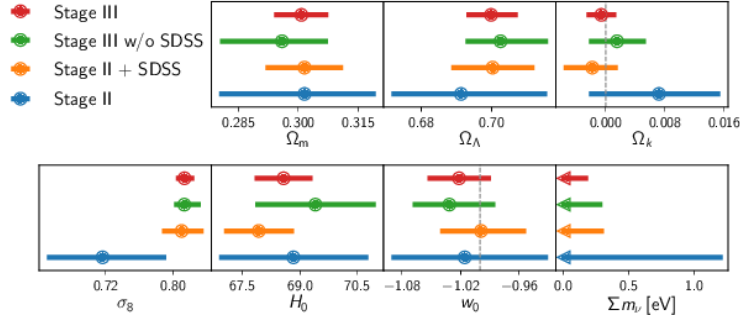


Figure 2.5: Cosmological parameters values for Stage-II and Stage-III experiments with and without SDSS, within a  $\Lambda$ CDM model with free  $\Sigma m_\nu$ . (Credits of the figure: Alam, Aubert, et al., 2021).

Figure 2.5 displays the constraints improvement in the cosmological parameters from Stage-II experiments to Stage-III including SDSS data. The central values are again all compatible. The improvement on the errors is at least from 2.5. In particular it is of 4.5 for the  $\Omega_k$  and 7.0 for  $\sigma_8$ . The LSS role is of great importance and its influence will even increase in the future.

## 2.2 EZmocks

During this thesis I extensively rely on the so-called EZmocks to test the various analysis and compute covariances. In this Section I briefly introduce them by completing the description given in Tamone et al., 2022 (see Chapter 3).

EZmocks are fast approximated mocks relying on the Zel'dovich approximation (ZA; Zel'dovich, 1970). The displacement field of the ZA is generated from a Gaussian random field in a  $5 h^{-1}\text{Gpc}$  box using a grid size of  $1024^3$  with a given initial linear power spectrum. The dark matter density at the wanted redshift is then obtained by moving the dark matter particles directly to their final positions. Thereafter the simulation box is populated with targets (galaxies or quasars) using an effective galaxy bias model calibrated onto the data clustering measurements (Chuang et al., 2015; C. Zhao et al., 2021). It describes the relationship between the dark matter density field  $\rho_m$  and the tracer density field  $\rho_t$ . This bias model (Baumgarten and Chuang, 2018; Chuang et al., 2015; C. Zhao et al., 2021) requires a critical density  $\rho_c$  to form dark matter haloes (Percival, 2005), an exponential cut-off  $\rho_{\text{exp}}$  (Neyrinck et al., 2014) and a density saturation  $\rho_{\text{sat}}$  for the stochastic generation of haloes:

$$\rho_t = B_s \theta(\rho_m - \rho_c) \rho_{\text{sat}} [1 - \exp(-\frac{\rho_m}{\rho_{\text{exp}}})],$$

$$\text{where } B_s = \begin{cases} 1 + X_\lambda, & \text{if } X_\lambda \geq 0 \\ \exp X_\lambda, & \text{if } X_\lambda < 0 \end{cases} \quad \text{and } \theta(x) = \begin{cases} 1, & \text{if } x \geq 0 \\ 0, & \text{if } x < 0 \end{cases}, \quad (2.4)$$

with  $X_\lambda$  a number generated from a gaussian distribution  $\mathcal{N}(0, \lambda)$  centered at 0 with a standard



deviation  $\lambda$ . Due to degeneracies with the other parameters,  $\lambda$  and  $\rho_{\text{sat}}$  are both fixed to 10.

The mocks are then populated following a probability distribution function (PDF)  $P(n_t) = Ab^{n_t}$ ,  $n_t$  being the number of tracers per grid cell,  $b$  is a free parameter, and the parameter  $A$  is constrained with the number density of QSOs in the box. Moreover the random motions are accounted for using a vector  $X_v$  generated from a 3D gaussian distribution  $\mathcal{N}(0, v)$ , the peculiar velocity becomes:  $u_t = u_{\text{ZA}} + X_v$ , where  $u_{\text{ZA}}$  is the linear peculiar velocity in the ZA Bernardeau et al., 2002. In total there are 4 free parameters, namely  $\rho_c$ ,  $\rho_{\text{exp}}$ ,  $b$  and  $v$ , that were calibrated to the data.

### **2.3 Preprint version: “The completed SDSS-IV extended baryon oscillation spectroscopic survey: growth rate of structure measurement from anisotropic clustering analysis in configuration space between redshift 0.6 and 1.1 for the emission-line galaxy sample”**

# The Completed SDSS-IV extended Baryon Oscillation Spectroscopic Survey: Growth rate of structure measurement from anisotropic clustering analysis in configuration space between redshift 0.6 and 1.1 for the Emission Line Galaxy sample

Amélie Tamone<sup>1\*</sup>, Anand Raichoor<sup>1</sup>, Cheng Zhao<sup>1</sup>, Arnaud de Mattia<sup>2</sup>, Claudio Gorgoni<sup>1</sup>, Etienne Burtin<sup>2</sup>, Vanina Ruhlmann-Kleider<sup>2</sup>, Ashley J. Ross<sup>3</sup>, Shadab Alam<sup>4</sup>, Will J. Percival<sup>5,6,7</sup>, Santiago Avila<sup>8,9</sup>, Michael J. Chapman<sup>5,6</sup>, Chia-Hsun Chuang<sup>10</sup>, Johan Comparat<sup>11</sup>, Kyle S. Dawson<sup>12</sup>, Sylvain de la Torre<sup>13</sup>, Héliou du Mas des Bourboux<sup>12</sup>, Stephanie Escoffier<sup>13</sup>, Violeta Gonzalez-Perez<sup>14,15</sup>, Jiamin Hou<sup>11</sup>, Jean-Paul Kneib<sup>1,13</sup>, Faizan G. Mohammad<sup>5,6</sup>, Eva-Maria Mueller<sup>16</sup>, Romain Paviot<sup>13</sup>, Graziano Rossi<sup>17</sup>, Donald P. Schneider<sup>18,19</sup>, Yuting Wang<sup>20</sup>, Gong-Bo Zhao<sup>20,21,15</sup>

<sup>1</sup> Institute of Physics, Laboratory of Astrophysics, Ecole Polytechnique Fédérale de Lausanne (EPFL), Observatoire de Sauverny, 1290 Versoix, Switzerland

<sup>2</sup> IRFU, CEA, Université Paris-Saclay, F-91191 Gif-sur-Yvette, France

<sup>3</sup> Center for Cosmology and AstroParticle Physics, The Ohio State University, Columbus, OH 43212

<sup>4</sup> Institute for Astronomy, University of Edinburgh, Royal Observatory, Blackford Hill, Edinburgh, EH9 3HJ, UK

<sup>5</sup> Waterloo Centre for Astrophysics, University of Waterloo, Waterloo, ON N2L 3G1, Canada

<sup>6</sup> Department of Physics and Astronomy, University of Waterloo, 200 University Ave W, Waterloo, ON N2L 3G1, Canada

<sup>7</sup> Perimeter Institute, Waterloo, ON N2L 2Y5, Canada

<sup>8</sup> Universidad Autónoma de Madrid, 28049, Madrid, Spain

<sup>9</sup> Instituto de Física Teórica UAM/CSIC, Universidad Autónoma de Madrid, 28049 Madrid, Spain

<sup>10</sup> Kavli Institute for Particle Astrophysics and Cosmology, Stanford University, 452 Lomita Mall, Stanford, CA 94305, USA

<sup>11</sup> Max-Planck-Institut für extraterrestrische Physik (MPE), Giessenbachstrasse 1, D-85748 Garching bei München, Germany

<sup>12</sup> University of Utah, Department of Physics and Astronomy, 115 S 1400 E, Salt Lake City, UT 84112, USA

<sup>13</sup> Aix Marseille Univ, CNRS, CNES, LAM, Marseille, France

<sup>14</sup> Astrophysics Research Institute, Liverpool John Moores University, 146 Brownlow Hill, Liverpool L3 5RF, UK

<sup>15</sup> Institute of Cosmology & Gravitation, University of Portsmouth, Dennis Sciama Building, Burnaby Road, Portsmouth PO1 3FX, UK

<sup>16</sup> Department of Physics, University of Oxford, Denys Wilkinson Building, Keble Road, Oxford OX1 3RH, U.K.

<sup>17</sup> Department of Physics and Astronomy, Sejong University, Seoul, 143-747, Korea

<sup>18</sup> Department of Astronomy and Astrophysics, The Pennsylvania State University, University Park, PA 16802

<sup>19</sup> Institute for Gravitation and the Cosmos, The Pennsylvania State University, University Park, PA 16802

<sup>20</sup> National Astronomical Observatories of China, Chinese Academy of Sciences, 20A Datun Road, Chaoyang District, Beijing 100012, China

<sup>21</sup> University of Chinese Academy of Sciences, Beijing, 100049, China

Accepted XXX. Received YYY; in original form ZZZ

## ABSTRACT

We present the anisotropic clustering of emission line galaxies (ELGs) from the Sloan Digital Sky Survey IV (SDSS-IV) extended Baryon Oscillation Spectroscopic Survey (eBOSS) Data Release 16 (DR16). Our sample is composed of 173,736 ELGs covering an area of 1170 deg<sup>2</sup> over the redshift range  $0.6 \leq z \leq 1.1$ . We use the Convolution Lagrangian Perturbation Theory in addition to the Gaussian Streaming Redshift-Space Distortions to model the Legendre multipoles of the anisotropic correlation function. We show that the eBOSS ELG correlation function measurement is affected by the contribution of a radial integral constraint that needs to be modelled to avoid biased results. To mitigate the effect from unknown angular systematics, we adopt a modified correlation function estimator that cancels out the angular modes from the clustering. At the effective redshift,  $z_{\text{eff}} = 0.85$ , including statistical and systematic uncertainties, we measure the linear growth rate of structure  $f\sigma_8(z_{\text{eff}}) = 0.35 \pm 0.10$ , the Hubble distance  $D_H(z_{\text{eff}})/r_{\text{drag}} = 19.1^{+1.9}_{-2.1}$  and the comoving angular diameter distance  $D_M(z_{\text{eff}})/r_{\text{drag}} = 19.9 \pm 1.0$ . These results are in agreement with the Fourier space analysis, leading to consensus values of:  $f\sigma_8(z_{\text{eff}}) = 0.315 \pm 0.095$ ,  $D_H(z_{\text{eff}})/r_{\text{drag}} = 19.6^{+2.2}_{-2.1}$  and  $D_M(z_{\text{eff}})/r_{\text{drag}} = 19.5 \pm 1.0$ , consistent with  $\Lambda$ CDM model predictions with Planck parameters.

**Key words:** cosmology : observations – cosmology : dark energy – cosmology : distance scale – cosmology : large-scale structure of Universe – galaxies : distances and redshifts

## 1 INTRODUCTION

For the last 20 years, physicists have known that the expansion of the Universe is accelerating (Riess et al. 1998; Perlmutter et al. 1999), but not why this is happening, although the mechanism has been given a name: dark energy. In the simplest mathematical model, the acceleration is driven by a cosmological constant  $\Lambda$ , inside Einstein's field equations of General Relativity (GR), and this model is referred to as the standard model of cosmology or the  $\Lambda$ CDM model. Precise measurements of the Cosmic Microwave Background (Planck Collaboration et al. 2016), combined with the imprint of the Baryon Acoustic Oscillations (BAO) in the clustering of galaxies (Eisenstein et al. 2005; Cole et al. 2005), in particular for those from the Baryon Oscillation Spectroscopic Survey (BOSS), (Alam et al. 2017) indicate that dark energy contributes 69% of the total content of the Universe, while dark and baryonic matter only contribute 26% and 5% respectively.

Measurements of BAO are only one component of the information available from a galaxy survey. The observed large-scale distribution of galaxies depends on the distribution of matter (which includes the BAO signal), the link between galaxies and the mass known as the bias, geometrical effects that project galaxy positions into observed redshifts and angles, and Redshift-Space Distortions (RSD).

RSD arise because the measured redshift of a galaxy is affected by its own peculiar velocity, a component that arises from the growth of cosmological structure. These peculiar velocities lead to an anisotropic clustering, as first described in the linear regime by Kaiser (1987). In linear theory, the growth rate of structure  $f$  is often parameterised using:

$$f(a) = \frac{d \ln D(a)}{d \ln a} \quad (1)$$

where  $D(a)$  is the linear growth function of density perturbations and  $a$  is the scale factor. In practice, RSD provide measurements of the growth rate via the quantity  $f(z)\sigma_8(z)$ , where  $\sigma_8(z)$  is the amplitude of the matter power spectrum at  $8 h^{-1} \text{Mpc}$  (Song & Percival 2009). In the framework of General Relativity, the growth rate  $f$  is related to the total matter content of the Universe  $\Omega_m$  through the generalized approximation (Peebles 1980):

$$f(z) \simeq \Omega_m(z)^\gamma \quad (2)$$

where the exponent  $\gamma$  depends on the considered theory of gravity and is predicted to be  $\gamma \simeq 0.55$  in GR (Linder & Cahn 2007). Therefore by measuring the growth rate of structure in the distribution of galaxies as function of redshift, we can put constraints on gravity, and test if dark energy could be due to deviations from GR (Guzzo et al. 2008).

BAO and RSD measurements are highly complementary, as they allow both geometrical and dynamical cosmological constraints from the same observations. In addition, BAO measurements break a critical degeneracy affecting RSD measurements: clustering anisotropy arises both due to RSD and also if one assumes a wrong cosmology to transform redshifts to comoving distances. The latter is known as the Alcock-Paczynski (AP) effect (Alcock & Paczynski 1979) and generates distortions both in the angular and radial components of the clustering signal. The AP effect shifts the BAO peak, while leaving the RSD signal unaffected, and hence anisotropic BAO measurements break the AP-RSD degeneracy and enhance RSD measurements.

Using BAO and RSD measurements, spectroscopic surveys of galaxies are now amongst the most powerful tools to test our cosmological models and in particular to probe the nature of dark en-

ergy. Up until now, the most powerful survey has been BOSS (Dawson et al. 2013), which made two  $\sim 1\%$  precision measurements of the BAO position at  $z = 0.32$ , and  $z = 0.57$  (Alam et al. 2017), coupled with two  $\sim 8\%$  precision measurements of  $f\sigma_8$  from the RSD signal. The extended Baryon Oscillation Spectroscopic Survey (eBOSS; Dawson et al. 2016) program is the follow-up for BOSS in the fourth generation of the Sloan Digital Sky Survey (SDSS; Blanton et al. 2017). With respect to BOSS, it explores large-scale structure at higher redshifts, covering the range  $0.6 < z < 2.2$  using four main tracers: Luminous Red Galaxies (LRGs), Emission Line Galaxies (ELGs), quasars used as direct tracers of the density field, and quasars from whose spectra we can measure the Ly $\alpha$  forest. In this paper we present RSD measurements obtained from ELGs in the final sample of eBOSS observations: Data Release 16 (DR16). Using the first two years of data released as DR14 (Abolfathi et al. 2018), BAO and RSD measurements have been made using the LRGs (Bautista et al. 2018; Icaza-Lizaola et al. 2019) and quasars (Ata et al. 2018; Gil-Marín et al. 2018; Zarrouk et al. 2018), but not the ELG sample, which was not complete for that data release.

The eBOSS ELG sample, covering  $0.6 < z < 1.1$ , is fully described in Raichoor et al. (2020). As well as allowing high redshift measurements, this sample is important because it is a pathfinder sample for future experiments as DESI (DESI Collaboration et al. 2016a,b), *Euclid* (Laureijs et al. 2011), PFS (Sugai et al. 2012; Takada et al. 2014), or *WFIRST* (Doré et al. 2018) which will also focus on ELGs. We analyse the first three even Legendre multipoles of the anisotropic correlation function to measure RSD and present a RSD+BAO joined measurement. A companion paper describes the BAO & RSD measurements made in Fourier-space (de Mattia et al. 2020), while BAO measurements in configuration space are included in Raichoor et al. (2020). A critical component for interpreting our measurements is the analysis of fast mocks catalogues (Lin et al. 2020; Zhao et al. 2020a). We also use mocks based on N-body simulations to understand the systematic errors (Alam et al. 2020; Avila et al. 2020).

The eBOSS ELG sample suffers from significant angular fluctuations because it was selected from imaging data with anisotropic properties, which imprint angular patterns (Raichoor et al. 2020) such that we cannot reliably use angular modes to measure cosmological clustering. Traditionally, when the modes affected are known they are removed from the measurement either by assigning weights to correct for observed fluctuations (Ross et al. 2011), or by nullifying those modes (Rybicki & Press 1992). In fact, these approaches are mathematically equivalent (Kalus et al. 2016). In the extreme case that we do not know the contaminant modes, one can consider nulling all angular modes. This can be achieved by matching the angular distributions of the galaxies and mask - an extreme form of weighting (Burden et al. 2017; Pinol et al. 2017) or, in the procedure we adopt, by using a modified statistic designed to be insensitive to angular modes.

The ELG studies described above are part of a coordinated release of the final eBOSS measurements of BAO and RSD in all samples including the LRGs over  $0.6 < z < 1.0$  (Bautista et al. 2020; Gil-Marín et al. 2020) and quasars over  $0.8 < z < 2.2$  (Hou et al. 2020; Neveux et al. 2020). For these samples, the construction of data catalogs is presented in Ross et al. (2020); Lyke et al. (2020), and N-body simulations for assessing systematic errors (Rossi et al. 2020; Smith et al. 2020). At the highest redshifts ( $z > 2.1$ ), our release includes measurements of BAO in the Lyman- $\alpha$  forest (du Mas des Bourboux et al. 2020). The cosmological interpretation of all of our results together with those from other

	$z_{\min}$	$z_{\max}$	NGC	SGC	ALL
Effective area [deg <sup>2</sup> ]	-	-	369.5	357.5	727.0
Reliable redshifts	0.6	1.1	83,769	89,967	173,736
	0.7	1.1	79,106	84,542	163,648
Effective redshift	0.6	1.1	0.849	0.841	0.845
	0.7	1.1	0.860	0.853	0.857

**Table 1.** Effective area and number of reliable redshifts per Galactic cap and in the combined ELG sample.

cosmological experiments is found in Collaboration et al. (2020). A SDSS BAO and RSD summary of all tracers measurements and their full cosmological interpretation can be found on the SDSS website<sup>1</sup>.

We summarise the ELG data used in Section 2, and the mock catalogues in Section 3. The analysis method that nulls angular modes, designed to reduce systematic errors is described in Section 4. The model fitted to the data is presented in Section 5. Section 6 validates with the mock catalogues our chosen modelling and the analysis method to reduce angular contamination. Finally, we present our results in Section 7, and conclusions in Section 8.

## 2 DATA

In this Section, we summarise the eBOSS ELG large-scale structure catalogues which are studied in this paper and refer the reader to Raichoor et al. (2020) for a complete description. The eBOSS ELG sample was selected on the *grz*-bands photometry of intermediate releases (DR3, DR5) of the DECam Legacy Survey imaging (DECaLS), a component of the DESI Imaging Legacy Surveys (Dey et al. 2019). This photometry is more than one magnitude deeper than the SDSS photometry. The target selection is slightly different in the two caps, as the DECaLS photometry is deeper in the SGC than in the NGC. The selected targets were then spectroscopically observed during approximately one hour with the BOSS spectrograph (Smee et al. 2013) at the 2.5-meter aperture Sloan Foundation Telescope at Apache Point Observatory in New Mexico (Gunn et al. 2006). We refer the reader to Raichoor et al. (2017) for a detailed description of the target selection and spectroscopic observations.

The catalogues used contain 173,736 ELGs with a reliable spectroscopic redshift,  $z_{\text{spec}}$ , between 0.6 and 1.1, within a footprint split in two caps, the North Galactic Cap (NGC) and South Galactic Cap (SGC). For the spectroscopic observations, each cap is split into two ‘chunks’, which are approximately rectangular regions where the tiling completeness is optimized. Table 1 presents the number of used  $z_{\text{spec}}$  and the effective area, i.e. the unmasked area weighted by tiling completeness, for each cap and for the combined sample; it also reports redshift information if one restricts to  $0.7 < z_{\text{spec}} < 1.1$ , as this range is used in the RSD analysis (see Section 7).

Different weights and angular veto masks are applied to data, to correct for variations of the survey selection function, as described in more details in Raichoor et al. (2020). In particular,

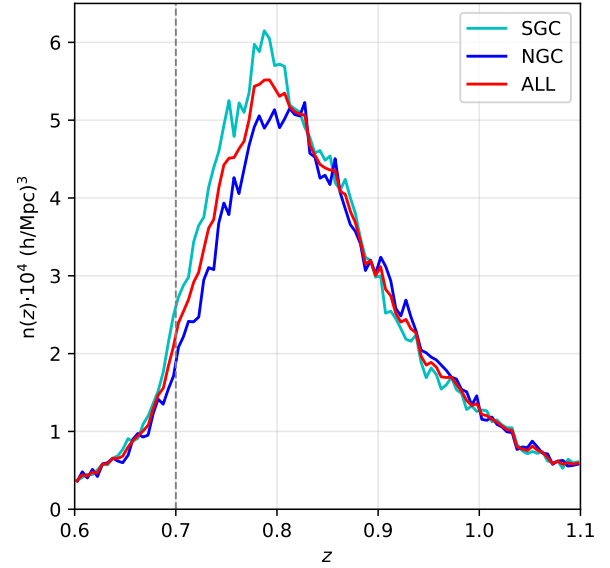


**Figure 1.** Redshift density of the eBOSS ELG sample per Galactic cap and for the combined sample.

weights are introduced to correct for fluctuations of the ELG density with imaging quality (systematic weight  $w_{\text{sys}}$ ), to account for fibre collisions (close-pair weight  $w_{\text{cp}}$ ) and to correct for redshift failures ( $w_{\text{noz}}$  weight). Figure 1 shows the redshift density ( $n(z)$ ) of the ELG sample for the two Galactic caps and the combined sample. The more numerous  $z_{\text{spec}} < 0.8$  ELGs in the SGC is a consequence of the target selection choice to explore a larger box in the  $g-r$  vs.  $r-z$  colour-colour diagram, enabled by the deeper photometry there (Raichoor et al. 2017). As in previous BOSS/eBOSS analyses (e.g. Anderson et al. 2014), we also define inverse-variance  $w_{\text{FKP}}$  weights,  $w_{\text{FKP}} = 1/(1 + n(z) \cdot P_0)$  (Feldman et al. 1994), with  $P_0 = 4000 \text{ h}^{-3} \text{ Mpc}^3$ .

Consistently with the other eBOSS analyses, we define the effective redshift ( $z_{\text{eff}}$ ) of the ELG sample as the weighted mean spectroscopic redshift of galaxy pairs ( $z_i, z_j$ ):

$$z_{\text{eff}} = \frac{\sum_{i,j} w_{\text{tot},i} w_{\text{tot},j} (z_i + z_j)/2}{\sum_{i,j} w_{\text{tot},i} w_{\text{tot},j}}, \quad (3)$$

where  $w_{\text{tot}} = w_{\text{sys}} \cdot w_{\text{cp}} \cdot w_{\text{noz}} \cdot w_{\text{FKP}}$  and the sum is performed over all galaxy pairs between  $25 \text{ h}^{-1} \text{ Mpc}$  and  $120 \text{ h}^{-1} \text{ Mpc}$ . We report in Table 1 the different  $z_{\text{eff}}$  values for the NGC, SGC, and combined sample for  $0.6 < z_{\text{spec}} < 1.1$  and  $0.7 < z_{\text{spec}} < 1.1$ .

A random catalogue of approximately 40 times the data density is created to account for the survey selection function of the weighted data. Angular coordinates of random objects are uniformly distributed and those objects outside the footprint and masks are rejected. Random objects are assigned data redshifts, according to the shuffled scheme introduced in Ross et al. (2012). As described in Raichoor et al. (2020), this was done per chunk, in separate sub-regions of approximately constant imaging depth, in order to account for the fact that targets selected in regions of shallower imaging have lower redshifts on average.

As shown in de Mattia & Ruhlmann-Kleider (2019) and de Mattia et al. (2020), using the shuffled- $z$  scheme leads to the suppression of radial modes and impacts the multipoles of the measured correlation function. This effect has to be modelled, a point we develop in Section 5.2.

<sup>1</sup> <https://www.sdss.org/science/final-bao-and-rsd-measurements/>.  
<https://www.sdss.org/science/cosmology-results-from-eboss/>

Despite the different corrections, the eBOSS ELG sample still suffers from significant angular systematics (see Section 4.1), likely due to unidentified systematics in the imaging data used to select ELG targets, a point further discussed in [de Mattia et al. \(2020\)](#). This triggered our using of the modified correlation function described in Section 4.2 to cancel the angular modes.

### 3 MOCKS

In this Section, we briefly describe the mock catalogues used in the analysis. Those mock catalogues are of two types: approximate mocks to estimate the covariance matrix and validate the pipeline analysis and precise N-body mocks to validate the model.

#### 3.1 EZmocks

A thousand EZmock catalogues for each Galactic cap are used to estimate the covariance matrices for parameter inference. These mocks rely on the Zel'dovich approximation ([Zel'dovich 1970](#)) to generate the dark matter density field, with  $1024^3$  grids in a  $5^3 h^{-3} \text{Gpc}^3$  comoving box. ELGs are then populated using an effective galaxy bias model, which is directly calibrated to the 2- and 3-point clustering measurements of the eBOSS DR16 ELG sample ([Chuang et al. 2015](#); [Zhao et al. 2020a](#)). The cosmology used to generate the EZmocks is a flat  $\Lambda$ CDM model with:

$$h = 0.6777, \Omega_m = 0.307115, \Omega_b = 0.048206, \sigma_8 = 0.8225, n_s = 0.9611 \quad (4)$$

To account for the redshift evolution of ELG clustering, the EZmock simulations are generated with seven redshift snapshots. These snapshots are converted to redshift space, to construct slices with the redshift ranges of (0.6, 0.7), (0.7, 0.75), (0.75, 0.8), (0.8, 0.85), (0.85, 0.9), (0.9, 1.0), and (1.0, 1.1). The slices are then combined, and the survey footprint and veto masks are applied to construct light-cone mocks that reproduce the geometry of the data.

Depending on how the radial and angular distributions of the eBOSS data are migrated to the light-cone mocks, two sets of EZmocks – without systematics and with systematics – are generated. For the mocks *without systematics*, only the radial selection is applied, to mimic the redshift evolution of the eBOSS ELG number density. Moreover, the radial selections are applied separately for different chunks, since their spectroscopic properties are different ([Raichoor et al. 2020](#)). Thus, the only observational effect applied on the angular distribution of the EZmocks without systematics is the footprint geometry and veto masks.

The EZmocks *with systematics*, however, encode observational systematic effects, namely angular photometric systematics, fibre collisions, and redshift failures. For example, a smoothed angular map of galaxy positions is extracted directly from the data, and applied to the mocks. The photometric and spectroscopic effects are then corrected by the exact same weighting procedure as in data (see [de Mattia et al. 2020](#); [Zhao et al. 2020a](#), for details). In particular, mock data redshifts are randomly assigned to mock random catalogues with the ‘shuffled-z’ scheme in chunks of homogeneous imaging depth (using the depth map of the eBOSS data). Moreover, a smoothed angular map of galaxy positions is extracted directly from the data, and applied to the mocks. The photometric and spectroscopic effects are then corrected by the exact same weighting procedure as in data (see [de Mattia et al. 2020](#); [Zhao et al. 2020a](#), for details).

In this study, we further use two variants of the EZmocks with

systematics, which differ in their random catalogues. The redshift distribution of the random objects should reflect the radial survey selection function of the corresponding galaxy catalogue. This can be achieved in two ways, either by sampling the random redshifts based on the true radial selection function  $n(z)$  of data, or by taking directly the shuffled redshifts from the galaxy catalogue. We dub these two schemes ‘sampled-z’ and ‘shuffled-z’, respectively. For the EZmocks with systematics only the ‘shuffled-z’ randoms are used.

#### 3.2 N-body mocks

The eBOSS ELG sample significantly differs from the other eBOSS tracers from a galaxy formation point-of-view. These galaxies are sites of active star formation with various astrophysical processes at play, such as the consumption of gas or the effect of the local environment. This means the kinematical properties of eBOSS ELGs could be different from those of the underlying dark matter haloes. One must thus test the robustness of any cosmological inference against galaxy formation physics. To do so, we tested our model against a wide variety of eBOSS ELG mock catalogues which include accurate non-linear evolution of dark matter and various deviations in galaxy kinematics from the underlying dark matter distribution. These tests are described in detailed in a companion paper [Alam et al. \(2020\)](#). Briefly, we employ two different N-body simulations, the MULTI DARK PLANCK (MDPL2; [Klypin et al. 2016](#)) and the OUTER RIM (OR; [Heitmann et al. 2019](#)).

The MDPL2 simulation provides a halo catalogue produced with the Rockstar halo finder ([Behroozi et al. 2013](#)) in a cubic box of  $1 h^{-1} \text{Gpc}$  using a flat  $\Lambda$ CDM cosmology with parameters:

$$h = 0.6777, \Omega_m = 0.307115, \Omega_b = 0.048206, \sigma_8 = 0.8228, n_s = 0.9611 \quad (5)$$

The OR simulation provides a halo catalogue produced with the Friends of Friends halo finder of [Davis et al. \(1985\)](#) in a cubic box of  $3 h^{-1} \text{Gpc}$  using a flat  $\Lambda$ CDM cosmology with parameters:

$$h = 0.71, \Omega_{\text{CDM}} h^2 = 0.1109, \Omega_b h^2 = 0.02258, \sigma_8 = 0.8, n_s = 0.963 \quad (6)$$

Three different parametrisations for the shape of the mean HOD (Halo Occupation Distribution) of central galaxies are used. The first parametrisation called SHOD is the standard HOD model where at least one central galaxy of a given type is found in massive enough dark matter haloes. Although this model is more appropriate for modelling magnitude or stellar mass selected samples ([Zheng et al. 2005](#); [White et al. 2011](#)), it can be modified to account for the incompleteness in mass of a sample such as the ELG one. The second parametrisation is called HMQ which essentially quenches galaxies at the centre of massive haloes and suppresses the presence of ELGs in the center of haloes, as suggested by observations and models of galaxy formation, and hence should provide more realistic realisation of star-forming ELGs ([Alam et al. 2019](#)). The third parametrisation, called SFHOD, accounts for the incompleteness of the ELG sample by modelling central galaxies with an asymmetric Gaussian ([Avila et al. 2020](#)). Such a shape is based on the results from the galaxy formation and evolution model presented in [Gonzalez-Perez et al. \(2018\)](#). In each of these models, besides the shape of the mean HOD, other aspects have been varied to mimic



different possible baryonic effects over the ELGs distribution such as the satellite distribution, infalling velocities, the off-centring of central galaxies and the existence of assembly bias.

In total 22 MDPL2 mocks were available, with 11 types of mocks for each of the SHOD and HMQ models. OR mocks encompassed 6 out of the 11 same types for each model, and five SFHOD models with assumptions that enhance the parameter space explored by the SHOD and HMQ ones are selected.

As the MDPL2 cosmology is close to our fiducial BOSS cosmology (Equation 7), we use the latter to analyse the MDPL2 mocks. We analyse the OR mocks with their own cosmology (Equation 6). For the covariance matrix, we use an analytical covariance as defined in [Grieb et al. \(2016\)](#).

## 4 METHOD

### 4.1 The two-point correlation function

To compute galaxy pair separations of data and EZmocks, observed redshifts need first to be converted into comoving distances. To do so, we use the same flat  $\Lambda$ CDM fiducial cosmology as in BOSS DR12 analysis ([Alam et al. 2017](#)):

$$h = 0.676, \quad \Omega_m = 0.31, \quad \Omega_\Lambda = 0.69, \quad \Omega_b h^2 = 0.022, \quad (7)$$

$$\sigma_8 = 0.8, \quad n_s = 0.97, \quad \sum m_\nu = 0.06 \text{ eV}$$

Afterwards, in order to quantify the anisotropic galaxy clustering in configuration space, one usually resorts to the two-point correlation function  $\xi$  (2PCF), which is defined as the excess probability of finding a pair of galaxies separated by a certain vector distance  $s$  with respect to a random uniform distribution. In the next Sections, we refer to that 2PCF as the 'standard 2PCF'.

An unbiased estimate  $\hat{\xi}$  of the correlation function  $\xi$  can be computed for a line of sight separation  $s_{\parallel}$  and transverse separation  $s_{\perp}$ , using the [Landy & Szalay \(1993\)](#), LS) estimator:

$$\hat{\xi}(s_{\perp}, s_{\parallel}) = \frac{DD(s_{\perp}, s_{\parallel}) - 2DR(s_{\perp}, s_{\parallel}) + RR(s_{\perp}, s_{\parallel})}{RR(s_{\perp}, s_{\parallel})}, \quad (8)$$

where  $DD$ ,  $DR$ , and  $RR$  are the normalised galaxy-galaxy, galaxy-random, and random-random pair counts, respectively. The pair separation can also be written in terms of  $s$  and  $\mu = s_{\parallel}/s = \cos(\theta)$ , where  $\theta$  is the angle between the pair separation vector  $s$  and the line of sight.

Projecting on the basis of Legendre polynomials, the two-dimensional correlation function is compressed into multipole moments of order  $l$  ([Hamilton 1992](#)):

$$\xi_\ell(s) \equiv \frac{2\ell + 1}{2} \int_{-1}^1 d\mu \xi(s, \mu) P_\ell(\mu) \quad (9)$$

$$= \frac{2\ell + 1}{2} \int_0^\pi d\theta \sqrt{1 - \mu^2} \xi(s_{\perp}, s_{\parallel}) P_\ell(\mu)$$

where  $P_\ell(\mu)$  is the Legendre polynomial of order  $\ell$ .

Equations 9 are integrated over a spherical shell of radius  $s$ , while measurements of  $\hat{\xi}(s_{\perp}, s_{\parallel})$  are performed in bins of width  $\Delta s$  in  $s_{\perp}, s_{\parallel}$ . Converting the last integral in Equation 9 to sums over bins leads to the following definition of the estimated multipoles of the correlation function ([Chuang & Wang 2013](#)):

$$\hat{\xi}_\ell(s) \equiv \frac{(2\ell + 1)\pi}{2} \sum_{i=1}^n \sqrt{1 - \mu_i^2} \hat{\xi}(s_{\perp}^i, s_{\parallel}^i) P_\ell(\mu_i) \quad (10)$$

where the sum extends over  $n$  bins in  $s_{\perp}, s_{\parallel}$  obeying:

$$s - \frac{\Delta s}{2} < \sqrt{s_{\parallel}^2 + s_{\perp}^2} < s + \frac{\Delta s}{2}$$

We use the public code CUTE ([Alonso 2012](#)) to evaluate the LS estimator of the correlation function from the data and FCFC code (fast correlation function calculator; [Zhao et al. 2020b](#)) for the mocks: both codes provide consistent measurements. For both mocks and data, we then compute the first even multipoles,  $\hat{\xi}_0, \hat{\xi}_2$  and  $\hat{\xi}_4$ , in bins of width  $\Delta s = 8 h^{-1} \text{Mpc}$  for each cap separately. The combined multipoles over both caps, referred as ALL, are computed by averaging the NGC and SGC multipoles, weighted by their respective effective areas,  $A_{\text{NGC}}$  and  $A_{\text{SGC}}$ :

$$\hat{\xi}_\ell^{\text{ALL}}(s_{\perp}, s_{\parallel}) = \frac{\hat{\xi}_\ell^{\text{NGC}}(s_{\perp}, s_{\parallel}) A_{\text{NGC}} + \hat{\xi}_\ell^{\text{SGC}}(s_{\perp}, s_{\parallel}) A_{\text{SGC}}}{A_{\text{NGC}} + A_{\text{SGC}}} \quad (11)$$

The top and middle left panels of Figure 2 show the standard 2PCF of the data and mean of the 1000 'shuffled-z' EZmocks with systematics, respectively. The squashing effect due to RSD can be observed for both data and EZmocks; the BAO signal is clearly visible in the EZmocks, but not in data, because of the overall low statistics, as seen in [Raichoor et al. \(2020\)](#). For the mocks, and for data to a lesser extent, we see a negative clustering at  $s_{\parallel} \sim 0$ : this is due to the 'shuffled-z' scheme adopted to assign redshifts to random objects, which creates an excess of  $DR$  and  $RR$  pairs at those values. The bottom left panel of Figure 2 displays the difference between the mean of the 1000 'shuffled-z' EZmocks without and with systematics: the systematics show up mostly at small  $s_{\perp}$  (radial, due to spectroscopic observations) and large  $s_{\parallel}$  (angular, due to the imaging systematics).

Figure 3 shows the standard 2PCF multipoles for the data and for the 'shuffled-z' EZmocks with or without systematics, separately for the NGC and the SGC. Adding systematics to the EZmocks improves the agreement with data, especially for the monopole in the SGC and for the quadrupole in both caps. The overall agreement is satisfactory. However, there are remaining discrepancies between the data and the EZmocks with systematics, the most significant ones being at intermediate scales,  $\sim 40 - 80 h^{-1} \text{Mpc}$ , in the NGC for the monopole and the quadrupole. As detailed in the next Section, those are likely due to remaining angular systematics in the data.

### 4.2 Modified 2PCF

In order to mitigate those systematics in our RSD analysis, we use a modified 2PCF built on the standard  $\xi(s_{\perp}, s_{\parallel})$  for the model and  $\hat{\xi}(s_{\perp}, s_{\parallel})$  for data and mocks. Actually, as will be shown in Section 6.3 with the EZmocks, fitting the standard 2PCF multipoles  $\hat{\xi}_\ell(s)$  does not allow us to recover unbiased cosmological parameters when data-like systematics are included in the mocks – and corrected as in data. The principle of the modified 2PCF is thus to null the angular modes from the clustering.

Our approach builds on the method presented in [Burden et al. \(2017\)](#) designed for the DESI survey, in which they proposed a modification of the correlation function that nulls the angular modes from the clustering. [Burden et al. \(2017\)](#) introduce the shuffled 2PCF which is a modification of the LS estimator from Equation 8:

$$\hat{\xi}_\ell^{\text{shuff}}(s_{\perp}, s_{\parallel}) = \frac{DD(s_{\perp}, s_{\parallel}) - 2DS(s_{\perp}, s_{\parallel}) + SS(s_{\perp}, s_{\parallel})}{RR(s_{\perp}, s_{\parallel})}, \quad (12)$$

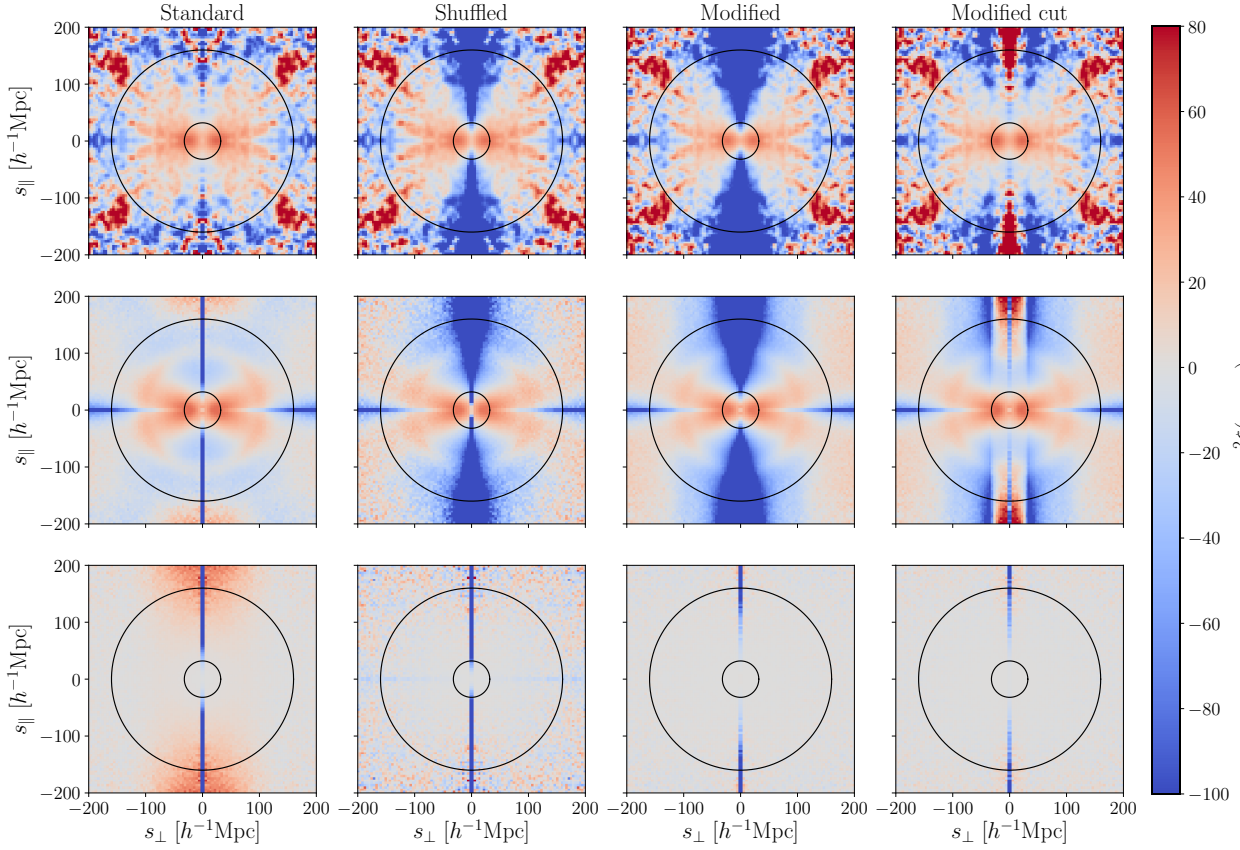


**Figure 2.** Two-dimensional correlation function in the directions perpendicular and parallel to the line-of-sight. Panels from left to right are for: standard 2PCF (Equation 8), shuffled 2PCF (Equation 12), modified 2PCF with no cut (Equation 13) and modified 2PCF with a cut (Equation 14). The top row displays the measurement from the eBOSS ELG data sample, the middle row displays the mean of the 1000 ‘shuffled-z’ EZmocks with systematics (100 mocks for the shuffled 2PCF), and the bottom row shows the difference between the mean of the 1000 ‘shuffled-z’ EZmocks with and without systematics (100 mocks for the shuffled 2PCF). For the modified 2PCF, all parameters are taken at their fiducial values (see text). The black circles illustrate our fiducial fitting range in  $s$  for the multipoles.

where  $S$  stands for a random catalog built with random picks of the data angular positions and with a radial distribution following the data one (according to the ‘shuffled-z’ scheme in our case). Using such a random  $S$  catalog, with the same angular clustering as that in the galaxy catalog, implies that angular modes are removed in the shuffled 2PCF, at the cost of an overall loss of information. Second column of Figure 2 shows the two-dimensional shuffled 2PCF of data (first row) and the mean (second row) of 100 EZmocks with systematics: angular signal at small  $s_{\perp}$  and large  $s_{\parallel}$  are removed. On the bottom row of the second column of Figure 2, we present the difference between the mean of EZmocks with and without systematics. As most systematics are removed compared to the standard 2PCF, this suggests that the nature of the uncorrected systematics mostly comes from angular signal and that the shuffled 2PCF removes them.

A model for the shuffled 2PCF was also presented in Burden et al. (2017) and shown to provide an unbiased isotropic BAO measurement. However, a more advanced modelling is required for a RSD analysis, as we are measuring anisotropic information from the monopole, quadrupole and hexadecapole. The model of Burden et al. (2017) involves subtracting terms integrated over the line of sight which thus include scales for which the RSD model may be invalid (see Section 5). Such small scales will be discarded from our fits. For that reason, we do not use the shuffled 2PCF for our

measurements on data and mocks, but rely on a modified 2PCF where we can control the boundaries of integration for both data and model. The modified 2PCF we adopt is based on:

$$\xi^{\text{mod}}(s_{\perp}, s_{\parallel}) = \xi(s_{\perp}, s_{\parallel}) \quad (13a)$$

$$- 2 \int_{-s_{\parallel}^{\text{max}}}^{s_{\parallel}^{\text{max}}} \xi(s_{\perp}, s'_{\parallel}) \bar{n}(\chi_{\text{mod}} + s'_{\parallel}/2) ds'_{\parallel} \quad (13b)$$

$$+ \int_0^{\infty} \bar{n}^2(\chi) d\chi \int_{-s_{\parallel}^{\text{max}}}^{s_{\parallel}^{\text{max}}} \xi(s_{\perp}, s'_{\parallel}) ds'_{\parallel}, \quad (13c)$$

where  $\bar{n}(\chi)$  is the normalized data radial density as a function of the comoving line-of-sight distance  $\chi$  and  $\chi_{\text{mod}}$  is the comoving line-of-sight distance at a given redshift  $z_{\text{mod}}$ , defined hereafter.  $s_{\parallel}^{\text{max}}$  is the maximum parallel scale included in the correction. Equation 13b corresponds to the cross-correlation between the three-dimensional overdensity and the projected angular overdensity and Equation 13c corresponds to the angular correlation function. We provide more details about Equation 13 in Appendix A. The third column of Figure 2 illustrates the modified 2PCF defined in Equation 13: it clearly shows its efficiency to remove the angular clustering in the data (top row) and in the mocks (middle row), with as a consequence a significant removal of the angular systematics. This can also be seen on the third bottom panel, where the system-

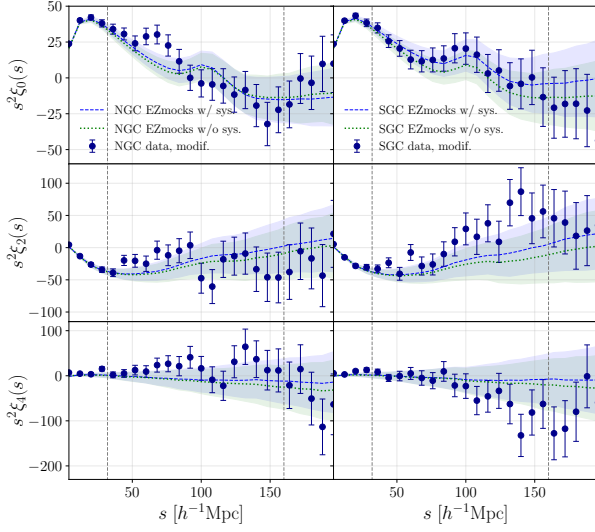


**Figure 3.** Multipoles of the standard 2PCF as measured from the eBOSS ELG data sample in each cap and from the mean of the shuffled-z EZmocks with and without systematics. The bands represent the one sigma dispersion around the mean of the mocks. Errors on data points come from one sigma dispersion of mocks with systematics. Vertical dashed lines define the baseline fitting range.

atics included are almost completely cancelled. We note that the modified 2PCF and the shuffled 2PCF are very similar.

In our implementation, we use  $s_{\parallel}^{\max} = 190 h^{-1}\text{Mpc}$  and  $z_{\text{mod}} = 0.83$  as baseline parameters. Both quantities are treated as parameters and chosen to minimise the systematics. One can note in Equations 13b and 13c that the integration does not depend on the value of  $s = \sqrt{s_{\perp}^2 + s_{\parallel}^2}$ . However, since the CLPT-GS model is not valid on small scales, our RSD analysis will be performed only for scales above a minimum value  $s_{\min}$ , namely  $s > s_{\min}$  ( $s_{\min} = 32 h^{-1}\text{Mpc}$  in our baseline settings, see Section 5). Introducing this selection in Equations 13b and 13c, and noting for clarity  $A(s'_{\parallel}) = \bar{n}(\chi_{\text{mod}} + s'_{\parallel}/2)$  and  $B = \int_0^{\infty} \bar{n}^2(\chi) d\chi$ , we end up with the following modified 2PCF:

$$\xi_{\text{cut}}^{\text{mod}}(s_{\perp}, s_{\parallel}) = \xi(s_{\perp}, s_{\parallel}) \quad (14a)$$

$$+ \int_{s_{\parallel}^{\min}(s_{\perp}) < |s'_{\parallel}| < s_{\parallel}^{\max}} (-2A(s'_{\parallel}) + B) \cdot \xi(s_{\perp}, s'_{\parallel}) ds'_{\parallel}, \quad (14b)$$

where  $s_{\parallel}^{\min}(s_{\perp})$  is defined as  $s_{\parallel}^{\min}(s_{\perp}) = \sqrt{(s_{\min}^{\text{cut}})^2 - s_{\perp}^2}$  with  $s_{\min}^{\text{cut}}$  the minimum value of  $s$  used in the correction. Except stated otherwise,  $s_{\min}^{\text{cut}}$  is fixed at  $s_{\min}$ , i.e. the minimum scale used in the RSD analysis. The right-column panels of Figure 2 shows the modified 2PCF defined in Equation 14: though cutting out scales smaller than  $s_{\min}$  in the integration removes less of the clustering amplitude for  $s_{\perp} < s_{\min}$  for both data and EZmocks (top and bottom), one can see that the efficiency to reduce angular systematics (the two right panels in last row of Figure 2) is of the same order as that of Equation 13, where no cut is imposed in the integration.

Equation 14 is the modified 2PCF we use in this paper for the RSD analysis for both measurements (on data and mocks) and modelling. We can then define Legendre multipoles  $\xi_{\text{cut},\ell}^{\text{mod}}$  using Equations 9 or 10. Multipoles of the modified 2PCF with a cut  $s_{\min}^{\text{cut}} = 32 h^{-1}\text{Mpc}$  as measured from the eBOSS ELG sample in separate caps and from EZmocks with and without systematics are

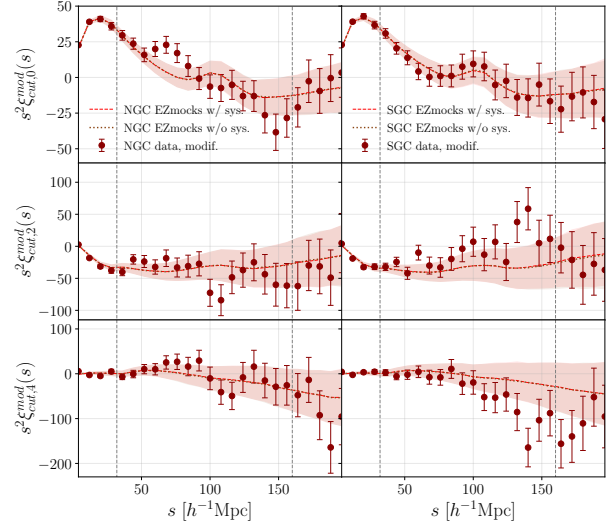


**Figure 4.** Multipoles of the modified 2PCF as measured from the eBOSS ELG data sample in each cap and from the mean of the shuffled-z EZmocks with and without systematics. The bands represent the one sigma dispersion around the mean of the mocks. We note that EZmocks with and without systematics mostly overlap, as a result of angular systematics being removed by the modified 2PCF. Errors on data points come from one sigma dispersion of mocks with systematics. Vertical dashed lines define the baseline fitting range.

shown in Figure 4 using  $z_{\text{mod}} = 0.83$  and  $s_{\parallel}^{\max} = 190 h^{-1}\text{Mpc}$ . EZmocks and data are more in agreement than in the case of the standard 2PCF multipoles, shown in Figure 3. It thus suggests that removing some of the angular modes allowed us to partially remove systematics.

We emphasize that the modified 2PCF introduced in Equation 13 does not aim at providing a model for the shuffled 2PCF defined in Equation 12. It is a 2PCF estimator that acts similarly to the shuffled 2PCF and removes angular modes significantly. Our need to discard small scales in the integration over  $s'_{\parallel}$  in Equations 13b and 13c, because of model inaccuracies, led us to adopt Equation 14 as a final 2PCF estimator, for both measurements and modelling.

### 4.3 Reconstruction

For the isotropic BAO part of the combined RSD+BAO measurements, we use the reconstructed galaxy field to improve our measurements (Eisenstein et al. 2007). Indeed applying reconstruction aims at correcting large-scale velocity flow effects, sharpening the BAO peak.

The reconstruction method used in this study follows the works of Burden et al. (2015) and Bautista et al. (2018) which describe a procedure to remove RSD effects. We apply three iterations and assume for the eBOSS ELG sample a linear bias  $b = 1.4$  and a growth rate  $f = 0.82$ . The smoothing scale is set at  $15 h^{-1}\text{Mpc}$ . Vargas-Magaña et al. (2018) showed that the choice of parameter values and cosmology used for reconstruction induces no bias in BAO measurements.

RSD measurements rely on the pre-reconstruction multipoles and those are then used jointly with the post-reconstruction monopole for the combined RSD+isotropic BAO fit.



#### 4.4 Covariance matrix

We estimate the multipole covariance matrix from the 1000 EZ-mocks as:

$$\mathbf{C}_{ij}^{\ell\ell'} = \frac{1}{N-1} \sum_{n=1}^N [\xi_{\ell}^n(s_i) - \bar{\xi}_{\ell}(s_i)] [\xi_{\ell'}^n(s_j) - \bar{\xi}_{\ell'}(s_j)] \quad (15)$$

where  $N$  is the number of EZmocks,  $(\ell, \ell')$  are multipole orders,  $(i, j)$  run over the separation bins and  $\bar{\xi}_{\ell}(s_i)$  is the average value over mocks for multipole  $\ell$  in bin  $s_i$ :

$$\bar{\xi}_{\ell}(s_i) = \frac{1}{N} \sum_{n=1}^N \xi_{\ell}^n(s_i) \quad (16)$$

In the case of RSD fitting, we use the first three even Legendre pre-reconstruction multipoles,  $\ell = 0, 2, 4$ . The procedure is the same whether we use the standard 2PCF or the modified one of Section 4.2. In the case of RSD+BAO fitting, we also consider the post-reconstruction monopole, so  $\ell = 0, 2, 4, 0_{\text{rec}}$ , where  $0_{\text{rec}}$  stands for the latter.

We then follow the procedure described in [Hartlap et al. \(2007\)](#) to obtain an unbiased estimator of the inverse covariance matrix, and multiply the inverse covariance matrix from the mocks by a correction factor  $(1 - (N_d + 1)/(N_m - 1))$  where  $N_m$  is the number of mocks and  $N_d$  the number of bins used in the analysis. To account for the uncertainty in the covariance matrix estimate, we rescale the fitted parameter errors as proposed in [Percival et al. \(2014\)](#).

Figure 5 shows the correlation matrices computed from the 1000 EZmocks, using the definition  $\mathbf{C}_{ij}/\sqrt{\mathbf{C}_{ii}\mathbf{C}_{jj}}$  for the 4 multipoles and their cross-correlations, that are used for the baseline RSD+BAO analysis. We can notice the differences between the modified and standard 2PCF multipoles, anti-correlations being stronger for the modified 2PCF than for the standard one. On the other hand, the pre- and post-reconstruction monopoles are less strongly correlated when the modified 2PCF is used.

## 5 MODEL

### 5.1 RSD : CLPT-GS model

Galaxy redshift measurements are a combination of the Hubble rate of expansion and the peculiar velocity of galaxies along the line-of-sight. Therefore what we are effectively measuring is a combination of both the matter density field and the velocity field. The galaxy correlation function is thus affected by multiple sources of non-linearities that are theoretically challenging to model. [Kaiser \(1987\)](#) was the first to derive the linear theory formalism in redshift space, to describe the effect of the peculiar motion of galaxies causing an apparent contraction of the structures along the line-of-sight. [Hamilton \(1992\)](#) then extended the formalism to real space. However the formalism is valid only on scales larger than  $\sim 80 h^{-1}\text{Mpc}$ , where we assume a linear coupling between the matter and velocity fields:

$$\nabla \cdot \mathbf{v} = -f\delta_m, \quad (17)$$

where  $f$  is the growth rate of structure,  $\mathbf{v}$  the velocity field and  $\delta_m$  the underlying matter density field. On smaller scales, the non-linear coupling between the velocity and the matter density fields becomes non-negligible and we need therefore to extend the above formalism beyond linear theory to account for the

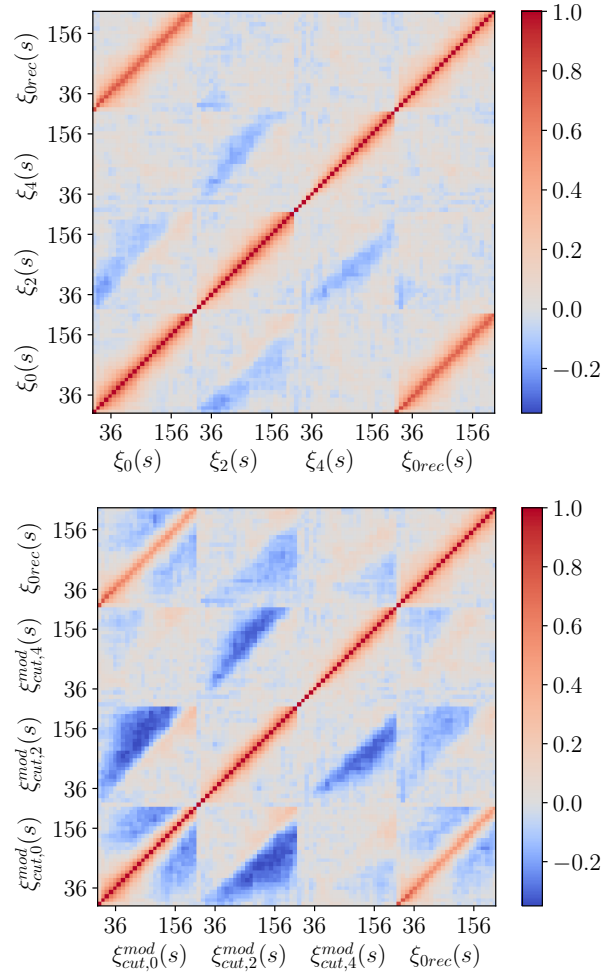


**Figure 5.** The complete RSD+BAO correlation matrices from 1000 EZ-mocks computed in  $8 h^{-1}\text{Mpc}$  bins from 0 to  $200 h^{-1}\text{Mpc}$  for the combined NGC+SGC sample, using the standard (top) and modified (bottom) RSD 2PCF. The latter is computed with  $s_{\text{min}}^{\text{cut}} = 32 h^{-1}\text{Mpc}$ ,  $z_{\text{mod}} = 0.83$ ,  $s_{\parallel}^{\text{max}} = 190 h^{-1}\text{Mpc}$  as in the baseline analysis. The post-reconstruction monopole for BAO is always computed from the standard 2PCF. On both axes we show the fiducial range of the RSD analysis, from 36 to  $156 h^{-1}\text{Mpc}$  in central bin values.

small-scales non-linearities.

In this work, we adopt the same perturbative approach that was previously used in other publications from BOSS ([Alam et al. 2015](#); [Satpathy et al. 2017](#)) and eBOSS ([Zarrouk et al. 2018](#); [Bautista et al. 2020](#)) to model RSD on quasi-linear scales ( $\sim 30 - 80 h^{-1}\text{Mpc}$ ), by combining the Lagrangian Perturbation Theory with Gaussian Streaming model.

#### 5.1.1 CLPT

The Convolution Lagrangian Perturbation Theory (CLPT) was introduced by [Carlson et al. \(2013\)](#) to give accurate predictions for correlation functions in real and redshift spaces for biased tracers. In this framework, we perform a perturbative expansion of the displacement field  $\Psi(\mathbf{q}, t)$ . With this approach,  $\Psi$  traces the trajectory of a mass element starting from an initial position  $\mathbf{q}$  in Lagrangian

coordinates to a final position  $\mathbf{x}$  in Eulerian coordinates through:

$$\mathbf{x}(\mathbf{q}, t) = \mathbf{q} + \mathbf{\Psi}(\mathbf{q}, t), \quad (18)$$

where the first order solution of this expansion corresponds to the Zel'dovich approximation (Zel'dovich 1970; White 2014). Under the assumption that the matter is locally biased, the tracer density field,  $\delta_X(\mathbf{x})$ , can be written in terms of the Lagrangian bias function  $F$  of a linear dark matter field  $\delta_m(\mathbf{x})$ :

$$1 + \delta_X(\mathbf{x}) = F[\delta_m(\mathbf{x})] \quad (19)$$

The CLPT model from Carlson et al. (2013) uses contributions up to second order bias,  $F_1$  and  $F_2$  whose explicit expression can be found in Matsubara (2008). The first Lagrangian bias  $F_1$  is related to Eulerian bias on large scale through  $b = 1 + F_1$ .

According to  $N$ -body simulations (Carlson et al. 2013), the CLPT model performs very well for the real space correlation function down to very small scales ( $10 h^{-1} \text{Mpc}$ ). It also shows a good accuracy for the monopole of the correlation function in redshift space down to  $\sim 20 h^{-1} \text{Mpc}$ . However, it suffers from some inaccuracies on quasi-linear scales ( $30\text{--}80 h^{-1} \text{Mpc}$ ) for the quadrupole in redshift space. To overcome this, Wang et al. (2014) proposed to extend the above formalism by combining it with the Gaussian Streaming Model (GS) proposed by Reid & White (2011). The method considers the real space correlation function  $\xi(r)$ , the pairwise infall velocity  $v_{12}(r)$  and the velocity dispersion  $\sigma_{12}(r)$  computed from CLPT as inputs to the GS model, as will be described in the next Section. The expressions for these functions in the CLPT model are given below (see Wang et al. 2014 for more details):

$$1 + \xi(r) = \int d^3q M_0(r, q) \quad (20)$$

$$v_{12}(r) = [1 + \xi(r)]^{-1} \int d^3q M_{1,n}(r, q) \quad (21)$$

$$\sigma_{12, \text{nm}}^2(r) = [1 + \xi(r)]^{-1} \int d^3q M_{2, \text{nm}}(r, q) \quad (22)$$

$$\sigma_{\parallel}^2(r) = \sum_{\text{nm}} \sigma_{12, \text{nm}}^2 \hat{r}_n \hat{r}_m \quad (23)$$

$$\sigma_{\perp}^2(r) = \sum_{\text{nm}} (\sigma_{12, \text{nm}}^2 \delta_{\text{nm}}^{\text{K}} - \sigma_{\parallel}^2) / 2 \quad (24)$$

Here  $M_0(r, q)$ ,  $M_{1,n}(r, q)$  and  $M_{2, \text{nm}}(r, q)$  are convolution kernels that depend on a linear matter power spectrum  $P_{\text{lin}}(k)$  and the first two Lagrangian bias parameters, as the bias expansion is up to second order. The vectors  $\hat{r}_n$ ,  $\hat{r}_m$  are unit vectors along the direction of the pair separation,  $\sigma_{12, \text{nm}}^2$  is the pairwise velocity dispersion tensor and  $\delta_{\text{nm}}^{\text{K}}$  is the Kronecker delta. The code<sup>2</sup> used in this paper to perform the CLPT calculations was developed by Wang et al. (2014). We use the software CAMB (Lewis et al. 2000) to compute the linear power spectrum  $P_{\text{lin}}(k)$  for the fiducial cosmology used for the fitting, namely the BOSS cosmology (Equation 7), except for the OR mocks.

### 5.1.2 The Gaussian Streaming model

In the GS model, the redshift space correlation function  $\xi^s(s_{\perp}, s_{\parallel})$  is modelled as:

$$1 + \xi^s(s_{\perp}, s_{\parallel}) = \int dr_{\parallel} [1 + \xi(r)] \mathcal{P}(r_{\parallel}) \quad (25)$$

where

$$\mathcal{P}(y) = \frac{1}{\sqrt{2\pi}\sigma_{12}(r, \mu)} \exp \left\{ -\frac{[s_{\parallel} - r_{\parallel} - \mu v_{12}(r)]^2}{2\sigma_{12}^2(r, \mu)} \right\} \quad (26)$$

and

$$\sigma_{12}^2(r, \mu) = \mu^2 \sigma_{\parallel}^2(r) + (1 - \mu^2) \sigma_{\perp}^2(r) + \sigma_{\text{FoG}}^2$$

$r_{\parallel}$  corresponds to the line-of-sight separation in real space, while  $s_{\parallel}$  is the line-of-sight separation in redshift space and  $s_{\perp}$  is the transverse separation both in redshift and real spaces. The quantity  $r = \sqrt{r_{\parallel}^2 + s_{\perp}^2}$  gives the pair separation in real space, and  $\mu = r_{\parallel}/r$  corresponds to the cosine of the angle between the pair separation vector  $r$  and the line of sight separation in real space  $r_{\parallel}$ . The parameter  $\sigma_{\text{FoG}}$  accounts for the proper motion of galaxies on small scales (Jackson 1972; Reid & White 2011), causing an elongation of the distribution of galaxies along the line of sight, an effect known as the *Finger of God*. In practice,  $\sigma_{\text{FoG}}$  is an isotropic velocity dispersion whose role is to account for the scale-dependence of the quadrupole on small scales.

### 5.2 Radial Integral Constraint

In this Section, we discuss the impact of the shuffled scheme used for redshift assignment in the random catalogues on the 2PCF measurement and modelling.

The LS estimator from Equation 8 effectively estimates the observed galaxy correlation function by comparing the observed (weighted) distribution of galaxies to the 3-dimensional survey selection function as sampled by the random catalogue. In principle, the normalisation of the LS estimator makes it insensitive to the survey selection function, if the random catalogue indeed samples the ensemble average of the galaxy density. With the shuffled- $z$  scheme, the data radial selection function is directly imprinted on the random catalogue and the density fluctuations are forced to be zero along the line-of-sight: radial modes are suppressed, which effectively modifies clustering measurements on large scales. This so-called radial integral constraint effect is not suppressed by the normalisation of the LS estimator and must be included in the 2PCF modelling. Note that in the case of the eBOSS ELG sample, the impact of the radial selection function is even increased by the division of the survey footprint into smaller chunks accounting for the variations of the radial selection function with imaging depth.

In de Mattia & Ruhlmann-Kleider (2019), modelling corrections due to the radial integral constraint were derived for the power spectrum analysis. These results are hereafter extended to the correlation function. The impact of the window function (superscript c) and radial integral constraint (superscript ic) on the correlation function multipoles were modelled in de Mattia & Ruhlmann-Kleider (2019) with the following equation:

$$\xi_{\ell}^{\text{cic}}(s) = \xi_{\ell}^{\text{c}}(s) - IC_{\ell}^{\delta, \text{ic}}(s) - IC_{\ell}^{\text{ic}, \delta}(s) + IC_{\ell}^{\text{ic}, \text{ic}}(s) \quad (27)$$

where  $\xi_{\ell}^{\text{c}}(s)$  are multipoles of the product of the correlation function  $\xi$  by the window function (see Equation 2.10 in de Mattia & Ruhlmann-Kleider (2019)) and, for each  $(i, j) \in \{(\delta, \text{ic}), (\text{ic}, \delta), (\delta, \delta)\}$ :

$$IC_{\ell}^{i, j}(s) = \int d\Delta \Delta^2 \sum_p \frac{4\pi}{2p+1} \xi_p(\Delta) \mathcal{W}_{\ell p}^{i, j}(s, \Delta). \quad (28)$$

$\mathcal{W}_{\ell p}^{i, j}$  are the window function multipoles, as given in equations 2.16 and 2.19 in de Mattia & Ruhlmann-Kleider (2019). However, the LS estimator (Equation 8) removes the window function

<sup>2</sup> [https://github.com/w11745881210/CLPT\\_GSRSD](https://github.com/w11745881210/CLPT_GSRSD)

effect with the  $RR(s, \mu)$  term in the denominator. Hence, calling  $\mathcal{W}_q^{\delta, \delta}$  the window function multipoles (e.g. Equation 2.11 in [de Mattia & Ruhlmann-Kleider \(2019\)](#)), we build the ratios:

$$\mathcal{W}_{\ell p, \text{new}}^{i, j}(s, \Delta) = \frac{2\ell + 1}{2} \int_{-1}^1 d\mu \frac{\sum_{q=0}^{q_{\max}} \mathcal{W}_q^{i, j}(s, \Delta) \mathcal{L}_q(\mu)}{\sum_{q=0}^{q_{\max}} \mathcal{W}_q^{\delta, \delta}(s) \mathcal{L}_q(\mu)} \mathcal{L}_\ell(\mu) \quad (29)$$

to be used instead of the  $\mathcal{W}_{\ell p}^{i, j}$  in Equation 28. In practice, we use  $q_{\max} = 6$ . In addition, a shot noise contribution to the integral constraint corrections must be accounted for, as given by terms  $SN_\ell^{ij}(s)$  of Equations 3.6 and 3.7 in [de Mattia & Ruhlmann-Kleider \(2019\)](#). We proceed similarly to account for the removal of the window function effect in the LS estimator, i.e. instead of the  $SN_\ell^{ij}(s)$  we use:

$$SN_{\ell, \text{new}}^{i, j}(s) = \frac{2\ell + 1}{2} \int_{-1}^1 d\mu \frac{\sum_{q=0}^{q_{\max}} SN_q^{i, j}(s) \mathcal{L}_q(\mu)}{\sum_{q=0}^{q_{\max}} \mathcal{W}_q^{\delta, \delta}(s) \mathcal{L}_q(\mu)} \mathcal{L}_\ell(\mu). \quad (30)$$

In practice, to include the radial integral constraint into our model, we correct the multipoles of the correlation function from the CLPT-GS model,  $\xi^S$  (as given by Equation 25) according to Equation 27.

### 5.3 RSD parameter space

We account for the AP effect by introducing two dilation parameters,  $\alpha_\perp$  and  $\alpha_\parallel$ , that rescale the observed separations,  $s_\perp, s_\parallel$ , into the true ones,  $s'_\perp, s'_\parallel$ . Hence, the standard 2PCF model at the true separation is:

$$\xi^S(s'_\perp, s'_\parallel) = \xi^S(\alpha_\perp s_\perp, \alpha_\parallel s_\parallel) \quad (31)$$

In our baseline analysis, this  $\xi^S(\alpha_\perp s_\perp, \alpha_\parallel s_\parallel)$  is used to compute the radial integral constraint correction (Equation 27) and the modified 2PCF (Equation 14).

The above dilation parameters relate true values of the Hubble distance  $D_H(z_{\text{eff}})$  and comoving angular diameter distance  $D_M(z_{\text{eff}})$  at the effective redshift to their fiducial values:

$$a_\parallel = \frac{D_H(z_{\text{eff}}) r_{\text{drag}}^{\text{fid}}}{D_H^{\text{fid}}(z_{\text{eff}}) r_{\text{drag}}} \quad (32)$$

$$a_\perp = \frac{D_M(z_{\text{eff}}) r_{\text{drag}}^{\text{fid}}}{D_M^{\text{fid}}(z_{\text{eff}}) r_{\text{drag}}} \quad (33)$$

where the superscript fid stands for values in the fiducial cosmology and  $r_{\text{drag}}$  is the comoving sound horizon at the redshift at which the baryon-drag optical depth equals unity ([Hu & Sugiyama 1996](#)).

The growth rate of structure  $f(z)$  defined in Equation 1 is taken into account in the correlation function model via  $v_{12}(r)$  and  $\sigma_{12}(r)$ , as those are proportional to  $f(z)$  and  $f^2(z)$ , respectively. The two Lagrangian biases  $F_1$  and  $F_2$  as described by Equation 19 are free parameters of the model. The second Lagrangian bias  $F_2$  impacts mainly the small scales ([Wang et al. 2014](#)) and thus is mostly degenerate with  $\sigma_{\text{FoG}}$  and not well constrained by the data. Due to its small impact on the scales of interest, we chose to fix  $F_2 = F_2(F_1)$  using the peak background splitting assumption ([Cole & Kaiser 1989](#)) with a Sheth-Tormen mass function ([Sheth & Tormen 1999](#)).

Altogether, we thus explore a five dimensional parameter space  $\mathbf{p} = \{\alpha_\parallel, \alpha_\perp, f(z), F_1, \sigma_{\text{FoG}}\}$  in our RSD analysis. The

growth rate and biases being degenerate with  $\sigma_8$ , we hereafter report values of  $f\sigma_8$  and  $b_1\sigma_8$ , where  $b_1 = 1 + F_1$ . As explained in [Gil-Marín et al. \(2020\)](#), to remove the  $h$  dependency of  $\sigma_8$ , we rescale  $\sigma_8$  by taking the amplitude of the power spectrum at  $8 \times \alpha_{\text{iso}} h^{-1} \text{Mpc}$  where  $\alpha_{\text{iso}}$  is defined hereafter.

### 5.4 Isotropic BAO

An alternative way to parametrize the AP effect is to decompose the distortion into an isotropic and anisotropic shifts. The isotropic component  $\alpha_{\text{iso}}$  is related to parallel and transverse shifts,  $\alpha_\parallel$  and  $\alpha_\perp$ , via:

$$\alpha_{\text{iso}} = \alpha_\parallel^{1/3} \alpha_\perp^{2/3} \quad (34)$$

It corresponds to the isotropic shift of the BAO peak position in the monopole of the correlation function; the anisotropic shift  $\epsilon$  is defined as  $1 + \epsilon = \alpha_\parallel \alpha_\perp^{-1/3}$ .

BAO measurements from the eBOSS ELG sample in configuration space are presented in [Raichoor et al. \(2020\)](#). We hereafter fit the post-reconstruction BAO using the same BAO model as in [Raichoor et al. \(2020\)](#):

$$\xi_{\text{BAO}}(s, \alpha_{\text{iso}}) = B \xi_{\text{temp}}(\alpha_{\text{iso}} \cdot s) + A_0 + A_1/s + A_2/s^2 \quad (35)$$

where  $B$  is the post-reconstruction bias, the  $A_i$ 's are broadband parameters with  $i = 0, 1, 2$ . The template  $\xi_{\text{temp}}$  is the Fourier transform of the following power spectrum:

$$P(k, \mu) = \frac{1 + \mu^2 \beta e^{-k^2 \Sigma_r^2/2}}{1 + k^2 \mu^2 \Sigma_s^2/2} \left( \frac{P_{\text{lin}} - P_{\text{nw}}}{e^{k^2((1-\mu^2)\Sigma_\perp^2 + \mu^2\Sigma_\parallel^2)/2}} + P_{\text{nw}} \right) \quad (36)$$

where  $P_{\text{lin}}$  is a linear power spectrum taken from CAMB and  $P_{\text{nw}}$  is a 'no-wiggle' power spectrum computed with the formula from [Eisenstein & Hu \(1998\)](#). We use the same smoothing scales as in [Raichoor et al. \(2020\)](#), i.e.  $\Sigma_r = 15 h^{-1} \text{Mpc}$ ,  $\Sigma_s = 3 h^{-1} \text{Mpc}$ ,  $\Sigma_\perp = 3 h^{-1} \text{Mpc}$ ,  $\Sigma_\parallel = 5 h^{-1} \text{Mpc}$  and we set  $\beta = 0.593$  (see also [Ross et al. 2016; Seo et al. 2016](#)).

For the modelling of the post-reconstruction BAO signal, we do not include a radial integral constraint correction as the effect on the post-reconstruction monopole is absorbed by the broadband parameters.

### 5.5 Parameter estimation

In this paper, we perform RSD measurements and a joint fit of RSD and isotropic BAO. For both RSD and combined RSD+BAO fits, we use a nested sampling algorithm called MULTINEST ([Feroz et al. 2009](#)) to infer the posterior distributions of the set of cosmological parameters  $\mathbf{p}$ . MULTINEST is a Monte Carlo method that efficiently computes the Bayesian evidence, but also accurately produces posterior inferences as a by-product. Our analysis makes use of the publicly available python version<sup>3</sup> of MULTINEST. For the frequentist fits of our analysis, we use the MINUIT algorithm<sup>4</sup> ([James & Roos 1975](#)) which is specifically used to get the best fits of data and single mocks. The likelihood  $\mathcal{L}$  is computed from the  $\chi^2$  assuming a Gaussian distribution:

$$\mathcal{L} \propto \exp \left( -\frac{\chi^2(\mathbf{p})}{2} \right) \quad (37)$$

<sup>3</sup> <https://johannesbuchner.github.io/PyMultiNest/>

<sup>4</sup> <https://github.com/scikit-hep/iminuit>

Parameter	Min value	Max value
$\alpha_{\parallel}, \alpha_{\perp}$	0.6	1.4
$f(z)$	0	1.5
$F_1$	-0.2	2
$\sigma_{\text{FoG}}$	0	10
$\alpha_{\text{iso}}$	0.8	1.2
$B$	Gaussian	

**Table 2.** Flat priors on the RSD model parameters used in the cosmological analysis of this paper.

where the  $\chi^2$  is constructed from the correlation function multipoles measured from data catalogs,  $\xi_{\ell}^d$ , and predicted by the model,  $\xi_{\ell}^m$ , as follows:

$$\chi^2(\mathbf{p}) = \sum_{i,j}^{\ell,\ell'} \left[ \xi_{\ell}^d(s_i) - \xi_{\ell}^m(s_i, \mathbf{p}) \right] \mathbf{C}_{ij}^{\ell\ell'} \left[ \xi_{\ell'}^d(s_j) - \xi_{\ell'}^m(s_j, \mathbf{p}) \right] \quad (38)$$

Here indexes  $(i, j)$  run over the separation bins and  $\mathbf{C}_{ij}^{\ell\ell'}$  is the inverse covariance matrix computed from the 1000 EZmocks (see Section 4.4). Indexes  $(\ell, \ell')$  run over the multipoles of the correlation function, where  $\ell = 0, 2, 4$  if RSD only and  $\ell = 0, 2, 4, 0_{\text{rec}}$  if a combined RSD+BAO fit is performed. We recall that  $\xi_{\ell}^d$  and  $\xi_{\ell}^m$  can be computed from a standard 2PCF or a modified one. The priors on the parameters of the RSD model are flat priors given in Table 2. Performing the joined fit RSD+BAO by combining the likelihoods allows the Gaussian assumption required to combine RSD and BAO posteriors as in Bautista et al. (2020) to be relaxed.

For the RSD+BAO fit, the BAO isotropic shift,  $\alpha_{\text{iso}}$  is related to the two anisotropic AP parameters through Equation 34. However we add an additional prior constraint by adding a flat prior on  $\alpha_{\text{iso}}$  from 0.8 to 1.2. Due to reconstruction, the  $B$  bias can be different than  $b_1$ , therefore  $B$  is not fixed at  $1 + F_1$  but is kept as a free parameter. As in Raichoor et al. (2020), we use a Gaussian prior on  $B$  of 0.4 width, centred around the  $B$  value obtained from the first bin of the fitting range when setting  $A_i$  to zero.

When fitting onto the combined data sample, we chose to have only one set of biases for the whole sample, neglecting the difference between caps.

Unless otherwise specified, we fit the RSD multipoles over a range in separation from 32 to 160  $h^{-1}\text{Mpc}$  and from 50 to 150  $h^{-1}\text{Mpc}$  for the post-reconstruction monopole, using in both cases 8  $h^{-1}\text{Mpc}$  bins and the BOSS cosmology (Equation 7) at the effective redshifts quoted in Table 1.

## 6 TESTS ON MOCKS

In this Section, we present tests on mocks in order to validate our analysis. We first demonstrate the robustness of our CLPT-GS model with accurate N-body mocks; we then validate our analysis choices with the approximate EZmocks for both RSD and RSD+BAO fits. Results from the latter tests are presented in Table 3.

### 6.1 CLPT-GS model validation

We quantify here the ability of the CLPT-GS model to recover the cosmological parameters from accurate mocks made from the

OUTER RIM N-body simulation. We present a summary of the results, and refer the reader to Alam et al. (2020), where those are presented in details.

First, the non-blind mocks described in Section 3.2 were analysed. The statistical uncertainty on the recovered parameter values in these accurate mocks are 0.5-0.6%, 0.3-0.5% and 1-2% in  $\alpha_{\parallel}$ ,  $\alpha_{\perp}$  and  $f\sigma_8$ , respectively. No statistically significant bias in the parameter values was observed, despite the wide range of ELG HOD models used.

A set of blind mocks was then analysed, to test for possible biases, primarily in  $f\sigma_8$ , that could arise due to theoretical approximations in the model. To create these mocks, the peculiar velocities of the galaxies were scaled by an undisclosed factor leading to a change in the expected value of  $f$  and thus  $f\sigma_8$ . The other cosmological parameters were unaffected. The mean deviations of the fitted cosmological parameters with respect to expectations are 0.9%, 0.7% and 1.6% in  $\alpha_{\parallel}$ ,  $\alpha_{\perp}$  and  $f\sigma_8$ , showing that the CLPT-GS model describes the blind mock catalogues remarkably well.

These tests on N-body mocks demonstrate that the CLPT-GS model provides unbiased RSD measurements, within the statistical error of the mocks. Following Alam et al. (2020), we adopt as our modelling systematic errors: 1.8%, 1.4% and 3.2% for  $\alpha_{\parallel}$ ,  $\alpha_{\perp}$  and  $f\sigma_8$  respectively. We note that these errors are an order of magnitude smaller than the statistical error of the eBOSS ELG sample (see Section 7), and will marginally affect the precision of our measurements.

### 6.2 Radial integral constraint modelling

In Section 5.2 we justified the use of the 'shuffled-z' scheme to assign redshifts to random objects, for both data and mocks, in order to reproduce the radial selection function of the survey. This scheme has a significant impact on the multipole measurements in the eBOSS ELG sample, as illustrated in Figure 6 with the EZmocks (dashed lines with shaded regions), using either the 'sampled-z' scheme (blue) or the 'shuffled-z' one (green). At large scales, the increase in the quadrupole and decrease in the hexadecapole are noticeable. We account for this radial integral constraint effect in our modelling with the formalism presented in Section 5.2, and we test hereafter the impact of that correction on the estimated cosmological parameters. Results are presented in the upper part of Table 3.

The baseline for this test is provided by fits on the 'sampled-z' EZmocks, using a standard 2PCF model based on CLPT-GS at the data effective redshift. When compared to the values expected for our fiducial cosmology, the results show deviations of 2.4%, 0.2%, and 0.9% for  $\alpha_{\parallel}$ ,  $\alpha_{\perp}$ , and  $f\sigma_8$ , respectively. Those small deviations may come from the fact that EZmocks are approximate mocks meant to determine the covariance matrix to be used in the measurements. The linear scales around the BAO are well reproduced but the small scales and hence the full shape fits are not accurate enough for model validation. In this sense, we note that the corresponding value of the isotropic BAO scale  $\alpha_{\text{iso}} = 1.007$  is consistent with the value measured in Raichoor et al. (2020) from the post-reconstruction monopole.

Performing a similar fit, i.e. without RIC correction, using the 'shuffled-z' scheme instead of the 'sampled-z' one, the previous cosmological parameter estimations are shifted by 4.0%, 5.3% and 4.2% for  $\alpha_{\parallel}$ ,  $\alpha_{\perp}$  and  $f\sigma_8$ . Those shifts are large, and explained by the significant differences in the multipoles between the 'sampled-z' and the 'shuffled-z' schemes due to the radial integral constraint effect (Figure 6). It justifies that we correct our modelling for this



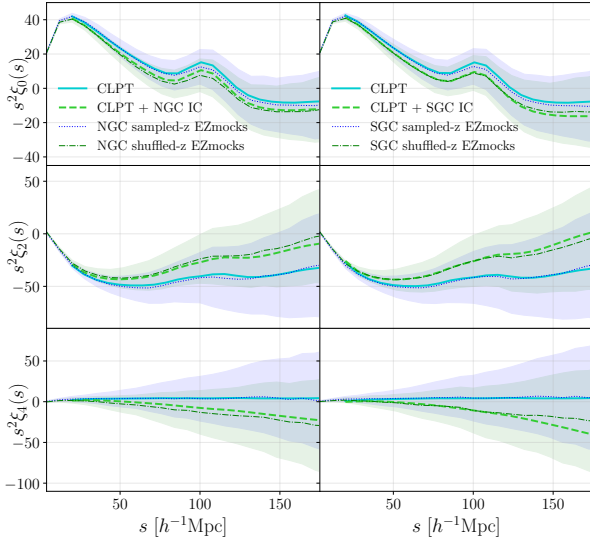


**Figure 6.** Multipoles of the standard 2PCF as measured in EZmocks with and without systematics, using the ‘sampled-z’ (blue) or the ‘shuffled-z’ (green) scheme. Left panels are for the NGC, right panels for the SGC. The dotted lines and the shaded area represent the mean of the mocks and the dispersion at  $1\sigma$  around the mean, respectively. Blue solid and dashed green lines are the CLPT-GS model prediction without and with the radial integral constraint correction, respectively. Cosmological parameters used for the model are:  $(\alpha_{\parallel}, \alpha_{\perp}, f, F_1, \sigma_{\text{FoG}}) = (1.0, 1.0, 0.84, 0.4, 2.0)$ .

effect. Including the correction as described in Section 5.2, the deviations are significantly reduced to 2.1%, 1.2%, and 0.2% for  $a_{\parallel}$ ,  $a_{\perp}$ , and  $f\sigma_8$ , respectively. The growth rate is almost perfectly recovered and the remaining biases in  $\alpha_{\parallel}$  and  $\alpha_{\perp}$  are reasonable. The observed shifts are taken as systematic errors due to the radial integral constraint (RIC) modelling in our final error budget (see Table 5).

### 6.3 Mitigating unknown angular systematics in RSD fits

As already mentioned, the eBOSS ELG sample suffers from unknown angular systematics that are not corrected by the photometric weights. These systematic effects bias our cosmological results (see below). In this Section, we show that the modified 2PCF (Section 4.2) is efficient at reducing those biases.

Here, our reference consists in fitting a RIC-corrected model onto ‘shuffled-z’ EZmocks without systematics using the standard 2PCF (see Standard 2PCF, ‘no systematics’ row in Table 3). Performing a similar fit on the ‘shuffled-z’ EZmocks *with* systematics, shifts those reference values by 0.3%, 2.2% and 9.6% for  $a_{\parallel}$ ,  $a_{\perp}$ , and  $f\sigma_8$ , respectively. The shift in  $f\sigma_8$  is significant and justifies our use of the modified 2PCF defined by Equation 14 in Section 4.2 to cancel the angular modes.

The free parameters  $z_{\text{mod}}$  and  $s_{\parallel}^{\text{max}}$  of the modified 2PCF are chosen by minimising the following quantity:

$$\chi_{\text{mod}}^2(z_{\text{mod}}, s_{\parallel}^{\text{max}}) = \Delta (C_{\text{cut}}^{\text{mod}})^{-1} \Delta^T, \quad (39)$$

where  $\Delta = \xi_{\text{cut, syst}}^{\text{mod}}(z_{\text{mod}}, s_{\parallel}^{\text{max}}) - \xi_{\text{cut}}^{\text{mod}}(z_{\text{mod}}, s_{\parallel}^{\text{max}})$  is the vector of differences between the multipoles of the modified 2PCF ( $\ell = 0, 2, 4$ ) measured from the mean of the EZmocks with and without systematics and restricted to our fiducial fitting range in  $s$ , and  $C_{\text{cut}}^{\text{mod}}$  is the covariance matrix built from the 1000 EZmocks

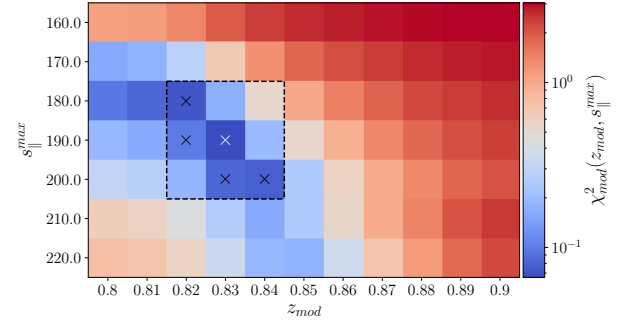


**Figure 7.**  $\chi_{\text{mod}}^2$  measuring the difference between multipoles of the modified 2PCF obtained on ‘shuffled-z’ EZmocks with and without systematics (Equation 39), as a function of the modified 2PCF free parameters,  $z_{\text{mod}}$  and  $s_{\parallel}^{\text{max}}$ . The dashed line encompasses the 8 neighbouring pixels around the minimum, marked with a white cross. Black crosses indicate pixels with  $\chi_{\text{mod}}^2 < 0.1$ . We note that the standard 2PCF would provide  $\chi^2 \sim 3$ .

without systematics, using the modified 2PCF. The minimisation yields  $z_{\text{mod}} = 0.83$  and  $s_{\parallel}^{\text{max}} = 190 h^{-1} \text{Mpc}$ . In the following we will choose those two parameters as our baseline choice. The 2D variations of  $\chi_{\text{mod}}^2$  with respect to both parameters are represented in Figure 7, which shows a valley around our minimum (represented by the darker blue pixels). The minimum  $\chi_{\text{mod}}^2$  reaches a value below 0.1 that indicates that the modified 2PCF successfully mitigates the systematic effects introduced in the mocks. Using the covariance matrix with systematics or using the modified 2PCF with no cut in  $s$  (see Equation 13) result in the same minima.

To quantify the systematic error related to the modified 2PCF, we compare in Table 3 fit results to the modified and standard 2PCF multipoles from the mean of the mocks for the ‘no systematics’ case (we recall that we use ‘shuffled-z’ EZmocks and a RIC-corrected model as baseline). We find deviations of 0.3%, 0.04%, 1.4% in  $\alpha_{\parallel}$ ,  $\alpha_{\perp}$  and  $f\sigma_8$ , respectively. Then, we vary  $z_{\text{mod}}$  and  $s_{\parallel}^{\text{max}}$  around their nominal values and take as a systematic error the largest of the observed deviations for each parameter. For  $z_{\text{mod}}$ , we obtain 0.3%, 0.2% and 1.8% for  $\alpha_{\parallel}$ ,  $\alpha_{\perp}$  and  $f\sigma_8$ , respectively. For  $s_{\parallel}^{\text{max}}$ , the equivalent numbers are 0.2%, 0.3% and 1.5%. The error we assign to using the modified 2PCF in the absence of systematics is taken conservatively as the sum in quadrature of the three effects previously described, which amounts to 0.5%, 0.4%, 2.7% for  $\alpha_{\parallel}$ ,  $\alpha_{\perp}$  and  $f\sigma_8$ , respectively. We also show that taking more extreme values for the parameters ( $s_{\parallel}^{\text{max}} = 200 h^{-1} \text{Mpc}$ ,  $z_{\text{mod}} = 0.87$  and  $s_{\parallel}^{\text{max}} = 100 h^{-1} \text{Mpc}$ ,  $z_{\text{mod}} = 0.84$ ) implies deviations that are at same level. This shows the robustness of the modified 2PCF to recover the correct values of the cosmological parameters in the absence of systematic effects in the mocks. We note that larger biases are observed when the parameter  $s_{\parallel}^{\text{min}}$  of the modified 2PCF is set to 0 in Equation 14 (see ‘no cut’ label in Table 3). This especially the case for  $f\sigma_8$ , which is expected since using the model for very small scales, where it is invalid, distributes model inaccuracies over all scales.

We now study the response of the modified 2PCF in the case of shuffled-z EZmocks with ‘all systematics’ (and a RIC-corrected model). Deviations with respect to results from the modified 2PCF and mocks without systematics are 0.3%, 0.9% and 1.7% for  $\alpha_{\parallel}$ ,  $\alpha_{\perp}$  and  $f\sigma_8$  respectively, showing a significant reduction with re-

spect to the corresponding results from the standard 2PCF reported at the beginning of the Section. This demonstrates that the modified 2PCF is key for this analysis as it reduces the bias on  $f\sigma_8$  by a factor of nearly 6. When compared to results from the standard 2PCF and mocks without systematics, the deviations in cosmological parameters are small (0.7%, 0.9% and 0.4% for  $\alpha_{\parallel}$ ,  $\alpha_{\perp}$  and  $f\sigma_8$ ), nevertheless, there is a mild increase of the dispersion of about 10% for  $\alpha_{\parallel}$ , 15% for  $\alpha_{\perp}$ , and 15% for  $f\sigma_8$ .

We also evaluate the impact of changes of  $z_{\text{mod}}$  and  $s_{\parallel}^{\text{max}}$  around their nominal values by considering the 8 neighbouring pixels around the minimum defined in Figure 7, which correspond to changes of  $\Delta z_{\text{mod}} \in \{0, \pm 0.01\}$  and  $\Delta s_{\parallel}^{\text{max}} \in \{0, \pm 10\} h^{-1} \text{Mpc}$ . First, we consider the shifts induced by a small increase in  $\chi_{\text{mod}}^2$ , i.e. pixels marked by black crosses in Figure 7 which have  $\chi_{\text{mod}}^2 < 0.1$ . The largest deviations with respect to mocks without systematics and the modified 2PCF with baseline parameters are obtained for  $s_{\parallel}^{\text{max}} = 200 h^{-1} \text{Mpc}$  and  $z_{\text{mod}} = 0.84$ : 0.3%, 0.9% and 2.1% for  $\alpha_{\parallel}$ ,  $\alpha_{\perp}$  and  $f\sigma_8$  respectively. These numbers become 0.6%, 0.8% and 0.7% when the comparison is made w.r.t. the standard 2PCF. The deviations are only marginally larger than those previously quoted, as expected since we are close to the minimum. Considering all neighbouring pixels, the largest biases are obtained for  $s_{\parallel}^{\text{max}} = 180 h^{-1} \text{Mpc}$  and  $z_{\text{mod}} = 0.84$ , which is the neighbouring pixel with the largest  $\chi_{\text{mod}}^2$  value. With respect to mocks without systematics and the modified 2PCF with baseline parameters, we observe deviations of 0.4%, 1.3% and 3.6% for  $\alpha_{\parallel}$ ,  $\alpha_{\perp}$  and  $f\sigma_8$ . These numbers become 0.7%, 1.2% and 2.3% when comparing to the standard 2PCF case. In the case of  $f\sigma_8$ , this is about twice the deviation observed for our baseline parameters when using the modified 2PCF and six times with the standard 2PCF. While the cosmological parameters are still better recovered with the modified 2PCF than with the standard one, the above results underline that the mitigation efficiency of the modified 2PCF strongly depends on the values of its two free parameters. For completeness, we observe that settings  $s_{\parallel}^{\text{max}}$  or  $z_{\text{mod}}$  to more extreme values ( $100 h^{-1} \text{Mpc}$  and 0.87, respectively) degrades significantly the efficiency of mitigation: this is understood since the systematics are no longer corrected as efficiently as with the baseline parameters.

Results of fits to EZmocks with systematics using the modified 2PCF (with  $(s_{\parallel}^{\text{max}}, z_{\text{mod}})$  at their baseline values) and the standard one are compared in Figures 8 and 9. Both the standard and modified 2PCFs provide similar  $\chi^2$  distributions, but due to systematics, the standard 2PCF fits are driven by extra-correlations in the quadrupole at intermediate scales (see middle panels of Figure 3) which results in clearly biased values for  $\alpha_{\perp}$  and  $f\sigma_8$ . Figure 9 shows that on average, the modified 2PCF brings a significant improvement for these two parameters.

#### 6.4 Joined RSD+BAO fit

As in de Mattia et al. (2020), we perform a joined fit of RSD and isotropic BAO. We take into account the cross-correlation between the pre-reconstruction multipoles and the post-reconstruction monopole, and combine their likelihoods, as explained in Section 5.5.

When fitting the 'shuffled-z' EZmocks without systematics using the standard 2PCF, combining with isotropic BAO has a small effect on the median best-fit parameter values of individual mocks. We indeed observe shifts of 0.2%, 0.2% and 0.9% for  $\alpha_{\parallel}$ ,  $\alpha_{\perp}$  and  $f\sigma_8$ , respectively (see second part of Table 3). The same is ob-

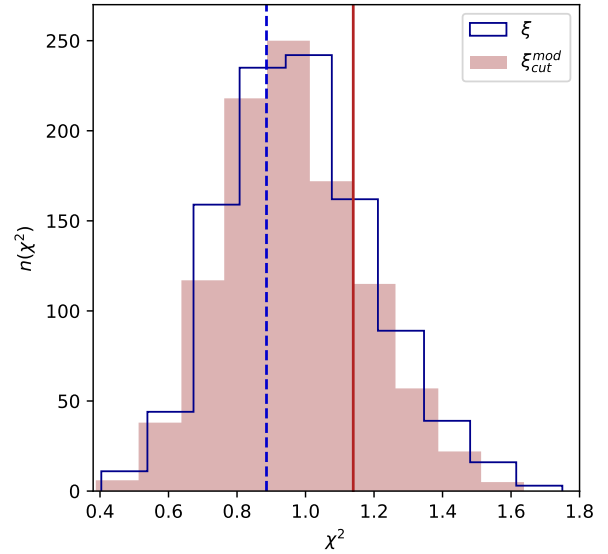


**Figure 8.**  $\chi^2$  distributions for RSD fits to multipoles of the standard (step line in blue) and modified 2PCF (filled in red) (using a cut in  $s$  at  $32 h^{-1} \text{Mpc}$  for the latter) in 1000 EZmocks with systematics. Dashed blue and solid red vertical lines are the  $\chi^2$  for the eBOSS ELG data sample for the standard and modified 2PCF, respectively.

served when using the modified 2PCF with the baseline parameters in the RSD part of the fit: shifts are of 0.3%, 0.2% and 0.2% for  $\alpha_{\parallel}$ ,  $\alpha_{\perp}$  and  $f\sigma_8$  compared to pure RSD fits with the modified 2PCF.

As already observed for pure RSD fits, adding systematics biases a lot the results compared to fits on EZmocks without systematics; for RSD+BAO fits with the standard 2PCF, all parameters are biased low, by 2.6% for  $\alpha_{\parallel}$ , 4.2% for  $\alpha_{\perp}$  and 8.8% for  $f\sigma_8$ . For the AP parameters, these deviations are larger than in the RSD fits.

It again motivates the use of the modified 2PCF to mitigate the systematics. As compared to RSD+BAO fits on mocks without systematics using the modified (standard) 2PCF, RSD+BAO fits with the modified 2PCF on mocks with systematics deviate by only 0.1% (0.9%) for  $\alpha_{\parallel}$ , 0.6% (0.8%) for  $\alpha_{\perp}$  and 1.9% (1.1%) for  $f\sigma_8$ , which are comparable to those in the pure RSD case. This suggests that with the standard 2PCF, RSD+BAO fits are driven by systematics in pre- and post-reconstruction multipoles that can be correlated and highlights again the need for the modified 2PCF.

## 7 RESULTS

In this Section we present the results and tests made on the eBOSS ELG data sample. We perform RSD and combined RSD+isotropic BAO measurements. All results are reported in Table 4.

Following de Mattia et al. (2020), we decided to limit the redshift range for the RSD fit to  $0.7 < z < 1.1$  due to the higher variations of the radial selection function with depth in the  $0.6 < z < 0.7$  interval. The posteriors become also more stable with this restricted redshift range. Limiting the RSD fit to  $0.7 < z < 1.1$  moves the effective redshift of the combined sample from 0.845 to 0.857 (Table 1). As we still keep the full range for the BAO part of the joined fit, we chose to fix the effective redshift to  $z_{\text{eff}} = 0.85$  for the combined RSD+BAO measurements. Indeed, as argued in de Mattia et al. (2020), changing the effective redshift from 0.845 to 0.857 induces shifts in the cosmological parameter measurements of 0.3%

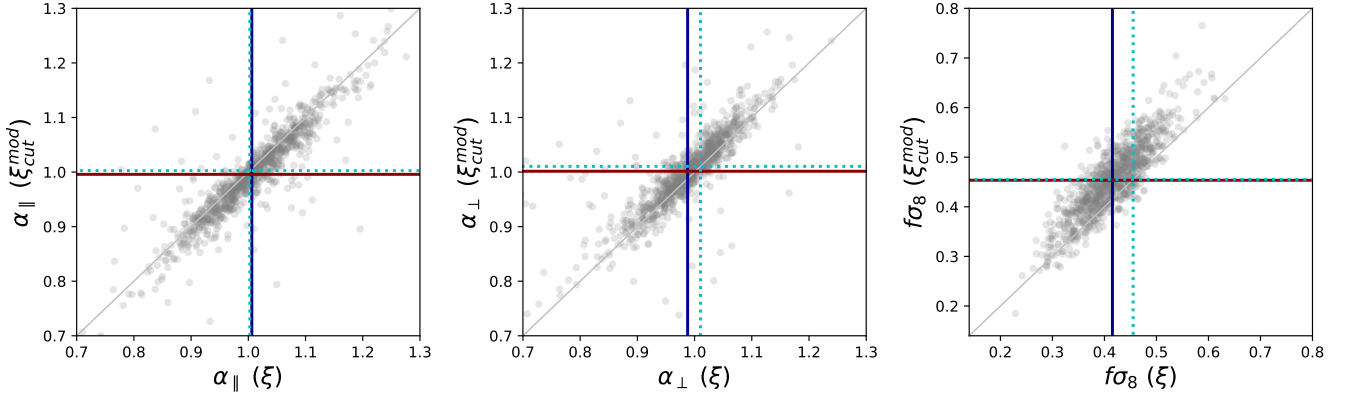


**Figure 9.** Comparison of parameter best-fit values for RSD fits based on the standard 2PCF (x-axis) and the modified one (y-axis) obtained for the 1000 EZmocks with systematics. Cyan dotted lines correspond to the mean of the fits on EZmocks without systematics using the standard 2PCF, which is the reference case here. Solid lines indicate the mean values of the parameters for the modified (red horizontal) and standard (blue vertical) 2PCF. The solid gray line is the identity.

for  $f\sigma_8$ , 0.7% for  $D_H/r_{\text{drag}}$  and 1.1% for  $D_M/r_{\text{drag}}$ , which are small compared to the statistical uncertainty.

Results of RSD+BAO fits to the combined data sample are presented in Figure 10, which compares data and best-fit model predictions for the post-reconstruction monopole and the pre-reconstructed 2PCF multipoles. The right panel corresponds to results obtained with the standard 2PCF. While both monopole best-fits provide reasonable BAO peak positions, the quadrupole best-fit displays an unphysical ‘BAO peak’ at  $s \sim 90 h^{-1}\text{Mpc}$ , driven by a bump in the data, likely due to remaining angular systematics, which as a consequence biases the AP parameters. The degeneracy between the AP parameters and the growth rate observed in the posteriors, presented in Figure 11 (blue contours), can explain the low value measured for  $f\sigma_8$ . The fact that the model provides a good fit to all multipoles, including the quadrupole, explains the low  $\chi^2$  obtained with the standard 2PCF, see Figure 8.

Pure RSD fits on the eBOSS ELG sample with the standard 2PCF give results far away from what is expected from EZmocks, for the combined sample and separate caps. Compared to values measured in data (‘baseline’ of RSD Standard 2PCF), RSD fits to EZmocks with systematics using the standard 2PCF provide a larger value of  $\alpha_{\parallel}$  in 33/1000 cases and the same fraction provides a smaller value of  $\alpha_{\perp}$ . However we observe no mock with a value of  $f\sigma_8$  smaller than that in data and only a few mocks with a value around 35% larger. We interpret those unlikely results as due to the remaining angular systematics present in the data and to the low significance BAO detection in the eBOSS ELG sample presented in Raichoor et al. (2020). Changing the redshift range to  $z_{\text{min}} = 0.6$  gives even more extreme results, with 14/1000 and 13/1000 mocks showing larger values of  $\alpha_{\parallel}$  and lower values of  $\alpha_{\perp}$  than in data, respectively. Adding the isotropic BAO to the fit (‘baseline’ of RSD+BAO Standard 2PCF) brings only slight changes to the previous results: 25/1000 mocks have a larger value than that measured for  $\alpha_{\parallel}$ , 132/1000 have a smaller value for  $\alpha_{\perp}$  and 2/1000 mocks have a smaller value for  $f\sigma_8$ . The data measurements are still far from expected in the mocks.

To mitigate the remaining angular systematics in the data sample, we fit the modified 2PCF from Equation 14 with the same baseline parameter values as for the EZmocks, i.e.  $z_{\text{mod}} = 0.83$  and

$s_{\parallel}^{\text{max}} = 190 h^{-1}\text{Mpc}$ , for which we observed that the systematic effects injected in the mocks were optimally reduced.

Cosmological parameter measurements for pure RSD fits with the modified 2PCF (‘baseline’ of RSD Modified 2PCF) are significantly different from those with the standard 2PCF: the value of  $\alpha_{\parallel}$  decreases by 17.8% and those of  $\alpha_{\perp}$  and  $f\sigma_8$  increase by 12.6% and 146.5%, respectively. Now 293/1000 mocks have a smaller value of  $\alpha_{\parallel}$ , 283/1000 a smaller value of  $\alpha_{\perp}$  and there are 135/1000 mocks with a smaller value of  $f\sigma_8$ . Overall the new measurements are all within one sigma from the median of the fits to ‘shuffled- $z$ ’ EZmocks with systematics using the modified 2PCF. Larger differences between fits to data with the standard and modified 2PCFs are observed in 36/1000 and 80/1000 mocks for  $\alpha_{\parallel}$  and  $\alpha_{\perp}$ . However no fit on mocks exhibits a difference as large as that in data for  $f\sigma_8$ .

Adding the post-reconstruction monopole of the standard 2PCF to the pre-reconstruction multipoles of the modified 2PCF for a joined RSD+BAO fit (‘baseline’ of RSD+BAO Modified 2PCF) changes the previous results of pure RSD fits, increasing the value of  $\alpha_{\parallel}$  by 8.2%, that of  $\alpha_{\perp}$  by 2.3% and decreasing the value of  $f\sigma_8$  by 8.9%. There are 285/1000 mocks with a higher value of  $\alpha_{\parallel}$ , 388/1000 with a lower value of  $\alpha_{\perp}$  and 61/1000 mocks with a lower value of  $f\sigma_8$ . In terms of the BAO isotropic shift derived from RSD fits using the modified 2PCF, adding the post-reconstruction monopole increases the value of  $\alpha_{\text{iso}}$  from 0.949 (‘baseline’ of RSD Modified 2PCF) to 0.995 (‘baseline’ of RSD+BAO Modified 2PCF) which is more consistent with the value measured by Raichoor et al. (2020). Compared with the results from BAO+RSD fits using the standard 2PCF, the value of  $\alpha_{\parallel}$  decreases by 10.4%, while those of  $\alpha_{\perp}$  and  $f\sigma_8$  increase by 9.4% and 103.5%, respectively (‘baseline’ of RSD+BAO Modified vs Standard 2PCF). The differences in measured parameter values between fits using the standard or modified 2PCF are more frequent on RSD+BAO fits to EZmocks with systematics than for pure RSD fits: 154/1000 mocks have a larger shift than the observed one for  $\alpha_{\parallel}$  and 139/1000 for  $\alpha_{\perp}$  instead of 36/1000 and 80/1000, respectively, for pure RSD fits as stated above. For  $f\sigma_8$  there is still no mock for which such a difference is observed. We conclude that, as already observed on mocks, the modified 2PCF, being less prone to systematics, provides a more reliable estimator to derive cosmological measure-

	$\alpha_{\parallel}$	$\alpha_{\perp}$	$f\sigma_8$
RSD			
Standard 2PCF			
no systematics & sampled-z, no IC corrections	$1.024^{+0.069}_{-0.071}$	$0.998^{+0.053}_{-0.054}$	$0.454^{+0.057}_{-0.058}$
no systematics, no IC corrections	$0.983^{+0.065}_{-0.068}$	$1.051^{+0.057}_{-0.059}$	$0.435^{+0.055}_{-0.055}$
<b>no systematics</b>	<b><math>1.003^{+0.067}_{-0.067}</math></b>	<b><math>1.010^{+0.053}_{-0.055}</math></b>	<b><math>0.455^{+0.057}_{-0.055}</math></b>
all systematics	$1.006^{+0.075}_{-0.073}$	$0.988^{+0.058}_{-0.056}$	$0.415^{+0.056}_{-0.057}$
Modified 2PCF			
<b>no systematics, baseline (<math>s_{\parallel}^{\max} = 190 h^{-1}\text{Mpc}</math>, <math>z_{\text{mod}} = 0.83</math>)</b>	<b><math>0.999^{+0.067}_{-0.070}</math></b>	<b><math>1.011^{+0.053}_{-0.056}</math></b>	<b><math>0.462^{+0.066}_{-0.067}</math></b>
no systematics, $s_{\parallel}^{\max} = 100 h^{-1}\text{Mpc}$ , $z_{\text{mod}} = 0.84$	$0.996^{+0.070}_{-0.064}$	$1.011^{+0.054}_{-0.048}$	$0.462^{+0.060}_{-0.056}$
no systematics, $s_{\parallel}^{\max} = 180 h^{-1}\text{Mpc}$ , $z_{\text{mod}} = 0.83$	$1.004^{+0.066}_{-0.070}$	$1.015^{+0.054}_{-0.058}$	$0.461^{+0.062}_{-0.055}$
no systematics, $s_{\parallel}^{\max} = 190 h^{-1}\text{Mpc}$ , $z_{\text{mod}} = 0.82$	$0.999^{+0.067}_{-0.070}$	$1.012^{+0.054}_{-0.055}$	$0.464^{+0.071}_{-0.073}$
no systematics, $s_{\parallel}^{\max} = 190 h^{-1}\text{Mpc}$ , $z_{\text{mod}} = 0.84$	$1.001^{+0.066}_{-0.067}$	$1.011^{+0.054}_{-0.054}$	$0.460^{+0.065}_{-0.061}$
no systematics, $s_{\parallel}^{\max} = 200 h^{-1}\text{Mpc}$ , $z_{\text{mod}} = 0.83$	$1.001^{+0.063}_{-0.069}$	$1.013^{+0.056}_{-0.055}$	$0.462^{+0.068}_{-0.069}$
no systematics, $s_{\parallel}^{\max} = 200 h^{-1}\text{Mpc}$ , $z_{\text{mod}} = 0.87$	$1.002^{+0.066}_{-0.071}$	$1.012^{+0.053}_{-0.055}$	$0.459^{+0.057}_{-0.057}$
no systematics, no cut	$1.020^{+0.088}_{-0.082}$	$1.012^{+0.055}_{-0.063}$	$0.435^{+0.112}_{-0.110}$
<b>all systematics, baseline (<math>s_{\parallel}^{\max} = 190 h^{-1}\text{Mpc}</math>, <math>z_{\text{mod}} = 0.83</math>)</b>	<b><math>0.996^{+0.075}_{-0.075}</math></b>	<b><math>1.001^{+0.063}_{-0.062}</math></b>	<b><math>0.454^{+0.066}_{-0.065}</math></b>
all systematics, $s_{\parallel}^{\max} = 100 h^{-1}\text{Mpc}$ , $z_{\text{mod}} = 0.84$	$0.995^{+0.073}_{-0.070}$	$0.986^{+0.063}_{-0.056}$	$0.422^{+0.057}_{-0.059}$
all systematics, $s_{\parallel}^{\max} = 180 h^{-1}\text{Mpc}$ , $z_{\text{mod}} = 0.82$	$1.001^{+0.072}_{-0.072}$	$1.006^{+0.062}_{-0.060}$	$0.454^{+0.068}_{-0.067}$
all systematics, $s_{\parallel}^{\max} = 180 h^{-1}\text{Mpc}$ , $z_{\text{mod}} = 0.83$	$0.999^{+0.073}_{-0.076}$	$1.001^{+0.063}_{-0.068}$	$0.449^{+0.065}_{-0.066}$
all systematics, $s_{\parallel}^{\max} = 180 h^{-1}\text{Mpc}$ , $z_{\text{mod}} = 0.84$	$0.995^{+0.073}_{-0.072}$	$0.998^{+0.063}_{-0.065}$	$0.445^{+0.059}_{-0.061}$
all systematics, $s_{\parallel}^{\max} = 190 h^{-1}\text{Mpc}$ , $z_{\text{mod}} = 0.82$	$1.002^{+0.071}_{-0.073}$	$1.007^{+0.066}_{-0.057}$	$0.455^{+0.068}_{-0.066}$
all systematics, $s_{\parallel}^{\max} = 190 h^{-1}\text{Mpc}$ , $z_{\text{mod}} = 0.84$	$1.000^{+0.072}_{-0.073}$	$1.001^{+0.062}_{-0.063}$	$0.447^{+0.065}_{-0.069}$
all systematics, $s_{\parallel}^{\max} = 200 h^{-1}\text{Mpc}$ , $z_{\text{mod}} = 0.82$	$1.003^{+0.069}_{-0.072}$	$1.009^{+0.062}_{-0.056}$	$0.457^{+0.079}_{-0.074}$
all systematics, $s_{\parallel}^{\max} = 200 h^{-1}\text{Mpc}$ , $z_{\text{mod}} = 0.83$	$1.003^{+0.069}_{-0.071}$	$1.008^{+0.061}_{-0.056}$	$0.453^{+0.071}_{-0.071}$
all systematics, $s_{\parallel}^{\max} = 200 h^{-1}\text{Mpc}$ , $z_{\text{mod}} = 0.84$	$0.996^{+0.073}_{-0.063}$	$1.002^{+0.061}_{-0.062}$	$0.452^{+0.066}_{-0.065}$
all systematics, $s_{\parallel}^{\max} = 200 h^{-1}\text{Mpc}$ , $z_{\text{mod}} = 0.87$	$0.997^{+0.071}_{-0.069}$	$0.996^{+0.062}_{-0.062}$	$0.438^{+0.056}_{-0.058}$
all systematics, no cut	$1.018^{+0.086}_{-0.082}$	$1.011^{+0.060}_{-0.061}$	$0.436^{+0.110}_{-0.109}$
all systematics, +1/2bins	$1.002^{+0.069}_{-0.070}$	$1.008^{+0.064}_{-0.071}$	$0.459^{+0.068}_{-0.073}$
RSD+BAO			
Standard 2PCF			
no systematics	$1.005^{+0.072}_{-0.073}$	$1.012^{+0.050}_{-0.052}$	$0.459^{+0.061}_{-0.059}$
all systematics	$0.979^{+0.080}_{-0.083}$	$0.969^{+0.062}_{-0.065}$	$0.418^{+0.062}_{-0.058}$
Modified 2PCF			
no systematics	$0.996^{+0.067}_{-0.069}$	$1.009^{+0.046}_{-0.045}$	$0.462^{+0.064}_{-0.065}$
all systematics	$0.997^{+0.068}_{-0.069}$	$1.003^{+0.052}_{-0.053}$	$0.455^{+0.066}_{-0.065}$
all systematics, +1/2bins	$0.997^{+0.070}_{-0.068}$	$1.004^{+0.054}_{-0.052}$	$0.460^{+0.071}_{-0.073}$

**Table 3. Results of RSD and BAO+RSD fits on 1000 EZmocks.** We present the median and the 0.16 and 0.84 quantiles of the distribution of the best-fit values. Except for the first measurement, we use 'shuffled-z' EZmocks.

ments from data and that adding BAO regularizes the measurements.

The left panel of Figure 10 shows the pre-reconstruction multipoles and the post-reconstruction monopole of the modified 2PCF used for the RSD+BAO fits along with predictions from the best-fit model. The agreement between the best-fit model and the measured multipoles is good and the excess of clustering in the quadrupole at intermediate scale is significantly reduced in data, no longer driving the fit. On the right panel we show the predictions from the standard 2PCF model using best-fit values from the RSD+BAO fit

with the modified 2PCF (in red on the graph). The model agrees quite well with the measured standard 2PCF multipoles, except at intermediate scales for the quadrupole, which are contaminated by systematics; we also note a better agreement for the lower  $s$  bins for the monopole. The posteriors of the modified 2PCF RSD+BAO fit are presented in Figure 11 (red contours). As discussed above, removing angular modes with the modified 2PCF leads to different cosmological parameter estimates than with the standard 2PCF, though with similar degeneracies. We also note that due to informa-



tion loss with the modified 2PCF, the posteriors are slightly wider than in the standard case.

We now test the robustness of the results from the above analysis with the modified 2PCF. Parameters of the latter were varied, removing the cut in the correction terms (i.e. using Equation 13), and varying  $z_{\text{mod}}$  and  $s_{\parallel}^{\text{max}}$  values, since, as stated in Section 6.3, those are the most sensitive parameters. As for EZmocks, we vary  $z_{\text{mod}}$  and  $s_{\parallel}^{\text{max}}$  values in the ranges  $\Delta z_{\text{mod}} \in \{0, \pm 0.01\}$  and  $\Delta s_{\parallel}^{\text{max}} \in \{0, \pm 10\} h^{-1}\text{Mpc}$  around their baseline values. We note that within the explored region, deviations in data measurements from the baseline results are in agreement with expectations from the mocks. Indeed staying on the diagonal defined by the crosses in Figure 7 gives small shifts with respect to baseline measurements and for most of the tested  $(z_{\text{mod}}, s_{\parallel}^{\text{max}})$  values, the deviations increase in accordance with the  $\chi^2_{\text{mod}}(z_{\text{mod}}, s_{\parallel}^{\text{max}})$  value from the mocks. In agreement with the mocks, the largest deviations are observed for  $z_{\text{mod}} = 0.84$  and  $s_{\parallel}^{\text{max}} = 180$ . Shifts with respect to our baseline results in the pure RSD case amount to 8.0%, 1.9% and 20.7% in  $\alpha_{\parallel}$ ,  $\alpha_{\perp}$  and  $f\sigma_8$  respectively. Shifts are slightly smaller in the RSD+BAO case: 4.2%, 1.8% and 17.2%. In the RSD case, such deviations are consistent with mocks at the  $3\sigma$  level for  $\alpha_{\parallel}$  and at the  $2\sigma$  level for  $\alpha_{\perp}$ , but no mock shows a difference as large as for data for  $f\sigma_8$ . As those parameter values are not optimal for our analysis (see Figure 7) large shifts are not surprising. Moreover, we know that our data sample suffers from systematic effects that are more complex than those introduced in the mocks, as observed when using the standard 2PCF (see Figure 3). Nevertheless, we adopt a conservative approach and add the above shifts, i.e. 4.2%, 1.8% and 17.2% in  $\alpha_{\parallel}$ ,  $\alpha_{\perp}$  and  $f\sigma_8$ , to our systematic budget to account for residual, uncorrected systematics in data. This error also includes the uncertainty due to the sensitivity of our results to the modified 2PCF free parameters.

When moving the  $s$ -bin centres by half a bin width (i.e.  $4 h^{-1}\text{Mpc}$ ), we observe large changes especially in  $\alpha_{\parallel}$ . The shifts for RSD+BAO fits are 5.7%, 0.2%, 1.7% in  $\alpha_{\parallel}$ ,  $\alpha_{\perp}$  and  $f\sigma_8$ , respectively. Larger shifts are observed in 124/1000, 788/1000 and 766/1000 mocks in  $\alpha_{\parallel}$ ,  $\alpha_{\perp}$  and  $f\sigma_8$  respectively. The observed shifts in data are therefore compatible with statistical fluctuations.

The measurements are stable when using the covariance matrix from 'shuffled-z' EZmocks without systematics: in the RSD+BAO case, we observe shifts of 0.6%, 0.2%, 1.7% in  $\alpha_{\parallel}$ ,  $\alpha_{\perp}$  and  $f\sigma_8$ , compatible with statistical fluctuations. They remain stable also when we remove the  $w_{\text{noz}}$  weights when computing the correlation function: we observe small shifts of 0.3% in  $\alpha_{\parallel}$ , 0.4% in  $\alpha_{\perp}$  and 1.7% in  $f\sigma_8$ . We finally checked the impact of changing the BOSS fiducial cosmology (Equation 7) to the OR one (Equation 6). Compared to our baseline results in the pure RSD case, we see deviations of 2.1% in  $\alpha_{\parallel}$ , 0.3% in  $\alpha_{\perp}$  and 2.6% in  $f\sigma_8$ . Those deviations are compatible with statistical fluctuations and considering the large systematic uncertainty already included for data instabilities, we do not add an extra systematic error.

Taking into account all systematic uncertainties from Table 5 and adding them in quadrature to statistical errors, we quote our final measurements from the joined RSD+BAO fit with multipoles of the modified 2PCF at the effective redshift  $z_{\text{eff}} = 0.85$ :

$$\alpha_{\parallel} = 1.034^{+0.105}_{-0.111}, \quad \alpha_{\perp} = 0.976^{+0.051}_{-0.051}, \quad f\sigma_8 = 0.348^{+0.103}_{-0.104}. \quad (40)$$

The linear bias of our combined data sample for a  $\sigma_8$  fixed at our

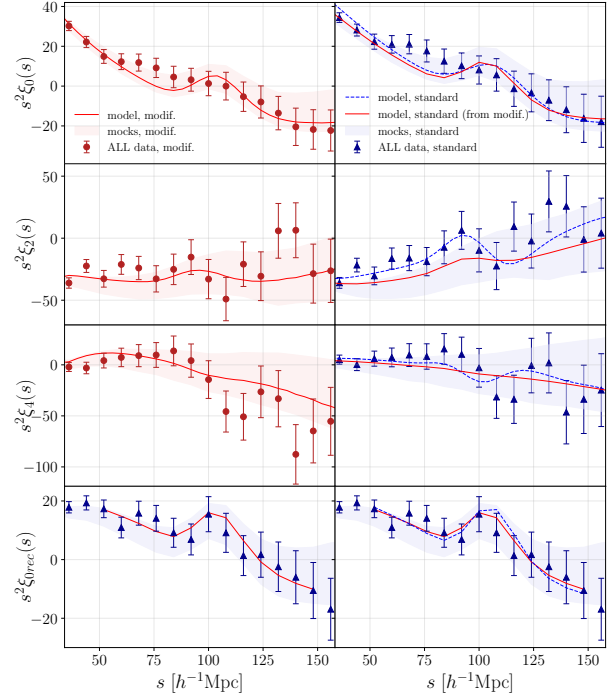


**Figure 10.** 2PCF multipoles from eBOSS ELG data compared to CLPTGS models. Left: pre-reconstruction multipoles from the modified 2PCF of Equation 14 with baseline parameter values, and post-reconstruction monopole from the standard 2PCF. The modified 2PCF model (in red) is that from the RSD+BAO fit to the four multipoles in the left panels. Right: multipoles of the standard 2PCF compared to the standard 2PCF model with parameters from the RSD+BAO fit to the multipoles in the right panels (in blue) and in the left panels (in red). The bands are one sigma dispersions of the EZmocks for the modified (red) and standard (blue) 2PCF.

fiducial cosmology (Equation 7) is measured to be  $b_1 = 1.52^{+0.16}_{-0.14}$ , where quoted errors are statistical only.

Converting the AP parameters into Hubble and comoving angular distances using Equations 33, we finally have:

$$\begin{aligned} D_H(z_{\text{eff}})/r_{\text{drag}} &= 19.1^{+1.9}_{-2.1} \\ D_M(z_{\text{eff}})/r_{\text{drag}} &= 19.9 \pm 1.0 \\ f\sigma_8(z_{\text{eff}}) &= 0.35 \pm 0.10 \end{aligned} \quad (41)$$

Those values are in agreement within less than one sigma with the values measured in Fourier space as reported in de Mattia et al. (2020). This allows to combine our two measurements into a consensus one for the eBOSS ELG sample, as presented in de Mattia et al. (2020):

$$\begin{aligned} D_H(z_{\text{eff}})/r_{\text{drag}} &= 19.6^{+2.2}_{-2.1} \\ D_M(z_{\text{eff}})/r_{\text{drag}} &= 19.5 \pm 1.0 \\ f\sigma_8(z_{\text{eff}}) &= 0.315 \pm 0.095 \end{aligned} \quad (42)$$

These results are compatible with a  $\Lambda\text{CDM}$  model using a Planck cosmology.

## 8 CONCLUSION

We performed a pure RSD analysis and a joined RSD+BAO analysis in configuration space for the eBOSS DR16 Emission Line Galaxies sample described in Raichoor et al. (2020). This sample is

	$\alpha_{\parallel}$	$\alpha_{\perp}$	$f\sigma_8$
RSD			
Standard 2PCF			
baseline	$1.163^{+0.087}_{-0.083}$ (1.159)	$0.847^{+0.071}_{-0.082}$ (0.855)	$0.155^{+0.069}_{-0.060}$ (0.074)
$z_{\min} = 0.6$	$1.212^{+0.086}_{-0.088}$ (1.188)	$0.801^{+0.096}_{-0.109}$ (0.847)	$0.100^{+0.079}_{-0.069}$ (0.061)
Modified 2PCF			
<b>baseline (<math>s_{\parallel}^{\max} = 190 h^{-1} \text{Mpc}</math>, <math>z_{\text{mod}} = 0.83</math>)</b>	<b><math>0.956^{+0.125}_{-0.109}</math> (0.863)</b>	<b><math>0.954^{+0.046}_{-0.050}</math> (0.950)</b>	<b><math>0.382^{+0.078}_{-0.094}</math> (0.424)</b>
no sys. cov	$0.983^{+0.132}_{-0.141}$ (0.854)	$0.965^{+0.050}_{-0.053}$ (0.954)	$0.373^{+0.083}_{-0.100}$ (0.429)
no $w_{\text{noz}}$	$0.949^{+0.13}_{-0.107}$ (0.862)	$0.956^{+0.053}_{-0.055}$ (0.951)	$0.385^{+0.081}_{-0.083}$ (0.423)
+1/2bins	$0.864^{+0.154}_{-0.088}$ (0.813)	$0.946^{+0.057}_{-0.054}$ (0.942)	$0.394^{+0.077}_{-0.095}$ (0.405)
OR cosmology (rescaled)	$0.976^{+0.113}_{-0.102}$ (0.907)	$0.951^{+0.050}_{-0.045}$ (0.954)	$0.372^{+0.080}_{-0.093}$ (0.401)
$z_{\min} = 0.6$	$1.018^{+0.121}_{-0.121}$ (0.929)	$0.935^{+0.039}_{-0.045}$ (0.942)	$0.323^{+0.081}_{-0.090}$ (0.366)
$s_{\parallel}^{\max} = 180 h^{-1} \text{Mpc}$ , $z_{\text{mod}} = 0.82$	$0.968^{+0.124}_{-0.115}$ (0.862)	$0.948^{+0.050}_{-0.051}$ (0.948)	$0.368^{+0.079}_{-0.088}$ (0.421)
$s_{\parallel}^{\max} = 180 h^{-1} \text{Mpc}$ , $z_{\text{mod}} = 0.83$	$0.993^{+0.121}_{-0.131}$ (0.862)	$0.945^{+0.049}_{-0.053}$ (0.935)	$0.348^{+0.084}_{-0.099}$ (0.404)
$s_{\parallel}^{\max} = 180 h^{-1} \text{Mpc}$ , $z_{\text{mod}} = 0.84$	$1.029^{+0.104}_{-0.141}$ (0.875)	$0.938^{+0.050}_{-0.051}$ (0.931)	$0.311^{+0.092}_{-0.087}$ (0.382)
$s_{\parallel}^{\max} = 190 h^{-1} \text{Mpc}$ , $z_{\text{mod}} = 0.82$	$0.925^{+0.139}_{-0.094}$ (0.855)	$0.952^{+0.055}_{-0.052}$ (0.951)	$0.404^{+0.077}_{-0.088}$ (0.438)
$s_{\parallel}^{\max} = 190 h^{-1} \text{Mpc}$ , $z_{\text{mod}} = 0.84$	$0.988^{+0.118}_{-0.125}$ (0.869)	$0.946^{+0.047}_{-0.052}$ (0.943)	$0.350^{+0.085}_{-0.093}$ (0.404)
$s_{\parallel}^{\max} = 200 h^{-1} \text{Mpc}$ , $z_{\text{mod}} = 0.82$	$0.906^{+0.138}_{-0.083}$ (0.847)	$0.970^{+0.062}_{-0.053}$ (0.956)	$0.444^{+0.075}_{-0.082}$ (0.458)
$s_{\parallel}^{\max} = 200 h^{-1} \text{Mpc}$ , $z_{\text{mod}} = 0.83$	$0.908^{+0.126}_{-0.085}$ (0.852)	$0.961^{+0.051}_{-0.051}$ (0.955)	$0.424^{+0.074}_{-0.081}$ (0.446)
$s_{\parallel}^{\max} = 200 h^{-1} \text{Mpc}$ , $z_{\text{mod}} = 0.84$	$0.934^{+0.136}_{-0.093}$ (0.880)	$0.957^{+0.049}_{-0.055}$ (0.953)	$0.391^{+0.079}_{-0.085}$ (0.226)
no cut	$0.936^{+0.190}_{-0.108}$ (0.84)	$0.958^{+0.061}_{-0.061}$ (0.958)	$0.405^{+0.133}_{-0.196}$ (0.458)
Separate caps			
SGC, standard 2PCF	$1.100^{+0.090}_{-0.085}$ (1.100)	$0.946^{+0.077}_{-0.078}$ (0.955)	$0.236^{+0.082}_{-0.087}$ (0.215)
SGC, modified 2PCF	$1.041^{+0.093}_{-0.097}$ (1.032)	$1.026^{+0.118}_{-0.091}$ (1.008)	$0.378^{+0.102}_{-0.116}$ (0.329)
NGC, standard 2PCF	$1.196^{+0.113}_{-0.212}$ (1.400)	$0.759^{+0.085}_{-0.067}$ (0.725)	$0.147^{+0.095}_{-0.059}$ (0.060)
NGC, modified 2PCF	$0.875^{+0.377}_{-0.089}$ (0.822)	$0.932^{+0.371}_{-0.104}$ (0.921)	$0.463^{+0.095}_{-0.108}$ (0.464)
RSD+BAO			
Standard 2PCF			
baseline	$1.154^{+0.071}_{-0.063}$ (1.153)	$0.892^{+0.040}_{-0.045}$ (0.909)	$0.171^{+0.058}_{-0.059}$ (0.157)
$z_{\min} = 0.6$	$1.198^{+0.060}_{-0.069}$ (1.183)	$0.846^{+0.046}_{-0.045}$ (0.860)	$0.109^{+0.064}_{-0.059}$ (0.104)
Modified 2PCF			
<b>baseline (<math>s_{\parallel}^{\max} = 190 h^{-1} \text{Mpc}</math>, <math>z_{\text{mod}} = 0.83</math>)</b>	<b><math>1.034^{+0.091}_{-0.098}</math> (1.042)</b>	<b><math>0.976^{+0.045}_{-0.045}</math> (0.978)</b>	<b><math>0.348^{+0.082}_{-0.084}</math> (0.316)</b>
no sys. cov	$1.040^{+0.093}_{-0.112}$ (1.050)	$0.974^{+0.046}_{-0.043}$ (0.978)	$0.342^{+0.085}_{-0.091}$ (0.308)
no $w_{\text{noz}}$	$1.037^{+0.089}_{-0.097}$ (1.044)	$0.980^{+0.044}_{-0.044}$ (0.981)	$0.342^{+0.088}_{-0.083}$ (0.314)
+1/2bins	$0.975^{+0.120}_{-0.101}$ (0.904)	$0.978^{+0.055}_{-0.049}$ (1.003)	$0.354^{+0.094}_{-0.110}$ (0.378)
$z_{\min} = 0.6$	$1.082^{+0.083}_{-0.102}$ (1.098)	$0.950^{+0.035}_{-0.041}$ (0.954)	$0.299^{+0.080}_{-0.076}$ (0.262)
$s_{\parallel}^{\max} = 180 h^{-1} \text{Mpc}$ , $z_{\text{mod}} = 0.82$	$1.047^{+0.082}_{-0.106}$ (1.049)	$0.971^{+0.043}_{-0.046}$ (0.972)	$0.333^{+0.082}_{-0.083}$ (0.304)
$s_{\parallel}^{\max} = 180 h^{-1} \text{Mpc}$ , $z_{\text{mod}} = 0.83$	$1.057^{+0.082}_{-0.097}$ (1.069)	$0.966^{+0.045}_{-0.043}$ (0.966)	$0.317^{+0.082}_{-0.076}$ (0.281)
$s_{\parallel}^{\max} = 180 h^{-1} \text{Mpc}$ , $z_{\text{mod}} = 0.84$	$1.077^{+0.077}_{-0.100}$ (1.087)	$0.958^{+0.042}_{-0.043}$ (0.957)	$0.288^{+0.081}_{-0.073}$ (0.255)
$s_{\parallel}^{\max} = 190 h^{-1} \text{Mpc}$ , $z_{\text{mod}} = 0.82$	$1.027^{+0.087}_{-0.103}$ (0.989)	$0.978^{+0.050}_{-0.045}$ (0.987)	$0.361^{+0.084}_{-0.086}$ (0.365)
$s_{\parallel}^{\max} = 190 h^{-1} \text{Mpc}$ , $z_{\text{mod}} = 0.84$	$1.058^{+0.082}_{-0.090}$ (1.069)	$0.968^{+0.044}_{-0.045}$ (0.967)	$0.319^{+0.080}_{-0.081}$ (0.282)
$s_{\parallel}^{\max} = 200 h^{-1} \text{Mpc}$ , $z_{\text{mod}} = 0.82$	$0.988^{+0.096}_{-0.089}$ (0.946)	$0.991^{+0.051}_{-0.047}$ (0.997)	$0.398^{+0.079}_{-0.087}$ (0.410)
$s_{\parallel}^{\max} = 200 h^{-1} \text{Mpc}$ , $z_{\text{mod}} = 0.83$	$1.009^{+0.093}_{-0.097}$ (0.950)	$0.988^{+0.050}_{-0.046}$ (0.995)	$0.383^{+0.079}_{-0.089}$ (0.401)
$s_{\parallel}^{\max} = 200 h^{-1} \text{Mpc}$ , $z_{\text{mod}} = 0.84$	$1.028^{+0.088}_{-0.099}$ (0.980)	$0.979^{+0.044}_{-0.045}$ (0.992)	$0.351^{+0.083}_{-0.084}$ (0.368)
no cut	$1.036^{+0.107}_{-0.131}$ (0.920)	$0.972^{+0.059}_{-0.053}$ (0.997)	$0.339^{+0.145}_{-0.128}$ (0.424)
Separate caps			
SGC, standard 2PCF	$1.074^{+0.085}_{-0.089}$ (1.069)	$0.935^{+0.055}_{-0.059}$ (0.938)	$0.241^{+0.085}_{-0.080}$ (0.225)
SGC, modified 2PCF	$1.025^{+0.086}_{-0.093}$ (1.023)	$0.988^{+0.069}_{-0.062}$ (0.979)	$0.355^{+0.104}_{-0.104}$ (0.314)
NGC, standard 2PCF	$1.229^{+0.089}_{-0.097}$ (1.204)	$0.682^{+0.072}_{-0.035}$ (0.874)	$0.085^{+0.048}_{-0.019}$ (0.163)
NGC, modified 2PCF	$0.872^{+0.168}_{-0.078}$ (0.824)	$0.920^{+0.064}_{-0.072}$ (0.906)	$0.450^{+0.090}_{-0.106}$ (0.458)

**Table 4.** RSD and BAO+RSD fits on the eBOSS ELG sample. We present the median and one sigma errors from the posterior distributions (as being the 0.16/0.84 quantiles from the distribution) and, in brackets, the best-fit value.

	$\alpha_{\parallel}$	$\alpha_{\perp}$	$f\sigma_8$
From Nbody-mocks			
CLPT modelling	1.8%	1.4%	3.2%
From EZmocks			
modelling RIC	2.1%	1.2%	0.2%
modified 2PCF	0.5%	0.4%	2.7%
From data			
uncorrected systematics	4.2%	1.8%	17.2%
Statistical uncertainties	+0.091 -0.098	+0.045 -0.045	+0.082 -0.084
Systematics uncertainties	0.052	0.025	0.062
Total	+0.105 -0.111	+0.051 -0.051	+0.103 -0.104

**Table 5.** Systematic error budget. The last row gives statistical and systematic errors added in quadrature.

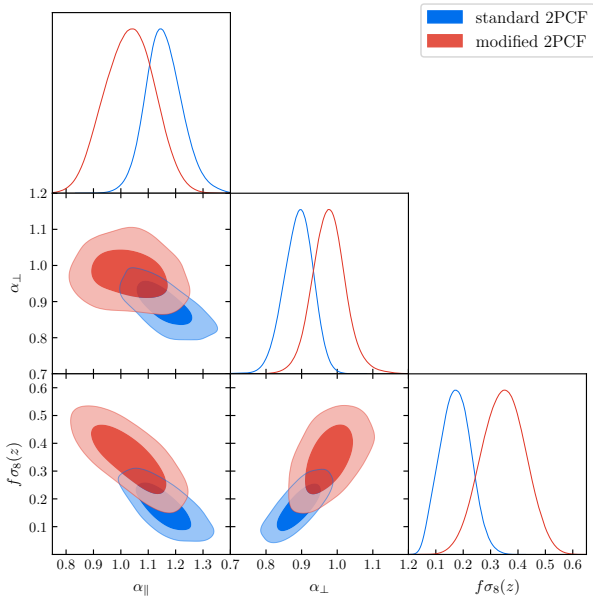


**Figure 11.** Posteriors of the RSD+BAO fits to standard (in blue) and modified (in red) 2PCF multipoles as measured from the eBOSS ELG sample.

composed of 173,736 galaxies with a reliable redshift in the range  $0.6 < z < 1.1$ , covering an effective area of  $\sim 730 \text{ deg}^2$  over the two NGC and SGC regions. The post-reconstruction BAO measurement in configuration space of this sample is analysed in [Raichoor et al. \(2020\)](#). The BAO and RSD measurements in Fourier space and a consensus of our results for the eBOSS ELG sample are presented in [de Mattia et al. \(2020\)](#).

Our RSD fit is done on the  $0.7 < z < 1.1$  data multipoles ( $\ell = 0, 2, 4$ ), using the CLPT-GS theoretical model. As part of the eBOSS ELG mock challenge ([Alam et al. 2020](#)), we first demonstrate the validity of the CLPT-GS model in our fitting range using realistic ELG mocks. Those are built from accurate N-body simulations, populated with a broad range of models describing ELG variety, and split into sets of ‘non-blind’ and ‘blind’ mocks.

A set of approximate mocks, the EZmocks ([Zhao et al. 2020a](#)), are used to estimate the covariance matrix and also to validate the analysis pipeline. As for the data, those EZmocks have redshifts

from randoms selected from the parent galaxy catalogue themselves, in order to properly reproduce the survey radial selection function. However this choice leads to radial mode suppression, which we account for in the correlation function modelling with a correction based on the formalism developed in [de Mattia & Ruhlmann-Kleider \(2019\)](#). We validate and quantify the error budget coming from that correction using the EZmocks.

The eBOSS ELG data sample is affected by residual angular systematics, which need to be corrected for before proceeding to RSD fits, to avoid biasing our cosmological measurements. To mitigate these angular systematics, we performed our RSD fits using a modified 2PCF estimator, which is computed consistently for the data, the EZmocks and the model, discarding the small scales where the accuracy of the CLPT-GS model is not demonstrated. We carefully assessed the validity of that approach with a set of the EZmocks in which we injected data-like systematics. We demonstrated the efficiency of our approach to remove angular systematics.

Once the validity of the RSD analysis and its error budget have been established, we performed a similar analysis for the isotropic BAO measurement on the reconstructed monopole ( $\ell = 0_{\text{rec}}$ ).

Finally, we did a series of tests on the RSD-only and RSD+BAO results from the ELG data sample. Due to the non-gaussianity of our results, the RSD+BAO joint fits are performed by combining their likelihoods. Taking into account all systematic errors from our budget as well as statistical errors, we obtain our final measurements from the joint RSD+BAO fit to the modified 2PCF multipoles at the effective redshift  $z_{\text{eff}} = 0.85$ :  $a_{\parallel} = 1.034^{+0.105}_{-0.111}$ ,  $a_{\perp} = 0.976^{+0.051}_{-0.051}$ , and  $f\sigma_8 = 0.348^{+0.103}_{-0.104}$ . From this joint analysis we obtain  $D_H(z_{\text{eff}})/r_{\text{drag}} = 19.1^{+1.9}_{-2.1}$ ,  $D_M(z_{\text{eff}})/r_{\text{drag}} = 19.9 \pm 1.0$  and  $f\sigma_8(z_{\text{eff}}) = 0.35 \pm 0.10$ . These results are in agreement within less than  $1\sigma$  with those found by [de Mattia et al. \(2020\)](#) with a RSD+BAO analysis performed in Fourier space. We also present a consensus result between the two analyses, fully described in [de Mattia et al. \(2020\)](#):  $D_H(z_{\text{eff}})/r_{\text{drag}} = 19.6^{+2.2}_{-2.1}$ ,  $D_M(z_{\text{eff}})/r_{\text{drag}} = 19.5 \pm 1.0$  and  $f\sigma_8(z_{\text{eff}}) = 0.315 \pm 0.095$ , which are in agreement with  $\Lambda$ CDM predictions based on Planck parameters.

The presence of remaining angular systematics in the eBOSS ELG data led us to develop a specific analysis tool, the modified 2PCF estimator presented in this paper, that we consistently applied to the data, mocks and RSD model. Such an approach, along with other developments based on the eBOSS data ([Kong et al. 2020](#); [Mohammad et al. 2020](#); [Rezaie et al. 2020](#)), will pave the way for the analysis of the RSD and BAO in the next generation of surveys that massively rely on ELGs, such as DESI, *Euclid*, PFS or *WFIRST*.

## ACKNOWLEDGEMENTS

AT, AR and CZ acknowledge support from the SNF grant 200020\_175751. AR, JPK acknowledge support from the ERC advanced grant LIDA. AdM acknowledges support from the P2IO LabEx (ANR-10-LABX-0038) in the framework “Investissements d’Avenir” (ANR-11-IDEX-0003-01) managed by the Agence Nationale de la Recherche (ANR, France). AJR is grateful for support from the Ohio State University Center for Cosmology and Particle Physics. SA is supported by the European Research Council (ERC) through the COSFORM Research Grant (#670193). VGP acknowledges support from the European Union’s Horizon 2020 research and innovation programme (ERC grant #769130).

EMM acknowledges support from the European Research Council (ERC) under the European Union's Horizon 2020 research and innovation programme (grant agreement No 693024). G.R. acknowledges support from the National Research Foundation of Korea (NRF) through Grants No. 2017R1E1A1A01077508 and No. 2020R1A2C1005655 funded by the Korean Ministry of Education, Science and Technology (MoEST), and from the faculty research fund of Sejong University. Authors acknowledge support from the ANR eBOSS project (ANR-16-CE31-0021) of the French National Research Agency.

Funding for the Sloan Digital Sky Survey IV has been provided by the Alfred P. Sloan Foundation, the U.S. Department of Energy Office of Science, and the Participating Institutions. SDSS-IV acknowledges support and resources from the Center for High-Performance Computing at the University of Utah. The SDSS web site is [www.sdss.org](http://www.sdss.org).

SDSS-IV is managed by the Astrophysical Research Consortium for the Participating Institutions of the SDSS Collaboration including the Brazilian Participation Group, the Carnegie Institution for Science, Carnegie Mellon University, the Chilean Participation Group, the Ecole Polytechnique Fédérale de Lausanne (EPFL), the French Participation Group, Harvard-Smithsonian Center for Astrophysics, Instituto de Astrofísica de Canarias, The Johns Hopkins University, Kavli Institute for the Physics and Mathematics of the Universe (IPMU) University of Tokyo, the Korean Participation Group, Lawrence Berkeley National Laboratory, Leibniz Institut für Astrophysik Potsdam (AIP), Max-Planck-Institut für Astronomie (MPIA Heidelberg), Max-Planck-Institut für Astrophysik (MPA Garching), Max-Planck-Institut für Extraterrestrische Physik (MPE), National Astronomical Observatories of China, New Mexico State University, New York University, University of Notre Dame, Observatório Nacional / MCTI, The Ohio State University, Pennsylvania State University, Shanghai Astronomical Observatory, United Kingdom Participation Group, Universidad Nacional Autónoma de México, University of Arizona, University of Colorado Boulder, University of Oxford, University of Portsmouth, University of Utah, University of Virginia, University of Washington, University of Wisconsin, Vanderbilt University, and Yale University.

This research used resources of the National Energy Research Scientific Computing Center, a DOE Office of Science User Facility supported by the Office of Science of the U.S. Department of Energy under Contract No. DE-AC02-05CH11231.

## DATA AVAILABILITY

Correlation functions, covariance matrices, and resulting likelihoods for cosmological parameters are (will be made) available (after acceptance) via the SDSS Science Archive Server: <https://sas.sdss.org/> (with the exact address tbd).

## REFERENCES

Abolfathi B., et al., 2018, *ApJS*, 235, 42  
 Alam S., Ho S., Vargas-Magaña M., Schneider D. P., 2015, *MNRAS*, 453, 1754  
 Alam S., et al., 2017, *MNRAS*, 470, 2617  
 Alam S., Peacock J. A., Kraljic K., Ross A. J., Comparat J., 2019, arXiv e-prints, p. arXiv:1910.05095  
 Alam S., et al., 2020, submitted  
 Alcock C., Paczynski B., 1979, *Nature*, 281, 358

Alonso D., 2012, preprint  
 Anderson L., et al., 2014, *MNRAS*, 441, 24  
 Ata M., Baumgarten F., Bautista J., Beutler F., et al. 2018, *MNRAS*, 473, 4773  
 Avila S., et al., 2020, submitted  
 Bautista J. E., et al., 2018, *ApJ*, 863, 110  
 Bautista J., et al., 2020, submitted  
 Behroozi P. S., Wechsler R. H., Wu H.-Y., 2013, *ApJ*, 762, 109  
 Blanton M. R., et al., 2017, *AJ*, 154, 28  
 Burden A., Percival W. J., Howlett C., 2015, *MNRAS*, 453, 456  
 Burden A., Padmanabhan N., Cahn R. N., White M. J., Samushia L., 2017, *J. Cosmology Astropart. Phys.*, 3, 001  
 Carlson J., Reid B., White M., 2013, *MNRAS*, 429, 1674  
 Chuang C.-H., Wang Y., 2013, *MNRAS*, 431, 2634  
 Chuang C.-H., Zhao C., Prada F., Munari E., et al. 2015, *MNRAS*, 452, 686  
 Cole S., Kaiser N., 1989, *MNRAS*, 237, 1127  
 Cole S., et al., 2005, *Monthly Notices of the Royal Astronomical Society*, 362, 505  
 Collaboration e., et al., 2020, submitted  
 DESI Collaboration et al., 2016a, preprint  
 DESI Collaboration et al., 2016b, arXiv e-prints  
 Davis M., Efstathiou G., Frenk C. S., White S. D. M., 1985, *ApJ*, 292, 371  
 Dawson K. S., et al., 2013, *AJ*, 145, 10  
 Dawson K. S., et al., 2016, *AJ*, 151, 44  
 Dey A., et al., 2019, *AJ*, 157, 168  
 Doré O., et al., 2018, arXiv e-prints, p. arXiv:1804.03628  
 Eisenstein D. J., Hu W., 1998, *ApJ*, 496, 605  
 Eisenstein D. J., et al., 2005, *ApJ*, 633, 560  
 Eisenstein D. J., Seo H.-J., Sirko E., Spergel D. N., 2007, *ApJ*, 664, 675  
 Feldman H. A., Kaiser N., Peacock J. A., 1994, *ApJ*, 426, 23  
 Feroz F., Hobson M. P., M. B., 2009, *MNRAS*, 398, 1601  
 Gil-Marín H., et al., 2018, *MNRAS*, 477, 1604  
 Gil-Marín H., et al., 2020, submitted  
 Gonzalez-Perez V., et al., 2018, *MNRAS*, 474, 4024  
 Grieb J. N., Sanchez A., Salazar-Albornoz S., Dalla Vecchia C., 2016, *MNRAS*, 457, 1577  
 Gunn J. E., et al., 2006, *AJ*, 131, 2332  
 Guzzo L., et al., 2008, *Nature*, 451, 541  
 Hamilton A. J. S., 1992, *ApJ*, 385, L5  
 Hartlap J., Simon P., Schneider P., 2007, *A&A*, 464, 399  
 Heitmann K., et al., 2019, *ApJS*, 245, 16  
 Hou J., et al., 2020, submitted  
 Hu W., Sugiyama N., 1996, *ApJ*, 471, 542  
 Icaza-Lizaola M., et al., 2019, arXiv e-prints  
 Jackson J. C., 1972, *MNRAS*, 156, 1P  
 James F., Roos M., 1975, *Computer Physics Communications*, 10, 343  
 Kaiser N., 1987, *MNRAS*, 227, 1  
 Kalus B., Percival W. J., Bacon D. J., Samushia L., 2016, *MNRAS*, 463, 467  
 Klypin A., Yepes G., Gottlöber S., Prada F., Heß S., 2016, *MNRAS*, 457, 4340  
 Kong H., et al., 2020, in prep.  
 Landy S., Szalay A. S., 1993, *Astrophysical Journal*, 412, 64  
 Laureijs R., et al., 2011, arXiv e-prints, p. arXiv:1110.3193  
 Lewis A., Challinor A., Lasenby A., 2000, *ApJ*, 538, 473  
 Limber D. N., 1953, *ApJ*, 117, 134  
 Lin S., et al., 2020, submitted  
 Linder E. V., Cahn R. N., 2007, *Astroparticle Physics*, 28, 481  
 Lyke B. W., et al., 2020, submitted  
 Matsubara T., 2008, *Phys. Rev. D*, 78, 083519  
 Mohammad F., et al., 2020, submitted  
 Neveux R., et al., 2020, submitted  
 Peebles P. J. E., 1980, The large-scale structure of the universe  
 Percival W. J., Ross A. J., Sanchez A., Samushia L. e. a., 2014, *MNRAS*, 439, 2531  
 Perlmuter S., et al., 1999, *ApJ*, 517, 565  
 Pinol L., Cahn R. N., Seljak U., White M., 2017, *J. Cosmology Astropart. Phys.*, 2017, 008



- Planck Collaboration et al., 2016, *A&A*, 594, A13  
 Raichoor A., Comparat J., Delubac T., Kneib J.-P., Yèche C., 2017, *MNRAS*  
 Raichoor A., et al., 2020, submitted  
 Reid B. A., White M., 2011, *MNRAS*, 417, 1913  
 Rezaie M., Seo H.-J., Ross A. J., Bunesco R. C., 2020, *MNRAS*, 495, 1613  
 Riess A. G., et al., 1998, *AJ*, 116, 1009  
 Ross A. J., et al., 2011, *MNRAS*, 417, 1350  
 Ross A. J., et al., 2012, *MNRAS*, 424, 564  
 Ross A. J., et al., 2016, *MNRAS*, 464, 1168  
 Ross A. J., et al., 2020, submitted  
 Rossi G., et al., 2020, submitted  
 Rybicki G. B., Press W. H., 1992, *ApJ*, 398, 169  
 Satpathy S., et al., 2017, *MNRAS*, 469, 1369  
 Seo H.-J., Beutler F., Ross A. J., Saito S., 2016, *MNRAS*, 460, 2453  
 Sheth R. K., Tormen G., 1999, *MNRAS*, 308, 119  
 Smee S. A., et al., 2013, *AJ*, 146, 32  
 Smith A., et al., 2020, submitted  
 Song Y.-S., Percival W. J., 2009, *J. Cosmology Astropart. Phys.*, 2009, 004  
 Sugai H., et al., 2012, in *Proc. SPIE*. p. 84460Y, doi:10.1117/12.926954  
 Takada M., et al., 2014, *PASJ*, 66, R1  
 Vargas-Magaña M., et al., 2018, *MNRAS*, 477, 1153  
 Wang L., Reid B., White M., 2014, *MNRAS*, 437, 588  
 White M., 2014, *MNRAS*, 439, 3630  
 White M., et al., 2011, *ApJ*, 728, 126  
 Zarrouk P., et al., 2018, *MNRAS*, 477, 1639  
 Zel'dovich Y. B., 1970, *A&A*, 5, 84  
 Zhao C., et al., 2020b, in preparation  
 Zhao C., et al., 2020a, submitted  
 Zheng Z., et al., 2005, *ApJ*, 633, 791  
 de Mattia A., Ruhlmann-Kleider V., 2019, *J. Cosmology Astropart. Phys.*, 2019  
 de Mattia A., et al., 2020, submitted  
 du Mas des Bourboux H., et al., 2020, submitted

## APPENDIX A: MODIFIED CORRELATION - DETAILS

We provide in this appendix more context to the Equation 13. Starting from Equation 3.8 of Burden et al. (2017), the shuffled correlation function can be written for a normalised data density  $\bar{n}(\chi)$  as:

$$\xi^{\text{shuff}}(\mathbf{r}, \mathbf{r}') = \langle \delta(\mathbf{r})\delta(\mathbf{r}') \rangle - 2\langle \delta(\mathbf{r}) \int \delta(\gamma, \chi') \bar{n}(\chi') d\chi' \rangle \quad (\text{A1})$$

$$+ \langle \int \delta(\gamma, \chi') \bar{n}(\chi') d\chi' \int \delta(\gamma', \chi'') \bar{n}(\chi'') d\chi'' \rangle \quad (\text{A2})$$

where  $\delta$  is the density field, and  $\mathbf{r}, \mathbf{r}'$  are the comoving positions,  $\gamma, \gamma'$  are the corresponding angular positions and  $\chi$  stands for line-of-sight positions.

The first term corresponds to the standard 2PCF. Using the same approximation as in Burden et al. (2017) (Equation 3.9) and doing the substitution  $\chi'$  to  $\Delta\chi = \chi' - \chi$ , the second term becomes:

$$\langle \delta(\mathbf{r}) \int \delta(\gamma, \chi') \bar{n}(\chi') d\chi' \rangle = \int \xi(\theta, \chi, \chi') \bar{n}(\chi') d\chi' \quad (\text{A3})$$

$$= \int \xi(\theta, \Delta\chi) \bar{n}(\chi + \Delta\chi) d\Delta\chi \quad (\text{A4})$$

writing  $\theta = \gamma' - \gamma$ . To be more flexible in the scales introduced in the correction, we further change  $\bar{n}(\chi + \Delta\chi)$  to  $\bar{n}(\chi_{\text{mod}} + \Delta\chi/2)$  where  $\chi_{\text{mod}} = (\chi + \chi')/2$  is fixed (without changing the variable of integration). As already stated, we emphasize that such approximations have no impact on the validity of our analysis as we use

the modified 2PCF as a new estimator applied consistently on data and model.

The third term corresponds to the angular correlation function  $w(\theta)$ . Using the same substitution as previously and the Limber approximation (Limber 1953), it becomes:

$$w(\theta) = \int \int \xi(\theta, \Delta\chi) \bar{n}(\chi) \bar{n}(\chi + \Delta\chi) d\chi d\Delta\chi \quad (\text{A5})$$

$$= \int \bar{n}^2(\chi) d\chi \int \xi(\theta, \Delta\chi) d\Delta\chi \quad (\text{A6})$$

Gathering all terms together we end up with the adopted modified 2PCF of Equation 13.

This paper has been typeset from a  $\text{\LaTeX}$  file prepared by the author.



## 3 Voids BAO analysis with the QSO sample of eBOSS

Another part of my thesis was dedicated to the BAO analysis of voids. I used the quasar sample of eBOSS to perform a BAO measurement on the cross-correlation of quasars and the voids defined by their distribution. This work has been submitted to the Monthly Notices of the Royal Astronomical Society (MNRAS).

I will first briefly contextualize the cosmic voids and then justify our void definition by showing their constraining power within the work we performed with ELG and LRG samples of SDSS (C. Zhao et al., 2022). Section 3.2 is the preprint of the publication on the extended work that we did on eBOSS quasars (Tamone et al., 2022).

### 3.1 Cosmic Voids

#### 3.1.1 Definitions and Algorithms

Along with the first evidences of matter structures in the Universe, large empty regions were discovered (Jõeveer et al., 1978). The first concrete detection of such a devoided area, referred to as a void, was made by Kirshner et al., 1981 in Bootes. The existence of voids were then confirmed by de Lapparent et al., 1986 and later within different surveys as 2dF (2 degree Field, Hoyle and Vogeley, 2004), CfA (Center for Astrophysics, Slezak et al., 1993) or SDSS (Tikhonov, 2007, Pan et al., 2012). With the venue of the massive surveys, visual inspection to find voids is not an option, and algorithms have to be developed by adopting a void definition.

No consensus for a specific definition exists. Voids could be under-dense regions as well as completely empty volumes depending on the interpretation. They can be for example inferred from a smooth density field (Colberg et al., 2005, Shandarin et al., 2006, Platen et al., 2007, Neyrinck, 2008, Sutter, Lavaux, Hamaus, et al., 2015), defined as expanding regions in a dark matter field (Hahn, Carollo, et al., 2007, Forero-Romero et al., 2009, Hoffman et al., 2012, Cautun et al., 2013), regions without shell-crossing (Abel et al., 2012, B. L. Falck et al., 2012, Shandarin et al., 2012) or empty regions within a discrete distribution (Hoyle and Vogeley,

2002, Foster and Nelson, 2009).

Concerning the void finder algorithms, they can be classified into different categories depending on their methodology. A class of void finder applicable to a large range of data kind such as projected distribution or discrete tracers, is based on a density criterion. From an estimated density contrast, the voids are defined as the under dense regions below a certain threshold (Hoyle and Vogeley, 2004, Padilla et al., 2005, Sánchez et al., 2017). They are usually spherically defined as the largest spheres satisfying the density criterion. A second class of algorithms delimits voids using geometrical structures, using for example Voronoi tessellation (ZOBOV, Neyrinck, 2008, VIDE Sutter, Lavaux, Hamaus, et al., 2015, Nadathur et al., 2019), ellipsoids (Colberg et al., 2005), grid cells (Shandarin et al., 2006) or Delaunay tetrahedral (DIVE, C. Zhao et al., 2016). Most of them allow non-spherical voids. Finally there are also void finders relying on a dynamical point of view by tracing the velocity field induced (Hahn, Carollo, et al., 2007, Lavaux and Wandelt, 2010, Hoffman et al., 2012).

Void properties such as shape, density or size are tracer and model dependent (Colberg et al., 2008, Cautun et al., 2018). Therefore a careful void definition has to be chosen specifically for the research purpose.

## DIVE

In particular in this thesis I use the Delaunay Triangulation Void finder (DIVE) introduced by C. Zhao et al., 2016. It relies on a discrete distribution of tracers and defines the voids geometrically. The algorithm is based on Delaunay Triangulation (DT, Delaunay, 1934). For a given set of points  $P$  in 3D, DT provides the triangulation  $DT(P)$  so that no point position of  $P$  falls inside the circumspheres of any tetrahedron in  $DT(P)$ . We note moreover that the DT of  $P$  is the dual graph of its Voronoi tessellation, i.e. the connections of the circumspheres give the Voronoi diagram of  $P$ .

Therefore for a discrete halo or galaxy distribution, the voids are defined as the empty circumspheres produced by DT algorithm. They are called DTvoids and are associated a size characterized by the radius of the circumspheres. Their positions are thus the centers of the spheres. Figure 3.1 shows some voids as detected by DIVE. We note that the voids are not disjoint as they can overlap. So an empty region is not represented by a single individual DTvoid but rather by a set of DTvoids.

### 3.1.2 Void Properties

Sheth and van de Weygaert, 2004 established a formalism to characterise the different voids evolution according to their environments, that drives the LSS hierarchical formation. The “void-in-cloud” are voids embedded in high density regions. Those regions are squeezed until disappearance because of the surrounding matter which collapses. The “void-in-void” describes under-densities within deeper under-densities. Those voids will merge, faster than



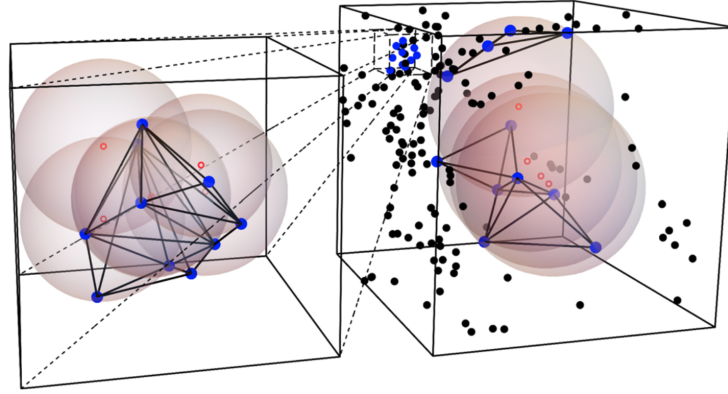


Figure 3.1: Some of the voids as found by the DIVE algorithm in a discrete distribution of tracers. Red points are the void centers, blue points the connected points associated to the voids. Solid lines are the tetrahedral edges. Large box has a length of  $80h^{-1}\text{Mpc}$  and voids shown have a radius between  $26$  and  $27h^{-1}\text{Mpc}$ . Zoomed box is of  $12h^{-1}\text{Mpc}$  length and void have radius smaller than  $4h^{-1}\text{Mpc}$ . (Credits of the figure: C. Zhao et al., 2016).

the Hubble flow.

The evolution of the voids plays thus a role in LSS formation. The matter is expelled on the outskirts of the voids due to their expansions and their decreases in density that generate a pressure. The matter is then compressed into walls and filaments surrounding the voids (Peebles, 1982, Icke and van de Weygaert, 1987, Hahn, Carollo, et al., 2007, Aragón-Calvo et al., 2010, van de Weygaert and Platen, 2011). We note that voids tend to evolve into spherical forms along the Universe expansion (Icke, 1984). Therefore the void density profile<sup>1</sup> has a low density center and reaches a peak density at its outskirts. This has been further tested in surveys and simulations (Hamaus et al., 2014).

Figure 3.2 displays the void density profile of DTvoids for different void sizes. While the general behaviour is as described previously, the smaller voids have a positive contrast even inside the voids. It means that those voids are “void-in-cloud” and that the two void populations can be distinguished using their sizes (C. Zhao et al., 2016).

We note therefore that the void abundance, i.e. void size function, depends on the cosmology and the epoch as it relies on the underlying density field (Sheth and van de Weygaert, 2004, Betancort-Rijo et al., 2009, Jennings et al., 2013). This void property was exploited to constrain dark energy equation of state (Pisani et al., 2015, Sutter, Lavaux, Hamaus, et al., 2015, Sutter, Carlesi, et al., 2015). For DTvoids C. Zhao et al., 2016 found an increase in the average radius when the tracer number density was decreasing. The small voids population is correlated with the matter halos while the large voids are anti-correlated. Both present two different bias on linear scales. Consistent results were found in Hamaus et al., 2014 that presents a study of spherical voids radius and their bias.

<sup>1</sup>Usually computed as the cross-correlation between the matter and the voids.

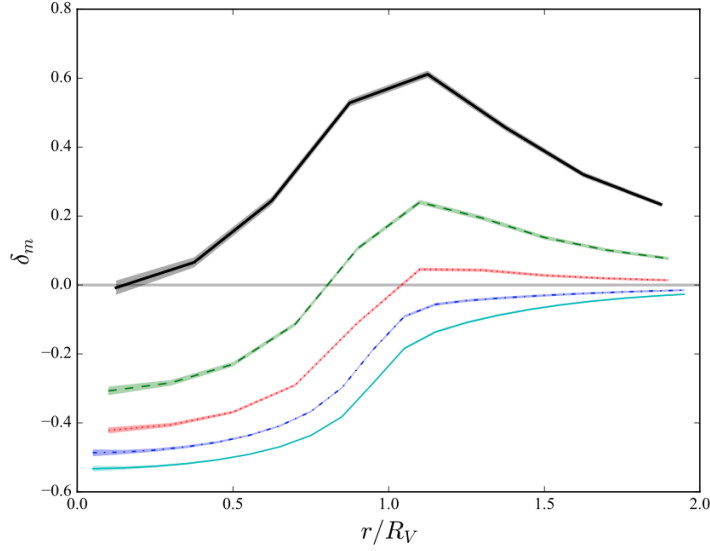


Figure 3.2: DTvoid density profile for different void sizes for mock catalogs as function of the distance to the center of the voids, rescaled by the void size. The horizontal line indicates the total mean density contrast. From top curve (black) to bottom (cyan) curve, void radii are within: (8,12), (12,16), (16,20), (20,25),  $> 25 h^{-1}\text{Mpc}$ . (Credits of the figure: C. Zhao et al., 2016).

### 3.1.3 Cosmology Measurements

Voids and their properties can be used to constrain cosmology. As seen previously, the number density of voids can help constraining cosmology by testing deviations from  $\Lambda\text{CDM}$  (Nadathur, 2016), constrain dark energy (Pisani et al., 2015) or other cosmological parameters (Betancort-Rijo et al., 2009).

Similarly to halos, void can present weak lensing as the light would be repulsed from the center of the voids (Amendola et al., 1999). Lensing measurement from voids was measured by different groups in large-scale structures data (Melchior et al., 2014, Clampitt and Jain, 2015, Sánchez et al., 2017). It was further shown that void lensing can help testing deviations from GR (Cai et al., 2015, Baker et al., 2018). Signatures of void lensing can also be detected on CMB lensing maps (Cai et al., 2017, Raghunathan et al., 2020, Vielzeuf et al., 2021). In particular iSW (integrated Sachs-Wolf, see Section 1.3.1) effect can be probed inside voids (Kovács et al., 2017, Kovács et al., 2019).

AP tests, testing the statistical isotropy, can be performed on (non spherical) voids by measuring for example the ellipticities of the voids. Indeed a shape distortion would be observed if the cosmology assumed is wrong, allowing parameter measurements such as  $\Omega_m$  (Sutter et al., 2012, Sutter et al., 2014, Q. Mao et al., 2017). However we note that the constraints inferred were rather weak as large voids, in particular, are less affected by peculiar velocities.

Voids can also be used for clustering analysis as it is sensitive to galaxy dynamics. Measurements of the growth rate in the vicinity of voids has been provided from the cross correlations of voids and galaxies (Paz et al., 2013, Hamaus et al., 2016, Nadathur et al., 2019, Aubert et al., 2022). Nadathur et al., 2020 showed that voids can break some degeneracies in the standard RSD and BAO measurements from galaxies.

BAO signal from voids was also detected in their clustering with matter or with themselves. The first detection was reported with DTvoids from SDSS galaxies (Kitaura et al., 2016). We note however that standard RSD analysis with voids is very complex to model as the void number density is not conserved under the change of spaces (Chuang et al., 2017).

### BAO with DTvoids

The overlapping of the DTvoids allows to increase considerably the statistics. The number of voids grows by a factor of  $\sim 10^2$ . This feature permits to detect a BAO peak in the clustering of the voids, due to the statistical advantage of this definition. With a method tested on mocks (Liang et al., 2016), DTvoids were then able to provide a first BAO signal (Kitaura et al., 2016).

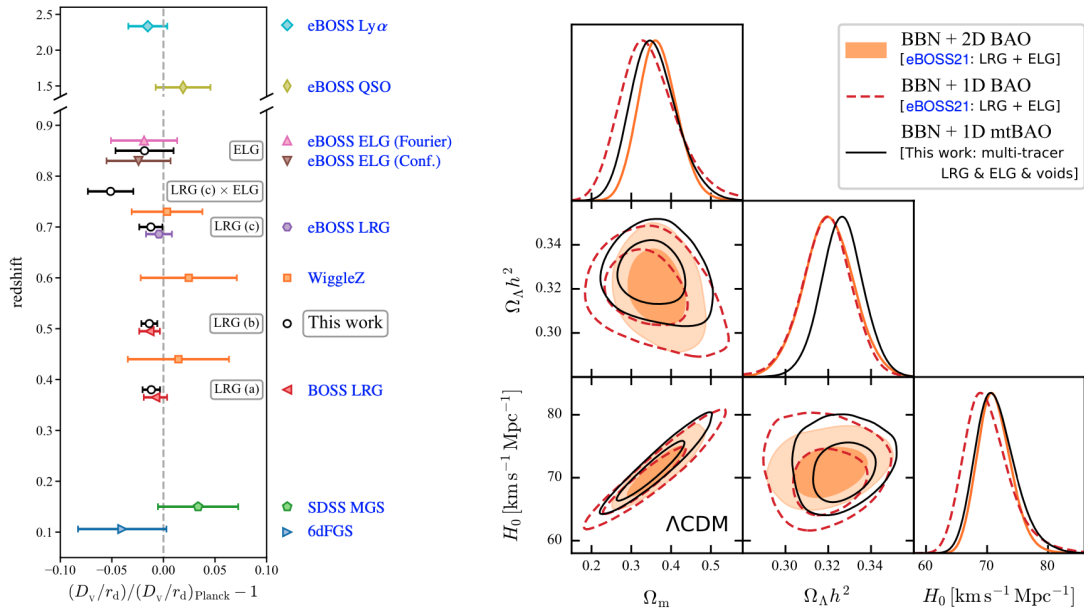


Figure 3.3: On the left: volume average distance measured from BAO for different SDSS samples. The void measurements are indicated in black. We note that the measurements are rescaled to the expected values from Planck for a  $\Lambda$ CDM model (Planck Collaboration et al., 2020). On the right: Constraints on different cosmological parameters ( $\Omega_m$ ,  $\Omega_\Lambda h^2$ ,  $H_0$ ) in a flat  $\Lambda$ CDM model with BBN constraints results. Orange contours (dashed red) are eBOSS results for anisotropic (isotropic) BAO of LRGs and ELGs. Black contours comes from void constraints. (Credits of the figures: C. Zhao et al., 2022).

C. Zhao et al., 2020 showed using BOSS LRGs that DTvoids, selected to trace under-densities,

can be used in combination with galaxy clustering to improve BAO measurements. We further investigated this property with LRGs and ELGs of eBOSS, results were presented in C. Zhao et al., 2022. We provided volume average distance measurements (Equation 1.143) from these different data samples. We weighted the different correlations (galaxies auto-correlation, galaxy-void cross-correlation and voids auto-correlation) by adding an optimal weight to the voids in order to minimize the error. The optimal weights are non-zero, i.e. adding voids help reducing the error compared to galaxies alone. Left panel of figure 3.3 reports the values and errors obtained from a combination of the voids and galaxy clustering. Uncertainties improve from 5 to 15 % (with sample variations) compared to the galaxy auto-correlation alone.

Right panel of figure 3.3 shows the contours of the multi-tracer voids constraints on cosmological parameters compared to ELGs and LRGs alone. Compared to the isotropic BAO, i.e. 1D BAO, of galaxies alone, voids significantly improves the uncertainties. For 2D BAO of galaxies, the multi-tracer void constraints do not necessarily improve but in average similar errors are found. Indeed in this case 2D BAO of galaxies provide constraints on  $D_A$  and  $D_H$ , while voids only constrain  $D_V$ .

### 3.2 Preprint version: “Void BAO measurements on quasars from eBOSS”

# Void BAO measurements on quasars from eBOSS

Amélie Tamone<sup>1,\*</sup>, Cheng Zhao<sup>1</sup>, Daniel Forero-Sánchez<sup>1</sup>, Andrei Variu<sup>1</sup>, Chia-Hsun Chuang<sup>2</sup>, Francisco-Shu Kitaura<sup>3,4</sup>, Jean-Paul Kneib<sup>1,5</sup>, Charling Tao<sup>6,7</sup>

<sup>1</sup>*Institute of Physics, Laboratory of Astrophysics, École Polytechnique Fédérale de Lausanne (EPFL), Observatoire de Sauverny, CH-1290 Versoix, Switzerland*

<sup>2</sup>*Kavli Institute for Particle Astrophysics and Cosmology, Stanford University, 452 Lomita Mall, Stanford, CA 94305, USA*

<sup>3</sup>*Instituto de Astrofísica de Canarias, s/n, E-38205, La Laguna, Tenerife, Spain*

<sup>4</sup>*Departamento de Astrofísica, Universidad de La Laguna, E-38206, La Laguna, Tenerife, Spain*

<sup>5</sup>*Aix Marseille Univ, CNRS, CNES, LAM, F13388 Marseille, France*

<sup>6</sup>*CPPM, Aix-Marseille Université, CNRS/IN2P3, CPPM UMR 7346, F13288 Marseille, France*

<sup>7</sup>*Tsinghua Center for Astrophysics, Department of Astronomy, Tsinghua University, Beijing 100084, P.R. China*

Accepted XXX. Received YYY; in original form ZZZ

## ABSTRACT

We present the clustering of voids based on the quasar (QSO) sample of the extended Baryon Oscillation Spectroscopic Survey Data Release 16 in configuration space. We define voids as overlapping empty circumspheres computed by Delaunay tetrahedra spanned by quartets of quasars, allowing for an estimate of the depth of underdense regions. To maximise the BAO signal-to-noise ratio, we consider only voids with radii larger than  $36h^{-1}\text{Mpc}$ . Our analysis shows a negative BAO peak in the cross-correlation of QSOs and voids. The joint BAO measurement of the QSO auto-correlation and the corresponding cross-correlation with voids shows an improvement in 70% of the QSO mocks with an average improvement of  $\sim 5\%$ . However, on the SDSS data, we find no improvement compatible with cosmic variance. For both mocks and data, adding voids does not introduce any bias. We find under the flat  $\Lambda\text{CDM}$  assumption, a distance joint measurement on data at the effective redshift  $z_{\text{eff}} = 1.48$  of  $D_V(z_{\text{eff}}) = 26.297 \pm 0.547$ . A forecast of a DESI-like survey with 1000 boxes with a similar effective volume recovers the same results as for light-cone mocks with an average of 4.8% improvement in 68% of the boxes.

**Key words:** cosmology : dark energy – cosmology : distance scale – cosmology : large-scale structure of Universe

## 1 INTRODUCTION

The accelerated expansion of the Universe is one of the greatest mysteries of current cosmology. It was observationally discovered by Riess et al. (1998) and Perlmutter et al. (1999) a bit more than 20 years ago, but still its nature, referred to as dark energy, remains unknown. In the context of precision cosmology, an accurate determination of the expansion history of the Universe is required to constrain the nature of dark energy and thus to test the  $\Lambda\text{CDM}$  model.

To this goal, baryon acoustic oscillations (BAO) provide a characteristic length that enables measurement of the expansion rate (Weinberg et al. 2013). BAO arises in the early Universe due to the counteracting plasma pressure and gravitation that produced sound waves. At photon decoupling, those waves stopped propagating, leaving an imprint detectable in the clustering of the galaxies and in the cosmic microwave background (CMB). The distance the waves travelled before they stopped, known as the sound horizon, can be used as a standard ruler (Blake & Glazebrook 2003).

The first BAO detections in the clustering of galaxies were made by Eisenstein et al. (2005) with Sloan Digital Sky Survey (SDSS) data and Cole et al. (2005) with Two Degree Field Galaxy Redshift Survey (2dFGRS). Since then, the era of spectroscopic surveys has risen with BAO as a key measurement. The largest survey to date

is SDSS with Baryon Oscillation Spectroscopic Survey (Dawson et al. 2013, BOSS) and at higher redshift with the extended Baryon Oscillation Spectroscopic Survey (Dawson et al. 2016, eBOSS). BAO was therefore measured at different redshifts in the clustering of various tracers such as luminous red galaxies (LRGs; Ross et al. 2016; Bautista et al. 2021; Gil-Marín et al. 2020), emission-line galaxies (ELGs; Raichoor et al. 2021), quasars (QSOs; Ata et al. 2018) and Lyman- $\alpha$  forests (Busca et al. 2013; du Mas des Bourboux et al. 2020).

Kitaura et al. (2016) measured for the first time a BAO signal in the clustering of underdense regions, defined as voids. More recently, Zhao et al. (2022) performed a multi-tracer with voids based on the analysis of ELG and LRG samples of BOSS and eBOSS. They showed that adding voids improved the BAO constraints of 5% to 15% for their samples (see also Zhao et al. (2020)). Their studies relied on a Delaunay Triangulation (DT; Delaunay 1934) definition of voids (DT-voids), which detects a void as the largest empty sphere defined by four tracers (Zhao et al. 2016). The voids are allowed to overlap, resulting in an increase of tracer number, which permits BAO detection, demarcating itself to other voids definitions used for redshift space clustering analysis (Nadathur et al. 2020; Aubert et al. 2022).

At the precision level of current and future surveys like the Dark Energy Spectroscopic Instrument (DESI Collaboration et al. 2016a,b, DESI), the 4-metre Multi-Object Spectroscopic Telescope (de Jong

\* E-mail: amelie.tamone@epfl.ch

	NGC	SGC	Total
Effective area [deg <sup>2</sup> ]	2860	1839	4699
N <sub>QSO</sub> in $0.8 < z < 2.2$	218'209	125'499	343'708
$n_{\text{QSO}} [(h^{-1}\text{Mpc})^{-3}]$	$1.43 \times 10^{-5}$	$1.60 \times 10^{-5}$	$1.53 \times 10^{-5}$
Effective redshift	-	-	1.48

**Table 1.** Effective areas, effective redshift and number of reliable redshifts per Galactic cap and in the combined QSO sample in the redshift range  $0.8 < z < 2.2$ .

et al. 2019, 4MOST) or Euclid (Laureijs et al. 2011), any reduction of measurement uncertainties will be crucial.

In this paper, we extend the work of Zhao et al. (2022) by analysing the QSO sample of eBOSS using DT-voids. We provide a distance measurement from the joint BAO analysis of QSO auto-correlation and QSO-voids cross-correlation. The analysis pipeline and the errors are assessed using fast approximated mocks and N-body simulations. We also forecast error improvement from voids with a DESI-like survey for QSOs.

We summarise the QSO sample and the void catalogue used in Section 2. Fast mock catalogues and N-body simulations are introduced in Section 3. Method for void selection and correlation computation are described in Section 4. The BAO model and the template used for void fitting are outlined in Section 5. Error assessments are estimated in Section 6 and results in Section 7 with our conclusions in Section 8.

## 2 DATA

We present in this section the eBOSS QSO sample used for the BAO analysis of this paper. We use the same QSO data catalogue as in the eBOSS DR16 analysis (Hou et al. 2021; Neveux et al. 2020), which was fully described in Ross et al. (2020).

The extended Baryon Oscillation Spectroscopic Survey (Dawson et al. 2016, eBOSS) program was part of the fourth generation of the Sloan Digital Sky Survey (Blanton et al. 2017, SDSS-IV) as an extension of the Baryon Oscillation Spectroscopic Survey (Dawson et al. 2013, BOSS). It aimed at observing the large-scale structure at higher redshifts. Started in 2014 until 2019, eBOSS used the double-armed spectrographs of BOSS (Smeed et al. 2013) at the 2.5-meter aperture Sloan Telescope at Apache Point Observatory (Gunn et al. 2006).

The eBOSS final release gathered reliable spectroscopic redshifts of over 340'000 QSOs in total, both in the South Galactic Cap (SGC) and North Galactic Cap (NGC), in a redshift range between 0.8 and 2.2. The QSOs were selected following the photometric target selection described in (Myers et al. 2015). The footprints of both cap samples are presented in Figure 1. Different statistics as the weighted areas, the number of QSOs and the number densities are gathered in the Table 1.

We apply weights to each individual QSO to account for observational and targeting systematics. We summarize here the different weights and refer to Ross et al. (2020) for a complete description. The angular systematics due to the imaging quality is mitigated through the weight  $w_{\text{sys}}$ . The weights  $w_{\text{cp}}$  and  $w_{\text{noz}}$  are respectively the close-pair and redshift failure corrections. To minimize the clustering variance, we follow Feldman et al. (1994) and apply the FKP weight  $w_{\text{FKP}} = (1 + n(z) \cdot P_0)^{-1}$  where  $n(z)$  is the weighted radial comoving number densities of QSO and  $P_0 = 6000 h^{-3} \text{Mpc}^3$ . The total weight applied to each QSO is then defined as their combination:

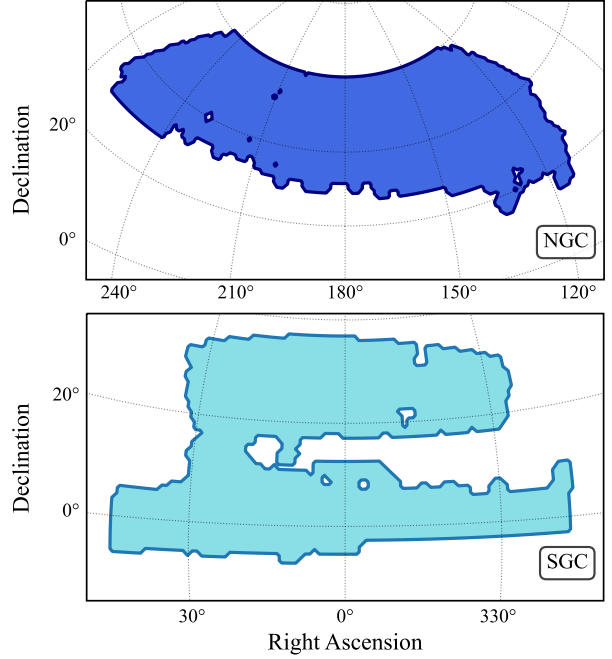


**Figure 1.** Footprint of eBOSS DR16 QSO samples in the North (top) and South (bottom) Galactic Caps.

$$w_{\text{tot}} = w_{\text{sys}} \cdot w_{\text{cp}} \cdot w_{\text{noz}} \cdot w_{\text{FKP}}. \quad (1)$$

Following the eBOSS analyses, the QSO effective redshift  $z_{\text{eff}}$  is defined as the weighted mean of spectroscopic redshift over all galaxy pairs  $(z_i, z_j)$  in the separation range between 25 and  $120 h^{-1} \text{Mpc}$ :

$$z_{\text{eff}} = \frac{\sum_{i,j} w_{\text{tot},i} w_{\text{tot},j} (z_i + z_j) / 2}{\sum_{i,j} w_{\text{tot},i} w_{\text{tot},j}}. \quad (2)$$

It gives for eBOSS QSO sample  $z_{\text{eff}} = 1.48$ , as presented in Table 1.

A QSO random catalogue is built with about 50 times the QSO density. To account for the angular and radial distribution of the survey selection function, angular positions of random objects are uniformly drawn within the footprint, and their redshifts are randomly assigned from the data redshifts (Ross et al. 2020). This radial selection introduces a radial integral constraint (de Mattia & Ruhlmann-Kleider 2019; Tamone et al. 2020, RIC) which can affect the multipoles. It was shown in Hou et al. (2021) and Neveux et al. (2020) that this effect was relatively small for QSO.

### 2.1 Void Catalogue

The void data catalogue is constructed using the Delaunay Triangulation Void finder (Zhao et al. 2016, DIVE<sup>1</sup>). It identifies the largest empty spheres formed by four distinct objects relying on the Delaunay triangulation (Delaunay 1934) algorithm in comoving space. It provides the radii and centres of the empty spheres that we define as voids and take them as tracers. This definition allows the spheres to overlap, which permits a large number of objects and thus to detect a BAO peak allowing BAO measurements (Kitaura et al. 2016).

<sup>1</sup> <https://github.com/cheng-zhao/DIVE>



	NGC	SGC	Total
$N_{\text{voids}}^{\text{tot}}$ in $0.8 < z < 2.2$	1'304'614	718'966	2'023'580
$N_{\text{voids}}$ with $36 < R < 80$	589'549	373'362	962'911
$n_{\text{voids}}^{\text{tot}}$ [ $(h^{-1}\text{Mpc})^{-3}$ ]	$8.18 \times 10^{-5}$	$9.55 \times 10^{-5}$	$9.01 \times 10^{-5}$

**Table 2.** Void number density and number of reliable redshifts per Galactic cap and in the combined QSO voids sample in the redshift range  $0.8 < z < 2.2$ .

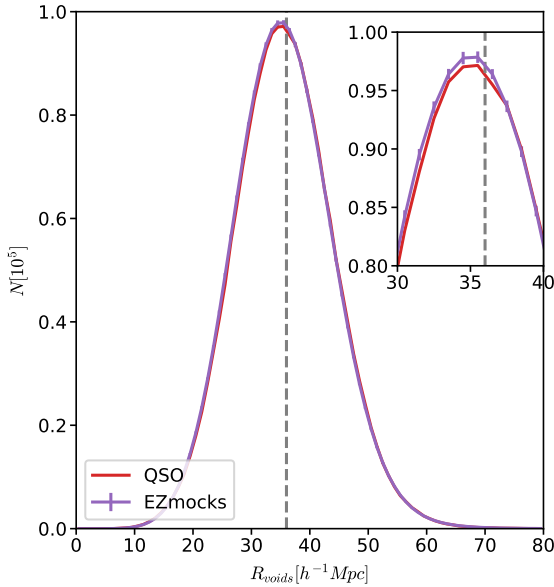


**Figure 2.** Radius of voids number density for the eBOSS QSO void sample and the EZmocks. Vertical line indicates the radius of  $36 h^{-1}\text{Mpc}$ .

DIVE is run over the whole NGC and SGC data samples. The resulting voids are kept if their centre lies within the redshift range and footprints and outside the veto masks of the survey. The total number of voids is more than five times larger than the number of QSOs; see Table 2. The radius range of the voids displayed on Figure 2, spreads up to  $80 h^{-1}\text{Mpc}$  with a mean radius around  $35 h^{-1}\text{Mpc}$ . This is about twice the typical values obtained for LRGs and ELGs analysis with the same void definition (Zhao et al. 2020, 2022). It can be easily explained due to the lower density of the QSO sample and the relationship between the number density and the size of the voids (Forero-Sánchez et al. 2022). Figure 3 show QSOs and big (small) voids densities of a slice of NGC sample in comoving space. From them, one can see that the size of the voids is important: large voids track underdensities, while small voids lie in overdensity regions. These two populations of voids are respectively voids-in-voids and void-in-clouds (Sheth & van de Weygaert 2004). A careful choice of the radius of voids has to be made in order to avoid small voids contamination and therefore reduce the uncertainty of BAO measured from underdensities.

The random catalogues for voids are generated according to the procedure described in Liang et al. (2016). We stack 100 mock realizations and shuffle the angular positions and (redshift, radius) pairs within redshifts and radius bins of respectively redshift 0.1 and  $2 h^{-1}\text{Mpc}$ . We then randomly subsample down to 50 times the number of voids.

	fiducial	EZmocks	OuterRim
$h$	0.676	0.6777	0.71
$\Omega_m$	0.31	0.307115	0.26479
$\Omega_b h^2$	0.022	0.02214	0.02258
$\sigma_8$	0.8	0.8225	0.8
$n_s$	0.97	0.9611	0.963
$\sum m_\nu$ [eV]	0.06	0	0

**Table 3.** Different Flat- $\Lambda$ CDM cosmologies used throughout the paper. Fiducial cosmology (Planck Collaboration et al. 2016) is used for the template power spectrum and distance measurements for EZmocks and data. EZmock cosmology is the cosmology for EZmock creation. OuterRim cosmology is the simulation cosmology and used for the fits to the N-body mocks.

### 3 MOCKS

We will introduce here different sets of mock catalogues used for this study. We work with approximate mocks to calibrate the data analysis pipeline and estimate the covariance matrices. We use N-body simulations to validate the QSO-only BAO model.

#### 3.1 EZmocks

EZmocks are fast approximated mocks relying on the Zel'dovich approximation (ZA; Zel'dovich 1970). The displacement field of the ZA is generated from a Gaussian random field in a  $5 h^{-1}\text{Gpc}$  box using a grid size of  $1024^3$  with a given initial linear power spectrum. The dark matter density at the wanted redshift is then obtained by moving the dark matter particles directly to their final positions. Thereafter the simulation box is populated with QSOs using an effective galaxy bias model calibrated to the eBOSS DR16 QSO clustering measurements (Chuang et al. 2015; Zhao et al. 2021). It describes the relationship between the dark matter density field  $\rho_m$  and the tracer density field  $\rho_t$ . This bias model (Chuang et al. 2015; Baumgarten & Chuang 2018; Zhao et al. 2021) requires a critical density  $\rho_c$  to form dark matter haloes (Percival 2005), an exponential cut-off  $\rho_{\text{exp}}$  (Neyrinck et al. 2014) and a density saturation  $\rho_{\text{sat}}$  for the stochastic generation of haloes. The mocks are then populated following a probability distribution function (PDF)  $P(n_t) = Ab^{n_t}$ ,  $n_t$  being the number of tracers per grid cell,  $b$  is a free parameter, and the parameter  $A$  is constrained with the number density of QSOs in the box. Moreover the random motions are accounted for using a vector  $X_v$  generated from a 3D gaussian distribution  $\mathcal{N}(0, \nu)$ , the peculiar velocity becomes:  $u_t = u_{\text{ZA}} + X_v$ , where  $u_{\text{ZA}}$  is the linear peculiar velocity in the ZA (Bernardeau et al. 2002). In total we have 4 free parameters, namely  $\rho_c$ ,  $\rho_{\text{exp}}$ ,  $b$  and  $\nu$ , that were calibrated to the data for the QSO eBOSS sample in Zhao et al. (2021).

The Flat- $\Lambda$ CDM cosmology used for EZmocks is summarized in Table 3.

For each different EZmocks set, we obtain a void catalogue by applying the same procedure than for the data.

##### 3.1.1 Cubic mocks

We take directly 1000 EZmocks boxes that were used for the light-cone generation of the QSO eBOSS EZmocks (Zhao et al. 2021). They are cubic boxes of  $5 h^{-1}\text{Gpc}$  referred to as the EZbox all over this paper. They have at an effective redshift of  $z = 1.48$  and a number density of  $n = 2.4 \cdot 10^{-5} (h^{-1}\text{Mpc})^{-3}$ . We used them to determine the best radius cut of the QSO voids for this analysis. To this end we also produce a set of 200 EZbox without BAO at the effective

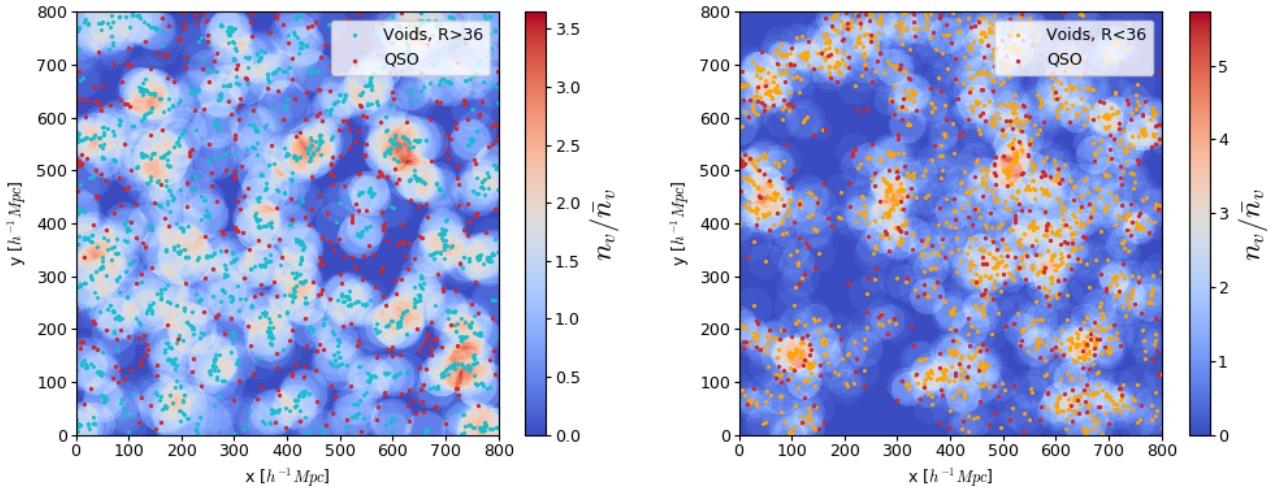


**Figure 3.** Number density of spherical voids for a slice of NGC data sample of size  $800 \times 800 \times 50 \, h^{-3} \text{Mpc}^3$ . QSOs are represented as red points. On the left: large voids, with radii larger than  $36 \, h^{-1} \text{Mpc}$ , center of voids are represented as red points. On the right: small voids, with radii smaller than  $36 \, h^{-1} \text{Mpc}$ , center of voids are represented as orange points.

redshift of the QSO sample using the same parameters than adopted in QSO eBOSS analysis<sup>2</sup>.

The 1000 mocks with BAO included were given as input a linear matter power spectrum generated with the software CAMB<sup>3</sup> (Lewis et al. 2000), while for the mocks without BAO, we use a linear power spectrum without wiggles generated following the model of Eisenstein & Hu (1998). Both linear power spectra, with and without wiggles, are produced with the same set of cosmological parameters gathered as the EZmocks cosmology of Table 3.

### 3.1.2 Light-cones

We use the same sets of light-cone EZmocks as the eBOSS DR16 analysis described in Zhao et al. (2021) to evaluate the covariance matrices and to test the data analysis pipeline. They are constituted of 1000 realizations with systematics included for each cap, NGC and SGC.

To recreate the clustering evolution, each light-cone mock is built by combining seven snapshots at different redshifts sharing the same initial conditions. The survey footprint and veto masks are then applied to match the data geometry.

Observational systematics effects from QSO data such as fibre collisions, redshift failure and photometric systematics are encoded into the EZmocks. Those effects are thereafter corrected by using some weights in the same way as for data (see Equation 1). A random catalogue is produced for each EZmock with redshifts of the QSO catalogue assigned randomly.

## 3.2 N-body simulations

To assess the bias and tune the BAO model, we work with the N-body simulations built for the DR16 eBOSS analysis and described in

Smith et al. (2020). They are produced from the OUTERIM simulations (Heitmann et al. 2019) at a single redshift snapshot of  $z = 1.433$ .

The OUTERIM simulations are produced in a cubic box of  $3 \, h^{-1} \text{Gpc}$  length with  $10^4 240^3$  dark matter particles each with a mass of  $m_p = 1.82 \cdot 10^9 \, M_\odot h^{-1}$  using the WMAP7 cosmology (Komatsu et al. 2011) given in Table 3. A Friends-of-Friends algorithm is used to detect dark matter haloes. The mocks are then populated with QSOs with 20 different halo occupation distribution (HOD) models and three different redshift smearing prescriptions described in Smith et al. (2020). Each different set is constituted of 100 realisations. In this paper, we will measure clustering, and BAO parameters on the 100 realisations of the 20 HOD mocks without smearing.

## 4 METHOD

This section presents details of the correlation function computation and the void selection.

### 4.1 Two-point correlation functions

To quantify the clustering of tracers in configuration space, we compute the two-point correlation function (2PCF)  $\xi$  expressing the surplus of pairs separated by a vector distance  $s$  compared to a random uniform distribution.

The observed redshifts are first converted into comoving distances using the same flat- $\Lambda$ CDM fiducial cosmology as in eBOSS DR16 analysis, summarized in Table 3. We then evaluate the pair counts of the different catalogues using the Fast Correlation Function Calculator (FCFC<sup>4</sup>, Zhao in preparation). We compute for QSOs and voids the unbiased Landy–Szalay estimator of the isotropic 2PCF (Landy & Szalay 1993, LS) for a pair separation of  $s$ :

$$\xi(s) = \frac{DD(s) - 2DR(s, \mu) + RR(s)}{RR(s)}, \quad (3)$$

where  $DD$ ,  $DR$  and  $RR$  are the normalized paircounts with  $D$  denoting the tracer and  $R$  the random catalogue.

<sup>2</sup> For the creation of the EZbox, we adopt parameters corresponding to  $z = 1.48$ , the effective redshift of our sample, and with a number density of  $n = 2.4 \cdot 10^{-5} \, (h^{-1} \text{Mpc})^{-3}$ :  $(\rho_c, \rho_{\text{exp}}, b, \nu) = (0.4, 0.95, 0.003, 450)$ .

<sup>3</sup> <https://camb.info/>

<sup>4</sup> <https://github.com/cheng-zhao/FCFC>



For the cross-correlation (XCF) between QSOs, subscript q, and voids, subscript v, we use the following generalized estimator (Szapudi & Szalay 1997):

$$\xi_x(s) = \frac{D_q D_v - R_q D_v - D_q R_v + R_q R_v}{R_q r_v}. \quad (4)$$

The two caps are combined into a single data sample for all the analysis by combining the paircounts (Zhao et al. 2022):

$$\begin{aligned} DD &= \frac{n_{\text{SGC}}^2 DD_{\text{SGC}} + n_{\text{NGC}}^2 DD_{\text{NGC}}}{(n_{\text{SGC}} + n_{\text{NGC}})^2}, \\ DR &= \frac{n_{\text{SGC}} n_{\text{r,SGC}} DR_{\text{SGC}} + w_\alpha n_{\text{NGC}} n_{\text{r,NGC}} DR_{\text{NGC}}}{(n_{\text{SGC}} + n_{\text{NGC}})(n_{\text{r,SGC}} + w_\alpha n_{\text{r,NGC}})}, \\ RR &= \frac{n_{\text{r,SGC}}^2 RR_{\text{SGC}} + w_\alpha^2 n_{\text{r,NGC}}^2 RR_{\text{NGC}}}{(n_{\text{r,SGC}} + w_\alpha n_{\text{r,NGC}})^2}. \end{aligned} \quad (5)$$

The weight  $w_\alpha$  corrects for the different ratio data-random between the two sample, i.e.  $w_\alpha = \frac{n_{\text{r,SGC}} n_{\text{NGC}}}{n_{\text{SGC}} n_{\text{r,NGC}}}$ , and  $n_i, n_{r,i}$  stand for the number of pairs in the data, random catalogues of the cap i, respectively.

In the case of EZbox we use the natural estimator instead of the LS estimator which does not require a random catalogue:

$$\xi(s) = \frac{DD(s)}{RR(s)_a} - 1, \quad (6)$$

where  $RR_a = \frac{4}{3}\pi(s_{\text{max}}^3 - s_{\text{min}}^3)\Delta\mu/L_{\text{box}}$  is the analytical pair count for uniform randoms in a periodic box, with  $L_{\text{box}}$  the box length and  $s_{\text{max}}, s_{\text{min}}, \Delta\mu$  are the separation bin boundaries.

Figure 4 shows the auto-correlation of eBOSS QSO sample and its cross-correlation with QSOs large voids with a minimum void radius of  $36h^{-1}\text{Mpc}$ .

## 4.2 Covariances

A covariance matrix  $C$  is computed for each sample, i.e. QSOs auto-correlation and cross-correlation with voids, from the monopoles of 1000 EZmocks:

$$C_{ij} = \frac{1}{N-1} \sum_{n=1}^N \left( \xi_0(s_i) - \frac{1}{N} \sum_{n=1}^N \xi_0(s_i) \right) \left( \xi_0(s_j) - \frac{1}{N} \sum_{n=1}^N \xi_0(s_j) \right), \quad (7)$$

where  $N$  is the total number of mocks and the subscripts  $i, j$  run over the separation bins within the range considered. Those matrices are used to assess the errors of data and EZmocks. When the mean of the mocks is fitted, the covariance matrix is divided by  $N$ . For the multi-tracer covariance of 2PCF and XCF fitted jointly, the sum also runs over the cross-correlations of the two monopoles.

To obtain an unbiased estimator of the inverse covariance matrix  $C^{-1}$ , we multiply by the correction factor (Hartlap et al. 2007), where  $N_d$  is the number of separation bins used in the fit:

$$C^{-1} = \left( 1 - \frac{N_b + 1}{N - 1} \right) C^{-1}. \quad (8)$$

Analytical gaussian covariance matrices are computed following Grieb et al. (2016) when fitting the QSO N-body mocks.

## 4.3 Voids

As mentioned previously, they are the two main populations of voids. The voids-in-clouds are tracers of overdensity regions, and voids-in-voids are tracers of underdense regions. These two types of voids

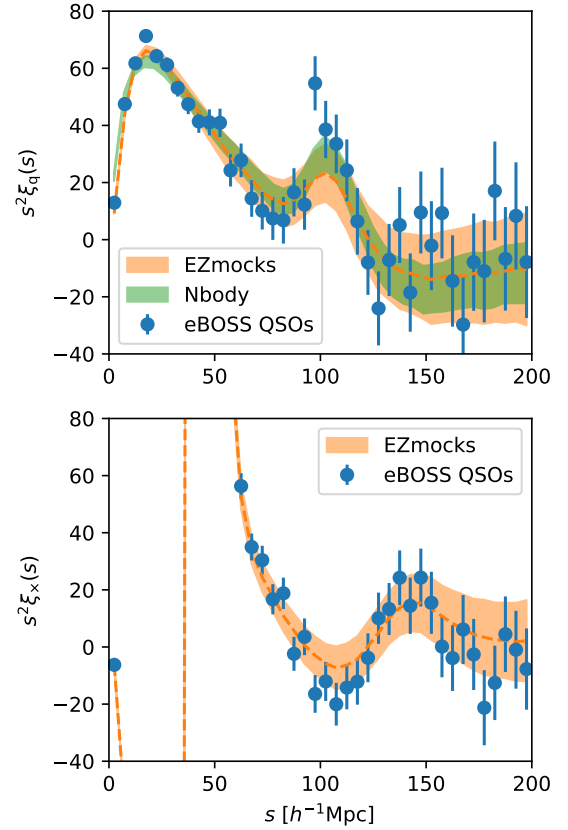


**Figure 4.** Top panel: auto-correlation of voids for the eBOSS QSOs sample with the standard deviation of EZmocks correlations as error bars. Mean of 1000 EZmocks is in dashed line and their dispersion is in orange shaded area. Green shaded area indicates the mean of the 20x100 N-body simulations without smearing, rescaled to match EZmock cosmology (we rescaled with a factor  $(r_d^{\text{EZ}} h^{\text{EZ}})/(r_d^{\text{OR}} h^{\text{OR}}) = 0.944$ , 'OR' indicates the OuterRim cosmology, and 'EZ' EZmocks). Bottom panel: same for the cross-correlation of QSOs with QSOs voids larger than  $36h^{-1}\text{Mpc}$ .

can be set apart by their radius (Zhao et al. 2016). Forero-Sánchez et al. (2022) showed that a constant radius cut gives a near-optimal signal-to-noise-ratio, SNR and that voids are less sensitive to observational systematics and therefore incompleteness. We chose to fix the maximum cut at  $R_{\text{max}}=80h^{-1}\text{Mpc}$  to avoid contamination due to geometrical exclusion effects of very large voids, and we investigated the best minimum radius cut  $R_{\text{min}}$  that will be used in the analysis.

### 4.3.1 Correlation function

Correlation functions for different radius cuts are shown on Figure 5 for QSO eBOSS EZmocks. The auto-correlation of voids (left panel of Figure 5) presents a very strong exclusion pattern, similar to what is observed for haloes due to their finite size (Sheth & Lemson 1999; Baldauf et al. 2013). Indeed even though the DT voids are not distinct from each other and can overlap, there is still an exclusion effect due to finite void size geometry (Chan et al. 2014; Zhao et al. 2016). As the minimum radius cut required to have large enough voids is about twice the value for LRG, see Zhao et al. (2020) and Zhao et al. (2022), the exclusion effect due to the spherical definition of the voids is therefore also shifted to the right. It implies that the exclusion pattern interferes with the BAO scale. Around  $100 h^{-1}\text{Mpc}$ , the correlation

is noisy, and the BAO excess density is not detectable due to the strong signal of the void exclusion. This is why we chose in this paper to leave aside the auto-correlation of voids in the analysis and concentrate on their cross-correlation with QSOs.

On the right panel of Figure 5 is the cross-correlation of QSOs with voids cut at different minimum radius  $R_{\min}$  for EZmocks. The exclusion effect is still present, but it mainly affects scales up to twice the minimum radius  $R_{\min}$ . Therefore it has fewer effects on the BAO scale even though this is not obvious to understand its real effect. We refer to the next section for analysis of non-wiggles boxes to quantify this effect.

#### 4.3.2 Selection of optimal radius

To understand the exclusion effect on the cross-correlation of voids and QSOs at the BAO scale and to find a quantifiable way to select the optimal radius, we rely on the EZbox produced with and without BAO.

The top left (right) panel of Figure 6 displays the void auto (cross)-correlation of EZbox with and without BAO. In the cross-correlation, a net negative peak around  $100h^{-1}\text{Mpc}$  can be seen from the BAO mocks compared to the ones without BAO wiggles. The bottom panels of Figure 6 show the difference between the two kinds of mocks, i.e.  $\xi^{\text{no BAO}} - \xi^{\text{BAO}}$ , another way to see the BAO excess that manifests itself as a clear bump. While we understand from the plots that a BAO peak is detectable from the void auto-correlation as well, we still chose not to include it in the analysis to avoid contamination from the exclusion effect in the model. Indeed if the exclusion effect is not perfectly modelled, the BAO fitting results might be biased.

To select the optimal radius threshold, we determine an SNR different to what was used in previous studies with DT voids (Liang et al. 2016). We rely on the EZbox for the SNR computation and compute the area  $A$  between the two EZbox curves over a selected separation range  $S$  around the BAO peak:

$$A = \sum_{s_i \in S} \xi_0^{\text{no BAO}}(s_i) - \xi_0^{\text{BAO}}(s_i). \quad (9)$$

For a radius cut  $R_{\min}$ , the signal  $S_A$  is then defined as the mean of  $A$  and the noise  $N_A$  as the standard deviation of  $A$  over the 200 EZbox. The SNR is  $S_A/N_A$ .

The BAO signal and noise both increase with the minimum radius, as the underdense regions are better selected, but the total number of retained voids decreases. We observe a slight shift of the BAO peak to the larger scale that we understand as remaining exclusion effects that spread on the BAO scale.

We compute the SNR for different radius cuts over different separation ranges  $S$ , as shown in Figure 7. The optimal ratio featuring the higher SNR for all  $S$  definitions is  $31h^{-1}\text{Mpc}$ . It corresponds to the quantile of the void radius distribution of about 0.55. Reporting this quantile from EZbox to data and EZmocks gives:

$$R_{\min}^{\text{optimal}} = 36h^{-1}\text{Mpc}. \quad (10)$$

We chose, therefore, this value as the optimal minimum radius cut for our analysis of EZmocks and data. The number of voids with this radius cut is presented in Table 2. There are a bit less than three times more voids than QSOs.

## 5 MODEL

Here we present the models for the two-point statistics to extract the BAO signature for the voids and QSOs.

### 5.1 Isotropic BAO

The BAO peak in the clustering of the tracers, positive for big voids and QSOs auto-correlations and negative for their cross-correlation, is shifted if a wrong cosmology is assumed when transforming redshifts to distances. This effect is known as the Alcock-Paczynski (AP) effect (Alcock & Paczynski 1979). We account for the AP effect with the isotropic AP dilation parameter  $\alpha$ :

$$\alpha = \frac{D_V r_{\text{d, fid}}}{D_{V, \text{fid}} r_{\text{d}}}. \quad (11)$$

Subscript 'fid' stands for fiducial values used in the analysis. Parameter  $r_{\text{d}}$  is the comoving sound horizon at the baryon drag epoch when the baryon optical depth is one (Hu & Sugiyama 1996), and  $D_V$  is a volume-averaged distance defined as:

$$D_V = \left( D_M(z)^2 \frac{cz}{H(z)} \right)^{\frac{1}{3}}, \quad (12)$$

with  $D_M$  the comoving angular diameter distance,  $H(z)$  the Hubble parameter at redshift  $z$ , and  $c$  the speed of light (Eisenstein et al. 2005).

The theoretical BAO model  $\xi_m$  for the correlation that we use is:

$$\xi_m(s) = B\xi_{\text{temp}}(\alpha s) + A_0 + A_1/s + A_2/s^2, \quad (13)$$

where  $B$  is the tracer bias, controlling the amplitude, and the  $A_i$  with  $i = 0, 1, 2$  are broadband parameters treated as nuisance parameters. The model relies on a 2PCF template  $\xi_{\text{temp}}$  which is the Fourier transform of the power spectrum  $P_{\text{temp}}$ :

$$\xi_{\text{temp}}(s) = \frac{1}{2\pi^2} \int P_{\text{temp}}(k) j_0(ks) e^{-k^2 a^2} k^2 dk. \quad (14)$$

The function  $j_0$  is the Bessel function at order 0 of the first kind. Here, the  $a$  parameter is damping the high  $k$  oscillations and is fixed at  $2h^{-1}\text{Mpc}$  following Variu (2022). Indeed they demonstrate that BAO measurements are unbiased and more robust against template noise with  $a=2h^{-1}\text{Mpc}$  compared to smaller values. The template power spectrum  $P_{\text{temp}}$  is (Xu et al. 2012):

$$P_{\text{temp}}(k) = (P_{\text{lin}}(k) - P_{\text{lin, nw}}(k)) e^{-k^2 \Sigma_{\text{nl}}^2/2} + P_{\text{lin, nw}}(k), \quad (15)$$

where  $\Sigma_{\text{nl}}$  is the BAO damping parameter of the tracer,  $P_{\text{lin}}$  and  $P_{\text{lin, nw}}$  are the linear matter power spectrum and its analogue without BAO wiggles, respectively, produced in the same way as for EZbox using the fiducial cosmology of Table 3.

### 5.2 De-wiggled BAO model

The de-wiggled template BAO model is not accurate for voids correlation functions (Zhao et al. 2020) because of oscillatory patterns inserted in power spectra due to void exclusion (Chan et al. 2014). Equation (15) is then modified to try to correct for this effect as:

$$P_t(k) = P_{\text{temp}}(k) \frac{P_{\text{tracer, nw}}(k)}{P_{\text{lin, nw}}(k)}. \quad (16)$$

The term  $P_{\text{tracer, nw}}(k)$  is the non-wiggle power spectrum of the tracer encoding broad-band and geometric effects. Those effects for DT voids are difficult to model. In a previous analysis study with voids, a parabolic parametrisation was introduced with an additional free parameter (Zhao et al. 2020, 2022) to model the non-wiggle ratio. However, this method does not work well for QSOs voids correlation as the exclusion effect is much stronger. This is why in this study, we rely on the second method, which is template-based (Zhao et al. 2022; Variu 2022).

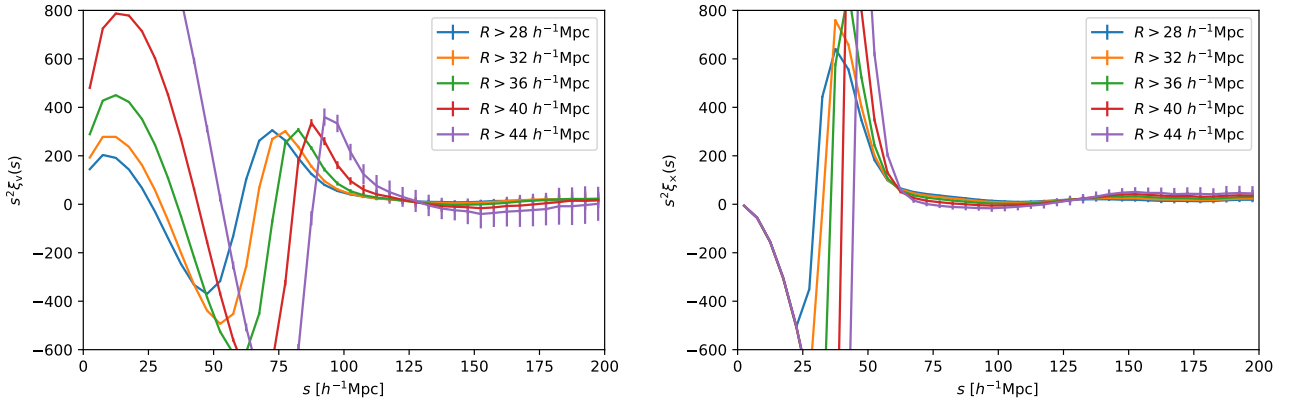


**Figure 5.** Correlation functions for different radius cuts of the mean of 1000 EZmocks with standard deviation errors. Radius range is from  $R_{\min} = R$  to  $R_{\max} = 80 h^{-1} \text{Mpc}$ . On the left: auto-correlation of QSOs voids. On the right: cross-correlation of QSOs and voids.

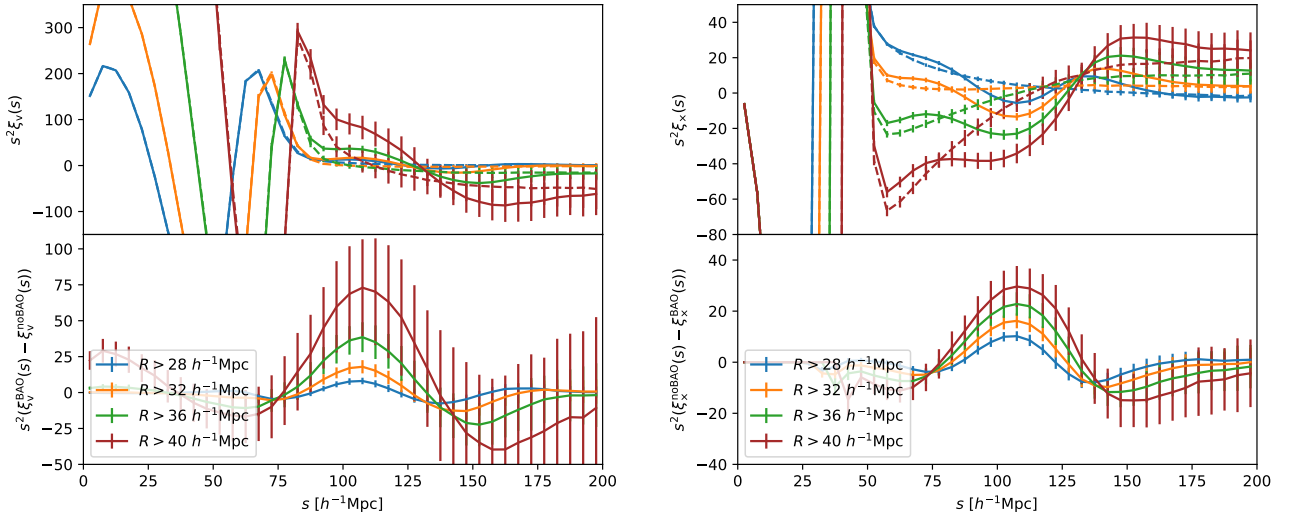


**Figure 6.** On the left, top panel: auto-correlation of QSO voids of the mean of 200 EZbox for a radius range from  $R_{\min} = R$  to  $R_{\max} = 80 h^{-1} \text{Mpc}$ , with standard deviation errors. Solid lines are for EZbox with BAO, dashed lines are for EZbox without BAO. Bottom left panel: mean difference of the auto-correlation of EZbox without BAO and EZbox with BAO, for different radius cut. On the right figures, same but for the cross-correlation of QSOs and voids.

Developed by Variu (2022) with the Cosmological GAussian Mock generator (CosmoGAME<sup>5</sup>), the de-wiggles tracer template is constructed with mocks without BAO wiggles. Those are Lagrangian mocks built on a Gaussian random field generated from  $P_{\text{lin,nw}}(k)$ , with a simple galaxy bias selection tuned to match eBOSS QSO EZ-mocks. Survey geometry and radial selection are then applied to the mock catalogues.

The template for the cross-correlation of QSOs and voids is obtained by averaging and stacking 2000, 1000, 100 mocks generated with CosmoGAME over a  $k$ -range  $k$  up to 0.3, 1, 2  $h\text{Mpc}^{-1}$ , respectively. Their power spectra are computed with POWSPEC<sup>6</sup>. The resulting concatenated template is shown in Figure 8, and its comparison with the power spectrum from 100 EZmocks is on the right panel of Figure 8.

### 5.3 Parameter estimation

To obtain BAO constrain we use the algorithm MULTINEST<sup>7</sup> (Feroz et al. 2009) and its python version PYMULTINEST<sup>8</sup> (Buchner et al. 2014), an efficient Monte-Carlo method that computes Bayesian evidence and produce posteriors. We use the following likelihood assuming the gaussianity of the distribution for a given set of parameters  $p$ :

$$L \propto \exp\left\{-\chi^2(p)/2\right\}, \quad (17)$$

where the chi-squared function  $\chi^2(p)$  is computed from the data  $\xi_d$  and the model prediction depending on the parameter set  $p$ ,  $\xi_{\text{temp}}(p)$ :

$$\chi^2(p) = (\xi_d - \xi_{\text{temp}}(p))^T C^{-1} (\xi_d - \xi_{\text{temp}}(p)). \quad (18)$$

<sup>5</sup> <https://github.com/cheng-zhao/CosmoGAME>

<sup>6</sup> <https://github.com/cheng-zhao/powspec>

<sup>7</sup> <https://github.com/farhanferoz/MultiNest>

<sup>8</sup> <https://github.com/JohannesBuchner/PyMultiNest>

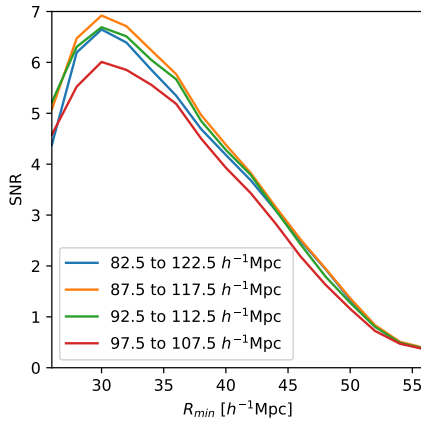


**Figure 7.** Signal-to-noise ratio  $SNR$  as defined with Equation 9 as a function of the minimum radius  $R_{\min}$ . Different curves are for different separation range  $S$  for which the minimum and maximum separation is indicated in the legend in  $h^{-1}\text{Mpc}$ .

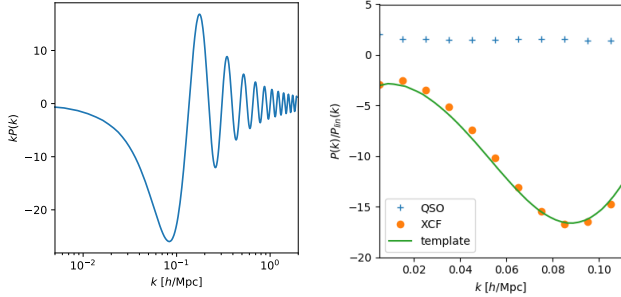


**Figure 8.** Left panel: De-wiggle template for the cross-correlation of QSOs and voids for the eBOSS QSO sample, generated with CosmoGAME. Right panel: Power spectrum divided by the linear power spectrum  $P_{\text{lin}}(k)$ . Blue crosses is for the mean QSOs auto-power spectrum of 100 EZmocks. Orange points is the QSOs and voids cross-power spectrum of 100 EZmocks. Solid green line is the cross-correlation template rescaled roughly to match the cross-correlation.

The resulting parameter covariances are rescaled to correct for the covariance matrix uncertainty propagation by Percival et al. (2014):

$$m_1 = \frac{1 + (N_d - N_{\text{par}}) \cdot B}{1 + A + (1 + N_{\text{par}}) \cdot B}, \quad (19)$$

where  $N_d$  the total number data bins used in the fit with  $N_{\text{par}}$  free parameters, and  $A$  and  $B$  are ( $N_m$  is the number of mocks used to estimate the covariance):

$$A = \frac{2}{(N_m - N_d - 1)(N_m - N_d - 4)}, \quad (20)$$

$$B = \frac{N_m - N_d - 2}{(N_m - N_d - 1) \cdot (N_m - N_d - 4)}. \quad (21)$$

Distribution variance of multiples best-fits values from mocks used for the covariance has to be rescaled by:

$$m_2 = \left(1 - \frac{N_d + 1}{N_m - 1}\right) m_1. \quad (22)$$

The parameter set for the multi-tracer analysis of the auto-correlation of QSOs and their cross-correlation with voids is:

	$\alpha$	$B_q$	$\Sigma_{\text{nl},q} [\text{Mpc}/h]$	$B_\times$	$\Sigma_{\text{nl},\times} [\text{Mpc}/h]$
Flat	0.8-1.2	0-100	0-100	0-100	0-100
$\xi_q$	0.8-1.2	1.27-1.40	5.2 (6.7)	-	-
$\xi_{\text{mt}}$	0.8-1.2	1.27-1.40	5.2 (6.7)	8.22-9.68	12.9

**Table 4.** Prior ranges of the BAO bayesian analysis for the three parameters  $\alpha$ ,  $B$ ,  $\Sigma_{\text{nl}}$ . Top row is for free parameters. Other rows are our fiducial choices when fitting the 2PCF or in the multi-tracer case. Value in parenthesis for  $\Sigma_{\text{nl},q}$  is the value used when fitting EZmocks.

$p = (\alpha, B_q, B_\times, \Sigma_{\text{nl},q}, \Sigma_{\text{nl},\times})$ . In the single tracer analysis, only one  $B$  and  $\Sigma_{\text{nl}}$  are used. Fits are performed with the BAO Fitter for muLTi-Tracers (BAOFLIT<sup>9</sup> code from Zhao et al. (2022)). When let free, we chose very wide priors for each parameter, it corresponds to the first row of Table 4. Broad-band parameters  $A_i$  of the polynomial term in Equation 13 are determined by linear regression with the least squares method.

## 6 TESTS ON MOCKS

We use eBOSS EZmocks to test the pipeline, calibrate the different settings for the analysis of data and assess systematics. N-body mocks are also used when dealing with QSOs only. We fit the auto-correlations of QSOs  $\xi_q$  (with Equation 15) and the cross-correlations with voids  $\xi_\times$  (with Equation 16) first separately, and then we perform a multi-tracer fit where both correlations are fitted simultaneously, noted  $\xi_{\text{mt}} \equiv \{\xi_q, \xi_\times\}$ . Voids used are selected by the criterion in Equation 10.

### 6.1 Fitting ranges

To choose our fiducial separation fit ranges, we fit the mean of the 1000 EZmocks for the QSO auto-correlation and cross-correlation, varying the fitting range. We aim to extract the maximum information and reduce the errors. Covariance matrices are divided by the number of mocks  $N_m$  used to construct it, i.e. rescaled by 0.001. All the parameters are let free, i.e. with broad enough priors of Table 4.

Results are shown in Figure 9. Minimum separation  $s_{\min}$  of the fit varies from 40 to 90  $h^{-1}\text{Mpc}$  every  $5h^{-1}\text{Mpc}$  and maximum separation  $s_{\max}$  from 140 to 180  $h^{-1}\text{Mpc}$ . Following Zhao et al. (2022), we define the bias to the fiducial value  $\alpha_{\text{fid}}$  of the fit for the AP parameter  $\alpha$  as a function of the median  $\alpha_{\text{med}}$  and the 1 sigma  $\sigma_\alpha$  values of the fit posterior:

$$\delta\alpha_{\text{med}} = \frac{\alpha_{\text{med}} - \alpha_{\text{fid}}}{\sqrt{1000}\sigma_\alpha}. \quad (23)$$

Fits for the QSO 2PCF are stable for a wide range of possibilities. We chose for consistency to adopt the range used in previous DR16 eBOSS analysis of Hou et al. (2021), a fitting range for auto-correlation of QSOs within  $[50, 150] h^{-1}\text{Mpc}$ .

For the cross-correlation of voids and QSOs, the possible fitting ranges are more limited. Indeed usual minimum range  $s_{\min}$  and lower are strongly affected by the exclusion effects. So to avoid contamination, we chose a conservative range of  $[80, 170] h^{-1}\text{Mpc}$  for the XCF, where the bias and errors are reasonable when varying the minimum and maximum fitting limits by  $5h^{-1}\text{Mpc}$ .

For our fiducial range, results for the mean of the EZmocks are in

<sup>9</sup> <https://github.com/cheng-zhao/BAOfit>

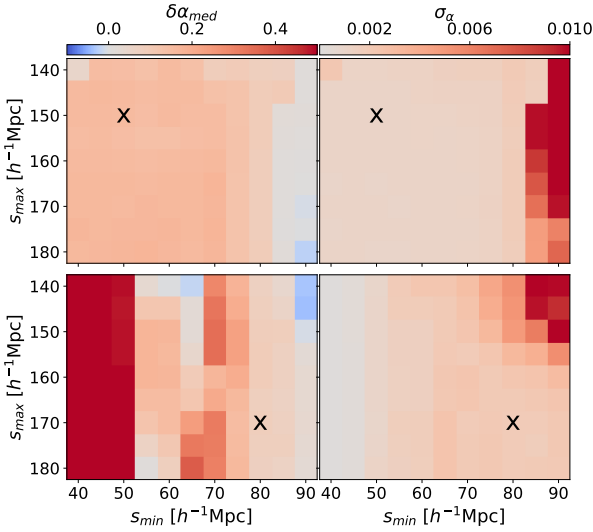


**Figure 9.** Bias  $\delta\alpha_{\text{med}}$  of the median of the fits from the fiducial value on the left column and evaluated 1 sigma error  $\sigma_\alpha$  from the posterior distribution on the right, for fits with different fitting ranges. On the top results for the QSOs 2PCF of the mean of the EZmocks and on the right results for the XCF of QSOs and voids for the mean of the EZmocks. Black crosses indicate the chosen range.

	$\alpha_{\text{med}}$	$\alpha_{\text{med}} - \alpha_{\text{fid}}$	$\sigma_\alpha$	$\max \Delta_s \alpha_{\text{med}} $
$\xi_q$	$1.0066^{+0.0365}_{-0.0361}$	0.0056	0.0011	0.0003
$\xi_x$	$1.0061^{+0.0594}_{-0.0602}$	0.0051	0.0019	0.0049
$\xi_{\text{mt}}$	$1.0063^{+0.0348}_{-0.0352}$	0.0053	0.0011	0.0011

**Table 5.** Fitting results of the AP parameter  $\alpha$  on the mean of EZmocks for  $R_{\text{min}} = 36 h^{-1}\text{Mpc}$  the fiducial separation range:  $[50, 150] h^{-1}\text{Mpc}$ ,  $[80, 170] h^{-1}\text{Mpc}$  for 2PCF  $\xi_{\text{qso}}$  and XCF  $\xi_v$ , respectively. The multi-tracer results is noted  $\xi_{\text{qso}} \times \xi_v$ . From left to right the columns are the median of the posterior with 1-sigma errors rescaled by  $\sqrt{1000}$ , the bias of the median of the fit to the fiducial value, the 1-sigma error of the distribution, the maximum bias from the fitted median when varying  $s_{\text{min}}$  or  $s_{\text{max}}$  by  $5h^{-1}\text{Mpc}$ .

Table 5. We also quote the maximum bias from the fitted  $\alpha_{\text{med}}$  when varying  $s_{\text{min}}$  or  $s_{\text{max}}$  by  $5h^{-1}\text{Mpc}$ . Results are not too sensitive to a small change in the fitted range.

## 6.2 Prior choice

We now investigate different priors on  $B$  and  $\Sigma_{\text{nl}}$  by fitting the EZmocks individually with the fiducial fitting range. Indeed without tighter priors, the dispersion of the errors on  $\alpha$  is quite large, and there is a significant bias on average. Moreover, their dispersion is not consistent with a normal distribution as in Vargha-Magaña et al. (2013).

We then test different prior sets to find the optimal choice on our respective fiducial fitting ranges. AP parameter  $\alpha$  is kept with wide flat priors. For the bias parameters  $B$ , we leave flat priors, but we narrow down the boundaries to  $N$  times  $\sigma$  around the median value given by the fit on the mean of the EZmocks for 2PCF and XCF separately, where  $\sigma$  is the 1-sigma dispersion of the posterior on this

parameter for the mean of the EZmocks<sup>10</sup>. We also test the same kind of narrower priors on  $\Sigma_{\text{nl}}$  parameters. Moreover, similarly to what is done in other BAO studies (Xu et al. 2012; Alam et al. 2017), we fix  $\Sigma_{\text{nl}}$  to the median posterior value from the EZmocks mean when fitting individual EZmocks ( $\Sigma_{\text{nl}} = 6.7$  for 2PCF and  $\Sigma_{\text{nl}} = 12.9$  for XCF). When fitting data 2PCF, we will use the median posterior value from N-body mocks ( $\Sigma_{\text{nl}} = 5.2$ ) as the BAO peak of approximated mocks as EZmocks is overdamped. It thus results in an overestimated value of  $\Sigma_{\text{nl}}$  in the EZmocks.

Different  $\alpha$  measurements with various priors ranges are presented in Table 6 for 2PCF and XCF. As the errors for the voids are quite large, we go down to  $N=3$  for XCF on the  $B$  parameter.

We then chose the optimal priors from the average goodness of fit rescaled by the degree of freedom,  $\langle\chi^2\rangle/\text{d.o.f.}$ , and the pull quantity (Bautista et al. 2021; Zhao et al. 2022):

$$g(\alpha_i) = \frac{\alpha_i - \langle\alpha_i\rangle}{\sigma_{\alpha,i}}, \quad (24)$$

where  $\alpha_i$  is the median value from the posterior distribution of  $\alpha$  for the  $i$ th EZmock realization and  $\sigma_{\alpha,i}$  is its error,  $\langle\alpha_i\rangle$  is the average  $\alpha$  value over all EZmocks. This quantity allows us to test for the gaussianity of the results. We want to have a distribution of the  $\alpha$  on the individual mocks similar to a standard distribution, i.e. a mean of 0 and a deviation of 1.

The selected priors are in bold in the table: we chose to fix the  $\Sigma_{\text{nl}}$  and have narrow constraints on  $B_{\text{qso}}$  with  $N = 5$  and  $N = 3$  for  $B_v$ . While the gaussianity of the pull quantity prefers slightly flat priors for  $\Sigma_{\text{nl}}$  in the 2PCF case, the reduced chi-square favours a fixed value. So for consistency with the previous analysis and with the XCF, we take fixed  $\Sigma_{\text{nl}}$ . We note that, except in the completely free case, all results are consistent with each other. The  $\alpha$  measurements are not very sensitive to the priors choices.

For the multi-tracer case, we use results from fits from separated correlations to fix  $\Sigma_{\text{nl}}$ , and we test only a few relevant cases.

## 6.3 Systematic error budget

We refer to mocks to make a systematic error budget summarized in Table 7. A systematic bias arises from the BAO model itself. For this, we take the deviation to AP parameter true value from the EZmocks mean of our fiducial separation range of Table 5. Indeed mean best-fit values from all individual N-body mocks give:  $\alpha_{\text{N-body}} = 1.0011 \pm 0.0193$ . The bias error is, therefore, smaller than the one from EZmocks for 2PCF. This is why we chose to quote the deviation from EZmocks for the auto-correlation alone to be conservative and consistent with the rest of the analysis with voids.

We quote a systematic bias for the maximum variation of  $\alpha_{\text{med}}$  when varying the fitting range of  $5 h^{-1}\text{Mpc}$ . We take the value in Table 5 for the mean of the EZmocks.

The last systematic taken into account in the final budget is the maximum variation of the mean of the individual value of the fit on the 1000 EZmock realizations when changing the priors on  $B$  and  $\Sigma_{\text{nl}}$ . We take a conservative choice and take as a reference for the systematic largest flat priors indicated in italic in Table 6.

The three contributions are added in quadrature to obtain the final systematic error  $\sigma_{\text{sys}}$ .

<sup>10</sup> Fit on the mean of the EZmocks on the fiducial fitting range gives: ( $B_{\text{qso}} = 1.336 \pm 0.013, \Sigma_{\text{nl,qso}} = 6.666 \pm 0.252$ ) for a fit on QSOs 2PCF, and ( $B_v = 8.949 \pm 0.242, \Sigma_{\text{nl,v}} = 12.870 \pm 0.588$ ) for a fit on XCF.



	$B$ Priors	$\Sigma_{\text{nl}}$ Priors	$\langle \alpha_i \rangle$	$\sigma_{\alpha_i}$	$\langle \sigma_{\alpha,i} \rangle$	$\frac{\sigma_{\alpha_i} - \langle \sigma_{\alpha,i} \rangle}{\sigma_{\alpha_i}}$	$\langle g(\alpha_i) \rangle$	$\sigma(g(\alpha_i))$	$\langle \chi^2 \rangle / \text{d.o.f.}$
$\xi_q$	-	-	1.023	0.034	0.111	-2.241	0.037	0.400	0.984
	$\pm 50\sigma$	$\pm 10\sigma$	<b>1.007</b>	<b>0.041</b>	<b>0.044</b>	<b>-0.068</b>	<b>-0.002</b>	<b>0.960</b>	<b>1.015</b>
	$\pm 10\sigma$	$\pm 10\sigma$	1.007	0.043	0.039	0.086	-0.012	1.031	1.038
	$\pm 10\sigma$	$\pm 5\sigma$	1.007	0.043	0.039	0.098	-0.019	1.043	1.052
	$\pm 5\sigma$	$\pm 5\sigma$	1.007	0.043	0.039	0.101	-0.013	1.042	1.066
	-	6.7	1.006	0.038	0.052	-0.352	0.001	0.874	0.975
	$\pm 50\sigma$	6.7	1.007	0.042	0.045	-0.072	-0.011	0.970	0.975
	$\pm 10\sigma$	6.7	1.007	0.043	0.039	0.097	-0.022	1.053	0.999
	$\pm 5\sigma$	<b>6.7</b>	<b>1.007</b>	<b>0.044</b>	<b>0.039</b>	<b>0.102</b>	<b>-0.026</b>	<b>1.058</b>	<b>1.014</b>
	-	5.2	1.006	0.038	0.051	-0.323	-0.017	0.894	0.974
$\xi_x$	$\pm 10\sigma$	5.2	1.008	0.044	0.036	0.165	-0.026	1.137	0.994
	-	-	1.020	0.040	0.100	-1.516	0.055	0.950	0.871
	$\pm 50\sigma$	$\pm 10\sigma$	1.008	0.047	0.073	-0.554	0.003	0.859	1.016
	$\pm 10\sigma$	$\pm 10\sigma$	1.008	0.049	0.062	-0.253	0.006	0.925	1.026
	$\pm 10\sigma$	$\pm 5\sigma$	1.007	0.051	0.061	-0.202	0.003	0.940	1.045
	$\pm 5\sigma$	$\pm 5\sigma$	1.008	0.051	0.060	-0.178	-0.004	0.939	1.057
	-	12.9	1.007	0.045	0.072	-0.581	-0.003	0.858	0.980
	$\pm 50\sigma$	12.9	1.006	0.046	0.072	-0.571	0.003	0.868	0.980
	$\pm 10\sigma$	12.9	1.007	0.051	0.061	-0.200	-0.007	0.953	0.986
	$\pm 5\sigma$	12.9	1.007	0.051	0.060	-0.181	-0.011	0.950	1.005
$\xi_{\text{mt}}$	$\pm 3\sigma$	<b>12.9</b>	<b>1.007</b>	<b>0.051</b>	<b>0.060</b>	<b>-0.176</b>	<b>-0.006</b>	<b>0.948</b>	<b>1.019</b>
	$\pm 50\sigma$	$\pm 10\sigma$	1.007	0.042	0.043	-0.014	-0.020	1.043	0.896
	$\pm 5\sigma$	$\pm 5\sigma$	1.009	0.040	0.037	0.083	-0.072	1.036	0.937
	$\pm 10\sigma$	6.7, 12.9	1.008	0.040	0.037	0.070	-0.036	1.013	0.882
	$\pm 5\sigma$	6.7, 12.9	1.008	0.039	0.037	0.067	-0.048	1.002	0.897
	$\pm 5\sigma, \pm 3\sigma$	<b>6.7, 12.9</b>	<b>1.009</b>	<b>0.039</b>	<b>0.037</b>	<b>0.066</b>	<b>-0.057</b>	<b>1.000</b>	<b>0.903</b>

**Table 6.** Fits on correlation functions of the 1000 individual EZmocks with different parameter priors. Results are rescaled according to Equations 19 and 22. Columns from left to right:  $B$  priors,  $\Sigma_{\text{nl}}$  priors, the median of the individual  $\alpha_i$  values, the standard deviation of the individual  $\alpha_i$  fit values, the median of the individual 1-sigma errors on  $\alpha_i$ , the relative difference to the mean of the individual errors  $\sigma_{\alpha,i}$ , mean of the individual  $g(\alpha_i)$  of Equation 24, the standard deviation of the individual  $g(\alpha_i)$ , mean reduced chi-squared of the individual fits.

	$\alpha_{\text{fit}} - \alpha_{\text{fid}}$	$\max \Delta_s \alpha_{\text{med}} $	$\max \Delta_{\text{prior}} \langle \alpha_i \rangle $	$\sigma_{\text{sys}}$
$\xi_q$	0.0056	0.0003	0.0001	0.0056
$\xi_{\text{mt}}$	0.0053	0.0011	0.0009	0.0055

**Table 7.** Systematic error budget. Different columns are the different contributions to the total error  $\sigma_{\text{sys}}$  for QSO 2PCF and the multi-tracer analysis.

	$\alpha_{\text{med}}$	$\sigma_{\alpha}$	$\alpha_{\text{med}} - \alpha_{36}$
$\xi_x, R_v > 34$	$1.0164^{+0.0545}_{-0.0589}$	0.0018	0.0103
$\xi_x, R_v > 38$	$0.9960^{+0.0615}_{-0.0639}$	0.0020	-0.0101
$\xi_{\text{mt}}, R_v > 34$	$1.0083^{+0.0360}_{-0.0347}$	0.0011	0.0020
$\xi_{\text{mt}}, R_v > 38$	$1.0052^{+0.0353}_{-0.0367}$	0.0011	-0.0011

**Table 8.** Fitting results of the AP parameter  $\alpha$  on the mean of EZmocks for the fiducial separation range with two different minimum voids radius cut for the XCF. From left to right, the columns are the median of the posterior with 1-sigma errors rescaled by  $\sqrt{1000}$ , the bias of the median of the fit to the fiducial value, the 1-sigma error of the distribution, the bias of the median of the fit to the value for the fiducial cut of  $36 h^{-1}\text{Mpc}$ .

#### 6.4 Change in radius cut

We test the template used for the BAO model and analysis robustness by observing the changes induced by a small variation of the minimum radius cut of the voids. For this, we use the same template model as for the fiducial analysis with  $R_{\text{min}} = 36 h^{-1}\text{Mpc}$  and vary  $R_{\text{min}}$  of the EZmocks XCF by  $2 h^{-1}\text{Mpc}$ .

Table 8 gives the results for the mean of the EZmocks for  $R_{\text{min}} = 34 h^{-1}\text{Mpc}$  and  $R_{\text{min}} = 38 h^{-1}\text{Mpc}$ . As mentioned, the template is not adapted for those radius cuts, so it inserts an expected mild bias compared to the fiducial measurements of Table 5 for the XCF. For the multi-tracer approach with XCF and 2PCF, the bias is small: a small change in the radius cut inserts, therefore a reasonable bias.

#### 6.5 Results on EZmocks

Let us now compare the BAO results of the QSOs auto-correlation and the multi-tracer joint fit of the 2PCF and the XCF. We consider the individual 1000 EZmocks realisations in the fiducial case (minimum radius cut, separation range and priors), i.e. the bold lines in Table 6.

We define the relative difference in errors between the two analyses:

$$\delta_i = \frac{\sigma_{\alpha,i,q} - \sigma_{\alpha,i,\text{mt}}}{\sigma_{\alpha,i,q}} \quad (25)$$

where  $\sigma_{\alpha,i,q}$  is the 1-sigma distribution error on  $\alpha_i$  for the 2PCF case, and  $\sigma_{\alpha,i,\text{mt}}$  in the multi-tracer case. This statistic is presented in Table 9 for the individual EZmocks. Figure 10 compares the errors from fits of QSO 2PCF only and those from the multi-tracer version.

There is an average of about 5% improvement with the contribution of voids in the analysis. A smaller error for the multi-tracer case is observed for around 70% of the EZmocks realisations. Taking only the improved mocks gives, on average better errors of 11.22%. Fitting QSO voids jointly with QSOs allows, therefore, a small improvement for most of the EZmocks on the same sample of data.

	$\langle \delta_i \rangle$	$\langle \delta_i   \delta_i > 0 \rangle$	$\#(\delta_i   \delta_i > 0)$
$\xi_{\text{mt}}$	5.41%	(11.22%)	71.6%

**Table 9.** Mean relative difference  $\delta_i$  of Equation 25 for the individual realisations of EZmocks, mean relative difference when  $\delta_i$  is positive, and proportion of realisations for which  $\delta_i$  is positive.

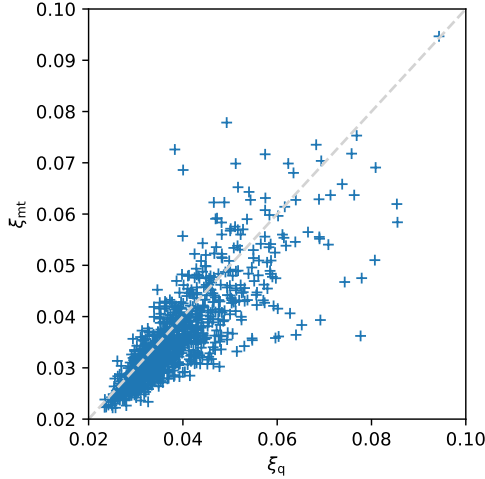


**Figure 10.** Errors from the 2PCF fits against the multi-tracer results which fits jointly the 2PCF and XCF.

In the previous study of Zhao et al. (2022) for eBOSS ELG and LRG samples, the best results on EZmocks were reported to give a larger average improvement ( $\sim 8\%$ ). However, we note that in this case, the void auto-correlation was also jointly fitted and helped reduce the uncertainties. Closer statistics are found when comparing the joint fit with the cross-correlation only. Moreover, with QSOs, some exclusion effects might still play an important role, and this makes the extraction of the BAO information more difficult.

## 7 RESULTS

In this Section, we present the results of the eBOSS DR16 QSO data sample. Table 10 displays the  $\alpha$  measurement and its derived value for our input cosmology, the volume-averaged distance of Equation 12. Fits are made on the fiducial fitting range with the selected priors for  $B$  and  $\Sigma_{\text{nl}}$ . For QSO 2PCF data fit, we fix  $\Sigma_{\text{nl}}$  to the value given by N-body mocks. Voids are selected according to their radius with a hard minimum cut range; see Equation 10.

### 7.1 eBOSS DR16 QSO sample

For data, we observe very similar results from QSOs only or adding voids. The reduced chi-squared is slightly better for the multi-tracer case. However, errors are not improved by the 2PCF joint fit with XCF compared to 2PCF alone. We note, moreover, that  $\Sigma_{\text{nl},\times}$  was estimated from EZmocks that tend to overestimate it. A better determination of  $\Sigma_{\text{nl},\times}$  could lead to better results. The best-fitting BAO models are shown in Figure 11. The data are well fitted on the fitting range in all cases. Results are consistent with the isotropic measurement of Neveux et al. (2020) on the same QSO eBOSS sample, in particular we recover similar errors (see also Hou et al. 2021).

	$\alpha_{\text{fit}}$	$\sigma_{\text{syst}}$	$\chi^2/\text{d.o.f.}$	$D_V(z = 1.48)/r_s$
$\xi_q$	$1.0172^{+0.0207}_{-0.0201}$	0.0056	1.49	$26.298 \pm 0.547$
$\xi_{\text{mt}}$	$1.0171^{+0.0212}_{-0.0196}$	0.0055	1.16	$26.297 \pm 0.547$

**Table 10.** Results on the eBOSS QSO data sample for the standard 2PCF analysis and with the void contribution multi-tracer with XCF. Median of the posterior of the fitted  $\alpha$  parameter and the 16th and 84th percentiles. Total systematic error. The goodness of fit is rescaled by the degree of freedom. The volume-averaged distance at the effective redshift.

	$\langle \alpha_i \rangle$	$\langle \delta_i \rangle$	$\#(\delta_i   \delta_i > 0)$
$\xi_{\text{mt}}$	$1.016 \pm 0.021$	2.09%	68.0%

**Table 11.** Mean  $\alpha$  measurement and 1-sigma dispersion for the 25 subsampled data, relative difference  $\delta_i$  of Equation 25 and proportion of realisations for which  $\delta_i$  is positive.

EZmocks results suggest that data measurement lies in the 30% hazard without improvement observed with a joint fit with the cross-correlation of voids. To recreate the randomness of the sampling of data, we create 25 subsamples of the eBOSS QSOs by removing 1/25 of the area with equal numbers of QSOs different for each of the samples. We then fit them in the same way as for the total sample.

Table 11 gathers the measurements for the 25 data subsamples. The average value is consistent with the data alone. Moreover, we have an average improvement of about 2% for almost 70% of the realisations. This result is in total agreement with the EZmocks. It implies that voids could still bring a small improvement for future QSOs surveys. Indeed an improvement is expected, but for a specific data sample, the improvement is not necessarily seen due to cosmic variance.

### 7.2 DESI-like volume survey forecasts

We further provide a forecast for a QSO survey with a similar effective volume to that of DESI for BAO constraints from QSOs. We repeat the same BAO analysis on 1000 EZbox with BAO.

The effective volume of EZbox is very close to the Year 5 DESI effective volume for an area of  $14'000 \text{ deg}^2$  (DESI Collaboration et al. 2016a) of QSOs. Therefore we directly use the covariance made from the 1000 EZbox without rescaling.

We perform BAO measurements on the 1000 individual realisations for the QSOs 2PCF alone and jointly fitted with their cross-correlation. Following the results of the SNR test of section 4.3.2 for the EZbox, the void radius cut is chosen to be  $31 h^{-1} \text{ Mpc}$ . For the BAO model, we recreate an appropriate template. The clustering of the boxes is consistent with that of the light-cone mocks and the data. In this case, it is appropriate to use the Lagrangian mocks generated for the light-cone mocks, but without radial selection and survey geometry cut, i.e. in their boxes format. The cross-power spectra are then computed for the optimal minimum radius cut of  $31 h^{-1} \text{ Mpc}$ . Measurements are gathered in Table 12.

We recover the same results as for the EZmocks. About 68% of the EZbox realisations have an error reduction when fitting the 2PCF and XCF simultaneously. This improvement is 4.9% on average. This means that increasing the volume, i.e. decreasing the statistical errors, does not help to have a general improvement of the BAO error by adding voids. This might be due to the low density of the QSOs samples. Therefore we expect the results from actual DESI data to be

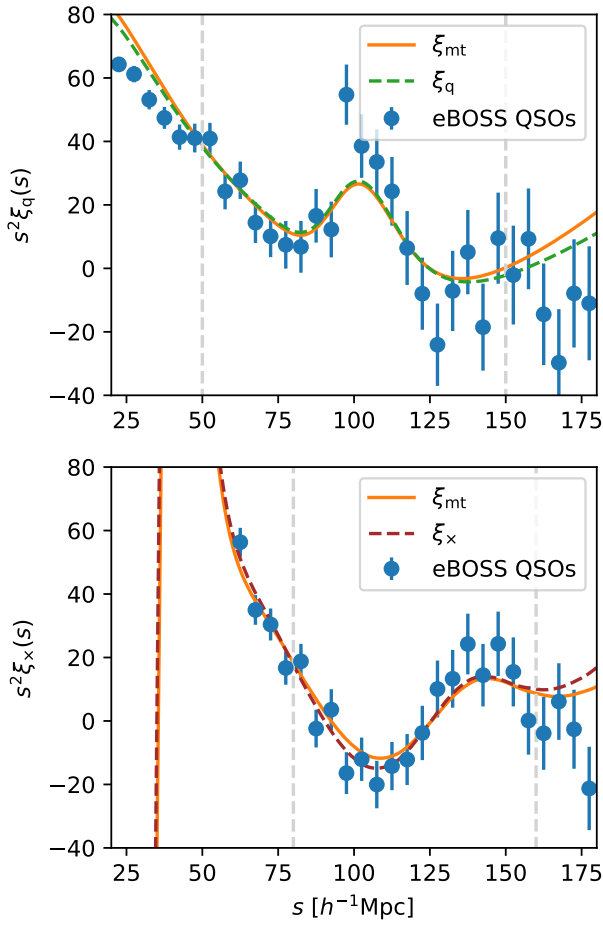


**Figure 11.** Best-fit models as fitted for the 2PCF or XCF alone or jointly.

	$\langle \alpha_i \rangle$	$\sigma_{\alpha_i}$	$\langle \sigma_{\alpha,i} \rangle$	$\langle \delta_i \rangle$	$\#(\delta_i   \delta_i > 0)$
$\xi_{\text{mt}}$	1.003	0.008	0.008	4.90%	68.2%

**Table 12.** Multi-tracer fitting results for the 1000 individual realisations of EZbox with BAO. Columns from left to right: median of the individual AP parameter  $\alpha_i$  fitting values, the standard deviation of the individual  $\alpha_i$  fit values, the median of the individual 1-sigma errors on  $\alpha_i$ , mean relative difference  $\delta_i$  of Equation 25 and proportion of realisations for which  $\delta_i$  is positive.  $\Sigma_{\text{nl}}$  of the fits are fixed from the EZbox mean fits, and we use a  $\pm 10\sigma$  priors on  $B$ .

better, as the density of the QSO boxes is still lower than the expected QSO density of DESI.

## 8 CONCLUSIONS

In this paper, we proposed a void analysis of the QSO eBOSS DR16 sample with voids. Due to the low density of the sample, the minimum size of the void required to mitigate the contamination by voids-in-clouds is about twice the size for the previous analysis (Zhao et al. 2021, 2022) with the same void definition.

To understand the BAO signal from the void correlations, we produced EZmocks with and without BAO signature. This allowed us to

choose the optimal radius cut to increase the BAO signal and minimize the noise. We are able to observe a negative BAO peak in the cross-correlation of QSOs and voids. However, we did not detect any signal in the auto-correlation of voids as geometric exclusion effects affect the BAO scale, since we are considering very large voids. We note that we explored other ways of extending the void catalogue including voids with smaller radii based on QSO local density arguments to increase the number density and alleviate the void exclusion effects. However, some biases appeared in this process, which make such attempts still unreliable. We leave a further investigation on this for future work.

We presented a multi-tracer fit of the 2PCF and XCF jointly. For EZmocks, the errors decreased for 70% of the realisations when voids were jointly fit with QSOs. We report an average of around 5% error improvement for the EZmocks. While we found less improvement than for the other tracers as LRGs and ELGs by adding the contribution of voids (Zhao et al. 2022), we argued that it might be caused by the difficulty of extracting the BAO information due to remaining void exclusion effects. Moreover, the auto-correlation of voids that have a non-negligible constraining power was not included.

For eBOSS QSOs sample data, no improvement was measured including voids. Our analysis showed the same behaviour as for EZmocks when we downsample the data into 25 subsamples. This confirmed that the result for the data is caused by cosmic variance.

We finally presented a forecast for the next batch of surveys like DESI, which will release a large sample of QSOs (DESI Collaboration et al. 2016a,b). Our results demonstrate that voids can still improve the isotropic BAO AP parameter for those data by almost 5%, a result which remains stable even if the volume is increased. Better improvement is expected for future QSO surveys with a higher number density such as J-PAS (Benitez et al. 2014) or WEAVE (Dalton et al. 2016; Pieri et al. 2016). Hence, we conclude, that voids can be potentially useful to further increase the BAO detection from forthcoming QSO catalogues.

## ACKNOWLEDGEMENTS

AT, CZ, DFS and AV acknowledge support from the SNF grant 200020\_175751.

Funding for the Sloan Digital Sky Survey IV has been provided by the Alfred P. Sloan Foundation, the U.S. Department of Energy Office of Science, and the Participating Institutions. SDSS-IV acknowledges support and resources from the Center for High-Performance Computing at the University of Utah. The SDSS web site is [www.sdss.org](http://www.sdss.org). SDSS-IV is managed by the Astrophysical Research Consortium for the Participating Institutions of the SDSS Collaboration including the Brazilian Participation Group, the Carnegie Institution for Science, Carnegie Mellon University, the Chilean Participation Group, the Ecole Polytechnique Federale de Lausanne (EPFL), the French Participation Group, Harvard-Smithsonian Center for Astrophysics, Instituto de Astrofísica de Canarias, The Johns Hopkins University, Kavli Institute for the Physics and Mathematics of the Universe (IPMU) University of Tokyo, the Korean Participation Group, Lawrence Berkeley National Laboratory, Leibniz Institut für Astrophysik Potsdam (AIP), Max-Planck-Institut für Astronomie (MPIA Heidelberg), Max-Planck-Institut für Astrophysik (MPA Garching), Max-Planck-Institut für Extraterrestrische Physik (MPE), National Astronomical Observatories of China, New Mexico State University, New York University, University of Notre Dame, Observatório Nacional / MCTI, The Ohio State University, Pennsylvania State University, Shanghai Astronomical Observatory, United Kingdom



Participation Group, Universidad Nacional Autónoma de México, University of Arizona, University of Colorado Boulder, University of Oxford, University of Portsmouth, University of Utah, University of Virginia, University of Washington, University of Wisconsin, Vanderbilt University, and Yale University.

This research used resources of the National Energy Research Scientific Computing Center, a DOE Office of Science User Facility supported by the Office of Science of the U.S. Department of Energy under Contract No. DE-AC02-05CH11231.

## DATA AVAILABILITY

Mock catalogues and data sample used in this paper are available via the SDSS Science Archive Server. In particular the QSO eBOSS sample can be found here: <https://data.sdss.org/sas/dr17/eboss/qso/DR16Q/>. For EZmocks, they are in: <https://data.sdss.org/sas/dr17/eboss/lss/EZmocks/>. Codes used for the analysis, correlation computations and void finder are all available, as indicated in the paper's footnotes.

## REFERENCES

- Alam S., et al., 2017, *MNRAS*, **470**, 2617
- Alcock C., Paczynski B., 1979, *Nature*, **281**, 358
- Ata M., et al., 2018, *MNRAS*, **473**, 4773
- Aubert M., et al., 2022, *MNRAS*, **513**, 186
- Baldauf T., Seljak U., Smith R. E., Hamaus N., Desjacques V., 2013, *Phys. Rev. D*, **88**, 083507
- Baumgarten F., Chuang C.-H., 2018, *MNRAS*, **480**, 2535
- Bautista J. E., et al., 2021, *MNRAS*, **500**, 736
- Benítez N., et al., 2014, arXiv e-prints, p. arXiv:1403.5237
- Bernardeau F., Colombi S., Gaztañaga E., Scoccimarro R., 2002, *Phys. Rep.*, **367**, 1
- Blake C., Glazebrook K., 2003, *ApJ*, **594**, 665
- Blanton M. R., et al., 2017, *AJ*, **154**, 28
- Buchner J., et al., 2014, *A&A*, **564**, A125
- Busca N. G., et al., 2013, *A&A*, **552**, A96
- Chan K. C., Hamaus N., Desjacques V., 2014, *Phys. Rev. D*, **90**, 103521
- Chuang C.-H., et al., 2015, *MNRAS*, **452**, 686
- Cole S., et al., 2005, *MNRAS*, **362**, 505
- DESI Collaboration et al., 2016a, preprint, p. arXiv:1611.00036 (arXiv:1611.00036)
- DESI Collaboration et al., 2016b, arXiv e-prints, p. arXiv:1611.00037
- Dalton G., et al., 2016, in Evans C. J., Simard L., Takami H., eds, Society of Photo-Optical Instrumentation Engineers (SPIE) Conference Series Vol. 9908, Ground-based and Airborne Instrumentation for Astronomy VI. p. 99081G, doi:10.1117/12.2231078
- Dawson K. S., et al., 2013, *AJ*, **145**, 10
- Dawson K. S., et al., 2016, *AJ*, **151**, 44
- Delaunay B., 1934, Bulletin de l'Académie des Sciences de l'URSS. Classe des sciences mathématiques et na, pp 793–800
- Eisenstein D. J., Hu W., 1998, *ApJ*, **496**, 605
- Eisenstein D. J., et al., 2005, *ApJ*, **633**, 560
- Feldman H. A., Kaiser N., Peacock J. A., 1994, *ApJ*, **426**, 23
- Feroz F., Hobson M. P., Bridges M., 2009, *MNRAS*, **398**, 1601
- Forero-Sánchez D., Zhao C., Tao C., Chuang C.-H., Kitaura F.-S., Variu A., Tamone A., Kneib J.-P., 2022, *MNRAS*, **513**, 5407
- Gil-Marín H., et al., 2020, *MNRAS*, **498**, 2492
- Grieb J. N., Sánchez A. G., Salazar-Albornoz S., Dalla Vecchia C., 2016, *MNRAS*, **457**, 1577
- Gunn J. E., et al., 2006, *AJ*, **131**, 2332
- Hartlap J., Simon P., Schneider P., 2007, *A&A*, **464**, 399
- Heitmann K., et al., 2019, *ApJS*, **245**, 16
- Hou J., et al., 2021, *MNRAS*, **500**, 1201
- Hu W., Sugiyama N., 1996, *ApJ*, **471**, 542
- Kitaura F.-S., et al., 2016, *Physical Review Letters*, **116**, 171301
- Komatsu E., et al., 2011, *ApJS*, **192**, 18
- Landy S. D., Szalay A. S., 1993, *ApJ*, **412**, 64
- Laureijs R., et al., 2011, arXiv e-prints, p. arXiv:1110.3193
- Lewis A., Challinor A., Lasenby A., 2000, *ApJ*, **538**, 473
- Liang Y., Zhao C., Chuang C.-H., Kitaura F.-S., Tao C., 2016, *MNRAS*, **459**, 4020
- Myers A. D., et al., 2015, *ApJS*, **221**, 27
- Nadathur S., et al., 2020, *MNRAS*, **499**, 4140
- Neveux R., et al., 2020, *MNRAS*, **499**, 210
- Neyrinck M. C., Aragón-Calvo M. A., Jeong D., Wang X., 2014, *MNRAS*, **441**, 646
- Percival W. J., 2005, *A&A*, **443**, 819
- Percival W. J., et al., 2014, *MNRAS*, **439**, 2531
- Perlmuter S., et al., 1999, *ApJ*, **517**, 565
- Pieri M. M., et al., 2016, in Reylé C., Richard J., Cambrésy L., Deleuil M., Pécontal E., Tresse L., Vauglin I., eds, SF2A-2016: Proceedings of the Annual meeting of the French Society of Astronomy and Astrophysics. pp 259–266 (arXiv:1611.09388)
- Planck Collaboration et al., 2016, *A&A*, **594**, A13
- Raichoor A., et al., 2021, *MNRAS*, **500**, 3254
- Riess A. G., et al., 1998, *AJ*, **116**, 1009
- Ross A. J., et al., 2016, *MNRAS*, **464**, 1168
- Ross A. J., et al., 2020, *MNRAS*, **498**, 2354
- Sheth R. K., Lemson G., 1999, *MNRAS*, **304**, 767
- Sheth R. K., van de Weygaert R., 2004, *MNRAS*, **350**, 517
- Smee S. A., et al., 2013, *AJ*, **146**, 32
- Smith A., et al., 2020, *MNRAS*, **499**, 269
- Szapudi I., Szalay A. S., 1997, arXiv e-prints, pp astro-ph/9704241
- Tamone A., et al., 2020, *MNRAS*, **499**, 5527
- Vargas-Magaña M., et al., 2013, *A&A*, **554**, A131
- Variu A., 2022, in preparation
- Weinberg D. H., Mortonson M. J., Eisenstein D. J., Hirata C., Riess A. G., Rozo E., 2013, *Phys. Rep.*, **530**, 87
- Xu X., Padmanabhan N., Eisenstein D. J., Mehta K. T., Cuesta A. J., 2012, *MNRAS*, **427**, 2146
- Zel'dovich Y. B., 1970, *A&A*, **5**, 84
- Zhao C., Tao C., Liang Y., Kitaura F.-S., Chuang C.-H., 2016, *MNRAS*, **459**, 2670
- Zhao C., et al., 2020, *MNRAS*, **491**, 4554
- Zhao C., et al., 2021, *MNRAS*, **503**, 1149
- Zhao C., et al., 2022, *MNRAS*, **511**, 5492
- de Jong R. S., et al., 2019, *The Messenger*, **175**, 3
- de Mattia A., Ruhlmann-Kleider V., 2019, *J. Cosmology Astropart. Phys.*, **2019**, 036
- du Mas des Bourboux H., et al., 2020, arXiv e-prints, p. arXiv:2007.08995

This paper has been typeset from a  $\text{\LaTeX}$  file prepared by the author.



## 4 Conclusion

I dedicated Chapter 1 to a general summary required for the understanding of this manuscript. The standard cosmological framework was first introduced in the context of general relativity. Then large scale structures (LSS) were shown to be a powerful probe for cosmology. Their observation is made possible thanks to spectroscopic surveys. Different features in LSS clustering can be observed. Baryon acoustic oscillations (BAO) are standard rulers and can be used to measure distances, and thus the Universe's expansion history. Redshift space distortions (RSD) are caused by the peculiar velocities of galaxies. They can be used to probe the growth of structures in the Universe. Both are important tools to constrain cosmological parameters.

During this thesis, I completed a full-shape analysis of the RSD from the ELG sample of eBOSS in configuration space in the redshift range between 0.6 and 1.1. This work is presented in Chapter 2. I aimed at obtaining a measurement of the growth rate and the AP parameters. The ELGs were affected by strong observational systematics. These systematics were biasing the cosmological measurements. To mitigate their effect, we introduced a modified correlation function estimator that we applied consistently to the data, the EZmocks and the model. We showed with approximated mocks that it greatly helped recovering the true fiducial cosmological values. Moreover the ELG clustering was also altered by the the so called radial integral constraint (RIC) due to the shuffled redshift assignment scheme used for randoms that suppresses radial modes. The RIC impact was very strong on the eBOSS ELG sample. To correct for this we implemented a theoretical modification to the model.

For the theoretical description of the clustering in redshift space I used Convolution Lagrangian Perturbation Theory (CLPT) with a model of Gaussian Streaming (GS). I was able to obtain the growth rate and AP parameters constraints while fitting jointly RSD and BAO. The BAO measurements were done on the post-reconstruction monopole of the ELGs and for the RSD on the three first even multipoles of the pre-reconstruction clustering.

Joint constraints between the configuration space and the Fourier space measurements were provided. They were afterward used for the final cosmological analysis of the last 20 years of

SDSS. SDSS BAO and RSD measurements are consistent with a flat  $\Lambda$ CDM model. Growth rate values were consistent with CMB predictions from Planck. In a  $w_0 w_a$ CDM model with SDSS data and Planck CMB measurements combined a DETF figure of merit of 134 was found, outpassing the initial expectations from a Stage III experiment.

In a second part of the dissertation introduced in Chapter 3, I performed a BAO analysis on voids from the quasar sample of eBOSS. The voids were found using the software DIVE that relies on Delaunay Triangulation. I first participated to the void BAO analysis on ELGs and LRGs of eBOSS where we showed that an improvement of 5 to 15 % in the uncertainties were reached in the data. We extended this work to QSOs.

A selection of the QSO voids was first made in order to keep the voids in underdense regions. For this a large void radius threshold was required due to the low quasar number density. As an effect of this large radius cut, strong exclusion effects were seen in the clustering. We produced approximate mocks without BAO to understand it and to select the optimal radius cut to enhance the BAO signal-to-noise. Although a BAO signal was still detected in the void auto-correlation (2PCF), we only used the void and QSO cross-correlation (XCF) as the exclusion effect was interfering in the BAO scale in the void 2PCF.

We performed a joint BAO fit of the XCF and the QSO 2PCF. To model the BAO we made use of a template to mimic the tracer power spectrum without BAO wiggles. In the EZmocks we observed an improvement for 70% of the mocks, with a total average improvement of about 5%. For data we didn't see any improvement due to cosmic variance. We furthermore created 25 subsample sets of data to confirm the cosmic variance results, as we recover an improvement from data in 70% of the cases. We also provided a forecast for a DESI-like volume survey using cubic boxes, and we recovered the same statistic results as from the EZmocks.

During this thesis, I was able to bring valuable cosmological measurements on an ELG sample that allowed to help constraining the standard model of cosmology. Furthermore the QSO voids study emphasized the strength of voids that have a significant constraining power.

The work effectuated paves the way for future analyses. ELG will massively be observed in the current and future generations of surveys. As in future surveys the statistical uncertainty will be small due to the large number of observations, the systematics will be a big concern. Therefore they will have to be well understood and treated carefully. The ELG analysis I performed will help the future data treatment and cosmological measurements. Indeed the careful considerations I took such as RIC and the angular modes mitigation could be needed in future analyses.

Moreover in the area of precision cosmology any constraints improvement is important. In particular, precise measurements from QSOs samples are critical due to their high redshifts that give us insights on the matter domination epoch of the Universe. I showed that voids could be a great solution to decrease the uncertainties by using the same dataset. Their use will then be very relevant in the future.

# Bibliography

- Abazajian, K., Addison, G., Adshead, P., Ahmed, Z., Allen, S. W., Alonso, D., Alvarez, M., Anderson, A., Arnold, K. S., Baccigalupi, C., Bailey, K., Barkats, D., Barron, D., Barry, P. S., Bartlett, J. G., Basu Thakur, R., Battaglia, N., Baxter, E., Bean, R., ... Zonca, A. (2019). CMB-S4 Science Case, Reference Design, and Project Plan. *arXiv e-prints*, Article arXiv:1907.04473, arXiv:1907.04473.
- Abbott, T., Abdalla, F. B., Allam, S., Amara, A., Annis, J., Armstrong, R., Bacon, D., Banerji, M., Bauer, A. H., Baxter, E., Becker, M. R., Benoit-Lévy, A., Bernstein, R. A., Bernstein, G. M., Bertin, E., Blazek, J., Bonnett, C., Bridle, S. L., Brooks, D., ... Dark Energy Survey Collaboration. (2016). Cosmology from cosmic shear with Dark Energy Survey Science Verification data., 94(2), Article 022001, 022001. <https://doi.org/10.1103/PhysRevD.94.022001>
- Abbott, T. M. C., Abdalla, F. B., Allam, S., Amara, A., Annis, J., Asorey, J., Avila, S., Ballester, O., Banerji, M., Barkhouse, W., Baruah, L., Baumer, M., Bechtol, K., Becker, M. R., Benoit-Lévy, A., Bernstein, G. M., Bertin, E., Blazek, J., Bocquet, S., ... NOAO Data Lab. (2018). The Dark Energy Survey: Data Release 1., 239(2), Article 18, 18. <https://doi.org/10.3847/1538-4365/aae9f0>
- Abbott, T. M. C., Abdalla, F. B., Avila, S., Banerji, M., Baxter, E., Bechtol, K., Becker, M. R., Bertin, E., Blazek, J., Bridle, S. L., Brooks, D., Brout, D., Burke, D. L., Campos, A., Carnero Rosell, A., Carrasco Kind, M., Carretero, J., Castander, F. J., Cawthon, R., ... DES Collaboration. (2019). Dark Energy Survey year 1 results: Constraints on extended cosmological models from galaxy clustering and weak lensing., 99(12), Article 123505, 123505. <https://doi.org/10.1103/PhysRevD.99.123505>
- Abdalla, E., Abellán, G. F., Aboubrahim, A., Agnello, A., Akarsu, Ö., Akrami, Y., Alestas, G., Aloni, D., Amendola, L., Anchordoqui, L. A., Anderson, R. I., Arendse, N., Asgari, M., Ballardini, M., Barger, V., Basilakos, S., Batista, R. C., Battistelli, E. S., Battye, R., ... Zumalacárregui, M. (2022). Cosmology intertwined: A review of the particle physics, astrophysics, and cosmology associated with the cosmological tensions and anomalies. *Journal of High Energy Astrophysics*, 34, 49–211. <https://doi.org/10.1016/j.jheap.2022.04.002>
- Abel, T., Hahn, O., & Kaehler, R. (2012). Tracing the dark matter sheet in phase space., 427(1), 61–76. <https://doi.org/10.1111/j.1365-2966.2012.21754.x>
- Adelberger, E. G., Garcia, A., Robertson, R. G. H., Snover, K. A., Balantekin, A. B., Heeger, K., Ramsey-Musolf, M. J., Bemmerer, D., Junghans, A., Bertulani, C. A., Chen, J. .-,

- Costantini, H., Prati, P., Couder, M., Uberseder, E., Wiescher, M., Cyburt, R., Davids, B., Freedman, S. J., ... Typel, S. (2011). Solar fusion cross sections. II. The pp chain and CNO cycles. *Reviews of Modern Physics*, 83(1), 195–246. <https://doi.org/10.1103/RevModPhys.83.195>
- Alam, S., Ata, M., Bailey, S., Beutler, F., Bizyaev, D., Blazek, J. A., Bolton, A. S., Brownstein, J. R., Burden, A., Chuang, C.-H., Comparat, J., Cuesta, A. J., Dawson, K. S., Eisenstein, D. J., Escoffier, S., Gil-Marín, H., Grieb, J. N., Hand, N., Ho, S., ... Zhao, G.-B. (2017). The clustering of galaxies in the completed SDSS-III Baryon Oscillation Spectroscopic Survey: cosmological analysis of the DR12 galaxy sample., 470, 2617–2652. <https://doi.org/10.1093/mnras/stx721>
- Alam, S., Aubert, M., Avila, S., Bland, C., Bautista, J. E., Bershad, M. A., Bizyaev, D., Blanton, M. R., Bolton, A. S., Bovy, J., Brinkmann, J., Brownstein, J. R., Burtin, E., Chabanier, S., Chapman, M. J., Choi, P. D., Chuang, C.-H., Comparat, J., Cousinou, M.-C., ... Zheng, Z. (2021). Completed SDSS-IV extended Baryon Oscillation Spectroscopic Survey: Cosmological implications from two decades of spectroscopic surveys at the Apache Point Observatory., 103(8), Article 083533, 083533. <https://doi.org/10.1103/PhysRevD.103.083533>
- Alam, S., de Mattia, A., Tamone, A., Ávila, S., Peacock, J. A., Gonzalez-Perez, V., Smith, A., Raichoor, A., Ross, A. J., Bautista, J. E., Burtin, E., Comparat, J., Dawson, K. S., du Mas des Bourboux, H., Escoffier, S., Gil-Marín, H., Habib, S., Heitmann, K., Hou, J., ... Zhao, G.-B. (2021). The completed SDSS-IV extended Baryon Oscillation Spectroscopic Survey: N-body mock challenge for the eBOSS emission line galaxy sample., 504(4), 4667–4686. <https://doi.org/10.1093/mnras/stab1150>
- Albrecht, A., Bernstein, G., Cahn, R., Freedman, W. L., Hewitt, J., Hu, W., Huth, J., Kamionkowski, M., Kolb, E. W., Knox, L., Mather, J. C., Staggs, S., & Suntzeff, N. B. (2006). Report of the Dark Energy Task Force. *arXiv e-prints*, Article astro-ph/0609591, astro-ph/0609591.
- Alcock, C., & Paczynski, B. (1979). An evolution free test for non-zero cosmological constant., 281, 358. <https://doi.org/10.1038/281358a0>
- Alpher, R. A., Bethe, H., & Gamow, G. (1948). The Origin of Chemical Elements. *Physical Review*, 73(7), 803–804. <https://doi.org/10.1103/PhysRev.73.803>
- Alpher, R. A., & Herman, R. (1948). Evolution of the Universe., 162(4124), 774–775. <https://doi.org/10.1038/162774b0>
- Amendola, L., Frieman, J. A., & Waga, I. (1999). Weak gravitational lensing by voids., 309(2), 465–473. <https://doi.org/10.1046/j.1365-8711.1999.02841.x>
- Annis, J., Newman, J. A., & Slosar, A. (2022). Snowmass2021 Cosmic Frontier: Report of the CF04 Topical Group on Dark Energy and Cosmic Acceleration in the Modern Universe. *arXiv e-prints*, Article arXiv:2209.08049, arXiv:2209.08049.
- Aragón-Calvo, M. A., van de Weygaert, R., & Jones, B. J. T. (2010). Multiscale phenomenology of the cosmic web., 408(4), 2163–2187. <https://doi.org/10.1111/j.1365-2966.2010.17263.x>
- Asaka, T., & Shaposhnikov, M. (2005). The nuMSM, dark matter and baryon asymmetry of the universe [rapid communication]. *Physics Letters B*, 620(1-2), 17–26. <https://doi.org/10.1016/j.physletb.2005.06.020>

- Asgari, M., Lin, C.-A., Joachimi, B., Giblin, B., Heymans, C., Hildebrandt, H., Kannawadi, A., Stölzner, B., Tröster, T., van den Busch, J. L., Wright, A. H., Bilicki, M., Blake, C., de Jong, J., Dvornik, A., Erben, T., Getman, F., Hoekstra, H., Köhlinger, F., ... Valentijn, E. (2021). KiDS-1000 cosmology: Cosmic shear constraints and comparison between two point statistics., *645*, Article A104, A104. <https://doi.org/10.1051/0004-6361/202039070>
- Ata, M., Baumgarten, F., Bautista, J., Beutler, F., Bizyaev, D., Blanton, M. R., Blazek, J. A., Bolton, A. S., Brinkmann, J., Brownstein, J. R., Burtin, E., Chuang, C.-H., Comparat, J., Dawson, K. S., de la Macorra, A., Du, W., du Mas des Bourboux, H., Eisenstein, D. J., Gil-Marín, H., ... Zhu, F. (2018). The clustering of the SDSS-IV extended Baryon Oscillation Spectroscopic Survey DR14 quasar sample: first measurement of baryon acoustic oscillations between redshift 0.8 and 2.2., *473*(4), 4773–4794. <https://doi.org/10.1093/mnras/stx2630>
- Aubert, M., Cousinou, M.-C., Escoffier, S., Hawken, A. J., Nadathur, S., Alam, S., Bautista, J., Burtin, E., Chuang, C.-H., de la Macorra, A., de Mattia, A., Gil-Marín, H., Hou, J., Jullo, E., Kneib, J.-P., Neveux, R., Rossi, G., Schneider, D., Smith, A., ... Zhao, C. (2022). The completed SDSS-IV extended Baryon Oscillation Spectroscopic Survey: growth rate of structure measurement from cosmic voids., *513*(1), 186–203. <https://doi.org/10.1093/mnras/stac828>
- Avila, S., Gonzalez-Perez, V., Mohammad, F. G., de Mattia, A., Zhao, C., Raichoor, A., Tamone, A., Alam, S., Bautista, J., Bianchi, D., Burtin, E., Chapman, M. J., Chuang, C.-H., Comparat, J., Dawson, K., Divers, T., du Mas des Bourboux, H., Gil-Marín, H., Mueller, E. M., ... Zhao, G. (2020). The Completed SDSS-IV extended Baryon Oscillation Spectroscopic Survey: exploring the Halo Occupation Distribution model for Emission Line Galaxies., *499*, 5486–5507. <https://doi.org/10.1093/mnras/staa2951>
- Bailes, M., Berger, B. K., Brady, P. R., Branchesi, M., Danzmann, K., Evans, M., Holley-Bockelmann, K., Iyer, B. R., Kajita, T., Katsanevas, S., Kramer, M., Lazzarini, A., Lehner, L., Losurdo, G., Lück, H., McClelland, D. E., McLaughlin, M. A., Punturo, M., Ransom, S., ... Vitale, S. (2021). Gravitational-wave physics and astronomy in the 2020s and 2030s. *Nature Reviews Physics*, *3*(5), 344–366. <https://doi.org/10.1038/s42254-021-00303-8>
- Baker, T., Clampitt, J., Jain, B., & Trodden, M. (2018). Void lensing as a test of gravity., *98*(2), Article 023511, 023511. <https://doi.org/10.1103/PhysRevD.98.023511>
- Baltz, E. A., & Murayama, H. (2003). Gravitino warm dark matter with entropy production. *Journal of High Energy Physics*, *2003*(5), Article 067, 067. <https://doi.org/10.1088/1126-6708/2003/05/067>
- Bardeen, J. M., Bond, J. R., Kaiser, N., & Szalay, A. S. (1986). The Statistics of Peaks of Gaussian Random Fields., *304*, 15. <https://doi.org/10.1086/164143>
- Bardeen, J. M. (1980). Gauge-invariant cosmological perturbations., *22*(8), 1882–1905. <https://doi.org/10.1103/PhysRevD.22.1882>
- Baumgarten, F., & Chuang, C.-H. (2018). Robustness of the covariance matrix for galaxy clustering measurements., *480*(2), 2535–2543. <https://doi.org/10.1093/mnras/sty1971>
- Bautista, J. E., Paviot, R., Vargas Magaña, M., de la Torre, S., Fromenteau, S., Gil-Marín, H., Ross, A. J., Burtin, E., Dawson, K. S., Hou, J., Kneib, J.-P., de Mattia, A., Percival, W. J., Rossi,

- G., Tojeiro, R., Zhao, C., Zhao, G.-B., Alam, S., Brownstein, J., ... Wang, Y. (2021). The completed SDSS-IV extended Baryon Oscillation Spectroscopic Survey: measurement of the BAO and growth rate of structure of the luminous red galaxy sample from the anisotropic correlation function between redshifts 0.6 and 1., *500*(1), 736–762. <https://doi.org/10.1093/mnras/staa2800>
- Begeman, K. G., Broeils, A. H., & Sanders, R. H. (1991). Extended rotation curves of spiral galaxies : dark haloes and modified dynamics., *249*, 523. <https://doi.org/10.1093/mnras/249.3.523>
- Behroozi, P. S., Conroy, C., & Wechsler, R. H. (2010). A Comprehensive Analysis of Uncertainties Affecting the Stellar Mass-Halo Mass Relation for  $0 < z < 4$ ., *717*(1), 379–403. <https://doi.org/10.1088/0004-637X/717/1/379>
- Bennett, C. L., Halpern, M., Hinshaw, G., Jarosik, N., Kogut, A., Limon, M., Meyer, S. S., Page, L., Spergel, D. N., Tucker, G. S., Wollack, E., Wright, E. L., Barnes, C., Greason, M. R., Hill, R. S., Komatsu, E., Nolte, M. R., Odegard, N., Peiris, H. V., ... Weiland, J. L. (2003). First-Year Wilkinson Microwave Anisotropy Probe (WMAP) Observations: Preliminary Maps and Basic Results., *148*(1), 1–27. <https://doi.org/10.1086/377253>
- Bergström, L. (2000). Non-baryonic dark matter: observational evidence and detection methods. *Reports on Progress in Physics*, *63*(5), 793–841. <https://doi.org/10.1088/0034-4885/63/5/2r3>
- Berlind, A. A., & Weinberg, D. H. (2002). The Halo Occupation Distribution: Toward an Empirical Determination of the Relation between Galaxies and Mass., *575*(2), 587–616. <https://doi.org/10.1086/341469>
- Bernardeau, F., Colombi, S., Gaztañaga, E., & Scoccimarro, R. (2002). Large-scale structure of the Universe and cosmological perturbation theory., *367*(1-3), 1–248. [https://doi.org/10.1016/S0370-1573\(02\)00135-7](https://doi.org/10.1016/S0370-1573(02)00135-7)
- Bertone, G., & Hooper, D. (2018). History of dark matter. *Reviews of Modern Physics*, *90*(4), Article 045002, 045002. <https://doi.org/10.1103/RevModPhys.90.045002>
- Betancort-Rijo, J., Patiri, S. G., Prada, F., & Romano, A. E. (2009). The statistics of voids as a tool to constrain cosmological parameters:  $\sigma_8$  and  $\Gamma$ ., *400*, 1835–1849. <https://doi.org/10.1111/j.1365-2966.2009.15567.x>
- Beutler, F., Blake, C., Colless, M., Staveley-Smith, L., & Jones, H. (2012). The 6dF Galaxy Survey: Baryon Acoustic Oscillations and the Local Hubble Constant. *American Astronomical Society Meeting Abstracts #219*, *219*, Article 402.01, 402.01.
- Beutler, F., Castorina, E., & Zhang, P. (2019). Interpreting measurements of the anisotropic galaxy power spectrum., *2019*(3), Article 040, 040. <https://doi.org/10.1088/1475-7516/2019/03/040>
- Beutler, F., Seo, H.-J., Saito, S., Chuang, C.-H., Cuesta, A. J., Eisenstein, D. J., Gil-Marín, H., Grieb, J. N., Hand, N., Kitaura, F.-S., Modi, C., Nichol, R. C., Olmstead, M. D., Percival, W. J., Prada, F., Sánchez, A. G., Rodríguez-Torres, S., Ross, A. J., Ross, N. P., ... Vargas-Magaña, M. (2017). The clustering of galaxies in the completed SDSS-III Baryon Oscillation Spectroscopic Survey: anisotropic galaxy clustering in Fourier space., *466*(2), 2242–2260. <https://doi.org/10.1093/mnras/stw3298>



- Bianchi, D., Percival, W. J., & Bel, J. (2016). Improving the modelling of redshift-space distortions-II. A pairwise velocity model covering large and small scales., *463*(4), 3783–3798. <https://doi.org/10.1093/mnras/stw2243>
- Blake, C., Brough, S., & Colless, M. e. a. (2011). The wigglez dark energy survey: the growth rate of cosmic structure since redshift  $z = 0.9$ ., *415*, 2876–2891.
- Blake, C., Davis, T., & Poole, G. B. e. a. (2011). The wigglez dark energy survey: testing the cosmological model with baryon acoustic oscillations at  $z = 0.6$ ., 2892–2909.
- Blanton, M. R., Bershad, M. A., Abolfathi, B., Albareti, F. D., Allende Prieto, C., Almeida, A., Alonso-Garcia, J., Anders, F., Anderson, S. F., Andrews, B., Aquino-Ortiz, E., Aragón-Salamanca, A., Argudo-Fernández, M., Armengaud, E., Aubourg, E., Avila-Reese, V., Badenes, C., Bailey, S., Barger, K. A., ... Zou, H. (2017). Sloan Digital Sky Survey IV: Mapping the Milky Way, Nearby Galaxies, and the Distant Universe., *154*(1), Article 28, 28. <https://doi.org/10.3847/1538-3881/aa7567>
- Blumenthal, G. R., Faber, S. M., Primack, J. R., & Rees, M. J. (1984). Formation of galaxies and large-scale structure with cold dark matter., *311*, 517–525. <https://doi.org/10.1038/311517a0>
- Bode, P., Ostriker, J. P., & Turok, N. (2001). Halo Formation in Warm Dark Matter Models., *556*(1), 93–107. <https://doi.org/10.1086/321541>
- Bond, J. R., Cole, S., Efstathiou, G., & Kaiser, N. (1991). Excursion Set Mass Functions for Hierarchical Gaussian Fluctuations., *379*, 440. <https://doi.org/10.1086/170520>
- Bonvin, V., Courbin, F., Suyu, S. H., Marshall, P. J., Rusu, C. E., Sluse, D., Tewes, M., Wong, K. C., Collett, T., Fassnacht, C. D., Treu, T., Auger, M. W., Hilbert, S., Koopmans, L. V. E., Meylan, G., Rumbaugh, N., Sonnenfeld, A., & Spiniello, C. (2017). H0LiCOW - V. New COSMOGRAIL time delays of HE 0435-1223:  $H_0$  to 3.8 per cent precision from strong lensing in a flat  $\Lambda$ CDM model., *465*, 4914–4930. <https://doi.org/10.1093/mnras/stw3006>
- Boyarsky, A., Ruchayskiy, O., & Shaposhnikov, M. (2009). The Role of Sterile Neutrinos in Cosmology and Astrophysics. *Annual Review of Nuclear and Particle Science*, *59*(1), 191–214. <https://doi.org/10.1146/annurev.nucl.010909.083654>
- Boylan-Kolchin, M., Bullock, J. S., & Kaplinghat, M. (2011). Too big to fail? The puzzling darkness of massive Milky Way subhaloes., *415*(1), L40–L44. <https://doi.org/10.1111/j.1745-3933.2011.01074.x>
- Buchert, T., Melott, A. L., & Weiss, A. G. (1994). Testing higher-order Lagrangian perturbation theory against numerical simulations I. Pancake models., *288*, 349–364.
- Bull, P., Akrami, Y., Adamek, J., Baker, T., Bellini, E., Beltrán Jiménez, J., Bentivegna, E., Camera, S., Clesse, S., Davis, J. H., Di Dio, E., Enander, J., Heavens, A., Heisenberg, L., Hu, B., Llinares, C., Maartens, R., Mörtzell, E., Nadathur, S., ... Winther, H. A. (2016). Beyond  $\Lambda$  CDM: Problems, solutions, and the road ahead. *Physics of the Dark Universe*, *12*, 56–99. <https://doi.org/10.1016/j.dark.2016.02.001>
- Bundy, K., Bershad, M. A., Law, D. R., Yan, R., Drory, N., MacDonald, N., Wake, D. A., Cherinka, B., Sánchez-Gallego, J. R., Weijmans, A.-M., Thomas, D., Tremonti, C., Masters, K., Coccato, L., Diamond-Stanic, A. M., Aragón-Salamanca, A., Avila-Reese, V., Badenes,

- C., Falcón-Barroso, J., ... Zhang, K. (2015). Overview of the SDSS-IV MaNGA Survey: Mapping nearby Galaxies at Apache Point Observatory., 798(1), Article 7, 7. <https://doi.org/10.1088/0004-637X/798/1/7>
- Busca, N. G., Delubac, T., Rich, J., Bailey, S., Font-Ribera, A., Kirkby, D., Le Goff, J.-M., Pieri, M. M., Slosar, A., Aubourg, É., Bautista, J. E., Bizyaev, D., Blomqvist, M., Bolton, A. S., Bovy, J., Brewington, H., Borde, A., Brinkmann, J., Carithers, B., ... York, D. G. (2013). Baryon acoustic oscillations in the Ly $\alpha$  forest of BOSS quasars., 552, Article A96, A96. <https://doi.org/10.1051/0004-6361/201220724>
- Cai, Y.-C., Neyrinck, M., Mao, Q., Peacock, J. A., Szapudi, I., & Berlind, A. A. (2017). The lensing and temperature imprints of voids on the cosmic microwave background., 466(3), 3364–3375. <https://doi.org/10.1093/mnras/stw3299>
- Cai, Y.-C., Padilla, N., & Li, B. (2015). Testing gravity using cosmic voids., 451, 1036–1055.
- Caldwell, R. R., Dave, R., & Steinhardt, P. J. (1998). Cosmological Imprint of an Energy Component with General Equation of State., 80(8), 1582–1585. <https://doi.org/10.1103/PhysRevLett.80.1582>
- Camacho-Quevedo, B., & Gaztañaga, E. (2022). A measurement of the scale of homogeneity in the early Universe., 2022(4), Article 044, 044. <https://doi.org/10.1088/1475-7516/2022/04/044>
- Carlson, J., Reid, B., & White, M. (2013). Convolution Lagrangian perturbation theory for biased tracers., 429, 1674–1685. <https://doi.org/10.1093/mnras/sts457>
- Carlson, J., White, M., & Padmanabhan, N. (2009). Critical look at cosmological perturbation theory techniques., 80(4), Article 043531, 043531. <https://doi.org/10.1103/PhysRevD.80.043531>
- Carlsten, S. G., Greene, J. E., Beaton, R. L., Danieli, S., & Greco, J. P. (2022). The Exploration of Local Volume Satellites (ELVES) Survey: A Nearly Volume-limited Sample of Nearby Dwarf Satellite Systems., 933(1), Article 47, 47. <https://doi.org/10.3847/1538-4357/ac6fd7>
- Carrasco, J. J. M., Hertzberg, M. P., & Senatore, L. (2012). The effective field theory of cosmological large scale structures. *Journal of High Energy Physics*, 2012, Article 82, 82. [https://doi.org/10.1007/JHEP09\(2012\)082](https://doi.org/10.1007/JHEP09(2012)082)
- Carroll, S. M., Press, W. H., & Turner, E. L. (1992). The cosmological constant., 30, 499–542. <https://doi.org/10.1146/annurev.aa.30.090192.002435>  
<https://ned.ipac.caltech.edu/level5/Carroll/frames.html>
- Carroll, S. M. (1997). Lecture Notes on General Relativity. *arXiv e-prints*, Article gr-qc/9712019, gr-qc/9712019.
- Castorina, E., & White, M. (2018). Beyond the plane-parallel approximation for redshift surveys., 476(4), 4403–4417. <https://doi.org/10.1093/mnras/sty410>
- Cautun, M., Paillas, E., Cai, Y.-C., Bose, S., Armijo, J., Li, B., & Padilla, N. (2018). The Santiago-Harvard-Edinburgh-Durham void comparison - I. SHEDding light on chameleon gravity tests., 476(3), 3195–3217. <https://doi.org/10.1093/mnras/sty463>
- Cautun, M., van de Weygaert, R., & Jones, B. J. T. (2013). NEXUS: tracing the cosmic web connection., 429(2), 1286–1308. <https://doi.org/10.1093/mnras/sts416>

- Chapman, M. J., Mohammad, F. G., Zhai, Z., Percival, W. J., Tinker, J. L., Bautista, J. E., Brownstein, J. R., Burtin, E., Dawson, K. S., Gil-Marín, H., de la Macorra, A., Ross, A. J., Rossi, G., Schneider, D. P., & Zhao, G.-B. (2022). The completed SDSS-IV extended Baryon Oscillation Spectroscopic Survey: measurement of the growth rate of structure from the small-scale clustering of the luminous red galaxy sample., *516*(1), 617–635. <https://doi.org/10.1093/mnras/stac1923>
- Chevallier, M., & Polarski, D. (2001). Accelerating Universes with Scaling Dark Matter. *International Journal of Modern Physics D*, *10*(2), 213–223. <https://doi.org/10.1142/S0218271801000822>
- Chiboucas, K., Jacobs, B. A., Tully, R. B., & Karachentsev, I. D. (2013). Confirmation of Faint Dwarf Galaxies in the M81 Group., *146*(5), Article 126, 126. <https://doi.org/10.1088/0004-6256/146/5/126>
- Chuang, C.-H., Kitaura, F.-S., Liang, Y., Font-Ribera, A., Zhao, C., McDonald, P., & Tao, C. (2017). Linear redshift space distortions for cosmic voids based on galaxies in redshift space., *95*(6), Article 063528, 063528. <https://doi.org/10.1103/PhysRevD.95.063528>
- Chuang, C.-H., Zhao, C., Prada, F., Munari, E., Avila, S., Izard, A., Kitaura, F.-S., Manera, M., Monaco, P., Murray, S., Knebe, A., Scóccola, C. G., Yepes, G., Garcia-Bellido, J., Marín, F. A., Müller, V., Skibba, R., Crocce, M., Fosalba, P., ... Turchaninov, V. (2015). nIFTy cosmology: Galaxy/halo mock catalogue comparison project on clustering statistics., *452*(1), 686–700. <https://doi.org/10.1093/mnras/stv1289>
- Clampitt, J., & Jain, B. (2015). Lensing measurements of the mass distribution in SDSS voids., *454*(4), 3357–3365. <https://doi.org/10.1093/mnras/stv2215>
- Clarkson, C. (2012). Establishing homogeneity of the universe in the shadow of dark energy. *Comptes Rendus Physique*, *13*(6-7), 682–718. <https://doi.org/10.1016/j.crhy.2012.04.005>
- Colberg, J. M., Pearce, F., Foster, C., Platen, E., Brunino, R., Neyrinck, M., Basilakos, S., Fairall, A., Feldman, H., Gottlöber, S., Hahn, O., Hoyle, F., Müller, V., Nelson, L., Plionis, M., Porciani, C., Shandarin, S., Vogeley, M. S., & van de Weygaert, R. (2008). The Aspen-Amsterdam void finder comparison project., *387*(2), 933–944. <https://doi.org/10.1111/j.1365-2966.2008.13307.x>
- Colberg, J. M., Sheth, R. K., Diaferio, A., Gao, L., & Yoshida, N. (2005). Voids in a  $\Lambda$ CDM universe., *360*(1), 216–226. <https://doi.org/10.1111/j.1365-2966.2005.09064.x>
- Cole, S., & Kaiser, N. (1989). Biased clustering in the cold dark matter cosmogony., *237*, 1127–1146. <https://doi.org/10.1093/mnras/237.4.1127>
- Cole, S., Lacey, C. G., Baugh, C. M., & Frenk, C. S. (2000). Hierarchical galaxy formation., *319*(1), 168–204. <https://doi.org/10.1046/j.1365-8711.2000.03879.x>
- Cole, S., Percival, W. J., Peacock, J. A., Norberg, P., Baugh, C. M., Frenk, C. S., Baldry, I., Bland-Hawthorn, J., Bridges, T., Cannon, R., Colless, M., Collins, C., Couch, W., Cross, N. J. G., Dalton, G., Eke, V. R., de Propris, R., Driver, S. P., Efstathiou, G., ... Team, T. 2. (2005). The 2dF Galaxy Redshift Survey: power-spectrum analysis of the final data set and cosmological implications., *362*(2), 505–534. <https://doi.org/10.1111/j.1365-2966.2005.09318.x>

- Coles, P. (2001). Large-scale Structure, Theory and Statistics. In H. J. de Vega, I. M. Khalatnikov, & N. G. Sanchez (Eds.), *Phase transitions in the early universe: theory and observations* (p. 217).
- Colin, P., Klypin, A. A., Kravtsov, A. V., & Khokhlov, A. M. (1999). Evolution of Bias in Different Cosmological Models., 523(1), 32–53. <https://doi.org/10.1086/307710>
- Collaboration, L. S. (2016). *Lsc instrument science white paper* (tech. rep.). <https://dcc.ligo.org/LIGO-T1600119/public>
- Colless, M., Dalton, G., Maddox, S., Sutherland, W., Norberg, P., Cole, S., Bland-Hawthorn, J., Bridges, T., Cannon, R., Collins, C., Couch, W., Cross, N., Deeley, K., De Propriis, R., Driver, S. P., Efstathiou, G., Ellis, R. S., Frenk, C. S., Glazebrook, K., ... Taylor, K. (2001). The 2dF Galaxy Redshift Survey: spectra and redshifts., 328(4), 1039–1063. <https://doi.org/10.1046/j.1365-8711.2001.04902.x>
- Conley, A., Guy, J., Sullivan, M., Regnault, N., Astier, P., Balland, C., Basa, S., Carlberg, R. G., Fouchez, D., Hardin, D., Hook, I. M., Howell, D. A., Pain, R., Palanque-Delabrouille, N., Perrett, K. M., Pritchett, C. J., Rich, J., Ruhlmann-Kleider, V., Balam, D., ... Walker, E. S. (2011). Supernova Constraints and Systematic Uncertainties from the First Three Years of the Supernova Legacy Survey., 192(1), Article 1, 1. <https://doi.org/10.1088/0067-0049/192/1/1>
- Conroy, C., Wechsler, R. H., & Kravtsov, A. V. (2006). Modeling Luminosity-dependent Galaxy Clustering through Cosmic Time., 647(1), 201–214. <https://doi.org/10.1086/503602>
- Contreras, C., Blake, C., Poole, G. B., Marin, F., Brough, S., Colless, M., Couch, W., Croom, S., Croton, D., Davis, T. M., Drinkwater, M. J., Forster, K., Gilbank, D., Gladders, M., Glazebrook, K., Jelliffe, B., Jurek, R. J., Li, I. .-, Madore, B., ... Yee, H. K. C. (2013). The WiggleZ Dark Energy Survey: measuring the cosmic growth rate with the two-point galaxy correlation function., 430(2), 924–933. <https://doi.org/10.1093/mnras/sts608>
- Contreras, S., Baugh, C. M., Norberg, P., & Padilla, N. (2013). How robust are predictions of galaxy clustering?, 432(4), 2717–2730. <https://doi.org/10.1093/mnras/stt629>
- Cooke, R. J., Pettini, M., & Steidel, C. C. (2018). One Percent Determination of the Primordial Deuterium Abundance., 855(2), Article 102, 102. <https://doi.org/10.3847/1538-4357/aab53>
- Cooray, A., & Sheth, R. (2002). Halo models of large scale structure., 372(1), 1–129. [https://doi.org/10.1016/S0370-1573\(02\)00276-4](https://doi.org/10.1016/S0370-1573(02)00276-4)
- Copi, C. J., Schramm, D. N., & Turner, M. S. (1995). Big-Bang Nucleosynthesis and the Baryon Density of the Universe. *Science*, 267(5195), 192–199. <https://doi.org/10.1126/science.7809624>
- Crnojević, D., Sand, D. J., Bennet, P., Pasetto, S., Spekkens, K., Caldwell, N., Guhathakurta, P., McLeod, B., Seth, A., Simon, J. D., Strader, J., & Toloba, E. (2019). The Faint End of the Centaurus A Satellite Luminosity Function., 872(1), Article 80, 80. <https://doi.org/10.3847/1538-4357/aafbe7>
- Crocce, M., & Scoccimarro, R. (2006). Renormalized cosmological perturbation theory., 73(6), Article 063519, 063519. <https://doi.org/10.1103/PhysRevD.73.063519>

- Danieli, S., van Dokkum, P., Merritt, A., Abraham, R., Zhang, J., Karachentsev, I. D., & Makarova, L. N. (2017). The Dragonfly Nearby Galaxies Survey. III. The Luminosity Function of the M101 Group., *837*(2), Article 136, 136. <https://doi.org/10.3847/1538-4357/aa615b>
- Davis, T. M., & Lineweaver, C. H. (2004). Expanding Confusion: Common Misconceptions of Cosmological Horizons and the Superluminal Expansion of the Universe., *21*, 97–109. <https://doi.org/10.1071/AS03040>
- Dawson, K. S., Kneib, J.-P., Percival, W. J., Alam, S., Albareti, F. D., Anderson, S. F., Armengaud, E., Aubourg, É., Bailey, S., Bautista, J. E., Berlind, A. A., Bershadsky, M. A., Beutler, F., Bizyaev, D., Blanton, M. R., Blomqvist, M., Bolton, A. S., Bovy, J., Brandt, W. N., ... Zou, H. (2016). The SDSS-IV Extended Baryon Oscillation Spectroscopic Survey: Overview and Early Data., *151*, Article 44, 44. <https://doi.org/10.3847/0004-6256/151/2/44>
- Dawson, K. S., Schlegel, D. J., Ahn, C. P., Anderson, S. F., Aubourg, É., Bailey, S., Barkhouser, R. H., Bautista, J. E., Beifiori, A., Berlind, A. A., Bhardwaj, V., Bizyaev, D., Blake, C. H., Blanton, M. R., Blomqvist, M., Bolton, A. S., Borde, A., Bovy, J., Brandt, W. N., ... Zheng, Z. (2013). The Baryon Oscillation Spectroscopic Survey of SDSS-III., *145*, Article 10, 10. <https://doi.org/10.1088/0004-6256/145/1/10>
- de Jong, R. S., Agertz, O., Berbel, A. A., Aird, J., Alexander, D. A., Amarsi, A., Anders, F., Andrae, R., Ansarinejad, B., Ansorge, W., Antilogus, P., Anwand-Heerwart, H., Arentsen, A., Arnadottir, A., Asplund, M., Auger, M., Azais, N., Baade, D., Baker, G., ... Zucker, D. (2019). 4MOST: Project overview and information for the First Call for Proposals. *The Messenger*, *175*, 3–11. <https://doi.org/10.18727/0722-6691/5117>
- de Jong, R. S., Bellido-Tirado, O., Chiappini, C., Depagne, É., Haynes, R., Johl, D., Schnurr, O., Schwöpe, A., Walcher, J., Dionies, F., Haynes, D., Kelz, A., Kitaura, F. S., Lamer, G., Minchev, I., Müller, V., Nuza, S. E., Olaya, J.-C., Piffl, T., ... Boland, W. (2012). 4MOST: 4-metre multi-object spectroscopic telescope. *Ground-based and Airborne Instrumentation for Astronomy IV*, *8446*, Article 84460T, 84460T. <https://doi.org/10.1117/12.926239>
- de la Torre, S., & Guzzo, L. (2012). Modelling non-linear redshift-space distortions in the galaxy clustering pattern: systematic errors on the growth rate parameter., *427*(1), 327–342. <https://doi.org/10.1111/j.1365-2966.2012.21824.x>
- de Lapparent, V., Geller, M. J., & Huchra, J. P. (1986). A Slice of the Universe., *302*, L1. <https://doi.org/10.1086/184625>
- de Mattia, A., & Ruhlmann-Kleider, V. (2019). Integral constraints in spectroscopic surveys., *2019*(8), 036.
- de Mattia, A., Ruhlmann-Kleider, V., Raichoor, A., Ross, A. J., Tamone, A., Zhao, C., Alam, S., Avila, S., Burtin, E., Bautista, J., Beutler, F., Brinkmann, J., Brownstein, J. R., Chapman, M. J., Chuang, C.-H., Comparat, J., du Mas des Bourboux, H., Dawson, K. S., de la Macorra, A., ... Zhao, G.-B. (2021). The completed SDSS-IV extended Baryon Oscillation Spectroscopic Survey: measurement of the BAO and growth rate of structure of the emission line galaxy sample from the anisotropic power spectrum between redshift 0.6 and 1.1., *501*(4), 5616–5645. <https://doi.org/10.1093/mnras/staa3891>

- Dekel, A., & Birnboim, Y. (2006). Galaxy bimodality due to cold flows and shock heating., 368(1), 2–20. <https://doi.org/10.1111/j.1365-2966.2006.10145.x>
- Del Popolo, A., & Le Delliou, M. (2017). Small Scale Problems of the  $\Lambda$ CDM Model: A Short Review. *Galaxies*, 5(1), 17. <https://doi.org/10.3390/galaxies5010017>
- Delaunay, B. (1934). Sur la sphere vide. A la memoire de Georges Voronoi. *Bulletin de l'Académie des Sciences de l'URSS. Classe des sciences mathématiques et na*, 793–800. <http://mi.mathnet.ru/eng/izv4937>
- DES Collaboration, Abbott, T. M. C., Aguena, M., Alarcon, A., Alves, O., Amon, A., Annis, J., Avila, S., Bacon, D., Baxter, E., Bechtol, K., Becker, M. R., Bernstein, G. M., Birrer, S., Blazek, J., Bocquet, S., Brandao-Souza, A., Bridle, S. L., Brooks, D., ... Zuntz, J. (2022). Dark Energy Survey Year 3 Results: Constraints on extensions to  $\Lambda$ CDM with weak lensing and galaxy clustering. *arXiv e-prints*, Article arXiv:2207.05766, arXiv:2207.05766.
- DESI Collaboration, Aghamousa, A., Aguilar, J., Ahlen, S., Alam, S., Allen, L. E., Allende Prieto, C., Annis, J., Bailey, S., Balland, C., Ballester, O., Baltay, C., Beaufore, L., Bebek, C., Beers, T. C., Bell, E. F., Bernal, J. L., Besuner, R., Beutler, F., ... Zu, Y. (2016). The DESI Experiment Part II: Instrument Design. *arXiv e-prints*, Article arXiv:1611.00037, arXiv:1611.00037.
- DESI Collaboration, & et al. (2016). The DESI Experiment Part I: Science, Targeting, and Survey Design. *ArXiv e-prints*, arXiv:1611.00036.
- Desjacques, V., Jeong, D., & Schmidt, F. (2018). Large-scale galaxy bias., 733, 1–193. <https://doi.org/10.1016/j.physrep.2017.12.002>
- Dey, A., Schlegel, D. J., Lang, D., Blum, R., Burleigh, K., Fan, X., Findlay, J. R., Finkbeiner, D., Herrera, D., Juneau, S., Landriau, M., Levi, M., McGreer, I., Meisner, A., Myers, A. D., Moustakas, J., Nugent, P., Patej, A., Schlafly, E. F., ... Zhou, Z. (2019). Overview of the DESI Legacy Imaging Surveys., 157(5), Article 168, 168. <https://doi.org/10.3847/1538-3881/ab089d>
- Di Valentino, E., Mena, O., Pan, S., Visinelli, L., Yang, W., Melchiorri, A., Mota, D. F., Riess, A. G., & Silk, J. (2021). In the realm of the Hubble tension-a review of solutions. *Classical and Quantum Gravity*, 38(15), Article 153001, 153001. <https://doi.org/10.1088/1361-6382/ac086d>
- Dodelson, S. (2003). *Modern Cosmology*.
- Dodelson, S., Gates, E. I., & Turner, M. S. (1996). Cold Dark Matter. *Science*, 274(5284), 69–75. <https://doi.org/10.1126/science.274.5284.69>
- Dolgov, A. D. (2002). Neutrinos in cosmology., 370(4-5), 333–535. [https://doi.org/10.1016/S0370-1573\(02\)00139-4](https://doi.org/10.1016/S0370-1573(02)00139-4)
- Drinkwater, M. J., Jurek, R. J., Blake, C., Woods, D., Pimblett, K. A., Glazebrook, K., Sharp, R., Pracy, M. B., Brough, S., Colless, M., Couch, W. J., Croom, S. M., Davis, T. M., Forbes, D., Forster, K., Gilbank, D. G., Gladders, M., Jelliffe, B., Jones, N., ... Yee, H. K. C. (2010). The WiggleZ Dark Energy Survey: survey design and first data release., 401(3), 1429–1452. <https://doi.org/10.1111/j.1365-2966.2009.15754.x>
- Driver, S. P., Norberg, P., Baldry, I. K., Bamford, S. P., Hopkins, A. M., Liske, J., Loveday, J., Peacock, J. A., Hill, D. T., Kelvin, L. S., Robotham, A. S. G., Cross, N. J. G., Parkinson, H. R.,

- Prescott, M., Conselice, C. J., Dunne, L., Brough, S., Jones, H., Sharp, R. G., ... Warren, S. J. (2009). GAMA: towards a physical understanding of galaxy formation. *Astronomy and Geophysics*, 50(5), 5.12–5.19. <https://doi.org/10.1111/j.1468-4004.2009.50512.x>
- Drlica-Wagner, A., Prescod-Weinstein, C., Yu, H.-B., Albert, A., Banerjee, A., Baryakhtar, M., Bechtol, K., Bird, S., Birrer, S., Bringmann, T., Caputo, R., Chakrabarti, S., Chen, T. Y., Croon, D., Cyr-Racine, F.-Y., Dawson, W. A., Dvorkin, C., Gluscevic, V., Gilman, D., ... Wechsler, R. H. (2022). Report of the Topical Group on Cosmic Probes of Dark Matter for Snowmass 2021. *arXiv e-prints*, Article arXiv:2209.08215, arXiv:2209.08215.
- du Mas des Bourboux, H., Rich, J., Font-Ribera, A., de Sainte Agathe, V., Farr, J., Etourneau, T., Le Goff, J.-M., Cuceu, A., Balland, C., Bautista, J. E., Brinkmann, J., Brownstein, J. R., Chabanier, S., Chaussidon, E., Dawson, K., González-Morales, A. X., Guy, J., Lyke, B. W., de la Macorra, A., ... Youles, S. (2020). The Completed SDSS-IV extended Baryon Oscillation Spectroscopic Survey: Baryon acoustic oscillations with Lyman- $\alpha$  forests. *arXiv e-prints*, Article arXiv:2007.08995, arXiv:2007.08995.
- Efstathiou, G., & Bond, J. R. (1999). Cosmic confusion: degeneracies among cosmological parameters derived from measurements of microwave background anisotropies., 304(1), 75–97. <https://doi.org/10.1046/j.1365-8711.1999.02274.x>
- Einstein, A. (1905). Zur Elektrodynamik bewegter Körper. *Annalen der Physik*, 322(10), 891–921. <https://doi.org/10.1002/andp.19053221004>
- Einstein, A., & de Sitter, W. (1932). On the Relation between the Expansion and the Mean Density of the Universe. *Proceedings of the National Academy of Science*, 18(3), 213–214. <https://doi.org/10.1073/pnas.18.3.213>
- Einstein, A. (1917). Kosmologische Betrachtungen zur allgemeinen Relativitätstheorie. *Sitzungsberichte der Königlich Preussischen Akademie der Wissenschaften (Berlin)*, 142–152.
- Eisenstein, D. J., & Hu, W. (1998). Baryonic Features in the Matter Transfer Function., 496, 605–614. <https://doi.org/10.1086/305424>
- Eisenstein, D. J., Seo, H.-J., Sirko, E., & Spergel, D. N. (2007). Improving Cosmological Distance Measurements by Reconstruction of the Baryon Acoustic Peak., 664, 675–679. <https://doi.org/10.1086/518712>
- Eisenstein, D. J., Seo, H.-J., & White, M. (2007). On the Robustness of the Acoustic Scale in the Low-Redshift Clustering of Matter., 664, 660–674. <https://doi.org/10.1086/518755>
- Eisenstein, D. J., Zehavi, I., Hogg, D. W., Scoccimarro, R., Blanton, M. R., Nichol, R. C., Scranton, R., Seo, H.-J., Tegmark, M., Zheng, Z., Anderson, S. F., Annis, J., Bahcall, N., Brinkmann, J., Burles, S., Castander, F. J., Connolly, A., Csabai, I., Doi, M., ... York, D. G. (2005). Detection of the Baryon Acoustic Peak in the Large-Scale Correlation Function of SDSS Luminous Red Galaxies., 633, 560–574. <https://doi.org/10.1086/466512>
- Falck, B., Wang, J., Jenkins, A., Lemson, G., Medvedev, D., Neyrinck, M. C., & Szalay, A. S. (2021). Indra: a public computationally-accessible suite of cosmological  $N$ -body simulations.
- Falck, B. L., Neyrinck, M. C., & Szalay, A. S. (2012). ORIGAMI: Delineating Halos Using Phase-space Folds., 754(2), Article 126, 126. <https://doi.org/10.1088/0004-637X/754/2/126>
- Feldman, H. A., Kaiser, N., & Peacock, J. A. (1994). Power-Spectrum Analysis of Three-dimensional Redshift Surveys., 426, 23. <https://doi.org/10.1086/174036>

- Ferraro, S., Sailer, N., Slosar, A., & White, M. (2022). Snowmass2021 Cosmic Frontier White Paper: Cosmology and Fundamental Physics from the three-dimensional Large Scale Structure. *arXiv e-prints*, Article arXiv:2203.07506, arXiv:2203.07506.
- Fisher, K. B. (1995). On the Validity of the Streaming Model for the Redshift-Space Correlation Function in the Linear Regime., *448*, 494. <https://doi.org/10.1086/175980>
- Flaugher, B., Miranda, V., Schlegel, D. J., Anderson, A. J., Andrade-Oliveira, F., Baxter, E. J., Bender, A. N., Bleem, L. E., Chang, C., Chang, C. C., Chen, T. Y., Dawson, K. S., Digel, S. W., Drlica-Wagner, A., Ferraro, S., Garcia, A., Heitmann, K., Kim, A. G., Linder, E. V., ... Zhang, Y. (2022). Report of the Topical Group on Dark Energy and Cosmic Acceleration: Complementarity of Probes and New Facilities for Snowmass 2021. *arXiv e-prints*, Article arXiv:2209.08654, arXiv:2209.08654.
- Font-Ribera, A., McDonald, P., Mostek, N., Reid, B. A., Seo, H.-J., & Slosar, A. (2014). DESI and other Dark Energy experiments in the era of neutrino mass measurements., *2014(5)*, Article 023, 023. <https://doi.org/10.1088/1475-7516/2014/05/023>
- Forero-Romero, J. E., Hoffman, Y., Gottlöber, S., Klypin, A., & Yepes, G. (2009). A dynamical classification of the cosmic web., *396(3)*, 1815–1824. <https://doi.org/10.1111/j.1365-2966.2009.14885.x>
- Foster, C., & Nelson, L. A. (2009). The Size, Shape, and Orientation of Cosmological Voids in the Sloan Digital Sky Survey., *699(2)*, 1252–1260. <https://doi.org/10.1088/0004-637X/699/2/1252>
- Frenk, C. S., & White, S. D. M. (2012). Dark matter and cosmic structure. *Annalen der Physik*, *524(9-10)*, 507–534. <https://doi.org/10.1002/andp.201200212>
- Friedmann, A. (1922). Über die Krümmung des Raumes. *Zeitschrift für Physik*, *10*, 377–386. <https://doi.org/10.1007/BF01332580>
- Fujii, Y. (1982). Origin of the gravitational constant and particle masses in a scale-invariant scalar-tensor theory., *26(10)*, 2580–2588. <https://doi.org/10.1103/PhysRevD.26.2580>
- Gamow, G. (1948). The Evolution of the Universe., *162(4122)*, 680–682. <https://doi.org/10.1038/162680a0>
- Gao, L., Springel, V., & White, S. D. M. (2005). The age dependence of halo clustering., *363(1)*, L66–L70. <https://doi.org/10.1111/j.1745-3933.2005.00084.x>
- Gardner, J. P., Mather, J. C., Clampin, M., Doyon, R., Greenhouse, M. A., Hammel, H. B., Hutchings, J. B., Jakobsen, P., Lilly, S. J., Long, K. S., Lunine, J. I., McCaughrean, M. J., Moun-tain, M., Nella, J., Rieke, G. H., Rieke, M. J., Rix, H.-W., Smith, E. P., Sonneborn, G., ... Wright, G. S. (2006). The James Webb Space Telescope., *123(4)*, 485–606. <https://doi.org/10.1007/s11214-006-8315-7>
- Garzilli, A., Magalich, A., Ruchayskiy, O., & Boyarsky, A. (2021). How to constrain warm dark matter with the Lyman- $\alpha$  forest., *502(2)*, 2356–2363. <https://doi.org/10.1093/mnras/stab192>
- Gil-Marín, H., Wagner, C., Verde, L., Porciani, C., & Jimenez, R. (2012). Perturbation theory approach for the power spectrum: from dark matter in real space to massive haloes in redshift space., *11*, Article 029, 029. <https://doi.org/10.1088/1475-7516/2012/11/029>



- Gil-Marín, H., Bautista, J. E., Paviot, R., Vargas-Magaña, M., de la Torre, S., Fromenteau, S., Alam, S., Ávila, S., Burtin, E., Chuang, C.-H., Dawson, K. S., Hou, J., de Mattia, A., Mohammad, F. G., Müller, E.-M., Nadathur, S., Neveux, R., Percival, W. J., Raichoor, A., ... Vivek, M. (2020). The Completed SDSS-IV extended Baryon Oscillation Spectroscopic Survey: measurement of the BAO and growth rate of structure of the luminous red galaxy sample from the anisotropic power spectrum between redshifts 0.6 and 1.0., *498*(2), 2492–2531. <https://doi.org/10.1093/mnras/staa2455>
- Goldberg, D. M., & Strauss, M. A. (1998). Determination of the Baryon Density from Large-Scale Galaxy Redshift Surveys., *495*(1), 29–43. <https://doi.org/10.1086/305284>
- Gonzalez-Perez, V., Comparat, J., Norberg, P., Baugh, C. M., Contreras, S., Lacey, C., McCullagh, N., Orsi, A., Helly, J., & Humphries, J. (2018). The host dark matter haloes of [O II] emitters at  $0.5 < z < 1.5$ ., *474*(3), 4024–4038. <https://doi.org/10.1093/mnras/stx2807>
- Goodman, J. (1995). Geocentrism reexamined., *52*(4), 1821–1827. <https://doi.org/10.1103/PhysRevD.52.1821>
- Green, D., Ruderman, J. T., Safdi, B. R., Shelton, J., Achúcarro, A., Adshead, P., Akrami, Y., Baryakhtar, M., Baumann, D., Berlin, A., Blinov, N., Boddy, K. K., Buschmann, M., Cabass, G., Caldwell, R., Castorina, E., Chen, T. Y., Chen, X., Coulton, W., ... Zurek, K. (2022). Snowmass Theory Frontier: Astrophysics and Cosmology. *arXiv e-prints*, Article arXiv:2209.06854, arXiv:2209.06854.
- Gunn, J. E., Carr, M., Rockosi, C., Sekiguchi, M., Berry, K., Elms, B., de Haas, E., Ivezić, Ž. ., Knapp, G., Lupton, R., Pauls, G., Simcoe, R., Hirsch, R., Sanford, D., Wang, S., York, D., Harris, E., Annis, J., Bartozek, L., ... Brinkman, J. (1998). The Sloan Digital Sky Survey Photometric Camera., *116*(6), 3040–3081. <https://doi.org/10.1086/300645>
- Gunn, J. E., & Gott, I., J. Richard. (1972). On the Infall of Matter Into Clusters of Galaxies and Some Effects on Their Evolution., *176*, 1. <https://doi.org/10.1086/151605>
- Gunn, J. E., & Peterson, B. A. (1965). On the Density of Neutral Hydrogen in Intergalactic Space., *142*, 1633–1636. <https://doi.org/10.1086/148444>
- Gunn, J. E., Siegmund, W. A., Mannery, E. J., Owen, R. E., Hull, C. L., Leger, R. F., Carey, L. N., Knapp, G. R., York, D. G., Boroski, W. N., Kent, S. M., Lupton, R. H., Rockosi, C. M., Evans, M. L., Waddell, P., Anderson, J. E., Annis, J., Barentine, J. C., Bartoszek, L. M., ... Wang, S.-i. (2006). The 2.5 m Telescope of the Sloan Digital Sky Survey., *131*(4), 2332–2359. <https://doi.org/10.1086/500975>
- Guo, H., Zheng, Z., Zehavi, I., Dawson, K., Skibba, R. A., Tinker, J. L., Weinberg, D. H., White, M., & Schneider, D. P. (2015). Velocity bias from the small-scale clustering of SDSS-III BOSS galaxies., *446*(1), 578–594. <https://doi.org/10.1093/mnras/stu2120>
- Guo, Q., White, S., Angulo, R. E., Henriques, B., Lemson, G., Boylan-Kolchin, M., Thomas, P., & Short, C. (2013). Galaxy formation in WMAP1 and WMAP7 cosmologies., *428*(2), 1351–1365. <https://doi.org/10.1093/mnras/sts115>
- Guo, Q., White, S., Li, C., & Boylan-Kolchin, M. (2010). How do galaxies populate dark matter haloes?, *404*(3), 1111–1120. <https://doi.org/10.1111/j.1365-2966.2010.16341.x>

- Guth, A. H. (1981). Inflationary universe: A possible solution to the horizon and flatness problems., 23(2), 347–356. <https://doi.org/10.1103/PhysRevD.23.347>
- Hahn, O., Carollo, C. M., Porciani, C., & Dekel, A. (2007). The evolution of dark matter halo properties in clusters, filaments, sheets and voids. *Monthly Notices of the Royal Astronomical Society*, 381(1), 41–51. <https://doi.org/10.1111/j.1365-2966.2007.12249.x>
- Hahn, O., Porciani, C., Carollo, C. M., & Dekel, A. (2007). Properties of dark matter haloes in clusters, filaments, sheets and voids., 375(2), 489–499. <https://doi.org/10.1111/j.1365-2966.2006.11318.x>
- Haiman, Z., Barkana, R., & Ostriker, J. P. (2001). Warm Dark Matter, small scale crisis, and the high redshift universe. In J. C. Wheeler & H. Martel (Eds.), *20th texas symposium on relativistic astrophysics* (pp. 136–142). <https://doi.org/10.1063/1.1419543>
- Hamaus, N., Pisani, A., Sutter, P. M., Lavaux, G., Escoffier, S., Wandelt, B. D., & Weller, J. (2016). Constraints on Cosmology and Gravity from the Dynamics of Voids. *Physical Review Letters*, 117(9), Article 091302, 091302. <https://doi.org/10.1103/PhysRevLett.117.091302>
- Hamaus, N., Sutter, P. M., & Wandelt, B. D. (2014). Universal Density Profile for Cosmic Voids. *Physical Review Letters*, 112(25), Article 251302, 251302. <https://doi.org/10.1103/PhysRevLett.112.251302>
- Hamilton, A. J. S. (1998). Linear redshift distortions: a review. *The Evolving Universe*, 185–275. [https://doi.org/10.1007/978-94-011-4960-0\\_17](https://doi.org/10.1007/978-94-011-4960-0_17)
- Hand, N., Seljak, U., Beutler, F., & Vlah, Z. (2017). Extending the modeling of the anisotropic galaxy power spectrum to  $k = 0.4 \text{ hMpc}^{-1}$ ., 2017(10), Article 009, 009. <https://doi.org/10.1088/1475-7516/2017/10/009>
- Harrison, E. R. (1970). Fluctuations at the Threshold of Classical Cosmology., 1(10), 2726–2730. <https://doi.org/10.1103/PhysRevD.1.2726>
- Hernquist, L. (1990). An Analytical Model for Spherical Galaxies and Bulges., 356, 359. <https://doi.org/10.1086/168845>
- Heymans, C., Grocutt, E., Heavens, A., Kilbinger, M., Kitching, T. D., Simpson, F., Benjamin, J., Erben, T., Hildebrandt, H., Hoekstra, H., Mellier, Y., Miller, L., Van Waerbeke, L., Brown, M. L., Coupon, J., Fu, L., Harnois-Déraps, J., Hudson, M. J., Kuijken, K., ... Velander, M. (2013). CFHTLenS tomographic weak lensing cosmological parameter constraints: Mitigating the impact of intrinsic galaxy alignments., 432(3), 2433–2453. <https://doi.org/10.1093/mnras/stt601>
- Heymans, C., Tröster, T., Asgari, M., Blake, C., Hildebrandt, H., Joachimi, B., Kuijken, K., Lin, C.-A., Sánchez, A. G., van den Busch, J. L., Wright, A. H., Amon, A., Bilicki, M., de Jong, J., Crocce, M., Dvornik, A., Erben, T., Fortuna, M. C., Getman, F., ... Wolf, C. (2021). KiDS-1000 Cosmology: Multi-probe weak gravitational lensing and spectroscopic galaxy clustering constraints., 646, Article A140, A140. <https://doi.org/10.1051/0004-6361/202039063>
- Hikage, C. (2014). Constraining halo occupation distribution and cosmic growth rate using multipole power spectrum., 441, L21–L25. <https://doi.org/10.1093/mnrasl/flu038>

- Hildebrandt, H., Viola, M., Heymans, C., Joudaki, S., Kuijken, K., Blake, C., Erben, T., Joachimi, B., Klaes, D., Miller, L., Morrison, C. B., Nakajima, R., Verdoes Kleijn, G., Amon, A., Choi, A., Covone, G., de Jong, J. T. A., Dvornik, A., Fenech Conti, I., ... Van Waerbeke, L. (2017). KiDS-450: cosmological parameter constraints from tomographic weak gravitational lensing., *465*(2), 1454–1498. <https://doi.org/10.1093/mnras/stw2805>
- Hinshaw, G., Larson, D., Komatsu, E., Spergel, D. N., Bennett, C. L., Dunkley, J., Nolta, M. R., Halpern, M., Hill, R. S., Odegard, N., Page, L., Smith, K. M., Weiland, J. L., Gold, B., Jarosik, N., Kogut, A., Limon, M., Meyer, S. S., Tucker, G. S., ... Wright, E. L. (2013). Nine-year Wilkinson Microwave Anisotropy Probe (WMAP) Observations: Cosmological Parameter Results., *208*(2), Article 19, 19. <https://doi.org/10.1088/0067-0049/208/2/19>
- Hoffman, Y., Metuki, O., Yepes, G., Gottlöber, S., Forero-Romero, J. E., Libeskind, N. I., & Knebe, A. (2012). A kinematic classification of the cosmic web., *425*(3), 2049–2057. <https://doi.org/10.1111/j.1365-2966.2012.21553.x>
- Hogg, D. W. (1999). Distance measures in cosmology. *arXiv Astrophysics e-prints*.
- Hou, J., Sánchez, A. G., Ross, A. J., Smith, A., Neveux, R., Bautista, J., Burtin, E., Zhao, C., Scoccamarro, R., Dawson, K. S., de Mattia, A., de la Macorra, A., du Mas des Bourboux, H., Eisenstein, D. J., Gil-Marín, H., Lyke, B. W., Mohammad, F. G., Mueller, E.-M., Percival, W. J., ... Vivek, M. (2021). The completed SDSS-IV extended Baryon Oscillation Spectroscopic Survey: BAO and RSD measurements from anisotropic clustering analysis of the quasar sample in configuration space between redshift 0.8 and 2.2., *500*(1), 1201–1221. <https://doi.org/10.1093/mnras/staa3234>
- Hoyle, F., & Vogeley, M. S. (2002). Voids in the Point Source Catalogue Survey and the Updated Zwicky Catalog., *566*(2), 641–651. <https://doi.org/10.1086/338340>
- Hoyle, F., & Vogeley, M. S. (2004). Voids in the Two-Degree Field Galaxy Redshift Survey., *607*(2), 751–764. <https://doi.org/10.1086/386279>
- Hubble, E. (1929). A Relation between Distance and Radial Velocity among Extra-Galactic Nebulae. *Proceedings of the National Academy of Science*, *15*(3), 168–173. <https://doi.org/10.1073/pnas.15.3.168>
- Huey, G., & Wandelt, B. D. (2006). Interacting quintessence, the coincidence problem, and cosmic acceleration., *74*(2), Article 023519, 023519. <https://doi.org/10.1103/PhysRevD.74.023519>
- Huynh, M., & Lazio, J. (2013). An Overview of the Square Kilometre Array. *arXiv e-prints*, Article arXiv:1311.4288, arXiv:1311.4288.
- Icke, V. (1984). Voids and filaments., *206*, 1P–3P. <https://doi.org/10.1093/mnras/206.1.1P>
- Icke, V., & van de Weygaert, R. (1987). Fragmenting the universe., *184*, 16–32.
- Ivezić, Ž., Kahn, S. M., Tyson, J. A., Abel, B., Acosta, E., Allsman, R., Alonso, D., AlSayyad, Y., Anderson, S. F., Andrew, J., Angel, J. R. P., Angeli, G. Z., Ansari, R., Antilogus, P., Araujo, C., Armstrong, R., Arndt, K. T., Astier, P., Aubourg, É., ... Zhan, H. (2019). LSST: From Science Drivers to Reference Design and Anticipated Data Products., *873*(2), Article 111, 111. <https://doi.org/10.3847/1538-4357/ab042c>
- Jackson, J. C. (1972). A critique of Rees's theory of primordial gravitational radiation., *156*, 1P. <https://doi.org/10.1093/mnras/156.1.1P>

- Jeans, J. H. (1902). The Stability of a Spherical Nebula. *Philosophical Transactions of the Royal Society of London Series A*, 199, 1–53. <https://doi.org/10.1098/rsta.1902.0012>
- Jennings, E., Li, Y., & Hu, W. (2013). The abundance of voids and the excursion set formalism., 434, 2167–2181.
- Jeong, D., & Komatsu, E. (2006). Perturbation Theory Reloaded: Analytical Calculation of Nonlinearity in Baryonic Oscillations in the Real-Space Matter Power Spectrum., 651(2), 619–626. <https://doi.org/10.1086/507781>
- Jõeveer, M., Einasto, J., & Tago, E. (1978). Spatial distribution of galaxies and of clusters of galaxies in the southern galactic hemisphere., 185, 357–370. <https://doi.org/10.1093/mnras/185.2.357>
- Kaiser, N. (1984). On the spatial correlations of Abell clusters., 284, L9–L12. <https://doi.org/10.1086/184341>
- Kaiser, N. (1987). Clustering in real space and in redshift space., 227, 1–21. <https://doi.org/10.1093/mnras/227.1.1>
- Karkare, K. S., Moradinezhad Dizgah, A., Keating, G. K., Breysse, P., & Chung, D. T. (2022). Snowmass 2021 Cosmic Frontier White Paper: Cosmology with Millimeter-Wave Line Intensity Mapping. *arXiv e-prints*, Article arXiv:2203.07258, arXiv:2203.07258.
- Kauffmann, G., White, S. D. M., Heckman, T. M., Ménard, B., Brinchmann, J., Charlot, S., Tremonti, C., & Brinkmann, J. (2004). The environmental dependence of the relations between stellar mass, structure, star formation and nuclear activity in galaxies., 353(3), 713–731. <https://doi.org/10.1111/j.1365-2966.2004.08117.x>
- Kazin, E. A., Sánchez, A. G., & Blanton, M. R. (2012). Improving measurements of  $H(z)$  and  $DA(z)$  by analysing clustering anisotropies. *Monthly Notices of the Royal Astronomical Society*, 419(4), 3223–3243. <https://doi.org/10.1111/j.1365-2966.2011.19962.x>
- Kirshner, R. P., Oemler, J., A., Schechter, P. L., & Sheckman, S. A. (1981). A million cubic megaparsec void in Bootes ?, 248, L57–L60. <https://doi.org/10.1086/183623>
- Kitaura, F.-S., Chuang, C.-H., Liang, Y., Zhao, C., Tao, C., Rodriguez-Torres, S., Eisenstein, D. J., Gil-Marín, H., Kneib, J.-P., McBride, C., Percival, W. J., Ross, A. J., Sánchez, A. G., Tinker, J., Tojeiro, R., Vargas-Magana, M., & Zhao, G.-B. (2016). Signatures of the Primordial Universe from Its Emptiness: Measurement of Baryon Acoustic Oscillations from Minima of the Density Field. *Physical Review Letters*, 116(17), Article 171301, 171301. <https://doi.org/10.1103/PhysRevLett.116.171301>
- Klypin, A., Kravtsov, A. V., Valenzuela, O., & Prada, F. (1999). Where Are the Missing Galactic Satellites?, 522(1), 82–92. <https://doi.org/10.1086/307643>
- Kovács, A., Sánchez, C., García-Bellido, J., Elvin-Poole, J., Hamaus, N., Miranda, V., Nadathur, S., Abbott, T., Abdalla, F. B., Annis, J., Avila, S., Bertin, E., Brooks, D., Burke, D. L., Carnero Rosell, A., Carrasco Kind, M., Carretero, J., Cawthon, R., Crocce, M., ... DES Collaboration. (2019). More out of less: an excess integrated Sachs-Wolfe signal from supervoids mapped out by the Dark Energy Survey., 484(4), 5267–5277. <https://doi.org/10.1093/mnras/stz341>
- Kovács, A., Sánchez, C., García-Bellido, J., Nadathur, S., Crittenden, R., Gruen, D., Huterer, D., Bacon, D., Clampitt, J., DeRose, J., Dodelson, S., Gaztañaga, E., Jain, B., Kirk, D.,

- Lahav, O., Miquel, R., Naidoo, K., Peacock, J. A., Soergel, B., ... DES Collaboration. (2017). Imprint of DES superstructures on the cosmic microwave background., *465*(4), 4166–4179. <https://doi.org/10.1093/mnras/stw2968>
- Kraljic, K., Arnouts, S., Pichon, C., Laigle, C., de la Torre, S., Vibert, D., Cadiou, C., Dubois, Y., Treyer, M., Schimd, C., Codis, S., de Lapparent, V., Devriendt, J., Hwang, H. S., Le Borgne, D., Malavasi, N., Milliard, B., Musso, M., Pogosyan, D., ... Wright, A. H. (2018). Galaxy evolution in the metric of the cosmic web., *474*(1), 547–571. <https://doi.org/10.1093/mnras/stx2638>
- Kravtsov, A. V., Berlind, A. A., Wechsler, R. H., Klypin, A. A., Gottlöber, S., Allgood, B., & Primack, J. R. (2004). The Dark Side of the Halo Occupation Distribution., *609*(1), 35–49. <https://doi.org/10.1086/420959>
- Kuijken, K., Heymans, C., Dvornik, A., Hildebrandt, H., de Jong, J. T. A., Wright, A. H., Erben, T., Bilicki, M., Giblin, B., Shan, H. .-, Getman, F., Grado, A., Hoekstra, H., Miller, L., Napolitano, N., Paolilo, M., Radovich, M., Schneider, P., Sutherland, W., ... Verdoes Kleijn, G. A. (2019). The fourth data release of the Kilo-Degree Survey: ugri imaging and nine-band optical-IR photometry over 1000 square degrees., *625*, Article A2, A2. <https://doi.org/10.1051/0004-6361/201834918>
- Kuruvilla, J., & Porciani, C. (2018). On the streaming model for redshift-space distortions., *479*(2), 2256–2276. <https://doi.org/10.1093/mnras/sty1654>
- Landy, S. D., & Szalay, A. S. (1993). Bias and Variance of Angular Correlation Functions., *412*, 64. <https://doi.org/10.1086/172900>
- Langlois, D. (2010). Inflation and Cosmological Perturbations. In G. Wolschin (Ed.), *Lecture notes in physics, berlin springer verlag* (pp. 1–57). [https://doi.org/10.1007/978-3-642-10598-2\\_1](https://doi.org/10.1007/978-3-642-10598-2_1)
- Laureijs, R., Amiaux, J., Arduini, S., Auguères, J. .-, Brinchmann, J., Cole, R., Cropper, M., Dabin, C., Duvet, L., Ealet, A., Garilli, B., Gondoin, P., Guzzo, L., Hoar, J., Hoekstra, H., Holmes, R., Kitching, T., Maciaszek, T., Mellier, Y., ... Zucca, E. (2011). Euclid Definition Study Report. *arXiv e-prints*, Article arXiv:1110.3193, arXiv:1110.3193.
- Lavaux, G., & Wandelt, B. D. (2010). Precision cosmology with voids: definition, methods, dynamics., *403*(3), 1392–1408. <https://doi.org/10.1111/j.1365-2966.2010.16197.x>
- Lemaitre, G. (1927). Un Univers homogène de masse constante et de rayon croissant rendant compte de la vitesse radiale des nébuleuses extra-galactiques. *Annales de la Soci&eacute;t&eacute; Scientifique de Bruxelles*, *47*, 49–59.
- Lesgourgues, J., & Pastor, S. (2006). Massive neutrinos and cosmology., *429*(6), 307–379. <https://doi.org/10.1016/j.physrep.2006.04.001>
- Lewis, A., & Challinor, A. (2006). Weak gravitational lensing of the CMB., *429*(1), 1–65. <https://doi.org/10.1016/j.physrep.2006.03.002>
- Liang, Y., Zhao, C., Chuang, C.-H., Kitaura, F.-S., & Tao, C. (2016). Measuring baryon acoustic oscillations from the clustering of voids., *459*, 4020–4028. <https://doi.org/10.1093/mnras/stw884>
- Lifshitz, E. M. (1946). On the gravitational stability of the expanding universe. *Zhurnal Eksperimentalnoi i Teoreticheskoi Fiziki*, *16*, 587–602.

- Lilly, S. J., Le Fevre, O., Hammer, F., & Crampton, D. (1996). The Canada-France Redshift Survey: The Luminosity Density and Star Formation History of the Universe to  $z$  approximately 1., 460, L1. <https://doi.org/10.1086/309975>
- Linder, E. V., & Cahn, R. N. (2007). Parameterized beyond-einstein growth. *Astroparticle Physics*, 28(4), 481–488. <https://doi.org/https://doi.org/10.1016/j.astropartphys.2007.09.003>
- Lynden-Bell, D. (1969). Galactic Nuclei as Collapsed Old Quasars., 223(5207), 690–694. <https://doi.org/10.1038/223690a0>
- Lynds, R., & Petrosian, V. (1986). Giant Luminous Arcs in Galaxy Clusters. *Bulletin of the American Astronomical Society*, 18, 1014.
- Maartens, R. (2011). Is the Universe homogeneous? *Philosophical Transactions of the Royal Society of London Series A*, 369, 5115–5137. <https://doi.org/10.1098/rsta.2011.0289>
- Macciò, A. V., Paduroiu, S., Anderhalden, D., Schneider, A., & Moore, B. (2012). Cores in warm dark matter haloes: a Catch 22 problem., 424(2), 1105–1112. <https://doi.org/10.1111/j.1365-2966.2012.21284.x>
- Madau, P., & Dickinson, M. (2014). Cosmic Star-Formation History., 52, 415–486. <https://doi.org/10.1146/annurev-astro-081811-125615>
- Madau, P., Pozzetti, L., & Dickinson, M. (1998). The Star Formation History of Field Galaxies., 498(1), 106–116. <https://doi.org/10.1086/305523>
- Majewski, S. R., Schiavon, R. P., Frinchaboy, P. M., Allende Prieto, C., Barkhouser, R., Bizyaev, D., Blank, B., Brunner, S., Burton, A., Carrera, R., Chojnowski, S. D., Cunha, K., Epstein, C., Fitzgerald, G., García Pérez, A. E., Hearty, F. R., Henderson, C., Holtzman, J. A., Johnson, J. A., ... Zamora, O. (2017). The Apache Point Observatory Galactic Evolution Experiment (APOGEE)., 154(3), Article 94, 94. <https://doi.org/10.3847/1538-3881/aa784d>
- Malavasi, N., Arnouts, S., Vibert, D., de la Torre, S., Moutard, T., Pichon, C., Davidzon, I., Kraljic, K., Bolzonella, M., Guzzo, L., Garilli, B., Scodeggio, M., Granett, B. R., Abbas, U., Adami, C., Bottini, D., Cappi, A., Cucciati, O., Franzetti, P., ... Zamorani, G. (2017). The VIMOS Public Extragalactic Redshift Survey (VIPERS): galaxy segregation inside filaments at  $z$  0.7., 465(4), 3817–3822. <https://doi.org/10.1093/mnras/stw2864>
- Mao, Q., Berlind, A. A., Scherrer, R. J., Neyrinck, M. C., Scoccimarro, R., Tinker, J. L., McBride, C. K., & Schneider, D. P. (2017). Cosmic Voids in the SDSS DR12 BOSS Galaxy Sample: The Alcock-Paczynski Test., 835(2), Article 160, 160. <https://doi.org/10.3847/1538-4357/835/2/160>
- Mao, Y.-Y., Zentner, A. R., & Wechsler, R. H. (2018). Beyond assembly bias: exploring secondary halo biases for cluster-size haloes., 474(4), 5143–5157. <https://doi.org/10.1093/mnras/stx3111>
- Matsubara, T. (2008). Nonlinear perturbation theory with halo bias and redshift-space distortions via the Lagrangian picture., 78(8), Article 083519, 083519. <https://doi.org/10.1103/PhysRevD.78.083519>
- McDonald, P. (2003). Toward a Measurement of the Cosmological Geometry at  $z \sim 2$ : Predicting  $\text{Ly}\alpha$  Forest Correlation in Three Dimensions and the Potential of Future Data Sets., 585(1), 34–51. <https://doi.org/10.1086/345945>

- McDonald, P., & Eisenstein, D. J. (2007). Dark energy and curvature from a future baryonic acoustic oscillation survey using the Lyman- $\alpha$  forest., 76(6), Article 063009, 063009. <https://doi.org/10.1103/PhysRevD.76.063009>
- McDonald, P., & Roy, A. (2009). Clustering of dark matter tracers: generalizing bias for the coming era of precision LSS., 2009(8), Article 020, 020. <https://doi.org/10.1088/1475-7516/2009/08/020>
- Melchior, P., Sutter, P. M., Sheldon, E. S., Krause, E., & Wandelt, B. D. (2014). First measurement of gravitational lensing by cosmic voids in SDSS., 440(4), 2922–2927. <https://doi.org/10.1093/mnras/stu456>
- Melott, A. L., Buchert, T., & Weiss, A. G. (1995). Testing higher-order Lagrangian perturbation theory against numerical simulations. II. Hierarchical models., 294, 345–365.
- Merritt, A., van Dokkum, P., & Abraham, R. (2014). The Discovery of Seven Extremely Low Surface Brightness Galaxies in the Field of the Nearby Spiral Galaxy M101., 787(2), Article L37, L37. <https://doi.org/10.1088/2041-8205/787/2/L37>
- Milgrom, M. (1983). A modification of the Newtonian dynamics as a possible alternative to the hidden mass hypothesis., 270, 365–370. <https://doi.org/10.1086/161130>
- Mo, H. J., & White, S. D. M. (1996). An analytic model for the spatial clustering of dark matter haloes., 282(2), 347–361. <https://doi.org/10.1093/mnras/282.2.347>
- Mo, H., van den Bosch, F. C., & White, S. (2010). *Galaxy Formation and Evolution*.
- Moore, B. (1994). Evidence against dissipation-less dark matter from observations of galaxy haloes., 370(6491), 629–631. <https://doi.org/10.1038/370629a0>
- Moore, B., Ghigna, S., Governato, F., Lake, G., Quinn, T., Stadel, J., & Tozzi, P. (1999). Dark Matter Substructure within Galactic Halos., 524(1), L19–L22. <https://doi.org/10.1086/312287>
- Mortonson, M. J., Weinberg, D. H., & White, M. (2013). Dark Energy: A Short Review. *arXiv e-prints*, Article arXiv:1401.0046, arXiv:1401.0046.
- Moster, B. P., Somerville, R. S., Maubetsch, C., van den Bosch, F. C., Macciò, A. V., Naab, T., & Oser, L. (2010). Constraints on the Relationship between Stellar Mass and Halo Mass at Low and High Redshift., 710(2), 903–923. <https://doi.org/10.1088/0004-637X/710/2/903>
- Nadathur, S., Carter, P., Percival, W. J., Winther, H. A., & Bautista, J. (2019). Beyond bao: improving cosmological constraints from boss with measurement of the void-galaxy cross-correlation. <https://arxiv.org/pdf/1904.01030v1>
- Nadathur, S. (2016). Testing cosmology with a catalogue of voids in the BOSS galaxy surveys., 461(1), 358–370. <https://doi.org/10.1093/mnras/stw1340>
- Nadathur, S., Woodfinden, A., Percival, W. J., Aubert, M., Bautista, J., Dawson, K., Escoffier, S., Fromenteau, S., Gil-Marín, H., Rich, J., Ross, A. J., Rossi, G., Magaña, M. V., Brownstein, J. R., & Schneider, D. P. (2020). The completed SDSS-IV extended baryon oscillation spectroscopic survey: geometry and growth from the anisotropic void-galaxy correlation function in the luminous red galaxy sample., 499(3), 4140–4157. <https://doi.org/10.1093/mnras/staa3074>
- Navarro, J. F., Frenk, C. S., & White, S. D. M. (1997). A Universal Density Profile from Hierarchical Clustering., 490(2), 493–508. <https://doi.org/10.1086/304888>

- Neveux, R., Burtin, E., de Mattia, A., Smith, A., Ross, A. J., Hou, J., Bautista, J., Brinkmann, J., Chuang, C.-H., Dawson, K. S., Gil-Marín, H., Lyke, B. W., de la Macorra, A., du Mas des Bourboux, H., Mohammad, F. G., Müller, E.-M., Myers, A. D., Newman, J. A., Percival, W. J., ... Zhao, G.-B. (2020). The completed SDSS-IV extended Baryon Oscillation Spectroscopic Survey: BAO and RSD measurements from the anisotropic power spectrum of the quasar sample between redshift 0.8 and 2.2., *499*(1), 210–229. <https://doi.org/10.1093/mnras/staa2780>
- Neyrinck, M. C. (2008). ZOBOV: a parameter-free void-finding algorithm., *386*(4), 2101–2109. <https://doi.org/10.1111/j.1365-2966.2008.13180.x>
- Neyrinck, M. C., Aragón-Calvo, M. A., Jeong, D., & Wang, X. (2014). A halo bias function measured deeply into voids without stochasticity., *441*(1), 646–655. <https://doi.org/10.1093/mnras/stu589>
- Ntelis, P., Hamilton, J.-C., Le Goff, J.-M., Burtin, E., Laurent, P., Rich, J., Guillermo Busca, N., Tinker, J., Aubourg, E., du Mas des Bourboux, H., Bautista, J., Palanque Delabrouille, N., Delubac, T., Eftekharzadeh, S., Hogg, D. W., Myers, A., Vargas-Magaña, M., Pâris, I., Petitjean, P., ... Yèche, C. (2017). Exploring cosmic homogeneity with the BOSS DR12 galaxy sample., *2017*(6), Article 019, 019. <https://doi.org/10.1088/1475-7516/2017/06/019>
- Okumura, T., Hikage, C., Totani, T., Tonegawa, M., Okada, H., Glazebrook, K., Blake, C., Ferreira, P. G., More, S., Taruya, A., Tsujikawa, S., Akiyama, M., Dalton, G., Goto, T., Ishikawa, T., Iwamuro, F., Matsubara, T., Nishimichi, T., Ohta, K., ... Yoshida, N. (2016). The Subaru FMOS galaxy redshift survey (FastSound). IV. New constraint on gravity theory from redshift space distortions at  $z$  1.4., *68*, Article 38, 38. <https://doi.org/10.1093/pasj/psw029>
- Omori, Y., Giannantonio, T., Porredon, A., Baxter, E. J., Chang, C., Crocce, M., Fosalba, P., Alarcon, A., Banik, N., Blazek, J., Bleem, L. E., Bridle, S. L., Cawthon, R., Choi, A., Chown, R., Crawford, T., Dodelson, S., Drlica-Wagner, A., Eifler, T. F., ... SPT Collaboration. (2019). Dark Energy Survey Year 1 Results: Tomographic cross-correlations between Dark Energy Survey galaxies and CMB lensing from South Pole Telescope +Planck., *100*(4), Article 043501, 043501. <https://doi.org/10.1103/PhysRevD.100.043501>
- Padilla, N. D., Ceccarelli, L., & Lambas, D. G. (2005). Spatial and dynamical properties of voids in a  $\Lambda$  cold dark matter universe., *363*(3), 977–990. <https://doi.org/10.1111/j.1365-2966.2005.09500.x>
- Padmanabhan, N., Xu, X., Eisenstein, D. J., Scalzo, R., Cuesta, A. J., Mehta, K. T., & Kazin, E. (2012). A 2 per cent distance to  $z = 0.35$  by reconstructing baryon acoustic oscillations - I. Methods and application to the Sloan Digital Sky Survey., *427*, 2132–2145. <https://doi.org/10.1111/j.1365-2966.2012.21888.x>
- Palanque-Delabrouille, N., Yèche, C., Schöneberg, N., Lesgourgues, J., Walther, M., Chabanier, S., & Armengaud, E. (2020). Hints, neutrino bounds, and WDM constraints from SDSS DR14 Lyman- $\alpha$  and Planck full-survey data., *2020*(4), Article 038, 038. <https://doi.org/10.1088/1475-7516/2020/04/038>



- Pan, D. C., Vogeley, M. S., Hoyle, F., Choi, Y.-Y., & Park, C. (2012). Cosmic voids in Sloan Digital Sky Survey Data Release 7., *421*(2), 926–934. <https://doi.org/10.1111/j.1365-2966.2011.20197.x>
- Park, C., Choi, Y.-Y., Vogeley, M. S., Gott, I., J. Richard, Kim, J., Hikage, C., Matsubara, T., Park, M.-G., Suto, Y., Weinberg, D. H., & SDSS Collaboration. (2005). Topology Analysis of the Sloan Digital Sky Survey. I. Scale and Luminosity Dependence., *633*(1), 11–22. <https://doi.org/10.1086/452625>
- Paz, D., Lares, M., Ceccarelli, L., Padilla, N., & Lambas, D. G. (2013). Clues on void evolution-II. Measuring density and velocity profiles on SDSS galaxy redshift space distortions., *436*(4), 3480–3491. <https://doi.org/10.1093/mnras/stt1836>
- Peacock, J. A. (2003). Large-scale surveys and cosmic structure. *arXiv e-prints*, Article astro-ph/0309240, astro-ph/0309240.
- Peacock, J. A., & Nicholson, D. (1991). The large-scale clustering of radio galaxies., *253*, 307–319. <https://doi.org/10.1093/mnras/253.2.307>
- Peacock, J. A., & Smith, R. E. (2000). Halo occupation numbers and galaxy bias., *318*(4), 1144–1156. <https://doi.org/10.1046/j.1365-8711.2000.03779.x>
- Peacock, J. A., & West, M. J. (1992). The power spectrum of Abell cluster correlations., *259*, 494–504. <https://doi.org/10.1093/mnras/259.3.494>
- Peacock, J. A. (1999). *Cosmological Physics*.
- Peccei, R. D., & Quinn, H. R. (1977). Constraints imposed by CP conservation in the presence of pseudoparticles., *16*(6), 1791–1797. <https://doi.org/10.1103/PhysRevD.16.1791>
- Peebles, P. J. E. (1965). The Black-Body Radiation Content of the Universe and the Formation of Galaxies., *142*, 1317. <https://doi.org/10.1086/148417>
- Peebles, P. J. E. (1973). Statistical Analysis of Catalogs of Extragalactic Objects. I. Theory., *185*, 413–440. <https://doi.org/10.1086/152431>
- Peebles, P. J. E. (1980). *The large-scale structure of the universe*.
- Peebles, P. J. E. (1982). Large-scale background temperature and mass fluctuations due to scale-invariant primeval perturbations., *263*, L1–L5. <https://doi.org/10.1086/183911>
- Peebles, P. J. E. (1993). *Principles of Physical Cosmology*.
- Peebles, P. J. E., & Yu, J. T. (1970). Primeval Adiabatic Perturbation in an Expanding Universe., *162*, 815. <https://doi.org/10.1086/150713>
- Pellejero Ibañez, M., Stücker, J., Angulo, R. E., Zennaro, M., Contreras, S., & Aricò, G. (2022). Modelling galaxy clustering in redshift space with a Lagrangian bias formalism and N-body simulations., *514*(3), 3993–4007. <https://doi.org/10.1093/mnras/stac1602>
- Penzias, A. A., & Wilson, R. W. (1965). A Measurement of Excess Antenna Temperature at 4080 Mc/s., *142*, 419–421. <https://doi.org/10.1086/148307>
- Percival, W. J. (2005). Cosmological structure formation in a homogeneous dark energy background., *443*(3), 819–830. <https://doi.org/10.1051/0004-6361:20053637>
- Percival, W. J. (2013). Large Scale Structure Observations. *arXiv e-prints*, Article arXiv:1312.5490, arXiv:1312.5490.
- Percival, W. J., Reid, B. A., Eisenstein, D. J., Bahcall, N. A., Budavari, T., Frieman, J. A., Fukugita, M., Gunn, J. E., Ivezić, Ž., Knapp, G. R., Kron, R. G., Loveday, J., Lupton, R. H., McKay,

- T. A., Meiksin, A., Nichol, R. C., Pope, A. C., Schlegel, D. J., Schneider, D. P., ... Zehavi, I. (2010). Baryon acoustic oscillations in the Sloan Digital Sky Survey Data Release 7 galaxy sample., *401*(4), 2148–2168. <https://doi.org/10.1111/j.1365-2966.2009.15812.x>
- Perivolaropoulos, L., & Skara, F. (2022). Challenges for  $\Lambda$ CDM: An update., *95*, Article 101659, 101659. <https://doi.org/10.1016/j.newar.2022.101659>
- Perlmutter, S., Aldering, G., Goldhaber, G., Knop, R. A., Nugent, P., Castro, P. G., Deustua, S., Fabbro, S., Goobar, A., Groom, D. E., Hook, I. M., Kim, A. G., Kim, M. Y., Lee, J. C., Nunes, N. J., Pain, R., Pennypacker, C. R., Quimby, R., Lidman, C., ... Project, T. S. C. (1999). Measurements of  $\Omega$  and  $\Lambda$  from 42 High-Redshift Supernovae., *517*(2), 565–586. <https://doi.org/10.1086/307221>
- Pietroni, M. (2008). Flowing with time: a new approach to non-linear cosmological perturbations., *2008*(10), Article 036, 036. <https://doi.org/10.1088/1475-7516/2008/10/036>
- Pisani, A., Sutter, P. M., Hamaus, N., Alizadeh, E., Biswas, R., Wandelt, B. D., & Hirata, C. M. (2015). Counting voids to probe dark energy., *92*(8), Article 083531, 083531. <https://doi.org/10.1103/PhysRevD.92.083531>
- Planck Collaboration, Aghanim, N., Akrami, Y., Ashdown, M., Aumont, J., Baccigalupi, C., Ballardini, M., Banday, A. J., Barreiro, R. B., Bartolo, N., Basak, S., Battye, R., Benabed, K., Bernard, J. .-, Bersanelli, M., Bielewicz, P., Bock, J. J., Bond, J. R., Borrill, J., ... Zonca, A. (2020). Planck 2018 results. VI. Cosmological parameters., *641*, Article A6, A6. <https://doi.org/10.1051/0004-6361/201833910>
- Platen, E., van de Weygaert, R., & Jones, B. J. T. (2007). A cosmic watershed: the WVF void detection technique., *380*(2), 551–570. <https://doi.org/10.1111/j.1365-2966.2007.12125.x>
- Polisensky, E., & Ricotti, M. (2011). Constraints on the dark matter particle mass from the number of Milky Way satellites., *83*(4), Article 043506, 043506. <https://doi.org/10.1103/PhysRevD.83.043506>
- Porto, R. A., Senatore, L., & Zaldarriaga, M. (2014). The Lagrangian-space Effective Field Theory of large scale structures., *2014*(5), Article 022, 022. <https://doi.org/10.1088/1475-7516/2014/05/022>
- Postman, M., & Geller, M. J. (1984). The morphology-density relation - The group connection., *281*, 95–99. <https://doi.org/10.1086/162078>
- Postman, M., & Lauer, T. R. (1995). Brightest Cluster Galaxies as Standard Candles., *440*, 28. <https://doi.org/10.1086/175245>
- Prakash, A., Licquia, T. C., Newman, J. A., Ross, A. J., Myers, A. D., Dawson, K. S., Kneib, J.-P., Percival, W. J., Bautista, J. E., Comparat, J., Tinker, J. L., Schlegel, D. J., Tojeiro, R., Ho, S., Lang, D., Rao, S. M., McBride, C. K., Ben Zhu, G., Brownstein, J. R., ... Prada, F. (2016). The SDSS-IV Extended Baryon Oscillation Spectroscopic Survey: Luminous Red Galaxy Target Selection., *224*(2), Article 34, 34. <https://doi.org/10.3847/0067-0049/224/2/34>
- Press, W. H., & Schechter, P. (1974). Formation of Galaxies and Clusters of Galaxies by Self-Similar Gravitational Condensation., *187*, 425–438. <https://doi.org/10.1086/152650>
- Primack, J. R., & Gross, M. A. K. (2001). Hot dark matter in cosmology. In D. O. Caldwell (Ed.), *Current aspects of neutrino physics* (pp. 287–308).

- Raccanelli, A., Bertacca, D., Doré, O., & Maartens, R. (2014). Large-scale 3D galaxy correlation function and non-Gaussianity., *2014*(8), 022–022. <https://doi.org/10.1088/1475-7516/2014/08/022>
- Raghunathan, S., Nadathur, S., Sherwin, B. D., & Whitehorn, N. (2020). The Gravitational Lensing Signatures of BOSS Voids in the Cosmic Microwave Background., *890*(2), Article 168, 168. <https://doi.org/10.3847/1538-4357/ab6f05>
- Raichoor, A., Comparat, J., Delubac, T., Kneib, J. .-, Yèche, C., Dawson, K. S., Percival, W. J., Dey, A., Lang, D., Schlegel, D. J., Gorgoni, C., Bautista, J., Brownstein, J. R., Mariappan, V., Seo, H. .-, Tinker, J. L., Ross, A. J., Wang, Y., Zhao, G. .-, ... Zhu, G. B. (2017). The SDSS-IV extended Baryon Oscillation Spectroscopic Survey: final emission line galaxy target selection., *471*(4), 3955–3973. <https://doi.org/10.1093/mnras/stx1790>
- Raichoor, A., de Mattia, A., Ross, A. J., Zhao, C., Alam, S., Avila, S., Bautista, J., Brinkmann, J., Brownstein, J. R., Burtin, E., Chapman, M. J., Chuang, C.-H., Comparat, J., Dawson, K. S., Dey, A., du Mas des Bourboux, H., Elvin-Poole, J., Gonzalez-Perez, V., Gorgoni, C., ... Zhao, G.-B. (2021). The completed SDSS-IV extended Baryon Oscillation Spectroscopic Survey: large-scale structure catalogues and measurement of the isotropic BAO between redshift 0.6 and 1.1 for the Emission Line Galaxy Sample., *500*(3), 3254–3274. <https://doi.org/10.1093/mnras/staa3336>
- Ratra, B., & Peebles, P. J. E. (1988). Cosmological consequences of a rolling homogeneous scalar field., *37*(12), 3406–3427. <https://doi.org/10.1103/PhysRevD.37.3406>
- Reid, B. A., & White, M. (2011). Towards an accurate model of the redshift-space clustering of haloes in the quasi-linear regime., *417*, 1913–1927. <https://doi.org/10.1111/j.1365-2966.2011.19379.x>
- Reid, B., Ho, S., Padmanabhan, N., Percival, W. J., Tinker, J., Tojeiro, R., White, M., Eisenstein, D. J., Maraston, C., Ross, A. J., Sánchez, A. G., Schlegel, D., Sheldon, E., Strauss, M. A., Thomas, D., Wake, D., Beutler, F., Bizyaev, D., Bolton, A. S., ... Vargas-Magana, M. (2016). SDSS-III Baryon Oscillation Spectroscopic Survey Data Release 12: galaxy target selection and large-scale structure catalogues., *455*(2), 1553–1573. <https://doi.org/10.1093/mnras/stv2382>
- Reid, B. A., Seo, H.-J., Leauthaud, A., Tinker, J. L., & White, M. (2014). A 2.5 per cent measurement of the growth rate from small-scale redshift space clustering of SDSS-III CMASS galaxies., *444*(1), 476–502. <https://doi.org/10.1093/mnras/stu1391>
- Riess, A. G., Casertano, S., Yuan, W., Macri, L. M., & Scolnic, D. (2019). Large Magellanic Cloud Cepheid Standards Provide a 1% Foundation for the Determination of the Hubble Constant and Stronger Evidence for Physics Beyond LambdaCDM. *arXiv e-prints*.
- Riess, A. G., Filippenko, A. V., Challis, P., Clocchiatti, A., Diercks, A., Garnavich, P. M., Gilliland, R. L., Hogan, C. J., Jha, S., Kirshner, R. P., Leibundgut, B., Phillips, M. M., Reiss, D., Schmidt, B. P., Schommer, R. A., Smith, R. C., Spyromilio, J., Stubbs, C., Suntzeff, N. B., & Tonry, J. (1998). Observational Evidence from Supernovae for an Accelerating Universe and a Cosmological Constant., *116*(3), 1009–1038. <https://doi.org/10.1086/300499>
- Riess, A. G., Strolger, L.-G., Casertano, S., Ferguson, H. C., Mobasher, B., Gold, B., Challis, P. J., Filippenko, A. V., Jha, S., Li, W., Tonry, J., Foley, R., Kirshner, R. P., Dickinson,

- M., MacDonald, E., Eisenstein, D., Livio, M., Younger, J., Xu, C., ... Stern, D. (2007). New Hubble Space Telescope Discoveries of Type Ia Supernovae at  $z \geq 1$ : Narrowing Constraints on the Early Behavior of Dark Energy., 659(1), 98–121. <https://doi.org/10.1086/510378>
- Robertson, H. P. (1935). Kinematics and World-Structure., 82, 284. <https://doi.org/10.1086/143681>
- Ross, A. J., Bautista, J., Tojeiro, R., Alam, S., Bailey, S., Burtin, E., Comparat, J., Dawson, K. S., de Mattia, A., du Mas des Bourboux, H., Gil-Marín, H., Hou, J., Kong, H., Lyke, B. W., Mohammad, F. G., Moustakas, J., Mueller, E.-M., Myers, A. D., Percival, W. J., ... Zhang, Y. (2020). The Completed SDSS-IV extended Baryon Oscillation Spectroscopic Survey: Large-scale structure catalogues for cosmological analysis., 498(2), 2354–2371. <https://doi.org/10.1093/mnras/staa2416>
- Ross, A. J., Samushia, L., Howlett, C., Percival, W. J., Burden, A., & Manera, M. (2015). The clustering of the SDSS DR7 main Galaxy sample - I. A 4 per cent distance measure at  $z = 0.15$ ., 449(1), 835–847. <https://doi.org/10.1093/mnras/stv154>
- Rubin, V. C., & Ford, J., W. Kent. (1970). Rotation of the Andromeda Nebula from a Spectroscopic Survey of Emission Regions., 159, 379. <https://doi.org/10.1086/150317>
- Ryden, B. (2016). *Introduction to Cosmology*.
- Sachs, R. K., & Wolfe, A. M. (1967). Perturbations of a Cosmological Model and Angular Variations of the Microwave Background., 147, 73. <https://doi.org/10.1086/148982>
- Sahni, V. (2002). The cosmological constant problem and quintessence. *Classical and Quantum Gravity*, 19(13), 3435–3448. <https://doi.org/10.1088/0264-9381/19/13/304>
- Salpeter, E. E. (1964). Accretion of Interstellar Matter by Massive Objects., 140, 796–800. <https://doi.org/10.1086/147973>
- Sánchez, C., Clampitt, J., Kovacs, A., Jain, B., Garcia-Bellido, J., Nadathur, S., Gruen, D., Hamaus, N., Huterer, D., Vielzeuf, P., Amara, A., Bonnett, C., DeRose, J., Hartley, W. G., Jarvis, M., Lahav, O., Miquel, R., Rozo, E., Rykoff, E. S., ... DES Collaboration. (2017). Cosmic voids and void lensing in the Dark Energy Survey Science Verification data., 465(1), 746–759. <https://doi.org/10.1093/mnras/stw2745>
- Schlegel, D., Kollmeier, J. A., & Ferraro, S. (2019). The MegaMapper: a  $z > 2$  spectroscopic instrument for the study of Inflation and Dark Energy. *Bulletin of the American Astronomical Society*, 51, Article 229, 229.
- Schlegel, D. J., Ferraro, S., Aldering, G., Baltay, C., BenZvi, S., Besuner, R., Blanc, G. A., Bolton, A. S., Bonaca, A., Brooks, D., Buckley-Geer, E., Cai, Z., DeRose, J., Dey, A., Doel, P., Drlica-Wagner, A., Fan, X., Gutierrez, G., Green, D., ... Zhou, R. (2022). A Spectroscopic Road Map for Cosmic Frontier: DESI, DESI-II, Stage-5. *arXiv e-prints*, Article arXiv:2209.03585, arXiv:2209.03585.
- Schmidt, M. (1963). 3C 273 : A Star-Like Object with Large Red-Shift., 197(4872), 1040. <https://doi.org/10.1038/1971040a0>
- Scoccimarro, R. (2004). Redshift-space distortions, pairwise velocities, and nonlinearities., 70(8), Article 083007, 083007. <https://doi.org/10.1103/PhysRevD.70.083007>

- Scoccimarro, R., & Frieman, J. (1996). Loop Corrections in Nonlinear Cosmological Perturbation Theory., *105*, 37. <https://doi.org/10.1086/192306>
- Scolnic, D. M., Jones, D. O., Rest, A., Pan, Y. C., Chornock, R., Foley, R. J., Huber, M. E., Kessler, R., Narayan, G., Riess, A. G., Rodney, S., Berger, E., Brout, D. J., Challis, P. J., Drout, M., Finkbeiner, D., Lunnan, R., Kirshner, R. P., Sanders, N. E., ... Smith, K. W. (2018). The Complete Light-curve Sample of Spectroscopically Confirmed SNe Ia from Pan-STARRS1 and Cosmological Constraints from the Combined Pantheon Sample., *859*(2), Article 101, 101. <https://doi.org/10.3847/1538-4357/aab9bb>
- Seljak, U. (2000). Analytic model for galaxy and dark matter clustering., *318*(1), 203–213. <https://doi.org/10.1046/j.1365-8711.2000.03715.x>
- Seo, H.-J., & Eisenstein, D. J. (2005). Baryonic Acoustic Oscillations in Simulated Galaxy Redshift Surveys., *633*, 575–588. <https://doi.org/10.1086/491599>
- Shandarin, S., Feldman, H. A., Heitmann, K., & Habib, S. (2006). Shapes and sizes of voids in the Lambda cold dark matter universe: excursion set approach., *367*(4), 1629–1640. <https://doi.org/10.1111/j.1365-2966.2006.10062.x>
- Shandarin, S., Habib, S., & Heitmann, K. (2012). Cosmic web, multistream flows, and tessellations., *85*(8), Article 083005, 083005. <https://doi.org/10.1103/PhysRevD.85.083005>
- Sherwin, B. D., van Engelen, A., Sehgal, N., Madhavacheril, M., Addison, G. E., Aiola, S., Allison, R., Battaglia, N., Becker, D. T., Beall, J. A., Bond, J. R., Calabrese, E., Datta, R., Devlin, M. J., Dünner, R., Dunkley, J., Fox, A. E., Gallardo, P., Halpern, M., ... Wollack, E. J. (2017). Two-season Atacama Cosmology Telescope polarimeter lensing power spectrum., *95*(12), Article 123529, 123529. <https://doi.org/10.1103/PhysRevD.95.123529>
- Sheth, R. K., Chan, K. C., & Scoccimarro, R. (2013). Nonlocal Lagrangian bias., *87*(8), Article 083002, 083002. <https://doi.org/10.1103/PhysRevD.87.083002>
- Sheth, R. K., & Tormen, G. (1999). Large-scale bias and the peak background split., *308*(1), 119–126. <https://doi.org/10.1046/j.1365-8711.1999.02692.x>
- Sheth, R. K., & van de Weygaert, R. (2004). A hierarchy of voids: much ado about nothing., *350*(2), 517–538. <https://doi.org/10.1111/j.1365-2966.2004.07661.x>
- Silk, J. (1968). Cosmic Black-Body Radiation and Galaxy Formation., *151*, 459. <https://doi.org/10.1086/149449>
- Slezak, E., de Lapparent, V., & Bijaoui, A. (1993). Objective Detection of Voids and High-Density Structures in the First CfA Redshift Survey Slice., *409*, 517. <https://doi.org/10.1086/172683>
- Slipher, V. M. (1913). The radial velocity of the Andromeda Nebula. *Lowell Observatory Bulletin*, *2*(8), 56–57.
- Slipher, V. M. (1917). Nebulae. *Proceedings of the American Philosophical Society*, *56*, 403–409.
- Smee, S. A., Gunn, J. E., Uomoto, A., Roe, N., Schlegel, D., Rockosi, C. M., Carr, M. A., Leger, F., Dawson, K. S., Olmstead, M. D., Brinkmann, J., Owen, R., Barkhouser, R. H., Honscheid, K., Harding, P., Long, D., Lupton, R. H., Loomis, C., Anderson, L., ... York, D. G. (2013). The Multi-object, Fiber-fed Spectrographs for the Sloan Digital Sky Survey and the Baryon Oscillation Spectroscopic Survey., *146*(2), Article 32, 32. <https://doi.org/10.1088/0004-6256/146/2/32>

- Smercina, A., Bell, E. F., Price, P. A., D'Souza, R., Slater, C. T., Bailin, J., Monachesi, A., & Nidever, D. (2018). A Lonely Giant: The Sparse Satellite Population of M94 Challenges Galaxy Formation., *863*(2), Article 152, 152. <https://doi.org/10.3847/1538-4357/aad2d6>
- Smith, R. E., Peacock, J. A., Jenkins, A., White, S. D. M., Frenk, C. S., Pearce, F. R., Thomas, P. A., Efsthathiou, G., & Couchman, H. M. P. (2003). Stable clustering, the halo model and non-linear cosmological power spectra., *341*(4), 1311–1332. <https://doi.org/10.1046/j.1365-8711.2003.06503.x>
- Smoot, G. F., Bennett, C. L., Kogut, A., Wright, E. L., Aymon, J., Boggess, N. W., Cheng, E. S., de Amici, G., Gulkis, S., Hauser, M. G., Hinshaw, G., Jackson, P. D., Janssen, M., Kaita, E., Kelsall, T., Keegstra, P., Lineweaver, C., Loewenstein, K., Lubin, P., ... Wilkinson, D. T. (1992). Structure in the COBE Differential Microwave Radiometer First-Year Maps., *396*, L1. <https://doi.org/10.1086/186504>
- Soucail, G., Fort, B., Mellier, Y., & Picat, J. P. (1987). A blue ring-like structure in the center of the A 370 cluster of galaxies., *172*, L14–L16.
- Spergel, D. N. (2015). The dark side of cosmology: Dark matter and dark energy. *Science*, *347*(6226), 1100–1102. <https://doi.org/10.1126/science.aaa0980>
- Springel, V., White, S. D. M., Tormen, G., & Kauffmann, G. (2001). Populating a cluster of galaxies - I. Results at  $[formmu2]z=0$ ., *328*(3), 726–750. <https://doi.org/10.1046/j.1365-8711.2001.04912.x>
- Steigman, G., & Turner, M. S. (1985). Cosmological constraints on the properties of weakly interacting massive particles. *Nuclear Physics B*, *253*, 375–386. [https://doi.org/10.1016/0550-3213\(85\)90537-1](https://doi.org/10.1016/0550-3213(85)90537-1)
- Sullivan, M., Guy, J., Conley, A., Regnault, N., Astier, P., Balland, C., Basa, S., Carlberg, R. G., Fouchez, D., Hardin, D., Hook, I. M., Howell, D. A., Pain, R., Palanque-Delabrouille, N., Perrett, K. M., Pritchet, C. J., Rich, J., Ruhlmann-Kleider, V., Balam, D., ... Walker, E. S. (2011). SNLS3: Constraints on Dark Energy Combining the Supernova Legacy Survey Three-year Data with Other Probes., *737*(2), Article 102, 102. <https://doi.org/10.1088/0004-637X/737/2/102>
- Sunyaev, R. A., & Zeldovich, I. B. (1980). Microwave background radiation as a probe of the contemporary structure and history of the universe., *18*, 537–560. <https://doi.org/10.1146/annurev.aa.18.090180.002541>
- Sunyaev, R. A., & Zeldovich, Y. B. (1970). Small-Scale Fluctuations of Relic Radiation., *7*, 3–19. <https://doi.org/10.1007/BF00653471>
- Sutter, P. M., Carlesi, E., Wandelt, B. D., & Knebe, A. (2015). On the observability of coupled dark energy with cosmic voids., *446*, L1–L5. <https://doi.org/10.1093/mnrasl/slu155>
- Sutter, P. M., Lavaux, G., Hamaus, N., Pisani, A., Wandelt, B. D., Warren, M., Villaescusa-Navarro, F., Zivick, P., Mao, Q., & Thompson, B. B. (2015). VIDE: The Void IDentification and Examination toolkit. *Astronomy and Computing*, *9*, 1–9. <https://doi.org/10.1016/j.ascom.2014.10.002>
- Sutter, P. M., Lavaux, G., Wandelt, B. D., & Weinberg, D. H. (2012). A First Application of the Alcock-Paczynski Test to Stacked Cosmic Voids., *761*(2), Article 187, 187. <https://doi.org/10.1088/0004-637X/761/2/187>

- Sutter, P. M., Pisani, A., Wandelt, B. D., & Weinberg, D. H. (2014). A measurement of the alcock-paczynski effect using cosmic voids in the sdss., *443*(4), 2983–2990.
- Takahashi, R., Sato, M., Nishimichi, T., Taruya, A., & Oguri, M. (2012). Revising the Halofit Model for the Nonlinear Matter Power Spectrum., *761*(2), Article 152, 152. <https://doi.org/10.1088/0004-637X/761/2/152>
- Tamone, A., Zhao, C., Forero-Sánchez, D., Variu, A., Chuang, C. .-, Kitaura, F. .-, Kneib, J. .-, & Tao, C. (2022). Void BAO measurements on quasars from eBOSS. *arXiv e-prints*, Article arXiv:2208.06238, arXiv:2208.06238.
- Tamone, A., Raichoor, A., Zhao, C., de Mattia, A., Gorgoni, C., Burtin, E., Ruhlmann-Kleider, V., Ross, A. J., Alam, S., Percival, W. J., Avila, S., Chapman, M. J., Chuang, C.-H., Comparat, J., Dawson, K. S., de la Torre, S., du Mas des Bourboux, H., Escoffier, S., Gonzalez-Perez, V., ... Zhao, G.-B. (2020). The completed SDSS-IV extended baryon oscillation spectroscopic survey: growth rate of structure measurement from anisotropic clustering analysis in configuration space between redshift 0.6 and 1.1 for the emission-line galaxy sample., *499*(4), 5527–5546. <https://doi.org/10.1093/mnras/staa3050>
- Taruya, A., Bernardeau, F., Nishimichi, T., & Codis, S. (2012). Direct and fast calculation of regularized cosmological power spectrum at two-loop order., *86*(10), Article 103528, 103528. <https://doi.org/10.1103/PhysRevD.86.103528>
- Taruya, A., & Hiramatsu, T. (2008). A Closure Theory for Nonlinear Evolution of Cosmological Power Spectra., *674*(2), 617–635. <https://doi.org/10.1086/526515>
- Taruya, A., Nishimichi, T., & Saito, S. (2010). Baryon acoustic oscillations in 2D: Modeling redshift-space power spectrum from perturbation theory., *82*(6), Article 063522, 063522. <https://doi.org/10.1103/PhysRevD.82.063522>
- Tegmark, M. (1997). Measuring cosmological parameters with galaxy surveys. *Physical Review Letters*, *79*(20), 3806–3809. <https://doi.org/10.1103/physrevlett.79.3806>
- Tegmark, M., Blanton, M. R., Strauss, M. A., Hoyle, F., Schlegel, D., Scoccimarro, R., Vogeley, M. S., Weinberg, D. H., Zehavi, I., Berlind, A., Budavari, T., Connolly, A., Eisenstein, D. J., Finkbeiner, D., Frieman, J. A., Gunn, J. E., Hamilton, A. J. S., Hui, L., Jain, B., ... SDSS Collaboration. (2004). The Three-Dimensional Power Spectrum of Galaxies from the Sloan Digital Sky Survey., *606*(2), 702–740. <https://doi.org/10.1086/382125>
- Tikhonov, A. V. (2007). Voids in the SDSS galaxy survey. *Astronomy Letters*, *33*(8), 499–511. <https://doi.org/10.1134/S1063773707080014>
- Tinker, J. L. (2007). Redshift-space distortions with the halo occupation distribution - II. Analytic model., *374*(2), 477–492. <https://doi.org/10.1111/j.1365-2966.2006.11157.x>
- Tinker, J. L., Weinberg, D. H., & Zheng, Z. (2006). Redshift-space distortions with the halo occupation distribution - I. Numerical simulations., *368*(1), 85–108. <https://doi.org/10.1111/j.1365-2966.2006.10114.x>
- Trujillo-Gomez, S., Klypin, A., Primack, J., & Romanowsky, A. J. (2011). Galaxies in  $\Lambda$ CDM with Halo Abundance Matching: Luminosity-Velocity Relation, Baryonic Mass-Velocity Relation, Velocity Function, and Clustering., *742*(1), Article 16, 16. <https://doi.org/10.1088/0004-637X/742/1/16>

- Tyson, J. A., Valdes, F., & Wenk, R. A. (1990). Detection of Systematic Gravitational Lens Galaxy Image Alignments: Mapping Dark Matter in Galaxy Clusters., 349, L1. <https://doi.org/10.1086/185636>
- Vale, A., & Ostriker, J. P. (2004). Linking halo mass to galaxy luminosity., 353(1), 189–200. <https://doi.org/10.1111/j.1365-2966.2004.08059.x>
- van de Weygaert, R., & Platen, E. (2011). COSMIC VOIDS: STRUCTURE, DYNAMICS AND GALAXIES. *International Journal of Modern Physics: Conference Series*, 01, 41–66. <https://doi.org/10.1142/s2010194511000092>
- Velten, H. E. S., vom Marttens, R. F., & Zimdahl, W. (2014). Aspects of the cosmological “coincidence problem”. *European Physical Journal C*, 74, Article 3160, 3160. <https://doi.org/10.1140/epjc/s10052-014-3160-4>
- Verde, L., Treu, T., & Riess, A. G. (2019). Tensions between the early and late universe. *Nature Astronomy*, 3(10), 891–895. <https://doi.org/10.1038/s41550-019-0902-0>
- Viel, M., Becker, G. D., Bolton, J. S., & Haehnelt, M. G. (2013). Warm dark matter as a solution to the small scale crisis: New constraints from high redshift Lyman- $\alpha$  forest data., 88(4), Article 043502, 043502. <https://doi.org/10.1103/PhysRevD.88.043502>
- Viel, M., Lesgourgues, J., Haehnelt, M. G., Matarrese, S., & Riotto, A. (2005). Constraining warm dark matter candidates including sterile neutrinos and light gravitinos with WMAP and the Lyman- $\alpha$  forest., 71(6), Article 063534, 063534. <https://doi.org/10.1103/PhysRevD.71.063534>
- Vielzeuf, P., Kovács, A., Demirbozan, U., Fosalba, P., Baxter, E., Hamaus, N., Huterer, D., Miquel, R., Nadathur, S., Pollina, G., Sánchez, C., Whiteway, L., Abbott, T. M. C., Allam, S., Annis, J., Avila, S., Brooks, D., Burke, D. L., Carnero Rosell, A., ... DES Collaboration. (2021). Dark Energy Survey Year 1 results: the lensing imprint of cosmic voids on the cosmic microwave background., 500(1), 464–480. <https://doi.org/10.1093/mnras/staa3231>
- Vlah, Z., Castorina, E., & White, M. (2016). The Gaussian streaming model and convolution Lagrangian effective field theory., 2016(12), Article 007, 007. <https://doi.org/10.1088/1475-7516/2016/12/007>
- von Marttens, R., Casarini, L., Mota, D. F., & Zimdahl, W. (2019). Cosmological constraints on parametrized interacting dark energy. *Physics of the Dark Universe*, 23, Article 100248, 100248. <https://doi.org/10.1016/j.dark.2018.10.007>
- Walker, A. G. (1937). On Milne’s Theory of World-Structure. *Proceedings of the London Mathematical Society*, 42, 90–127. <https://doi.org/10.1112/plms/s2-42.1.90>
- Walsh, D., Carswell, R. F., & Weymann, R. J. (1979). 0957+561 A, B: twin quasistellar objects or gravitational lens?, 279, 381–384. <https://doi.org/10.1038/279381a0>
- Wang, J., & White, S. D. M. (2007). Discreteness effects in simulations of hot/warm dark matter., 380(1), 93–103. <https://doi.org/10.1111/j.1365-2966.2007.12053.x>
- Wang, L., Reid, B., & White, M. (2014). An analytic model for redshift-space distortions., 437(1), 588–599. <https://doi.org/10.1093/mnras/stt1916>
- Wang, Y., Zhao, G.-B., Zhao, C., Philcox, O. H. E., Alam, S., Tamone, A., de Mattia, A., Ross, A. J., Raichoor, A., Burtin, E., Paviot, R., de la Torre, S., Percival, W. J., Dawson, K. S., Gil-Marín, H., Bautista, J. E., Hou, J., Koyama, K., Peacock, J. A., ... Schneider, D. P.



- (2020). The clustering of the SDSS-IV extended Baryon Oscillation Spectroscopic Survey DR16 luminous red galaxy and emission line galaxy samples: cosmic distance and structure growth measurements using multiple tracers in configuration space., 3470–3483. <https://doi.org/10.1093/mnras/staa2593>
- Wechsler, R. H., Bullock, J. S., Primack, J. R., Kravtsov, A. V., & Dekel, A. (2002). Concentrations of Dark Halos from Their Assembly Histories., 568(1), 52–70. <https://doi.org/10.1086/338765>
- Wechsler, R. H., & Tinker, J. L. (2018). The Connection Between Galaxies and Their Dark Matter Halos., 56, 435–487. <https://doi.org/10.1146/annurev-astro-081817-051756>
- Weinberg, D. H., Mortonson, M. J., Eisenstein, D. J., Hirata, C., Riess, A. G., & Rozo, E. (2013). Observational probes of cosmic acceleration., 530, 87–255. <https://doi.org/10.1016/j.physrep.2013.05.001>
- White, M., Reid, B., Chuang, C.-H., Tinker, J. L., McBride, C. K., Prada, F., & Samushia, L. (2015). Tests of redshift-space distortions models in configuration space for the analysis of the BOSS final data release., 447(1), 234–245. <https://doi.org/10.1093/mnras/stu2460>
- Wilson, M. J., Peacock, J. A., Taylor, A. N., & de la Torre, S. (2017). Rapid modelling of the redshift-space power spectrum multipoles for a masked density field., 464(3), 3121–3130. <https://doi.org/10.1093/mnras/stw2576>
- Yamamoto, K., Nakamichi, M., Kamino, A., Bassett, B. A., & Nishioka, H. (2006). A Measurement of the Quadrupole Power Spectrum in the Clustering of the 2dF QSO Survey., 58, 93–102. <https://doi.org/10.1093/pasj/58.1.93>
- York, D. G., Adelman, J., Anderson, J., John E., Anderson, S. F., Annis, J., Bahcall, N. A., Bakken, J. A., Barkhouser, R., Bastian, S., Berman, E., Boroski, W. N., Bracker, S., Briegel, C., Briggs, J. W., Brinkmann, J., Brunner, R., Burles, S., Carey, L., Carr, M. A., ... SDSS Collaboration. (2000). The Sloan Digital Sky Survey: Technical Summary., 120(3), 1579–1587. <https://doi.org/10.1086/301513>
- Zehavi, I., Weinberg, D. H., Zheng, Z., Berlind, A. A., Frieman, J. A., Scoccimarro, R., Sheth, R. K., Blanton, M. R., Tegmark, M., Mo, H. J., Bahcall, N. A., Brinkmann, J., Burles, S., Csabai, I., Fukugita, M., Gunn, J. E., Lamb, D. Q., Loveday, J., Lupton, R. H., ... SDSS Collaboration. (2004). On Departures from a Power Law in the Galaxy Correlation Function., 608(1), 16–24. <https://doi.org/10.1086/386535>
- Zehavi, I., Zheng, Z., Weinberg, D. H., Frieman, J. A., Berlind, A. A., Blanton, M. R., Scoccimarro, R., Sheth, R. K., Strauss, M. A., Kayo, I., Suto, Y., Fukugita, M., Nakamura, O., Bahcall, N. A., Brinkmann, J., Gunn, J. E., Hennessy, G. S., Ivezić, Ž., Knapp, G. R., ... SDSS Collaboration. (2005). The Luminosity and Color Dependence of the Galaxy Correlation Function., 630(1), 1–27. <https://doi.org/10.1086/431891>
- Zel'dovich, Y. B. (1970). Gravitational instability: An approximate theory for large density perturbations., 5, 84–89.
- Zeldovich, Y. B. (1972). A hypothesis, unifying the structure and the entropy of the Universe., 160, 1P. <https://doi.org/10.1093/mnras/160.1.1P>

- Zhao, C., Tao, C., Liang, Y., Kitaura, F.-S., & Chuang, C.-H. (2016). DIVE in the cosmic web: voids with Delaunay triangulation from discrete matter tracer distributions., *459*, 2670–2680. <https://doi.org/10.1093/mnras/stw660>
- Zhao, C., Chuang, C.-H., Bautista, J., de Mattia, A., Raichoor, A., Ross, A. J., Hou, J., Neveux, R., Tao, C., Burtin, E., Dawson, K. S., de la Torre, S., Gil-Marín, H., Kneib, J.-P., Percival, W. J., Rossi, G., Tamone, A., Tinker, J. L., Zhao, G.-B., ... Mueller, E.-M. (2021). The completed SDSS-IV extended Baryon Oscillation Spectroscopic Survey: 1000 multi-tracer mock catalogues with redshift evolution and systematics for galaxies and quasars of the final data release., *503*(1), 1149–1173. <https://doi.org/10.1093/mnras/stab510>
- Zhao, C., Chuang, C.-H., Kitaura, F.-S., Liang, Y., Pellejero-Ibanez, M., Tao, C., Vargas-Magaña, M., Variu, A., & Yepes, G. (2020). Improving baryon acoustic oscillation measurement with the combination of cosmic voids and galaxies., *491*(3), 4554–4572. <https://doi.org/10.1093/mnras/stz3339>
- Zhao, C., Variu, A., He, M., Forero-Sánchez, D., Tamone, A., Chuang, C.-H., Kitaura, F.-S., Tao, C., Yu, J., Kneib, J.-P., Percival, W. J., Shan, H., Zhao, G.-B., Burtin, E., Dawson, K. S., Rossi, G., Schneider, D. P., & de la Macorra, A. (2022). The completed SDSS-IV extended Baryon Oscillation Spectroscopic Survey: cosmological implications from multitracer BAO analysis with galaxies and voids., *511*(4), 5492–5524. <https://doi.org/10.1093/mnras/stac390>
- Zhao, G.-B., Raveri, M., Pogosian, L., Wang, Y., Crittenden, R. G., Handley, W. J., Percival, W. J., Beutler, F., Brinkmann, J., Chuang, C.-H., Cuesta, A. J., Eisenstein, D. J., Kitaura, F.-S., Koyama, K., L’Huillier, B., Nichol, R. C., Pieri, M. M., Rodriguez-Torres, S., Ross, A. J., ... Zhang, H. (2017). Dynamical dark energy in light of the latest observations. *Nature Astronomy*, *1*, 627–632. <https://doi.org/10.1038/s41550-017-0216-z>
- Zheng, Z., Berlind, A. A., Weinberg, D. H., Benson, A. J., Baugh, C. M., Cole, S., Davé, R., Frenk, C. S., Katz, N., & Lacey, C. G. (2005). Theoretical Models of the Halo Occupation Distribution: Separating Central and Satellite Galaxies., *633*(2), 791–809. <https://doi.org/10.1086/466510>
- Zu, Y., & Weinberg, D. H. (2013). The redshift-space cluster-galaxy cross-correlation function - I. Modelling galaxy infall on to Millennium simulation clusters and SDSS groups., *431*(4), 3319–3337. <https://doi.org/10.1093/mnras/stt411>
- Zwicky, F. (1933). Die Rotverschiebung von extragalaktischen Nebeln. *Helvetica Physica Acta*, *6*, 110–127.

# Amélie Tamone

## Ph.D. Student

### Personal Data

---

**Place and Date of birth:** Switzerland | May 1, 1994  
**Nationality:** Swiss  
**Address:** EPFL SB IPHYS LASTRO  
Observatoire de Sauverny  
1290 Versoix, Switzerland  
**Phone (private):** +41 76 616 24 93  
**E-Mail:** amelie.tamone@epfl.ch



### Education

---

**Ph.D. in Astrophysics - EPFL**

14 ECTS obtained

**Lausanne, Switzerland**

*Oct 2018 - (Oct 2022)*

**Master of Science in Physics - EPFL**

*Minor in Financial Engineering*

134 ECTS obtained

**Lausanne, Switzerland**

*Sep 2016 - Jul 2018*

**Exchange year - The University of Nottingham**

**Nottingham, UK**

*Sep 2015 - Jun 2016*

**Bachelor of Science in Physics - EPFL**

*Students representative in 2nd year*

180 ECTS obtained

**Lausanne, Switzerland**

*Sep 2013 - Jul 2016*

**Swiss Maturity - Collège Sismondi**

*Physics-Maths and Latin | Extra-Muros | Treasurer of the student union*

with honour | Awards: Latin Price, Rotary Price

**Genève, Switzerland**

*Jul 2013*

### Research Experience

---

**Ph.D. - EPFL**

*Cosmology with Large Spectroscopic Surveys*

Supervisor: Pr. J.-P. Kneib

Topics: RSD and BAO analysis for eBOSS and DESI, DT voids, multi-tracers analysis.

**Lausanne, Switzerland**

*Oct 2018 - Now*

**Master's Thesis - EPFL**

*Strong Lensing with Models of Cold and Warm Dark Matter*

Supervisor: Pr. F. Courbin

Project: Simulating strong lensing and study its observational signature with different models of cosmology ; cold and warm dark matter.

**Lausanne, Switzerland**

*Feb 2018 - Jul 2018*

**Semester Project- EPFL**

*Denoising Autoencoder*

**Lausanne, Switzerland**

*Feb 2017 - Jun 2017*

Supervisor: Dr. M. Gentile

Project: PCA and Denoising Autoencoder applied to noisy galaxy images to recover the real ellipticities. Followed the online course *Machine Learning* by Stanford University on Coursera platform.

### Summer research placement - EPFL

Lausanne, Switzerland

*Morphology of Galaxies in Voids*

Jun 2016 - Aug 2016

Supervisor: Dr. E. Ricciardelli

Project: Study of visual morphology of galaxies in voids, compared to more dense populations. First use of astrophysical softwares and large catalogs.

### Third year project - University of Nottingham

Nottingham, UK

*Eclipsing Binary Stars*

Oct 2015 - Jun 2016

Supervisor: Lect. S. Bamford

Project: Image collection of eclipsing binary stars systems at the University's telescope. Data reduction and study of system's properties and the telescope's resolution.

## Academic activities

---

### Collaboration meetings and workshops

DESI Collaboration meeting - <i>online</i>	Dec 2021
DESI Collaboration meeting - <i>online</i>	Mar 2021
DESI Collaboration meeting - <i>online</i>	Dec 2020
DESI Collaboration meeting - <i>online</i>	Mar 2020
DESI Survey Validation and Target Selection workshop - <i>Columbus, USA</i>	Dec 2019
eBOSS Clustering working group workshop - <i>Paris, France</i>	Sep 2019
DESI Collaboration meeting - <i>Berkeley, USA</i>	Jul 2019
eBOSS Collaboration meeting - <i>Paris, France</i>	Dec 2018
DESI Collaboration meeting - <i>Barcelona, Spain</i>	Oct 2018

### Conferences

Colloque national Action Dark Energy 2020 - <i>online</i>	Oct 2020
---	----------

### Outreach

Demonstrator at "Cité des métiers" - <i>Genève, Switzerland</i>	Nov 2018
Public tours of the Observatory of Geneva - <i>Versoix, Switzerland</i>	Jan 2019 - Dec 2021

## Teaching

---

Teaching assistant for the following university courses:

<b>Astrophysics II</b> , BSc Physics at EPFL for Pr. P. Jablonka	FS2021, FS2020, FS2019
<b>Advanced Physics II</b> , BSc Physics at EPFL for Pr. J.-P. Ansermet	SS2021, SS2020
<b>Physics II</b> , BSc Civil Engineering at EPFL for Pr. P. Jablonka	SS2019
<b>Advanced Analysis II</b> , BSc Physics at EPFL for Pr. J. Stubbe	SS2018
<b>Advanced Analysis I</b> , BSc Physics at EPFL for Pr. J. Stubbe	FS2017
<b>Advanced Physics I</b> , BSc Physics at EPFL for Pr. P. Ricci	FS2017

Part of the teaching team for the following high school class:

## Other skills

---

### Languages

**French:** Native   |   **English:** Proficient   |   **German:** Intermediate   |   **Italian:** Elementary

### Computer skills

Python,  $\text{\LaTeX}$ , MATLAB, C++